

## Abstract

# Manipulating and Measuring States of a Superfluid Optomechanical Resonator in the Quantum Regime

Yiqi Wang

2023

Quantum optomechanics describes utilizing optics to precisely manipulate and read out the motional degrees of freedom of a mechanical oscillator. If the mechanical oscillator is very weakly coupled to its environment, then the optomechanical interaction can be used to control the state of the mechanical oscillator in a quantum way. Applying these systems to advanced sensing techniques has inaugurated experiments on dark matter searches, gravitational wave detection, quantum gravitational phenomena tests, and sensing beyond the standard quantum limit. I am motivated by asking: “What is the largest and most tangible object to reveal purely quantum phenomena?” In addition, I seek to use mechanics to explore quantum-enhanced applications.

In this thesis, I describe my work toward preparing quantum states of mechanical motion in a cavity optomechanical system. The system is a Fabry-Pérot cavity that is filled with superfluid helium. A density wave of the helium serves as the mechanical resonator, whose effective mass is  $\sim 1$  ng. The radiation pressure of the light is used as a gentle quantum “drumstick” to control the motion of the helium, while the helium, in exchange, imprints information about its motion on the emitted light. For such a large object, a myriad of different factors conspire to mask quantum effects. However, I can circumvent some of the obstacles by leveraging the material properties of superfluid helium and by using single-photon counting techniques.

In the experiment, I manipulated and characterized the state of the mechanics through optomechanical coupling and by performing photon counting measurements on the scattered light. I measured this mechanical resonator’s second/third/fourth-order coherence functions while it was in a thermal state with less than three phonons. In addition, I drove this mechanical resonator to a nearly coherent state. The state had around two phonons’ worth of fluctuations while its amplitude corresponded to  $4 \times 10^4$  phonons. More striking quantum effects are related to states that are excluded by classical theories. Following the DLCZ protocol, I conditionally prepared non-classical photon-phonon entangled states. Their photon-phonon coherences violated a classical bound set by Cauchy-Schwarz inequality with a four-sigma significance.

I will also discuss our next steps using an even larger cavity to observe more macroscopic and more striking quantum features. Such a system shows prospects for dark matter detection, gravitational wave detection, and testing non-standard modified quantum theory.

Manipulating and Measuring States of a Superfluid Optomechanical  
Resonator in the Quantum Regime

A Dissertation  
Presented to the Faculty of the Graduate School  
of  
Yale University  
in Candidacy for the Degree of  
Doctor of Philosophy

by  
Yiqi Wang

Dissertation Director: Jack G. E. Harris

December 2023

Copyright © 2023 by Yiqi Wang  
All rights reserved.

## Acknowledgments

There are so many people whom I would like to express my gratitude and appreciation to. There are so much invaluable guidance, encouragement, and assistance throughout the past six years that make this achievement possible. I am humbled and honored to have had the privilege of working with so many exceptional individuals throughout this long journey. Their collective contributions have shaped my academic growth and have left an indelible mark on my personal and professional development.

First and foremost, I extend my heartfelt thanks to my advisor, Jack Harris, for his unwavering support and expert guidance. His insightful discussion, constructive feedback, and continuous encouragement played a crucial role in shaping this work and refining my academic abilities. I always remember the discussion with him, big or small, long or short, research or life. I am grateful for his patience, dedication, and belief in my potential. His impact will continue to guide me in my future endeavors.

I am also indebted to the members of my thesis committees, Prof. Rob Schoelkopf and Prof. Shruti Puri, for their valuable insights, constructive suggestions, and rigorous evaluation. Their expertise in the field has immensely enriched the quality of this thesis. I also would like to thank Prof. Cindy Regal for lending her time to read my thesis and providing insightful questions.

I owe my gratitude to the team working on this experiment. I joined this project when the experiment was ready to run. The most indispensable person on this project was, undoubtedly, Yogesh Patil. So many discussions in science, suggestions over my posters and presentations, and advice about my interviews were provided during our time in the lab and on the way we head home. I would also acknowledge Lucy Yu and Sean Frazier for their dedicated efforts on this project. We joined Yale and Harris group the same year and worked on the same project for the past three years. Their contributions have added depth and credibility to this work. There are so many shared memories with the team in the lab, whether it was transferring helium, debugging the experiment, discussing results, or worrying about the future. I also wish the best of luck to the team who are continuing this work for more exciting discoveries.

I am deeply grateful to work on another amazing project, levitated helium drop, with a bunch of awesome people in my first three years. Charles Brown was a senior graduate student when I joined the group, who spent a lot of time working with me and teaching me about the basics of cryogenics, vacuum experiments, and optomechanics. Now as a professor at Yale, he is always willing to advise on my professional development and life. I would like to thank Mehdi Namazi, who was a postdoc working with me and mentored me on experiments. Besides, he is a fun guy to talk to, and always comes up with endless memes. I want to acknowledge Mehmet Tuna Uysal, who worked with us as an undergraduate and contributed greatly to data acquisition and data analysis. I am grateful to Glen Harris. Though we only overlapped for a couple of months, I learned a

lot about superfluid helium and experiment skills from him. It has been a pleasure to work with Igor Brandao, Theophilus Human, who took over the drop experiment after me, and I look forward to seeing more exciting discoveries from this project.

I would like to acknowledge all members of Harris group, an assembly of great people that I was fortunate to work with. Their knowledge and ideas, shared through countless lunches, fruitful discussions after seminars, and presentations in group journal clubs, have broadened my horizons in research and enriched my spirit in life. Thank you Giovanna, Chitres, Justin, Yiming, and many others, for creating a creative and friendly lab atmosphere and making my time at Yale enjoyable. Thanks to our lab alumni Luyao, Haitan, and Jack Sankey for advising me on my career choice.

I would like to express my appreciation to Prof. David Moore, Prof. Laura Newburgh for letting me borrow the equipment and liquid nitrogen when it was an emergency need. I am also thankful to Prof. Meng Cheng, Prof. Radim Filip, Prof. Konrad Lehnert, Prof. Steve Girvin, and Prof. Michel Devoret for meeting with me, asking constructive questions, and discussing science. I would like to acknowledge Prof. Jakob Reichel for helping machine the fibers used in this experiment.

I am extremely thankful to the wonderful administration of the physics department, particularly to Daphne Klemme, for her dedicated help over the past six years. I also would like to acknowledge the support and assistance received from Wright Lab. Vinnie, Dave, and Craig, thank you all for helping me to machine experimental pieces, bearing my coming up with bizarre requirements, and trying your best to accomplish them. Thank you Frank for helping us move cryostats, and fixing various facilities.

Throughout this long journey, there were up and down, happy and frustrating moments. I am fortunate to have some of my best friends to go through these moments and brighten up my time in New Haven. Thank you Bingjun, Hanwen, Junlin, and Tao, for hanging out, hiking, skiing, swimming, playing basketball, dinners, road trips, heading to concerts, celebrating Chinese New Year, having hotpot, helping me move, and countless other things. Thank you Xinyuan, Xiaotie, Zhiyang, and Tianning, for your long-time friendships over the past ten years, numerous chats across continents, sharing your feelings, and listening to my thoughts. Thank you my furry friends, The Dude and Chowder, who always cheer me up and make my time at home lovely.

Finally, I would like to express my deep appreciation to my family for their unconditional love, encouragement, and understanding throughout my life. Their unwavering support has been a constant source of motivation during my years away from home. Particularly, the past three years have been difficult due to COVID and other issues. Every Friday night's phone call from you really comforts me internally.

# Contents

<b>1</b>	<b>Introduction</b>	<b>1</b>
<b>2</b>	<b>Quantum Optomechanics</b>	<b>8</b>
2.1	Optomechanical Dynamics . . . . .	8
2.1.1	Radiation Pressure . . . . .	8
2.1.2	Optical Cavities and Mechanical Resonators . . . . .	10
2.1.3	Optomechanical Coupling . . . . .	12
2.1.4	Dynamical Equations . . . . .	14
2.2	Dynamical Backaction . . . . .	15
2.2.1	Optical Spring Effects and Optomechanical Damping Rates . . .	15
2.2.2	Optomechanical Cooling . . . . .	18
2.3	Optomechanics in the Resolved-Sideband Regime . . . . .	21
2.3.1	Optical Output Spectrum . . . . .	22
2.3.2	Quantum Sideband Asymmetry . . . . .	24
2.4	Figure of Merit: Quantum Optomechanical Device . . . . .	24
2.4.1	Cooperativity . . . . .	25
2.4.2	Strong Coupling . . . . .	27
2.4.3	Photon Blockade Parameter . . . . .	29
2.5	Relevant Optomechanical Regimes . . . . .	30
<b>3</b>	<b>Quantum Statistics</b>	<b>31</b>
3.1	Photon Statistics . . . . .	32
3.1.1	Photon Counting Distribution . . . . .	32
3.1.2	Photon Correlations and Coherences . . . . .	34
3.1.3	Bunching and Anti-Bunching . . . . .	36
3.2	Coherence Functions of Various States . . . . .	40
3.2.1	Zero-Delay Second-Order Coherence . . . . .	40
3.2.2	High-Order Coherence . . . . .	42
3.2.3	Post-Selected States . . . . .	43

3.3	Decoherence of Different states . . . . .	50
3.3.1	Decoherence of a Thermal State . . . . .	50
3.3.2	Decoherence of Post-Selected States . . . . .	54
3.3.3	Decoherence of a Displaced Thermal State . . . . .	56
3.4	Quasi-Probability Distributions . . . . .	57
3.4.1	Quantum Distribution Theory . . . . .	57
3.4.2	General Representation of Quasi-Probability Distributions . . . . .	62
3.4.3	Reconstructing the Wigner Function . . . . .	64
3.4.4	Relation between Moments and Cumulants of the Quasi-Probability Distribution . . . . .	66
3.5	Classical Bounds and Nonclassical Criteria . . . . .	69
3.5.1	Nonclassical States and Nonclassical Criteria . . . . .	69
3.5.2	Hierarchy in Quantum States . . . . .	77
<b>4</b>	<b>Quantum Macroscopicity</b>	<b>79</b>
4.1	Macroscopicity . . . . .	81
4.2	Modified Quantum Theory . . . . .	85
4.2.1	Deformed Commutator . . . . .	85
4.2.2	Nonlocal Dynamics . . . . .	86
<b>5</b>	<b>Superfluid Helium Filled Fabry-Pérot Cavity</b>	<b>90</b>
5.1	Experiment Overview . . . . .	90
5.2	Fiber Fabrication and Device Description . . . . .	92
5.3	Optical Mode and Mechanical Mode . . . . .	93
5.3.1	Optical Mode . . . . .	94
5.3.2	Mechanical Mode . . . . .	96
5.4	Optomechanical Coupling . . . . .	97
5.4.1	Single-Mode Coupling . . . . .	99
5.4.2	Beyond Single-Mode Coupling . . . . .	100
5.4.3	Numerical Simulation . . . . .	104
5.5	Superfluid Helium in Optomechanics . . . . .	108
5.5.1	Mechanical Dissipation in Helium . . . . .	109
5.5.2	Mechanical Nonlinearity . . . . .	111
<b>6</b>	<b>Experiment Setup and System Characterization</b>	<b>113</b>
6.1	Measurement Setups . . . . .	113
6.1.1	Basic Optical Setup . . . . .	113
6.1.2	Measurement Scheme . . . . .	117
6.1.3	Second Optical Setup . . . . .	119
6.1.4	Single-Photon Detector . . . . .	121

6.2	System Characterization . . . . .	127
6.2.1	Optical Resonance . . . . .	127
6.2.2	Mechanical Resonance . . . . .	130
6.3	Characterizing the Optomechanical Coupling . . . . .	132
6.3.1	Spectrum of Photon Counts . . . . .	133
6.3.2	Optomechanical Dynamical Backaction . . . . .	141
6.4	Characterizing Weakly Coupled Mechanical Modes . . . . .	146
<b>7</b>	<b>Thermal States and Phonon Added/Subtracted States</b>	<b>150</b>
7.1	Measuring the Motional State by the Light . . . . .	150
7.1.1	Photon-Phonon Correspondence . . . . .	151
7.1.2	Characterizing the Quantum Sideband Asymmetry . . . . .	152
7.2	Statistics from Photon Counts . . . . .	154
7.2.1	Statistical Estimation of Coherence . . . . .	154
7.2.2	Statistical Confidence of the Estimation . . . . .	154
7.2.3	Constructing the Photon Coherences . . . . .	158
7.2.4	Subtracting Systematic Imperfections . . . . .	160
7.3	Characterizing the Thermal State . . . . .	164
7.3.1	Measuring the Phonon Coherence Functions . . . . .	164
7.3.2	Phonon Coherence Experimental Results . . . . .	165
7.3.3	Characterizing the Power Dependence of the Coherences . . . . .	166
7.3.4	Gaussianity Justification . . . . .	167
7.4	Characterizing Post-Selected States . . . . .	168
<b>8</b>	<b>Displaced Thermal States</b>	<b>171</b>
8.1	Dynamics of a DTS . . . . .	172
8.2	Measurement Setup . . . . .	173
8.3	Experiment Characterization . . . . .	174
8.3.1	Mechanical Susceptibility Measurement . . . . .	175
8.3.2	Linewidth Measurement . . . . .	176
8.3.3	Quantum Sideband Asymmetry . . . . .	177
8.4	Statistics of Displaced Thermal States . . . . .	179
8.4.1	The Second-Order Coherence . . . . .	179
8.4.2	Fano Factor . . . . .	185
8.4.3	Background Characterization and Subtraction . . . . .	188
8.4.4	Unidentified Oscillation Signal . . . . .	193
8.5	Applications of Mechanical Coherent States . . . . .	194
8.5.1	Acoustic Interferometric Measurement . . . . .	194
8.5.2	Constraining a Modified Quantum Theory: Nonlocal Dynamics .	196

<b>9 Photon-Phonon Entangled States</b>	<b>199</b>
9.1 DLCZ Scheme . . . . .	200
9.2 Cross- and Auto-Coherences of Pulses . . . . .	201
9.2.1 Effects of the Exciting Probability . . . . .	203
9.3 Measured Non-classical Photon-Phonon Coherences . . . . .	205
9.3.1 Experiment Setup . . . . .	205
9.3.2 Violating the Cauchy-Schwarz Inequality . . . . .	206
9.3.3 The Time-Dependence of the Cross-Coherence . . . . .	209
9.3.4 Limits on the Non-classicality Witness . . . . .	210
<b>10 Summary and Outlooks</b>	<b>212</b>
10.1 Optomechanics with a macroscopic cavity . . . . .	212
10.1.1 Description of the Macroavity . . . . .	212
10.1.2 Proposed Scientific Goals . . . . .	214
10.2 Conclusion . . . . .	218
<b>Appendices</b>	<b>220</b>
<b>A Theory of Quantum Optomechanics in Superfluid Helium</b>	<b>221</b>
A.1 Introduction . . . . .	221
A.2 Classic Nonlinear Equations for Superfluid Helium Optomechanics . . . . .	221
A.3 Hamiltonian Representations . . . . .	222
A.4 Quantization of the Mechanical Hamiltonian . . . . .	224
A.4.1 Three-Phonon Process . . . . .	225
A.4.2 Perturbed Energy Levels . . . . .	225
A.5 Quantization of the Optomechanical Coupling . . . . .	227
A.5.1 Linear Optomechanical Interaction . . . . .	227
A.5.2 Nonlinear Optomechanical Interaction . . . . .	228
<b>B Basics of a Fabry-Pérot Cavity</b>	<b>230</b>
B.1 Wave Equation and Paraxial Approximation . . . . .	230
B.2 Gaussian Mode in a Fabry-Pérot Cavity . . . . .	231
B.3 Transmission Spectrum of a Fabry-Pérot cavity . . . . .	233
<b>C Gauss-Hermite Quadrature</b>	<b>234</b>
<b>D Asymptotic Behaviors of a Maximum Likelihood Estimator</b>	<b>235</b>
<b>Bibliography</b>	<b>237</b>

# List of Figures

1.1	Schematic of the experiment device . . . . .	4
2.1	Schematic of a Fabry-Pérot cavity with a movable end mirror . . . . .	13
3.1	$g^{(2)}(0)$ of a $m$ -photon-added thermal state as a function of $n_{\text{th}}$ . . . . .	70
3.2	Critical $n_{\text{th}}$ of a $k$ -photon-added thermal state to violate the Chebyshev inequality . . . . .	72
3.3	Cross- and auto- coherences of a single-photon-added/subtracted thermal state as a function of $n_{\text{th}}$ . . . . .	74
3.4	Heirarchy in quantum states . . . . .	78
4.1	Sketch of a superposition of spacetime geometry caused by a massive object in a spatial superposition state . . . . .	80
4.2	Sketch of a cyclic squeezing of a mechanical coherent state . . . . .	88
5.1	Photos of the optomechanical device . . . . .	91
5.2	Assembly of the experimental devices . . . . .	92
5.3	Schematic of different boundaries for optical waves and mechanical waves	103
5.4	Numerical verification of using Hermite-Gaussian modes as eigenstates .	104
5.5	Numerical evaluations of the overlap between the optical intensity and the mechanical amplitude . . . . .	105
5.6	Numerical estimating the overlap owing to the non-Hermiticity and different boundary conditions . . . . .	106
5.7	Measured weakly coupling rates compared to the numerical simulation results . . . . .	107
5.8	Mechanical quality factor as a function of frequency due to the Landau-Beliaev process . . . . .	110
6.1	Schematic of the basic optical setup . . . . .	115
6.2	Time sequence of various controls in the “Lock-Hold” measurement scheme	118
6.3	Drifted count rate spectrum in the “hold” period . . . . .	119

6.4	Addition optical setup to generate optical beat notes . . . . .	120
6.5	Characterization results of the AOM . . . . .	122
6.6	Voltage signal of photons measured by the SNSPD . . . . .	123
6.7	Characterization of SNSPD afterpulsing effects and bursts of counts . . . . .	125
6.8	The bias current dependence of the performance of the SNSPD . . . . .	127
6.9	SNSPD false counts at various bias currents . . . . .	128
6.10	Measurd spectrum of one optical mode . . . . .	129
6.11	Measured optical resonance frequencies of a filled cavity . . . . .	130
6.12	Experimental characterization of mechanical modes . . . . .	131
6.13	Schematic of continuous drive setup and the optical spectrum in continuous drive scheme . . . . .	134
6.14	Measured photon count rate spectrum . . . . .	137
6.15	Photon count spectrum optical input power dependence . . . . .	140
6.16	The power-dependence of the optomechanical backactions . . . . .	142
6.17	Optomechanical parametric amplification effect . . . . .	145
6.18	Spectrum of the weakly coupled mechanical modes . . . . .	147
6.19	The power dependence of a weakly coupled transverse mode . . . . .	148
7.1	Sideband count rates as a function of $T_{MC}$ . . . . .	153
7.2	Schematic of the effect of the finite acquisition time . . . . .	161
7.3	Measured second-/third-/fourth-order coherence functions of a mechanical thermal state . . . . .	165
7.4	The power dependence of the mechanical thermal state coherences . . . . .	167
7.5	Mean phonon occupancies and coherences of post-selected states . . . . .	169
8.1	Schematic of the Wigner function of a displaced thermal state . . . . .	172
8.2	Schematics of the optical setup for preparing DTS . . . . .	173
8.3	Schematic of the circuit to generate the RF drive to the AOM . . . . .	174
8.4	The power dependence of the displaced thermal state . . . . .	175
8.5	Ring-down measurement of a driven state . . . . .	176
8.6	Driven states response spectrum . . . . .	177
8.7	Quantum sideband asymmetry of the driven states . . . . .	178
8.8	Examples of the displaced thermal states coherences . . . . .	180
8.9	Coherences of displaced thermal states . . . . .	181
8.10	Mechanical linewidths and $g_m^{(2)}(0)$ of displaced thermal states . . . . .	182
8.11	Fano factors of displaced thermal states . . . . .	186
8.12	Schematics of the experiment settings to characterize different contributions to Fano factors . . . . .	187
8.13	The heating effect of the drive power . . . . .	188
8.14	Example of subtracting an off-set in measured coherence . . . . .	189

8.15	The bias current dependence of the background Coherence . . . . .	190
8.16	Subtracting classical coherence background . . . . .	192
8.17	Unidentified rare oscillation signal in coherence . . . . .	193
8.18	SQL in an acoustic interferometric measurement . . . . .	195
8.19	Constraining nonlocality length scale . . . . .	198
9.1	Pulsed optomechanical interactions in frequency space and DLCZ scheme	200
9.2	$g_{r b}^{(2)}(0)$ as a function of $n_m$ at various $p_b$ . . . . .	204
9.3	Schematics of the DLCZ experiment setup and pulsed sequence . . . . .	206
9.4	Count rates of two pulsed drives . . . . .	207
9.5	Violation of the Cauchy-Schwarz inequality . . . . .	208
9.6	The delay-time dependence of the value of cross-coherences . . . . .	209
9.7	Limit of the non-classicality witness . . . . .	210
10.1	Photos of a macro cavity . . . . .	213
10.2	Schematic of the new filter cavities . . . . .	214
10.3	Ground State cooling of the macro-cavity . . . . .	215
10.4	Expected violation of the Cauchy-Schwarz inequality in the macro-cavity	216
10.5	Expected Hanbury-Brown-Twiss effects in the macro-cavity . . . . .	216
10.6	Schematic of the proposed experimental setup to entangle multiple devices	218

# List of Symbols

$\alpha$	Optical field amplitude	1
$\alpha_{3\text{pp}}$	Acoustic amplitude attenuation coefficient due to three-phonon scattering	$\text{m}^{-1}$
$\alpha_{\text{ovlp}}$	Normalized dimensionless overlap function between the profiles of the optical intensity and the mechanical mode	1
$\beta_0$	Dimensionless parameter characterizing modification of the commutator	1
$\chi_{\text{cav}}$	Optical susceptibility	s
$\chi_{\text{m,eff}}$	Effective mechanical susceptibility including optomechanical backactions	$\text{kg s}^{-2}$
$\chi_{\text{m}}$	Mechanical susceptibility	$\text{kg s}^{-2}$
$\delta\hat{a}, \delta\hat{a}^\dagger$	Ladder operators for the optical fluctuation	$\text{s}^{-1}$
$\Delta p$	Pressure fluctuation in the liquid helium	Pa
$\Delta t_{\text{bin}}$	Time bin size in data analysis	s
$\Delta$	Optical detuning in a rotating frame of $\omega_L$ , $\Delta = \omega - \omega_L$	$\text{s}^{-1}$
$\delta\omega$	Optomechanics induced mechanical frequency shift	$\text{s}^{-1}$
$\Delta\omega_{\text{FSR,emptycav}}$	Free spectral range of the empty optical cavity	$\text{s}^{-1}$
$\Delta\omega_{\text{FSR,filledcav}}$	Free spectral range of the optical cavity filled with liquid helium	$\text{s}^{-1}$
$\Delta\omega_{\text{FSR,m}}$	Free spectral range of the mechanical oscillator	$\text{s}^{-1}$
$\Delta\omega_{\text{FSR}}$	Free spectral range	$\text{s}^{-1}$
$\delta\omega_{\text{Trans,emptycav}}$	Transverse mode splitting of the empty optical cavity	$\text{s}^{-1}$
$\delta\omega_{\text{Trans,m}}$	Transverse mode splitting of the mechanical oscillator	$\text{s}^{-1}$

$\epsilon$	Dimensionless parameter that characterizes the nonlocal dynamics in Ref. [1]	1
$\epsilon$	Ratio of the dark photon count rate to the scattered photon count rate	1
$\epsilon$	Ratio of the nonlocality length scale to the zero-point-fluctuation of an oscillator, $\epsilon(l_k/x_{ZPF})^2 \$$	1
$\epsilon_0$	Vacuum permittivity	$\text{C V}^{-1}\text{m}^{-1}$
$\eta_\kappa$	Input coupling efficiency	1
$\eta_{\text{det}}$	Total measurement efficiency	1
$\eta_{\text{FCI}}$	Maximal transmission rate of the filter cavity FCI	1
$\eta_{\text{misc}}$	Transmission rate of fibers and connections	1
$\eta_{\text{SNSPD}}$	Maximal measurement efficiency of the SNSPD	1
$\eta_{\text{supp,tot}}$	Suppression rate of two filter cavities	1
$\gamma_3$	Coefficient for the cubic term in the phonon dispersion	$\text{kg}^{-2} \text{ m}^{-2} \text{ s}^2$
$\gamma_{3\text{pp}}$	Three-phonon scattering induced mechanical damping rate	$\text{s}^{-1}$
$\Gamma_{\text{AS}}$	Anti-Stokes scattered arrival photon rate	$\text{s}^{-1}$
$\gamma_{\text{AS}}$	Anti-Stokes scattering rate	$\text{s}^{-1}$
$\Gamma_{\text{bkg}}$	Background photon count rate	$\text{s}^{-1}$
$\gamma_{\text{eff}}$	Effective mechanical damping rate	$\text{s}^{-1}$
$\Gamma_G$	GAWBS scattered photon count rate	$\text{s}^{-1}$
$\gamma_{m0}$	Intrinsic mechanical damping rate	$\text{s}^{-1}$
$\gamma_m$	Mechanical mode decay rate	$\text{s}^{-1}$
$\gamma_{\text{opt}}$	Optomechanics induced mechanical damping rate	$\text{s}^{-1}$
$\Gamma_{\text{QSA}}$	The difference between the Stokes and the anti-Stokes scattering count rates	$\text{s}^{-1}$
$\Gamma_{\text{res}}$	On-resonance photon count rate	$\text{s}^{-1}$
$\Gamma_S$	Stokes scattered arrival photon rate	$\text{s}^{-1}$
$\gamma_S$	Stokes scattering rate	$\text{s}^{-1}$

$\hat{\epsilon}, \hat{\epsilon}^\dagger$	Ladder operators for background photons	1
$\hat{D}(\alpha)$	The displacement operator $\hat{D}(\alpha) = \exp(\alpha\hat{a}^\dagger - \alpha^*\hat{a})$	1
$\hat{\mathcal{L}}_1$	Lindblad generator	1
$\hat{\mathcal{S}}(\zeta)$	Squeezing operator with squeezing amplitude $\zeta$ defined as $\hat{\mathcal{S}}(\zeta) \equiv \exp\left[\frac{1}{2}\left(\zeta^*\hat{a}^2 - \zeta\hat{a}^\dagger\hat{a}\right)\right]$	1
$\hat{\omega}$	Expected mechanical resonance frequency from the optical resonance	$\text{s}^{-1}$
$\hat{\rho}_{+k}$	Density matrix of a $k$ -photon-added thermal state	1
$\hat{\rho}_{-k}$	Density matrix of a $k$ -photon-subtracted thermal state	1
$\hat{\rho}_{\text{th}}$	Density matrix operator of a thermal state	1
$\hat{\rho}_{n_{\text{th}}}$	Density matrix of a thermal state with a mean occupancy $n_{\text{th}}$	1
$\hat{a}$	Annihilation operator for the optical mode	1
$\hat{a}^\dagger$	Creation operator for the optical mode	1
$\hat{a}_{\text{AS}}$	Operator of the anti-Stokes scattered optical field	1
$\hat{a}_{\text{in}}$	Input optical field operator	$\text{s}^{-1/2}$
$\hat{a}_{\text{out,b(r)}}$	Operator of the output field from a blue(red)-detuned input	1
$\hat{a}_{\text{out}}$	Output optical field operator	$\text{s}^{-1/2}$
$\hat{a}_{\text{S}}$	Operator of the Stokes scattered optical field	1
$\hat{b}$	Annihilation operator for the mechanical mode	1
$\hat{b}^\dagger$	Creation operator for the mechanical mode	1
$\hat{d}$	The fluctuation of a displaced state $\hat{d} = \hat{a} - \alpha$	1
$\hat{d}_{\text{in}}$	The fluctuation of the input field $\hat{d}_{\text{in}} = \hat{a}_{\text{in}} - \alpha$	$\text{s}^{-1/2}$
$\hat{f}_{\text{in}}$	Internal input drive operator	$\text{s}^{-1/2}$
$\hat{g}_{E_1, E_2}^{(2)}(\tau)$	Estimated cross-coherence function of $E_1$ and $E_2$	1
$\hat{g}_{\text{ML}}^{(2)}(\tau)$	Estimated $g^{(2)}(\tau)$ based on Maximum Likelihood estimation	1
$\hat{p}$	Estimated probability $p$	1

$\hat{p}$	Operator of the optical field that is from blue(red)-detuned inputs and passes through filter cavities	1
$\hat{p}$	Operator of the optical field that passes through filter cavities	1
$\hat{p}(E)$	Estimated probability of the event E	1
$\kappa$	Optical cavity total decay rate	$s^{-1}$
$\kappa_0$	Optical cavity internal decay rate	$s^{-1}$
$\kappa_{ex}$	Optical cavity external decay rate	$s^{-1}$
$\kappa_{FCi}$	Linewidth of the cascade filter cavity FCi	$s^{-1}$
$\kappa_{FCi}$	Linewidth of the cascade filter cavity FCi	$s^{-1}$
$\kappa_{GAWBS}$	Linewidth of the GAWBS mode	$s^{-1}$
$\kappa_L$	“Linewidth” of the input laser	$s^{-1}$
$\kappa_{NBFC}$	Linewidth of the narrowband filter cavity	$s^{-1}$
$\kappa_n$	n-th cumulant	1
$\lambda(t)$	The relative coherence function $\lambda(t) = g^{(2)}(t) - 1$	1
$\lambda_{cav}$	Photon blockade parameter	1
$\lambda_m$	Wavelength of the mechanical wave	m
$\mathbf{B}$	Magnetic field	T
$\mathbf{E}$	Electric field	$V m^{-1}$
$\mathbf{g}$	Electromagnetic momentum density	$kg s^{-1} m^{-2}$
$\mathbf{S}$	Poynting vector	$W m^{-2}$
$\mathcal{C}$	Optomechanical cooperativity	1
$\mathcal{C}_0$	Single-photon optomechanical cooperativity $\mathcal{C}_0 = \mathcal{C}/n_{cav}$	1
$\mathcal{C}_{qu}$	Quantum optomechanical cooperativity $\mathcal{C}_{qu} = \mathcal{C}/n_{m,th}$	1
$\mathcal{D}$	Photon blockade parameter	1
$\mathcal{F}_{cav}$	Finesse of the cavity	1

$\mathcal{F}_m$	Finesse of the mechanical mode	1
$\mathcal{S}$	Schrödinger operator	J s
$\mu$	Grüneisen constant	1
$\mu$	Macroscopicity defined in Ref. [2]	1
$\mu_0$	Vacuum permeability	$\text{kg m s}^{-2}\text{A}^{-2}$
$\mu_n$	n-th moment	1
$\omega_{\text{cav}}$	Optical mode resonance frequency	$\text{s}^{-1}$
$\omega_d$	Drive beat note frequency	$\text{s}^{-1}$
$\omega_{\text{GAWBS}}$	Resonance frequency of the GAWBS mode	$\text{s}^{-1}$
$\omega_L$	Input laser frequency	$\text{s}^{-1}$
$\omega_m$	Mechanical mode resonance frequency	$\text{s}^{-1}$
$\overleftrightarrow{\mathbf{T}}$	Maxwell stress tensor	$\text{N m}^{-2}$
$\overleftrightarrow{T}$	Mechanical stress tensor	$\text{kg m}^{-1} \text{s}^{-2}$
$\phi_G$	Guoy phase shift	rad
$\Pi_{xp}$	Parity operator in the phase space	1
$\psi$	Normalized density wave function	1
$\rho$	Mass density	$\text{kg m}^{-3}$
$\rho$	Mass density of liquid helium	$\text{kg m}^{-3}$
$\rho_0$	Average mass density of liquid helium	$\text{kg m}^{-3}$
$\sigma_n$	Standard deviation of $n$	1
$\tau$	Delay time between two events	s
$\tau_e$	Single electron coherence time	s
$\tau_{\text{AOM,th}}$	Thermal transient time scale of the AOM	s
$\tau_{\text{ap}}$	Time constant of the afterpulsing effect	s
$\tau_c$	Decoherence time	s

$\tau_D$	Dead time of the detector	s
$\tilde{\rho}$	Normalized changed of the mass density $\tilde{\rho} = (\rho - \rho_0)/\rho_0$	1
$\tilde{\rho}$	Weyl-transformed density matrix	1
$\tilde{\rho}_0$	Normalized zero-point fluctuation of the mass density	1
$\tilde{p}$	Dimensionless momentum $\tilde{p} = p/\sqrt{\hbar m \omega_0}$	1
$\tilde{q}$	Dimensionless position $\tilde{q} = \sqrt{(m\omega_0)}/\hbar q$	1
$\tilde{x}, \tilde{p}, \tilde{t}$	Dimensionless variables, defined as $\tilde{x} \equiv x/x_{ZPF}$ , $\tilde{p} \equiv p/p_{ZPF}$ , and $\tilde{t} \equiv \omega t$	1
$\varsigma$	The correction coefficient of the mechanical mode energy level in liquid	1
$\xi$	The ratio of the thermal phonon number to the displacement amplitude square $\epsilon = n_{th}/ \alpha ^2$	1
$\{A, B\}$	Poisson bracket of $A$ and $B$	1
$A^-, A^+$	Downward transitions and upwards transitions rates in the mechanical state	$s^{-1}$
$c$	Speed of light in vacuum	$m s^{-1}$
$C(E)$	Number of success events E	1
$C_{S/A/N}^{[\hat{\rho}]}(\lambda)$	Characteristic functions of the Wigner, $Q$ - and $P$ -representation of a state $\hat{\rho}$	1
$F$	Fano factor	1
$f_{\text{filter}(\omega)}$	Transfer function of the two filter cavities	1
$f_{\text{GAWBS}}$	Susceptibility of GAWBS modes	1
$G$	Optomechanical coupling strength	$m^{-1}s^{-1}$
$g$	Fabry-Pérot cavity g-parameter	1
$g$	Multi-photon optomechanical coupling strength	$s^{-1}$
$g_{a,b}^{(2)}$	Cross coherence function between states $\hat{a}$ and $\hat{b}$	1
$G^{(n)}$	The $n$ th-order normally ordered correlation function	1
$g^{(n)}$	The $n$ th-order normally ordered coherence function	1
$g_m^{(n)}(\tau)$	$n$ -th order anti-normally ordered coherence function of the mechanical oscillator	1

$g_{\text{pred}}^{(n)}(0)$	Predicted $n$ -th order coherence function of the mechanical oscillator	1
$g_0$	Single photon optomechanical coupling strength $g_0 = Gx_{\text{ZPF}}$	$\text{s}^{-1}$
$g_{\text{bkg}}^{(2)}$	Second-order coherence function of background photons	1
$g_{\text{DTS}}^{(2)}$	Second-order coherence function of a DTS	1
$g_E$	Coupling strength between the mechanical mode and an external oscillator	$\$ \text{s}^{-1}$
$g_{\text{pt}}$	Single photon photothermal coupling strength	$\text{s}^{-1}$
$g_{\text{r b}}^{(2)}(\tau)$	Cross-coherence of blue-detuned and red-detuned pulses	1
$g_{\text{r r}}^{(2)}(\tau), g_{\text{b b}}^{(2)}(\tau)$	Auto-coherences of the blue- or red-detuned pulse	1
$g_{\text{ta}}$	Single photon heating rate	$\text{s}^{-1} \text{ K}^{-1}$
$g_T$	Coupling rate between the mechanical modes and the temperature fluctuations	$\text{s}^{-1} \text{ K}^{-1}$
$h^{(n)}$	The $n$ th-order anti-normally ordered coherence function	1
$h_m^{(n)}(\tau)$	$n$ -th order normally ordered coherence function of the mechanical oscillator	1
$H_m$	Hermite polynomial of order $m$	1
$k^{(q,m,n)}$	Wave number of a Hermite-Gaussian mode $(q, m, n)$	$\text{m}^{-1}$
$L_{\text{cav}}$	Optical cavity length	m
$l_k$	Non-locality length scale	m
$l_P$	Planck length	m
$m_e$	Mass of an electron	m
$m_{\text{eff}}$	Effective mass of the oscillator	kg
$n$	Sequence index in a repeated experiment	1
$n_{\text{m,th}}^{\text{DTS}}$	Effective phonon occupancy of the displaced thermal state	1
$n_{\text{cav,th}}$	Photon occupancy due to the thermal bath	1
$n_{\text{cav}}$	Intra-cavity circulating photon number	1
$n_f$	Final phonon number after sideband cooling	1

$n_{\text{He}}$	Refractive index of liquid helium	1
$n_{\text{init}}$	Initial phonon number before sideband cooling	1
$n_{\text{m,base}}$	Phonon number corresponds to the base temperature	1
$n_{\text{m,d}}$	Driven phonon number	1
$n_{\text{m,heat}}$	Phonon number of a thermal bath including the all laser inputs	1
$n_{\text{m,probe}}$	Phonon number of a thermal bath including the probe laser input	1
$n_{\text{m,th}}$	Phonon occupancy due to the thermal bath	1
$n_{\text{min}}$	Minimal phonon number that can be achieved by the sideband cooling	1
$n_{\text{m}}$	Phonon occupancy of a mechanical mode	1
$n_{\text{m}}^{\pm k}$	Mean phonon occupancy of a $k$ -phonon added/subtracted state	1
$n_{\text{th}}$	Thermal occupancy $n_{\text{th}} = 1 / (\exp [\hbar\omega/k_{\text{B}}T] - 1)$	1
$n_{\text{th}}^{\pm k}$	Mean phonon occupancy of a $k$ -phonon added/subtracted thermal state	1
$p$	Pressure in liquid helium	$\text{kg m}^{-1} \text{s}^{-2}$
$p$	$p$ -value of the null-hypothesis test	1
$P(\alpha)$	$P$ -function of a state	1
$p(\text{E})$	Probability of the event E	1
$P_n$	The probability to find $n$ photons	1
$P_1$	Power of the optical drive at $\omega = -\omega_{\text{m}}/2$	W
$P_2$	Power of the output optical field from AOM	W
$P_{\text{b(r)}}$	Optical power of the blue(red)-detuned pulse	W
$p_{\text{b}}$	Exciting probability of a blue-detuned pulse	1
$P_{\text{in}}$	Input optical power to AOM	W
$P_{\text{in}}$	Input power into the cavity	W
$P_{\text{RF}}$	RF power to AOM	W
$p_{\text{r}}$	Reading probability of a red-detuned pulse	1

$P_{\text{threshold}}$	Threshold power of the blue-detuned drive	W
$P_{\text{th}}(k, \lambda)$	Probability distribution of a thermal state with a mean occupancy $\lambda$	1
$p_{\text{ZPF}}$	Momentum zero-point fluctuation of a harmonic oscillator	$\text{kg m s}^{-1}$
$Q(\alpha)$	$Q$ -function of a state	1
$Q_m$	Mechanical quality factor	1
$R$	Photon count rate	$\text{s}^{-1}$
$R$	Radius of curvature of the Gaussian mode wavefront	m
$r_1, r_2$	Radii of curvature of two end mirrors in the fiber cavity	m
$S_{xx}^{\text{add}}(\omega)$	Added noise spectrum of the measured displacement \$	$\text{m}^2 \text{ s}$
$S_{xx}^{\text{imp}}(\omega)$	Impresion noise spectrum of the measured displacement \$	$\text{m}^2 \text{ s}$
$S_{\hat{a}_{\text{out}}^\dagger \hat{a}_{\text{out}}}(\omega)$	Spectrum of the output field $\hat{a}_{\text{out}}$	$\text{s}^{-1}$
$S_{\hat{b}^\dagger \hat{b}}(\omega)$	Spectrum of $\hat{b}^\dagger \hat{b}$	$\text{s}^{-1}$
$S_{\hat{x}\hat{x}}(\omega)$	Spectrum of the displacement $\hat{x}$	$\text{m}^2 \text{ s}^{-1}$
$S_{\sigma\sigma}$	Spectrum of the intensity fluctuation	$\text{s}^{-1}$
$S_{FF}(\omega)$	Spectrum of the radiation pressure force	$\text{J}^2 \text{ s}^2 \text{ m}^{-1}$
$T_{\text{aq}}$	Data acquisition time	s
$t_{\text{b(r)}}$	Duration of the blue(red)-detuned pulse	s
$T_{\text{bath}}$	Temperature of the thermal bath	K
$t_{\text{delay}}$	Delay time between the end of the “write” pulse and the begining of the “read” pulse	s
$T_{\text{fiber}}$	Temperature of the fiber	K
$T_{\text{MC}}$	Mixing chamber temperature	K
$V$	Bell inequality visibility	1
$V_{\text{eff}}$	Effective volume of the mechanical mode	$\text{m}^3$
$v_{\text{fiber}}$	Speed of sound in fiber	$\text{m s}^{-1}$

$v_{\text{He}}$	Speed of sound in liquid helium	$\text{m s}^{-1}$
$W(x, p)$	Wigner-function of a state	1
$w(z)$	Beam radius of the Gaussian mode at $z$	m
$w_0$	Beam waist of the Gaussian mode	m
$x$	Displacement of a harmonic oscillator	m
$x_{\text{ZPF}}$	Zero-point fluctuation amplitude of a mechanical oscillator $x_{\text{ZPF}} = \sqrt{\frac{\hbar}{2m_{\text{eff}}\omega_m}}$	m
$Z_{\text{fiber}}$	Acoustic impedance of the fiber	$\text{kg m}^{-2}\text{s}^{-1}$
$Z_{\text{He}}$	Acoustic impedance of liquid helium	$\text{kg m}^{-2}\text{s}^{-1}$
$g_{\text{exp}}^{(2)}(\tau)$	Estimated $g^{(2)}(\tau)$ based on the experiment result	1

*“Quantum phenomena do not occur in a Hilbert space. They occur in a laboratory.”*

– Asher Peres

# CHAPTER 1

## Introduction

In my graduate research, as an experimentalist, I am always motivated by asking

*“What is the most macroscopic and tangible object which preserves purely quantum effects?”*

In the past century, quantum mechanics has revolutionized people’s understanding of physics and led to numerous applications. Today, there is a growing demand for the preparation of various quantum states across different platforms in order to fully utilize quantum-enhanced advantages in sensing, information, and computation [3, 4]. However, one challenge lies in the fact that while quantum mechanics is well-established in microscopic systems such as atoms and molecules, it becomes increasingly difficult to demonstrate these phenomena on a macroscopic scale. Experimentally demonstrating quantum phenomena in larger objects<sup>1</sup> would lay the groundwork for scaling up quantum machines, such as quantum computers of larger geometric size and quantum sensors of larger mass and size. Moreover, it would provide opportunities to test quantum mechanics in previously inaccessible regimes. Such tests could constrain a number of modified quantum theories that have been proposed even for years, whose differences with usual quantum mechanics are most evident at macroscopic scales [5–9].

On the application side, we seek to use these purely quantum effects to store, transmit and even process information in an essentially quantum way. This leads to various applications in different fields. For instance, certain quantum states manifest information capacities outperforming any classical states (defined as a state whose quasi-probability function is non-negative) prepared in the same object, which advances communication [10–16]. In the job of sensing, quantum states such as squeezed states [17–20], Fock states [21], superposition states[22], or entangled states [23–25] can be used to surpass the standard quantum limit. Regarding computation, replacing classical bits of information with quantum states of two-level systems (known as qubits) has been shown to lead to speed up for solving certain problems [26–31].

---

<sup>1</sup>Large objects can refer to a system of many degrees of freedom and a system with a large geometric size and a large mass. The latter is the focus of this thesis.

On the fundamental side, the two pearls of theoretical physics discoveries in the 20th century, quantum mechanics and general relativity, accurately describe the dynamics of microscopic systems on one hand, and the geometry of spacetime in gravitationally dominated systems on the other hand. A natural question to raise is, what will happen if we preserve quantum mechanical phenomena, such as superposition or entanglement, in large objects such that we can also measure their gravitational effects [32, 33]? In addition to this purely empirical curiosity, there are reasons to question the applicability of quantum theory beyond certain scales. One of them is that it is difficult to reconcile quantum theory with general relativity, in which spacetime itself is treated as a dynamic quantity. More intuitively speaking, in quantum mechanics, a massive object can be prepared in a spatial superposition state. According to general relativity, any mass will curve space-time. Therefore, it leads to a super-positioned spacetime, which is not well-defined in general relativity [34–36]. The experimental observation of macroscopic quantum phenomena is well-motivated to test new theoretical frameworks [1, 9, 37–39] or may even lead to new scientific discoveries.

The manifestation of quantum effects in a large object is often hindered by a variety of factors, for example in the very short de Broglie wavelengths on very closely spaced energy levels associated with large objects. In addition, it is extremely challenging to isolate a large object from its environment. Coupling to an uncontrolled and unmeasured environment generically leads to the loss of quantum effects.

Nevertheless, with meticulous and precisely controlled experiments, purely quantum effects can be revealed. Mechanical resonators are regarded as an excellent system to test quantum mechanics, as their isolation, coupling, and hybridization can be engineered and controlled in the quantum regime [40–42]. Mechanical resonators also offer tremendous potential as components of hybrid quantum systems, as they can be integrated with superconducting qubits, photons, and spins, due to their ability to couple to a broad range of forces while being nearly isolated from the environment.

Optomechanics (as evident from its etymological origin) describes utilizing optics to precisely manipulate and read out the motional degrees of freedom of a mechanical oscillator [43–50]. The radiation pressure of the light is used as a gentle “drumstick” to drive the motion of the mechanical resonator. The mechanical resonator, in exchange, imprints its motion on the light. This interaction is unitary, which means the optical and the mechanical systems evolve coherently.

Experiments that use near-infrared and visible light can take advantage of the fact that these frequencies are high enough that their quantum states can be preserved at room temperature. Moreover, well-developed technology exists for controlling and producing a range of quantum states, which can be transferred from light to motion via the unitary optomechanical interaction. Therefore, this system allows for manipulations and measurements of the state of the mechanical resonator in the quantum regime.

The implementations of optomechanical systems vary in size, frequency scale, and the

manner of coupling [18, 51–54]. The common idea behind the different designs is that an optical resonator is detuned by the motion of some mechanical element, and the radiation pressure of the optical field modulates the mechanical motion in turn. For example, there are cavities with moveable end mirrors, such as LIGO [18, 55]. The positions of the mirrors change the cavity length and therefore the cavity resonance frequency. Alternatively, a mechanical resonator placed in the middle of a rigid optical cavity can also modulate the cavity frequency (this approach is used by the membrane in the middle or levitated particles experiments [52, 54, 56]). Optomechanical crystals, which are nanodevices with periodic patterns in a dielectric material that supports both optical and mechanical modes, are another extremely successful implementation [51, 57]. Moreover, to extend ideas into the microwave domain, a superconducting LC circuit couples to the vibrations of the capacitor or the inductor in a manner that results in the same physics as optics-based optomechanical systems [58–62]. These microwave systems are of special interest because of the significant development in superconductor-based quantum computers.

In general, low losses in mechanical modes, high optical finesse, strong optomechanical coupling, and cryogenic temperature are all preferred for quantum optomechanics. The goal is that the overall unitary coupling strength overcomes all kinds of dissipations in the system, which is a milestone for applications and tests in the quantum world.

To overcome the aforementioned challenges, the work described in this thesis used an optomechanical system that is built using superfluid helium. Superfluid helium offers plenty of material properties that benefit optomechanical applications, such as ultra-low optical absorption and ultra-low acoustic loss [63]. Hence, superfluid helium is possibly the best material to host quantum effects on the macroscopic scale.

It is distinct from most quantum optical and quantum acoustic materials in that it is a liquid. As the ancient Chinese philosopher Laozi described water, “天下之至柔，驰骋天下之至坚。”<sup>2</sup> It means: “The world’s most flexible gallops between the world’s most firm.” Unlike most conventional solid-based devices, the geometry of the liquid in our devices is defined by its “container” and the mechanical mode frequency can be tuned over a wide range via straightforward pressurization. Liquid helium can also be hybridized with other quantum systems. For instance, experiments on electron bubbles in helium [64, 65], ions in helium [66, 67] and electrons on helium surfaces [68, 69] have been experimentally demonstrated.

In my experiment, the optomechanical system is a superfluid-helium-filled optical cavity. Fig. 1.1 shows a schematic of the device. We start with a miniature Fabry-Pérot cavity formed between the end faces of two optical fibers. The two fibers are 200 μm in diameter with their end faces separated by ~70 μm. The alignment is achieved using a glass ferrule, which confines two fibers coaxially. This empty cavity is filled with superfluid helium. The experiment is operated in a dilution fridge at a temperature ~20 mK.

---

<sup>2</sup>Quoted from Chapter 43, 《Tao Te Ching (道德经)》

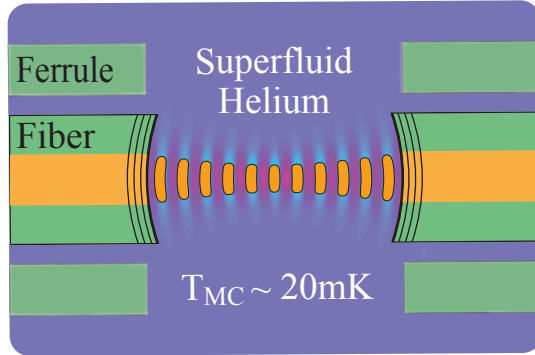


Figure 1.1: Device schematic: An optical Fabry-Pérot cavity, which is formed by two fiber end faces, is filled with superfluid  $^4\text{He}$ . Blue shading denotes the instantaneous  $^4\text{He}$  density in a mechanical mode. Orange denotes the optical mode intensity.

We coated the fiber end faces with highly reflective mirrors for optical waves with a wavelength equal to 1550 nm. The optical mode studied in this thesis is a Hermite-Gaussian mode. The mechanical resonator is the density wave of the liquid helium confined by the same end faces, as shown in the blue shadings of Fig. 1.1. The effective mass of the mechanical mode (defined in Eq. 2.16) is  $\sim 1 \text{ ng}$ .

The optomechanical interaction is mainly achieved by the photoelastic effect. More specifically, helium is attracted to the high optical intensity area by the electrostrictive force, while the density wave of helium detunes the optical resonance frequency. This coupling is unitary, and its strength is proportional to the overlap between the intensity of the optical mode and the amplitude (*i.e.*, change of helium density) of the mechanical mode.

The mechanical mode and the optical mode are determined by the same differential equations and the same boundary conditions, resulting in the same spatial eigenmodes for both the optical and the mechanical resonators. Since different eigenmodes are orthogonal to each other, it is straightforward to show that, to a good approximation, only one mechanical mode couples to any given optical mode. This relation is named the single-mode optomechanical coupling.

In the measurement, we employed single photon counting techniques to achieve the required quantum measurement and control. This is because the information about the mechanical state is transferred into the optical output, which is sent to single photon detectors. The mechanical state can be characterized by the arrival time of photons. Furthermore, we utilize the so-called measurement-backaction-induced nonlinearity to conditionally prepare some quantum states. This is possible because the arrival of one Stokes/anti-Stokes photon heralds the addition/subtraction of one phonon to/from the mechanical mode. Therefore, the state of the mechanics can be post-selected by performing

photon counting measurements on the light emerging from the cavity.

As a proof-of-principle demonstration, we first characterized a mechanical thermal state under this scheme. The mechanical mode with resonance frequency  $\omega_m/2\pi \sim 315$  MHz, which coupled to the 1550 nm optical mode, was thermalized to near its ground state [70–72]. The phonon occupancy was determined from the asymmetric photon count rates of the two mechanical sidebands. The high-order coherences of arrival photons were also measured, and verified the Gaussianity of the thermal state with a high degree of statistical significance [72].

In separate measurements, we drove the mechanical mode using an optical beat note, producing a displaced thermal state. The first- and second-order coherences of anti-Stokes scattered photons were used to characterize this state. We experimentally demonstrated that the mechanical mode maintained around two phonons' worth of thermal fluctuation while being driven to a coherent amplitude corresponding to  $4 \times 10^4$  phonons.

More striking quantum effects and quantum advantages are related to states which are excluded by classical theory [3, 4, 73]. Following the DLCZ protocol [74–76], a non-classical photon-phonon entangled state was conditionally prepared. The measured photon-phonon cross-correlation violated a classical bound with four-sigma significance, which verified the non-classicality of the state.

Along this line, we are still exploring even larger mechanical resonators in more exotic quantum states, like mechanical non-Gaussian states and squeezed states. Furthermore, we are also aiming to entangle massive resonators separated in space. These massive macroscopic resonators in quantum regimes also hold promise for developing hybrid quantum technologies that exploit the enhanced sensing and measurement capabilities of quantum mechanics.

The main objective of this thesis is to give a comprehensive account of the experiments that were carried out during my graduate studies. Additionally, the thesis provides a concise overview of quantum optomechanics, quantum statistics, and macroscopic quantum effects, along with the theoretical results that I derived in order to analyze and interpret our data. Finally, I also offer a glimpse into the future prospects of this experiment with some straightforward calculations.

The main structure of the thesis is as follows:

- **Chapter 2** In this chapter, I present a brief overview of quantum optomechanics. The chapter begins with a simplified classical model, which is used to derive the fundamental optomechanical dynamics in detail. This is followed by a discussion centered on the phenomena in the resolved-sideband regime, as this is relevant to the experiment in this thesis. To compare the performance of different systems, I also discuss the figure of merit for quantum optomechanics systems. Finally, the basic parameters of the device used in this work are provided to address the relevant optomechanical effects discussed in this chapter.

- **Chapter 3** This chapter aims to discuss the statistical properties of quantum states that are relevant to the experiment in this thesis. I start with a brief overview of photon statistics, including photon counting statistics, correlations, and coherences. Especially, I focus on the coherence functions of various relevant states because coherences are independent of the detection efficiency. Detailed derivations of the decoherence process of some relevant states are also provided. Additionally, this chapter also briefly discusses different quasi-probability distributions and their relations to coherence functions. Finally, I discuss various criteria in the experiment to distinguish non-classical states from classical states.
- **Chapter 4** This chapter briefly discusses the motivation for studying macroscopic quantum phenomena. I talk about one possible measure to access the macroscopicity of the quantum phenomena across different platforms. Then, I focus on two possible non-standard modified quantum theories that are proposed to be tested by optomechanical systems phenomenologically.
- **Chapter 5** This chapter describes the superfluid-helium-filled Fabry-Pérot cavity that is studied in this thesis. I describe the basic properties of the cavity, such as its geometry, optical properties, acoustic properties, etc. Then, I present the expected optical and mechanical modes of this optomechanical cavity. Particularly, I show the approximated single-mode optomechanical coupling relation (*i.e.*, a given optical Gaussian mode only couples to one mechanical mode). Finally, I also study the possible mechanisms for a given optical mode coupling to other mechanical modes (besides the mainly coupled one).
- **Chapter 6** In this chapter, I describe the experiment setups and the measurement scheme in detail. I characterized the optical and mechanical modes in this device. The optomechanical coupling is then characterized by the observed optomechanical dynamical backactions. Finally, I showed the weak coupling of a given optical to some other mechanical modes.
- **Chapter 7** This chapter starts by showing how we use photon counting statistics to interpret phonon statistics by the photon-phonon correspondence in Stokes and anti-Stokes scattering. It is followed by the statistical methods I implemented in this work to estimate the true coherences of photons. With these, I further demonstrate the measurement results of an undriven mechanical mode (thermal state). I also show the coherence functions of some post-selected states.
- **Chapter 8** This chapter describes the protocol for preparing a displaced thermal state in the mechanical oscillator. I talk about the setup used to generate optical drive beat notes. Then, I show the properties of the mechanical mode when it is driven. The statistical properties of arrival photon times measure the phonon number

variance, proving this device’s capability to maintain low noise while being driven to large amplitude. In addition, I discuss two potential applications of using this massive mechanical oscillator in a highly displaced thermal state.

- **Chapter 9** This chapter describes the protocol for preparing and verifying entangled photon-phonon pairs. I start with a brief overview of the DLCZ scheme. Then, I present the theoretical prediction of the coherences in this device. The measured coherences violate the classical bound set by the Cauchy-Schwarz inequality, proving the nonclassicality of the joint state. Finally, I talk about the several limits to have a more obvious violation in this device.
- **Chapter 10** This chapter outlooks the potential results of a macro-cavity. I present two major technical improvements that are expected to be achieved by using the new design. With these improvements, I present several scientific goals that we aim to accomplish in macro-cavity. A more ‘macroscopic’ and more ‘quantum’ mechanical oscillator may lead to new insights into future quantum applications and their prospects for new scientific discoveries.

*“Let there be light, and there was light.”*

– Genesis

# CHAPTER 2

## Quantum Optomechanics

Light is a versatile tool in a wide range of fields due to its unique properties, such as high speed, low power consumption, and non-invasiveness. It couples to various systems by photothermal effects, photoelastic effects, radiation pressure, or by changing a material’s refractive index. Therefore, light can be used to control various systems, including biological cells, electronic devices, and mechanical systems. The ability to use light as a control tool has led to numerous breakthroughs and advancements in various fields, including communication, biotechnology and quantum technology.

Optomechanics is the study of the interaction between light and mechanical motion. It involves the manipulation of optical and mechanical systems to develop practical applications, such as ultra-sensitive sensors and precision measurements.

Quantum optomechanics is motivated by the aim of using the mature toolbox of cavity quantum optics to study and use quantum effects in the motion of massive, macroscopic degrees of freedom. The field has gained significant attention in recent years, as dramatic improvements in system designs have made it possible to access the mechanical motion in the quantum regime. These systems include micro-mirrors, cantilevers, levitated particles, membranes, bulk acoustic waves, phononic crystals and even the large suspended mirror of LIGO [18, 52, 53, 59–62]. Quantum optomechanics shows vast perspectives of providing new insights into quantum physics and advancing quantum technologies based on mechanical motion, such as sensing, communication, and computing [11, 15, 18, 27, 28].

### 2.1 Optomechanical Dynamics

#### 2.1.1 Radiation Pressure

Light, as an electromagnetic wave, carries energy and momentum. In free space, energy conservation gives

$$\frac{d}{dt} \left( \frac{1}{2} \epsilon_0 \int_V d^3r [\mathbf{E} \cdot \mathbf{E} + c^2 \mathbf{B} \cdot \mathbf{B}] \right) + \int_S dA \mathbf{S} \cdot \hat{\mathbf{n}} = 0. \quad (2.1)$$

The first term is the total energy of the electromagnetic field, found by integrating the electromagnetic energy density over a volume  $V$ . The second term is the energy flux of the electromagnetic field through the surface  $S = \partial V$ , where

$$\mathbf{S} = \frac{1}{\mu_0} \mathbf{E} \times \mathbf{B} \quad (2.2)$$

is the Poynting vector. The Poynting vector  $\mathbf{S}$  could be interpreted as an energy current density through a surface.

An energy current density also means a flow of momentum. The Maxwell stress tensor is defined as:

$$\overleftrightarrow{\mathbf{T}} = \epsilon_0 \left[ \mathbf{EE} + c^2 \mathbf{BB} - \frac{1}{2} \mathbf{I} (|\mathbf{E}|^2 + c^2 |\mathbf{B}|^2) \right], \quad (2.3)$$

and the electromagnetic momentum density is

$$\mathbf{g} = \frac{\mathbf{S}}{c^2} = \epsilon_0 (\mathbf{E} \times \mathbf{B}). \quad (2.4)$$

In addition, we have the local conservation law for momentum:

$$\frac{\partial \mathbf{g}}{\partial t} + \nabla \cdot (-\overleftrightarrow{\mathbf{T}}) = 0. \quad (2.5)$$

Eq. (2.1) to (2.5) yield the radiation force exerted on an object, which is given by  $\int_S dA - \overleftrightarrow{\mathbf{T}} \cdot \hat{\mathbf{n}}$ .

The concept of the photon originated from Albert Einstein's explanation of the photoelectric effect, in which he proposed the discreteness of light energy and momentum [77]. For a coherent state of light, which can be regarded as an idealized description of the output of a laser, the number of photons arriving at the detector in a given time interval follows the Poisson distribution, which leads to fluctuations in the measured photocurrent. This type of statistical noise is called "shot noise". The corresponding fluctuation in the radiation pressure is called radiation pressure shot noise (RPSN). The fluctuation of the photon number (photocurrent) can be written as

$$\sigma_n^2 = \langle n^2 \rangle - \langle n \rangle^2 = \left( \langle \hat{a}^\dagger \hat{a}^\dagger \hat{a} \hat{a} \rangle - \langle \hat{a}^\dagger \hat{a} \rangle^2 \right) + \langle \hat{a}^\dagger \hat{a} \rangle. \quad (2.6)$$

The second term in Eq. (2.6) is indeed the statistical variance.

The history of the experimental demonstration on radiation pressure starts in 1900 with a light mill configuration [78] and in 1901 with the deflection of a torsion balance under illumination by a lamp [79]. In recent experiments, radiation pressure shot noise has been discovered on mechanical resonators [80–82]. The ability of radiation pressure

to cool mechanical resonators was investigated and implemented even in a wide range of experiments [81–84], including LIGO’s kilogram-scale mirrors [18, 19].

## 2.1.2 Optical Cavities and Mechanical Resonators

### 2.1.2.1 Optical Cavity

To enhance the coupling between light and mechanics, most experiments arrange for the light to travel back and forth in an optical cavity multiple times. Optical cavities can be realized in various forms. Here, a simple Fabry-Pérot resonator is used as an example to show a unifying mathematical description of optical cavities.

A Fabry-Pérot resonator consists of two highly reflective mirrors facing each other. If the two mirrors are separated by a distance  $L_{\text{cav}}$ , this resonator contains a series of resonances with frequencies  $\omega_{\text{cav}} \approx m\pi c/L_{\text{cav}}$ , where the integer  $m$  is the longitudinal mode index. The free spectral range (FSR) (the spacing between two consecutive resonances) of the cavity

$$\Delta\omega_{\text{FSR}} = \pi \frac{c}{L_{\text{cav}}}. \quad (2.7)$$

Another useful parameter to characterize a cavity is its finesse  $\mathcal{F}$ , which describes the average number of round-trips before the light leaves the cavity. It is defined as

$$\mathcal{F} \equiv \frac{\Delta\omega_{\text{FSR}}}{\kappa}, \quad (2.8)$$

where  $\kappa$  is the overall light intensity decay rate originating from the material absorption, scattering, and mirrors’ transmissivity.

For an ideal Fabry-Pérot cavity, the only loss mechanicsm is the transmission through the two end mirrors. For a non-ideal cavity, the total cavity loss rate can be written as the sum of two contributions: the loss at the input cavity mirror  $\kappa_{\text{ex}}$  and the unrecorded internal loss  $\kappa_0$  due to absorption, scattering, and the transmission loss at the second cavity mirror. The loss  $\kappa_{\text{ex}}$  is considered to be useful because it is associated with the coupling between the input-output mode (which is accessible to the experimentalist) and the intra-cavity light. The input coupling efficiency  $\eta_{\kappa}$  is defined as

$$\eta_{\kappa} = \frac{\kappa_{\text{ex}}}{\kappa}, \quad (2.9)$$

where  $\kappa = \kappa_0 + \kappa_{\text{ex}}$ .

The dynamics of the optical cavity can be well described by input-output theory, which allows us to take the quantum fluctuations into account. The equation of motion for the field amplitude  $\hat{a}$  inside the cavity (in a rotating frame at the input laser frequency  $\omega_L$ ) is

given by

$$\dot{\hat{a}} = -\frac{\kappa}{2}\hat{a} + i\Delta\hat{a} + \sqrt{\kappa_{\text{ex}}}\hat{a}_{\text{in}} + \sqrt{\kappa_0}\hat{f}_{\text{in}}. \quad (2.10)$$

Here, instead of a complex number as in classical theory, the amplitude  $\hat{a}$  is an operator in the Heisenberg picture.  $\Delta = \omega_L - \omega_{\text{cav}}$  is the laser detuning from the cavity resonance. For an open quantum system, the field emitted from the Fabry-Pérot cavity reads

$$\hat{a}_{\text{out}} = \hat{a}_{\text{in}} - \sqrt{\kappa_{\text{ex}}}\hat{a}. \quad (2.11)$$

By taking the average of Eq. (2.10) and (2.11), for a steady state, the mean intra-cavity field amplitude  $\langle \hat{a} \rangle$  is:

$$\langle \hat{a} \rangle = \frac{\sqrt{\kappa_{\text{ex}}} \langle \hat{a}_{\text{in}} \rangle}{\kappa/2 - i\Delta}. \quad (2.12)$$

This equation directly leads to the well-known optical susceptibility, which is defined as the ratio between the intracavity field and the input field:

$$\chi_{\text{cav}}(\omega) \equiv \frac{1}{-i(\Delta) + \kappa/2}. \quad (2.13)$$

This is an approximate result under the assumption that all the cavity resonances are resolved, which is generally true for a high finesse optical cavity (A more general discussion about the susceptibility of a low finesse cavity could be found in Ref. [85]). Therefore, the mean intra-cavity circulating photon number is

$$n_{\text{cav}} = |\langle \hat{a} \rangle|^2 = \frac{\kappa_{\text{ex}}}{\Delta^2 + (\kappa/2)^2} \frac{P_{\text{in}}}{\hbar\omega_L}, \quad (2.14)$$

where  $P_{\text{in}}$  is the input power into the cavity, with  $P = \hbar\omega_L |\langle \hat{a}_{\text{in}} \rangle|^2$ .

### 2.1.2.2 Mechanical Resonator

The mechanical resonator can be any vibrational mode of any object. For a high- $Q$  oscillator, the mode spectrum is sufficiently sparse to study the single mode dynamics by neglecting other modes.

The time evolution of a harmonic oscillator's displacement  $x(t)$  is governed by the following equation:

$$m_{\text{eff}} \frac{dx^2(t)}{dt^2} + m_{\text{eff}}\gamma_m \frac{dx(t)}{dt} + m_{\text{eff}}\omega_m^2 x(t) = F_{\text{ex}}(t). \quad (2.15)$$

Here,  $m_{\text{eff}}$  is the effective mass,  $\omega_m$  is the mechanical mode frequency,  $\gamma_m$  is the mechan-

ical mode loss rate, and  $F_{\text{ex}}(t)$  denotes the force exerted on the mechanical oscillator. The effective mass  $m_{\text{eff}}$  can be evaluated by equilibrating the potential energy of the field to the potential energy of an effective oscillator with the same frequency oscillating and the same maximal amplitude  $x_{\text{max}}$  [86]. That is

$$m_{\text{eff}}\omega_m^2x_{\text{max}}^2/2 = \int d^3r \rho(r)\omega_m^2x_{\text{max}}^2u^2(r)/2, \quad (2.16)$$

where  $u(r)$  is the normalized field profile. Eq. (2.15) can be solved either in the time domain or in the frequency domain. For brevity of the following content, only the result in the frequency domain is presented.

By operating Fourier transformation on both sides of Eq. (2.15), we have

$$-m_{\text{eff}}\omega^2x[\omega] + m_{\text{eff}}\omega_m^2x[\omega] - i\omega m_{\text{eff}}\gamma_m x[\omega] = F_{\text{ex}}[\omega]. \quad (2.17)$$

Therefore, the mechanical susceptibility  $\chi_m$  reads

$$\chi_m(\omega) = [m_{\text{eff}}(\omega_m^2 - \omega^2) - im_{\text{eff}}\gamma_m\omega]^{-1}. \quad (2.18)$$

In the quantum picture, the Hamiltonian of a harmonic oscillator is

$$\hat{H} = \hbar\omega_m\hat{b}^\dagger\hat{b} + \frac{1}{2}\hbar\omega_m, \quad (2.19)$$

where  $\hat{b}^\dagger$  and  $\hat{b}$  are phonon creation and annihilation operators, respectively. They are formulated in the following expressions:

$$\hat{x} = x_{\text{ZPF}}(\hat{b} + \hat{b}^\dagger), \quad \hat{p} = -im_{\text{eff}}\omega_m x_{\text{ZPF}}(\hat{b} - \hat{b}^\dagger). \quad (2.20)$$

$x_{\text{ZPF}}$  is the zero-point fluctuation amplitude of the mechanical resonator, defined as:

$$x_{\text{ZPF}} = \sqrt{\frac{\hbar}{2m_{\text{eff}}\omega_m}}. \quad (2.21)$$

It describes the spread of the mechanical ground state in the coordinate, originating from the Heisenberg uncertainty principle.

### 2.1.3 Optomechanical Coupling

In this section, we discuss the optomechanical coupling in a Fabry-Pérot cavity with a movable end mirror. This example aims to demonstrate the mathematical formulation of the general coupling framework. Further, I will restrict the theory to the single-mode coupling regime, in which only one optical mode of resonance  $\omega_{\text{cav}}$  couples to one mechanical

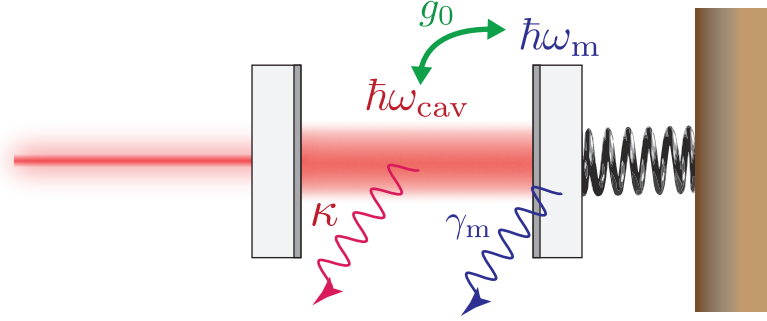


Figure 2.1: Schematic of a Fabry-Pérot cavity with a movable end mirror.

resonance  $\omega_m$ . A schematic of such a cavity is shown in Fig. 2.1.

The uncoupled system can be represented by two harmonic oscillators:

$$\hat{H}_0 = \hbar\omega_{\text{cav}} \hat{a}^\dagger \hat{a} + \hbar\omega_m \hat{b}^\dagger \hat{b}. \quad (2.22)$$

If the cavity resonance depends on the displacement  $x$  of the mechanics, its resonance frequency can be expanded as

$$\omega_{\text{cav}}(x) \approx \omega_{\text{cav}} + x \partial \omega_{\text{cav}} / \partial x + \dots. \quad (2.23)$$

The coupling strength is further defined as the optical resonance frequency shift per displacement. That is,

$$G = -\partial \omega_{\text{cav}} / \partial x. \quad (2.24)$$

For a Fabry-Pérot cavity of length  $L_{\text{cav}}$ , we have  $G = \omega_{\text{cav}} / L_{\text{cav}}$ . The optical cavity Hamiltonian can be reexpressed by keeping the leading linear term in the expansion Eq. (2.23) as

$$\hbar\omega_{\text{cav}}(x)\hat{a}^\dagger \hat{a} \approx \hbar(\omega_{\text{cav}} - G\hat{x})\hat{a}^\dagger \hat{a}. \quad (2.25)$$

Substituting Eq. (2.20) and (2.25) into Eq. (2.22), we have an additional interaction Hamiltonian

$$\hat{H}_{\text{int}} = -\hbar g_0 \hat{a}^\dagger \hat{a} (\hat{b} + \hat{b}^\dagger), \quad (2.26)$$

where  $g_0 = Gx_{\text{ZPF}}$  is the vacuum optomechanical coupling strength or the single photon coupling strength. This parameter is useful as it is normalized to the single quanta level, which benefits discussions in quantum optomechanics. For simplicity, the Hamiltonian is

usually described in a rotating frame at the laser frequency  $\omega_L$ , given by

$$\hat{H} = -\hbar\Delta\hat{a}^\dagger\hat{a} + \hbar\omega_m\hat{b}^\dagger\hat{b} - \hbar g_0\hat{a}^\dagger\hat{a}(\hat{b} + \hat{b}^\dagger). \quad (2.27)$$

Notably, the interaction Hamiltonian in Eq. (2.27) is nonlinear. A linearization approximation is often applied to cavity optomechanics to simplify various calculations. It is based on the assumption that the optical cavity is driven to a large amplitude. We introduce the cavity optical field fluctuation term  $\delta\hat{a}$  to split the total field as

$$\hat{a} = \bar{\alpha} + \delta\hat{a}. \quad (2.28)$$

The interaction Hamiltonian can then be reduced into a Hamiltonian of linear interactions:

$$\hat{H}_{\text{int}}^{(\text{lin})} = -\hbar g_0\sqrt{n_{\text{cav}}}(\delta\hat{a}^\dagger + \delta\hat{a})(\hat{b} + \hat{b}^\dagger). \quad (2.29)$$

Here, we have dropped one higher-order term:  $-\hbar g_0\delta\hat{a}^\dagger\delta\hat{a}$  in the small fluctuation limit, and  $\sqrt{n_{\text{cav}}} = |\bar{\alpha}|$  is the average of the field amplitude.

The linearized approach is sufficient for understanding many aspects of cavity optomechanics, including displacement detection down to the SQL, optomechanical ground-state cooling theory, optomechanical hybridization in the strong-coupling regime, optomechanically induced transparency, optomechanical light squeezing, and nearly all entanglement and state transfer techniques presented in the literature [44].

Quantum effects can also be observed in the linearized regime. Proving their quantumness usually requires a quantitative comparison, such as with the oscillator's or light field's zero-point fluctuations. However, the drawback of relying solely on the linearized interaction is that it always transforms Gaussian states of the mechanics and light field into other Gaussian states. Although these states can be squeezed or entangled, they will never have a negative Wigner density [4].

Nevertheless, there are ways to move beyond the linear regime, such as by introducing nonlinearity at the later stage of the experiment by using single-photon sources or single-photon detectors to conditionally create nontrivial quantum states. These strategies are similar to those employed in quantum optics [87–89]. A more detailed discussion can be found in Sec. 3.2.3 and Sec. 3.5.2.

## 2.1.4 Dynamical Equations

In the discussion above, we have not included any lossy channels in the Hamiltonian. Apart from the coupling between the optical cavity and the mechanical resonator, both systems couple to external drives and the environment, which can be treated in the input-output formalism by using the quantum Langevin equations.

The complete coupled dynamical equations are

$$\delta\dot{a} = \left(i\Delta - \frac{\kappa}{2}\right)\delta\hat{a} + ig\left(\hat{b} + \hat{b}^\dagger\right) + \sqrt{\kappa_{\text{ex}}}\delta\hat{a}_{\text{in}}(t) + \sqrt{\kappa_0}\hat{f}_{\text{in}}(t), \quad (2.30\text{a})$$

$$\dot{\hat{b}} = \left(-i\omega_m - \frac{\gamma_m}{2}\right)\hat{b} + ig\left(\delta\hat{a} + \delta\hat{a}^\dagger\right) + \sqrt{\gamma_m}\hat{b}_{\text{in}}(t). \quad (2.30\text{b})$$

These linearly coupled equations can be Fourier transformed into the frequency domain as

$$-i\omega\delta\hat{a}[\omega] = \left(i\Delta - \frac{\kappa}{2}\right)\delta\hat{a}[\omega] + ig\left[\hat{b}[\omega] + \hat{b}^\dagger[\omega]\right] + \sqrt{\kappa_{\text{ex}}}\delta\hat{a}_{\text{in}}[\omega] + \sqrt{\kappa_0}\hat{f}_{\text{in}}[\omega], \quad (2.31\text{a})$$

$$-i\omega\hat{b}[\omega] = \left(-i\omega_m - \frac{\gamma_m}{2}\right)\hat{b}[\omega] + ig\left[\delta\hat{a}[\omega] + (\delta\hat{a}^\dagger)[\omega]\right] + \sqrt{\gamma_m}\hat{b}_{\text{in}}[\omega]. \quad (2.31\text{b})$$

Also, linearized classical equations of motion for light and mechanics sometimes are useful for Gaussian optomechanics with linear drives, and are given by

$$-i\omega\delta\alpha[\omega] = \left(i\Delta - \frac{\kappa}{2}\right)\delta\alpha[\omega] + iG\bar{\alpha}x[\omega] \quad (2.32\text{a})$$

$$-m_{\text{eff}}\omega^2x[\omega] = -m_{\text{eff}}\omega_m^2x[\omega] + i\omega m_{\text{eff}}\gamma_m x[\omega] + \hbar G\{\bar{\alpha}^*\delta\alpha[\omega] + \bar{\alpha}(\delta\alpha^*)[\omega]\} \quad (2.32\text{b})$$

Here, we use the relation  $(\delta\alpha^*)[\omega] = \delta\alpha[-\omega]^*$ .

## 2.2 Dynamical Backaction

This section will mainly discuss the dynamical effects of the radiation-pressure force. We solve the linearly coupled equations of motion between the light and the mechanics shown in Eq. (2.30a), (2.30b), (2.31a) and (2.31b). Because the thermal reservoir is Markovian and the system linearly responds to the external drive, we also use Eq. (2.32a) and (2.32b) for the following discussion and analysis.

### 2.2.1 Optical Spring Effects and Optomechanical Damping Rates

In the weak coupling limit ( $g_0 \ll \kappa$ ), the mechanical susceptibility acquires an additional term  $\Sigma(\omega)$  to the original susceptibility because of the optomechanical coupling, becoming:

$$\chi_{\text{m,eff}}^{-1}(\omega) = \chi_{\text{m}}^{-1}(\omega) + \Sigma(\omega). \quad (2.33)$$

This additional term can be solved by combining the coupled Eq. (2.32a) and (2.32b) to find

$$\Sigma(\omega) = 2m_{\text{eff}}\omega_m g^2 \left\{ \frac{1}{(\Delta + \omega) + i\kappa/2} + \frac{1}{(\Delta - \omega) - i\kappa/2} \right\}, \quad (2.34)$$

where  $g$  is the optomechanical coupling strength defined as  $g = g_0\sqrt{n_{\text{cav}}}$ .

To see this effect on the original bare mechanical resonator more explicitly, we split this term into real and imaginary parts as

$$\Sigma(\omega) \equiv m_{\text{eff}}\omega [2\delta\omega_m(\omega) - i\gamma_{\text{opt}}(\omega)]. \quad (2.35)$$

Thus, the total susceptibility becomes

$$\chi_{m,\text{eff}}^{-1}(\omega) = m_{\text{eff}} \left\{ (\omega_m + \delta\omega_m(\omega))^2 - \omega^2 - (\delta\omega_m(\omega))^2 - i\omega [\gamma_m + \gamma_{\text{opt}}(\omega)] \right\}. \quad (2.36)$$

Compared to Eq. (2.18), Eq. (2.36) implies a mechanical frequency shift  $\delta\omega_m(\omega)$  and an additional optomechanical damping rate  $\gamma_{\text{opt}}(\omega)$ . This intuitive understanding is appropriate when the mechanical frequency shift is much smaller than the drive frequency, *i.e.*,  $\delta\omega_m(\omega) \ll \omega_m^2$ , so that we can drop  $(\delta\omega_m(\omega))^2$  in Eq. (2.36).

Explicit expressions for these two parts are

$$\delta\omega_m(\omega) = g^2 \frac{\omega_m}{\omega} \left[ \frac{\Delta + \omega}{(\Delta + \omega)^2 + \kappa^2/4} + \frac{\Delta - \omega}{(\Delta - \omega)^2 + \kappa^2/4} \right], \quad (2.37a)$$

$$\gamma_{\text{opt}}(\omega) = g^2 \frac{\omega_m}{\omega} \left[ \frac{\kappa}{(\Delta + \omega)^2 + \kappa^2/4} - \frac{\kappa}{(\Delta - \omega)^2 + \kappa^2/4} \right]. \quad (2.37b)$$

They are the exact solution of the linearized coupled equation Eq. (2.32a) and (2.32b).

The power dependence of these two parameters only appears in  $g^2 = g_0^2 n_{\text{cav}}$ , which indicates that both the damping and spring effects are proportional to the circulating photon number inside the cavity, and hence, the incident laser power.

For a given optical input at detuning  $\Delta$ , the dependence of  $\Sigma(\omega)$  on  $\omega$  is more complicated. In general, the overall susceptibility generated by Eq. (2.37a) and (2.37b) is a non-Lorentzian shape, which is difficult to interpret by a simple frequency shift and a linewidth broadening. In the weak coupling limit ( $g \ll \kappa$ ), it is a good approximation to evaluate these modifications at the original resonance frequency  $\omega_m$ . Typically, the mechanical damping rate is far slower than the cavity damping rate ( $\gamma_{\text{eff}} \ll \kappa$ ). This allows us to neglect the dependence on  $\omega$  and treat the modifications as constants with values of  $\delta\omega_m(\omega_m)$  and  $\gamma_{\text{opt}}(\omega_m)$  over the range of the mechanical linewidth  $\gamma_{\text{eff}}$ . This assumption has been found to be mostly accurate for high- $Q$  mechanical resonators in various experiments [72, 90]. Therefore, in the following discussions, we will take these assumptions.

### 2.2.1.1 Optical Spring Effects

When  $\omega = \omega_m$ , the mechanical frequency shift induced by the light field reads:

$$\delta\omega_m = g^2 \left( \frac{\Delta - \omega_m}{\kappa^2/4 + (\Delta - \omega_m)^2} + \frac{\Delta + \omega_m}{\kappa^2/4 + (\Delta + \omega_m)^2} \right). \quad (2.38)$$

In the Doppler regime  $\kappa \gg \omega_m$ , this reduces to

$$\delta\omega_m(\Delta)|_{\kappa \gg \omega_m} = g^2 \frac{2\Delta}{\kappa^2/4 + \Delta^2}. \quad (2.39)$$

This implies that the optomechanical interaction softens the mechanical spring for a red-detuned ( $\Delta < 0$ ) laser and hardens the spring for a blue-detuned ( $\Delta > 0$ ) laser.

In the resolved-sideband regime ( $\kappa \ll \omega_m$ ), when the drive is at either of the two sidebands ( $\Delta = \pm\omega_m$ ), the mechanical frequency shift is

$$\delta\omega_m(\Delta = \pm\omega_m)|_{\kappa \ll \omega_m} = \pm g^2 \left( \frac{1}{2\omega_m} \right). \quad (2.40)$$

If  $g \ll \kappa \ll \omega_m$ , this frequency shift is negligible.

### 2.2.1.2 Optomechanical Damping Rate

The optomechanics-induced damping rate is

$$\gamma_{\text{opt}} = n_{\text{cav}} g_0^2 \left( \frac{\kappa}{\kappa^2/4 + (\Delta + \omega_m)^2} - \frac{\kappa}{\kappa^2/4 + (\Delta - \omega_m)^2} \right). \quad (2.41)$$

The sign of this damping rate can be either positive or negative. Therefore, we can use the light of different detunings to either cool or amplify the mechanical motion.

In the resolved-sideband regime, for a red detuned laser ( $\Delta = -\omega_m$ ), the induced damping rate is

$$\gamma_{\text{opt}}(\Delta = -\omega_m)|_{\kappa \ll \omega_m} = +n_{\text{cav}} g_0^2 \frac{4}{\kappa}. \quad (2.42)$$

The interaction increases the mechanical damping rate. This can be exploited to cool the motion of the mechanical oscillator as discussed in Sec. 2.2.2.

Similarly, for a blue detuned laser ( $\Delta = +\omega_m$ ), the induced damping rate is given by

$$\gamma_{\text{opt}}(\Delta = +\omega_m)|_{\kappa \ll \omega_m} = -n_{\text{cav}} g_0^2 \frac{4}{\kappa}. \quad (2.43)$$

The interaction decreases the mechanical damping rate. In this scenario, the total effective mechanical damping rate  $\gamma_{\text{eff}} = \gamma_m + \gamma_{\text{opt}}$  can even become negative. This net

anti-damping effect in the mechanical system results in parametric amplification, which is similar to a laser surpassing threshold [91].

As you can see, the light acts as a control knob to adjust the frequency and damping rate of the coupled mechanical resonator through optomechanical interaction.

## 2.2.2 Optomechanical Cooling

To operate the optomechanical system in the quantum realm, both the mechanical oscillator and the optical cavity should be prepared close to their quantum ground states. The average thermal occupancy can be calculated using the formula  $n_{\text{th}} = 1/(\exp[\hbar\omega/k_B T] - 1)$ . Optical light (visible to infrared) is near its ground state even at room temperature (300 K). However, for most mechanical resonators, even at a typical dilution fridge temperature of 10-20 mK, it is often difficult to passively cool them to their ground state. Some researchers overcome this hurdle by designing their mechanical frequencies in the GHz range [51, 59, 61, 75, 92]. Active cooling approaches allow for preparing mechanical ground states in a broader range of mechanics.

A red-detuned optical input can broaden the mechanical resonance (see Sec. 6.3.2.2). This broadening further removes the energy of the oscillator, which is the so-called optomechanical sideband cooling effect. Intuitively, this cooling utilizes cavity resonance to enhance the phonon absorption process. Sideband cooling has been implemented in various types of optomechanical systems [18, 51, 81–84]. In this section, I will briefly discuss the theoretical description of this cooling effect in both classical and quantum pictures.

In the classical theory, a mechanical resonator with linewidth  $\gamma_m$  coupled to a thermal reservoir of temperature  $T_{\text{bath}}$  has a mean phonon number

$$n_{\text{init}} = \frac{k_B T_{\text{bath}}}{\hbar \omega_m}. \quad (2.44)$$

The optical damping rate reduces the mechanical mode mean occupancy number to

$$n_f = \frac{k_B T_{\text{bath}}}{\hbar(\omega_m + \omega_{\text{opt}})} \frac{\gamma_m}{\gamma_m + \gamma_{\text{opt}}}, \quad (2.45)$$

where  $n_f$  is the final phonon number after cooling. This classical interpretation is valid till the zero-point fluctuation of the radiation pressure force starts to set the bound of the achievable mean occupancy number.

By introducing quantum fluctuations in the calculation, some corresponding quantum effects appear in the sideband cooling effect. This approach is crucial in the case of cooling the mechanical mode to the quantum ground state, which has been demonstrated in several proposals and experiments [51, 52, 54, 58, 83, 84, 93–96]. In the following, we will restrict our discussion to the weak-coupling regime  $g \ll \kappa$ , where we could use the aforementioned perturbative result in Sec. 2.2.1.

Input photons can be scattered either downwards or upwards in the frequency domain. To look into this, we can decompose the interaction Hamiltonian Eq. (2.29) into two parts:

$$\text{Stokes scattering: } -\hbar g \left( \hat{a}^\dagger \hat{b}^\dagger + \hat{a} \hat{b} \right), \quad (2.46a)$$

$$\text{anti-Stokes scattering: } -\hbar g \left( \hat{a}^\dagger \hat{b} + \hat{a} \hat{b}^\dagger \right). \quad (2.46b)$$

$\hat{a}$  represents  $\delta \hat{a}$  to simplify the writing here and in all following content unless otherwise specified. In the former process, one input photon converts into one cavity photon and one phonon. While in the latter, one input photon absorbs one phonon to produce one cavity photon.

Clearly, the anti-Stokes scattering is relevant for cooling as it removes phonons from the oscillator. The presence of the optical cavity makes the system prefer one scattering process over another. Typically, for a red-detuned input ( $\Delta < 0$ ), the anti-Stokes scattering process is enhanced over the Stokes scattering process. As a result, the input laser effectively cools the oscillator. In the resolved-sideband regime, the scattering process can be interpreted in a rather simple picture, which will be covered in Sec. 2.3.

The net downward rate is given by

$$\gamma_{\text{opt}} = A^- - A^+, \quad (2.47)$$

where  $A^-$  and  $A^+$  are downward transitions and upwards transitions in the mechanical state, respectively. Thus, the dynamics of the mean phonon number is [44]

$$\dot{n} = (n + 1) (A^+ + A_{\text{th}}^+) - n (A^- + A_{\text{th}}^-), \quad (2.48)$$

where  $A_{\text{th}}^+ = n_{\text{m,th}} \gamma_m$  and  $A_{\text{th}}^- = (n_{\text{m,th}} + 1) \gamma_m$  are the extra transition rates due to the thermal reservoir of  $n_{\text{m,th}}$  coupled to the oscillator. The final equilibrium phonon number  $n_f$  can be solved as

$$n_f = \frac{A^+ + n_{\text{m,th}} \gamma_m}{\gamma_{\text{opt}} + \gamma_m}, \quad (2.49)$$

where  $A^\pm$  can be evaluated by Fermi's golden rule. Let's define the quantum noise spectrum as the following

$$S_{FF}(\omega) = \int_{-\infty}^{+\infty} dt e^{i\omega t} \langle \hat{F}(t) \hat{F}(0) \rangle, \quad (2.50)$$

which is the Fourier component of the autocorrelation of the radiation pressure force as

$\hat{F} = \hbar G \hat{a}^\dagger \hat{a}$ . The transition rates can be reexpressed as

$$A^\pm = \frac{x_{\text{ZPF}}^2}{\hbar^2} S_{FF}(\omega = \mp\omega_m). \quad (2.51)$$

The force spectrum of a driven cavity is given by

$$S_{FF}(\omega) = \frac{g\hbar^2}{x_{\text{ZPF}}} \frac{\kappa}{\kappa^2/4 + (\Delta + \omega)^2}. \quad (2.52)$$

Let us first consider the relatively simple result in an optimal case in which the system is decoupled from the thermal reservoir, *i.e.*,  $\gamma_m = 0$ . The final phonon number in Eq. (2.49), which is the minimal phonon number that this cooling effect could achieve, is reduced to

$$n_{\min} = \frac{A^+}{\gamma_{\text{opt}}} = \frac{A^+}{A^- - A^+}. \quad (2.53)$$

Combining Eq. (2.51) to (2.53), we obtain the minimal phonon number for a given mechanical mode as

$$n_{\min} = \left( \frac{A^-}{A^+} - 1 \right)^{-1} = \left( \frac{(\kappa/2)^2 + (\Delta - \omega_m)^2}{(\kappa/2)^2 + (\Delta + \omega_m)^2} - 1 \right)^{-1}. \quad (2.54)$$

Note that, it is possible to cool the oscillator even in the sideband-unresolved regime ( $\kappa \gtrsim \omega_m$ ).

In the resolved-sideband regime ( $\kappa \ll \omega_m$ ), the minimal phonon number can be minimized at red-detuning ( $\Delta = -\omega_m$ ), given by

$$n_{\min} = \left( \frac{\kappa}{4\omega_m} \right)^2 \ll 1. \quad (2.55)$$

In principle, this makes ground-state cooling permitted.

In the opposite regime ( $\kappa \gg \omega_m$ ), the limitation of the minimal phonon occupancy stems from the shot noise of the radiation pressure exerting on the oscillator, given by

$$n_{\min} = \frac{\kappa}{4\omega_m} \gg 1. \quad (2.56)$$

When considering the coupling to a thermal reservoir, the final phonon number Eq. (2.49) can be expressed as the outcome of the coupling between two baths with average occupa-

tions of  $n_{\min}$  and  $n_{m,\text{th}}$  with coupling rates of  $\gamma_{\text{opt}}$  and  $\gamma_m$ , respectively. That is,

$$n_f = \frac{\gamma_{\text{opt}} n_{\min} + \gamma_m n_{m,\text{th}}}{\gamma_{\text{opt}} + \gamma_m}. \quad (2.57)$$

The final phonon number is a result of the interaction of the system with two thermal environments, which leads to energy exchanges. This equation can represent a simple model of the interaction between a quantum system and a thermal environment, and it highlights the importance of understanding the coupling between the system and its environment for accurate predictions of its thermal behavior.

The result shown in Eq. (2.57) is indeed a quantum description of the optomechanical backaction cooling [96]. We note that the discussion above has ignored the existence of thermal occupancy in the optical cavity. This is clearly a good approximation for visible or infrared light due to their high frequency. However, for microwave cavities, the cavity occupation deviates from zero by a nonnegligible occupation  $n_{\text{cav},\text{th}}$ . As a result, in the resolved-sideband regime, the final phonon number is modified to

$$n_f = n_{m,\text{th}} \frac{\gamma_m}{\gamma_{\text{eff}}} + n_{\text{cav},\text{th}} + \frac{\kappa^2}{16\omega_m^2}. \quad (2.58)$$

Note that  $n_f > n_{\text{cav},\text{th}}$ . This indicates the final phonon number is jointly limited by thermal fluctuations of the input field and the mechanical resonator [44].

## 2.3 Optomechanics in the Resolved-Sideband Regime

In this section, I will mainly discuss the results of quantum optomechanics in the resolved-sideband regime ( $\kappa \ll \omega_m$ ), as this is relevant to the experiment in this thesis. In this regime, the mechanical motion is much faster than the optical decoherence rate, so the cavity could be approximated to be lossless during mechanical oscillations. Additionally, the mechanical sidebands are well separated from the optical cavity resonance in the frequency domain. In this regime (and in the rotating wave approximation (RWA)), choosing the right optical input detuning allows us to select the desired optomechanical scattering process.

Optomechanical devices in the resolved-sideband regime turn out to be useful in various applications. One of them is developing sensitive detectors for small forces, displacements, and masses. For example, if the shift of the mechanical frequency due to the signal is much smaller than the width of the optical resonance, such a modulation can only be detected in the resolved-sideband regime. Moreover, these optomechanical devices have been used to explore quantum behaviors of mechanical systems by selecting desired scattering processes, such as creating nonclassical mechanical states [61, 62, 92], two-mode squeezed states [75], or even entangled states between multiple massive mechanical res-

onators [59, 97]. They are important for building acoustic quantum networks and quantum memories [11, 15].

In Sec. 2.2.2, we briefly mentioned the decomposition of the linearized interaction Hamiltonian Eq. (2.29) into the Stokes and the anti-Stokes scattering terms. In the resolved-sideband regime, for a red-detuned input ( $\Delta \approx -\omega_m$ ), we have two harmonic oscillators of nearly equal frequency (in this rotating frame at  $\omega_L$ ) as shown in Eq. (2.27). The term that describes the interchange of quanta between two oscillators is the anti-Stokes scattering term given in Eq. (2.46b). It represents a process of removing a phonon and creating a photon or *vice versa*. The Stokes scattering process Eq. (2.46a) is omitted as the energy is not “conserved” in this process, or in other words because they are strongly off-resonant. Keeping only the resonant term in a rotating frame is known as the rotating wave approximation (RWA). This is relevant for cooling as the phonon energy can be transferred into the colder photon mode. It is also referred to as a “beam-splitter” interaction or a “state-swap” interaction in quantum optics.

In contrast, for a blue-detuned input ( $\Delta \approx +\omega_m$ ), we only keep the Stokes scattering term Eq. (2.46a). This term represents a process of creating/annihilating a photon-phonon pair, known as a “two-mode squeezing” interaction.

The discussion in this section revolves around these two crucial processes, which have been incorporated into the experiment in this thesis to read out or conditionally prepare the mechanical state.

### 2.3.1 Optical Output Spectrum

The output optical field  $\hat{a}_{\text{out}}$  of the optomechanical cavity has a spectrum  $S_{\hat{a}_{\text{out}}^\dagger \hat{a}_{\text{out}}}$  that relates to mechanical spectrum  $S_{\hat{x}\hat{x}}$ . Using the input-output formalism in Eq. (2.31a) and (2.31b), we can construct the output spectrum of the light [44, 98]. In the resolved-sideband regime and low-temperature limit ( $k_B T \ll \hbar\omega_{\text{cav}}$ ), the linearized coupled equations of motion can be simplified as

$$-i\omega\hat{a}[\omega] = \left(i\Delta - \frac{\kappa}{2}\right)\hat{a}[\omega] + i\frac{g_0\sqrt{n_{\text{cav}}}}{x_{\text{ZPF}}}\hat{x}, \quad (2.59a)$$

$$-i\omega\hat{b}[\omega] = \left(-i\omega_m - \frac{\gamma_{\text{eff}}}{2}\right)\hat{b}[\omega] + \sqrt{\gamma_m}\hat{b}_{\text{in}}[\omega]. \quad (2.59b)$$

Note that noise correlations that are associated with the inputs of the system are given by

$$\left\langle \hat{a}_{\text{in}}(t)\hat{a}_{\text{in}}^\dagger(t') \right\rangle = \delta(t - t'), \quad (2.60\text{a})$$

$$\left\langle \hat{a}_{\text{in}}^\dagger(t)\hat{a}_{\text{in}}(t') \right\rangle = 0, \quad (2.60\text{b})$$

$$\left\langle \hat{b}_{\text{in}}(t)\hat{b}_{\text{in}}^\dagger(t') \right\rangle = (n_{\text{m,th}} + 1)(t - t'), \quad (2.60\text{c})$$

$$\left\langle \hat{b}_{\text{in}}^\dagger(t)\hat{b}_{\text{in}}(t') \right\rangle = n_{\text{m,th}}\delta(t - t'). \quad (2.60\text{d})$$

Here we approximate that the optical field has zero thermal occupation, which is valid even at room temperature for optical light. Therefore, by formal integrals, the output field spectrum reads

$$S_{\hat{a}_{\text{out}}^\dagger\hat{a}_{\text{out}}}(\omega) = \kappa_{\text{ex}}n_{\text{cav}}2\pi\delta(\omega) + \kappa_{\text{ex}}g_0^2n_{\text{cav}}/x_{\text{ZPF}}^2|\chi_{\text{cav}}(\omega + \Delta)|^2 S_{\hat{x}\hat{x}}(\omega), \quad (2.61)$$

where the first term corresponds to the optical input field and the second term corresponds to the optical field scattered by the mechanical motion through the optomechanical coupling.  $\chi_{\text{cav}}(\omega)$  is the bare optical cavity susceptibility Eq. (2.13). The spectrum of the mechanical position  $\hat{x}$  can be rewritten as

$$S_{\hat{x}\hat{x}}(\omega) = x_{\text{ZPF}}^2 [S_{\hat{b}^\dagger\hat{b}}(\omega) + S_{\hat{b}\hat{b}^\dagger}(\omega)]. \quad (2.62)$$

$S_{\hat{b}^\dagger\hat{b}}(\omega)$  is enhanced around  $\omega = +\omega_{\text{m}}$ , and  $S_{\hat{b}\hat{b}^\dagger}$  is enhanced around  $\omega = -\omega_{\text{m}}$ , corresponding to the anti-Stokes and Stokes scattering processes, respectively, which produce the output field with the mechanical susceptibility  $\chi_{\text{m}}(\omega)$  having an effective linewidth  $\gamma_{\text{eff}}$ . This is explicitly seen through the oscillator's Langevin equation 2.59b [99, 100], as shown in the result of the formal integral:

$$S_{\hat{b}^\dagger\hat{b}}(\omega) = \frac{n_{\text{m}}\gamma_{\text{eff}}}{(\gamma_{\text{eff}}/2)^2 + (\omega - \omega_{\text{m}})^2}, \quad (2.63\text{a})$$

$$S_{\hat{b}\hat{b}^\dagger}(\omega) = \frac{(n_{\text{m}} + 1)\gamma_{\text{eff}}}{(\gamma_{\text{eff}}/2)^2 + (-\omega - \omega_{\text{m}})^2}. \quad (2.63\text{b})$$

In summary, the optical output spectrum consists of the bare optical input and two frequency-resolved mechanical sidebands with linewidth  $\gamma_{\text{eff}}$  at either the blue-shifted ( $\omega = +\omega_{\text{m}}$ ) or the red-shifted ( $\omega = -\omega_{\text{m}}$ ) sideband, which corresponds to the anti-Stokes and the Stokes scattering processes, respectively. If the optical input is red-detuned from the optical cavity  $\omega_{\text{cav}}$  by one mechanical resonance, *i.e.*,  $\omega_{\text{L}} = \omega_{\text{cav}} - \omega_{\text{m}}$ , its blue-shifted sideband (the anti-Stokes scattering process) is significantly enhanced by the presence of the cavity resonance. Similarly, the red-shifted sideband (the Stokes scattering process) of a blue-detuned optical input  $\omega_{\text{L}} = \omega_{\text{cav}} + \omega_{\text{m}}$  is also enhanced.

### 2.3.2 Quantum Sideband Asymmetry

The phenomenon known as quantum sideband asymmetry occurs when a quantum system interacts with an electromagnetic field. In the field of optomechanics, this term refers to the discrepancy between the Stokes and the anti-Stokes scattering processes that occur when a weak optical field drives a mechanical resonator. This asymmetry arises due to the dissimilarity between the processes of absorption and emission of a quantum by a quantum system.

The output spectrum in Eq. (2.61) has two Lorentzians at  $\pm\omega_m$  if the input laser is at optical resonance ( $\Delta = 0$ ). Although the two Lorentzians share the same shape, their amplitudes differ. As shown in Eq. (2.63a) and (2.63b), the red-detuned sideband is proportional to  $n_m$ , the blue-detuned sideband is proportional to  $n_m + 1$ , and the difference is precisely one phonon, which originates from the non-zero commutator of the bosonic creation operator  $\hat{b}$  and the annihilation operator  $\hat{b}^\dagger$ , *i.e.*,  $[\hat{b}^\dagger, \hat{b}] = 1$ .

This asymmetry is most commonly characterized by the noise spectrum through heterodyne measurements. [51, 58, 70, 101, 102]. The ratio of the sideband asymmetry changes as a function of the mechanical phonon number. This asymmetry ratio is rendered progressively smaller by an increasing phonon number, until it becomes negligible when the phonon number is sufficiently large ( $n_m \gg 1$ ). This asymmetry also provides a tool to determine the temperature of the mechanical mode via calibrating the phonon number to the single quantum imbalance, which is known as the sideband quantum thermometer.

In the resolved-sideband regime, one way to measure the quantum sideband asymmetry is by first using a blue-detuned ( $\Delta = +\omega_m$ ) and then a red-detuned ( $\Delta = -\omega_m$ ) input laser. When the input laser is blue-detuned, as discussed in Sec. 2.3, the scattered light is dominated by the Stokes scattering process, whose rate is proportional to  $\langle \hat{b}\hat{b}^\dagger \rangle = n_m + 1$ . In contrast, when the input laser is red-detuned, the dominant anti-Stokes scattering rate is proportional to  $\langle \hat{b}^\dagger\hat{b} \rangle = n_m$ . Notice that this discussion is within the weak coupling regime, where we have omitted the dynamical backaction effects discussed in Sec. 2.2. The result including the dynamical backactions is covered in Sec. 6.3.2.

## 2.4 Figure of Merit: Quantum Optomechanical Device

Quantum optomechanical systems are available in different platforms, which include variations in the frequency, size, and geometry of the mechanical resonator, cavity frequency and geometry, coupling mechanism, and more. Despite these differences, researchers aim to identify universal parameters that can be used to evaluate the performance of the system. The manipulation and measurement of the mechanical resonator in the fully quantum regime are enabled by certain parameters, and even slight changes to these parameters can lead to a significant shift in the system's performance. This section will explore several figures of merit for optomechanical systems and will discuss the unique phenomena

and applications associated with special regimes. In some regimes, the distinct quantum advantages of optomechanical systems cannot be explained by any classical theories.

### 2.4.1 Cooperativity

The narrative of quantum control involves a struggle between the coupling rate and overall dissipation. The dissipation in the system means the loss of important quantum features. In linear optomechanical systems, cooperativity is a measure of the relationship between the energy exchange rate and the rates at which each subsystem loses energy. That is

$$\mathcal{C} = 4g^2/\gamma_m\kappa. \quad (2.64)$$

This definition is similar to the Purcell factor in atomic physics, which evaluates the coupling strength between cavity fields and atomic assemblies.

In the resolved-sideband regime, it is directly related to the maximum cooling rate attained in the red-detuned sideband ( $\Delta = -\omega_m$ ) as

$$\gamma_{\text{opt}}|_{\kappa \ll \omega_m} = 4n_{\text{cav}} \frac{g_0^2}{\kappa} = \frac{4g^2}{\kappa} = \gamma_m \mathcal{C}. \quad (2.65)$$

Higher cooperativity in linear optomechanics would indicate the ability to cool closer to the quantum ground state and the preparation of mechanical quantum states with high fidelity [103, 104].

In optomechanical systems, electromagnetically induced transparency refers to the phenomenon of absorption cancellation in the presence of an optical field. When one laser (the “control” laster) is placed at the red-detuned sideband ( $\Delta = -\omega_m$ ), the transmission of a “probe” beam is given by

$$|\mathcal{R}_p|^2 = \left| \frac{4n_{\text{cav}}g_0^2}{4n_{\text{cav}}g_0^2 + \gamma_m\kappa - 2i(\omega - \omega_m)\kappa} \right|^2. \quad (2.66)$$

The field at the cavity resonance ( $\omega = +\omega_m$ ) gives

$$|\mathcal{R}_p|^2 = \left( \frac{\mathcal{C}}{\mathcal{C} + 1} \right)^2, \quad (2.67)$$

from which we can see that  $\mathcal{C} > 1$  is necessary to change the transmission over 50%.

Regarding the final phonon number presented in Eq. (2.49), it is worth mentioning that in the resolved-sideband regime and for the limit where  $\gamma_{\text{opt}} \gg \gamma_m$ , the reduction in thermal occupation can be described using quantum cooperativity as

$$\lim_{\gamma_{\text{opt}}/\gamma_m \rightarrow \infty} n_f = n_{\min} + \frac{\gamma_m}{\gamma_{\text{opt}}} n_{m,\text{th}} = n_{\min} + \frac{1}{\mathcal{C}_{\text{qu}}}, \quad (2.68)$$

where  $\mathcal{C}_{\text{qu}} = \mathcal{C}/n_{\text{m,th}}$  is the quantum cooperativity. If quantum cooperativity  $\mathcal{C}_{\text{qu}} > 1$ , the state transfer rate between light and mechanics is faster than the mechanical decoherence rate.

#### 2.4.1.1 Single-Photon Strong Cooperativity

A more fundamental parameter that is independent of the drive laser power is the single-photon cooperativity, given by [44]

$$\mathcal{C}_0 = \frac{4g_0^2}{\kappa\gamma_m}. \quad (2.69)$$

The system's loss is compared to the strength of the unitary interaction between a single photon and phonon, determining this ratio. When this ratio exceeds 1, known as the single-photon strong cooperativity regime ( $\mathcal{C}_0 > 1$ ), the mechanical resonator can respond to a single photon before it dissipates. This way, the mechanical resonator can access the discrete nature of photons, which is a fundamental quantum aspect of light.

It is clear to see from Eq. (2.69) that achieving the single-photon strong cooperativity requires a strong coupling and small losses. Let's take a Fabry-Pérot cavity with a movable end mirror (shown in Fig. 2.1) as an example to show this more explicitly. Eq. (2.69) can be reexpressed as

$$\mathcal{C}_0 = \left( \frac{\omega_{\text{cav}}x_{\text{ZPF}}}{L_{\text{cav}}} \right)^2 \frac{4}{\kappa\gamma_m} = \frac{2\hbar}{\pi c} \frac{Q_m \mathcal{F}}{m L_{\text{cav}}} \left( \frac{\omega_{\text{cav}}}{\omega_m} \right)^2. \quad (2.70)$$

Here,  $Q_m = \omega_m/\gamma_m$  is the mechanical quality factor. It demands engineering an ultra-large  $Q_m$  and  $\mathcal{F}$  to overcome the smallness of the Plank constant  $\hbar$ . Eq. (2.69) also presents challenges in building a macroscopic quantum optomechanical system, as the cooperativity decreases for large mechanical mass and a long cavity.

Achieving single-photon strong cooperativity is a milestone goal in the optomechanical field. If one could reach this limit, one could take advantage of the coupling at the single-photon level to obtain a range of interesting phenomena, including non-classical states of light or motion [62, 92, 105–108], and quantum information processing.

In the context of measurements at the standard quantum limit (SQL), the ratio of quantum backaction to thermal force noise yields

$$\frac{S_{FF}(\omega_m)}{S_{FF}^{\text{th}}(\omega_m)} = \mathcal{C}_0 \frac{n_{\text{cav}}}{n_{\text{th,m}}} = \frac{16\eta_\kappa P_{\text{in}} g_0^2 \omega_m}{\kappa^2 \gamma_m \omega_{\text{cav}} k_B T} \frac{1}{1 + 4\omega_m^2/\kappa^2}. \quad (2.71)$$

Having this ratio larger than unity is important for optomechanical experiments to observe the effects of radiation-pressure shot noise on the mechanical oscillator, and to further demonstrate detection sensitivity at the standard quantum limit [109]. Large  $\mathcal{C}_0$  makes

these experiments feasible even with moderate optical input power.

Furthermore, the optical spring effect shifts the mechanical frequency, as demonstrated by Eq. (2.40). If the single-photon cooperativity exceeds the resolved-sideband ratio,  $C_0 > \omega_m/\kappa$ , it becomes possible to resolve a single photon by detecting the mechanical frequency. Moreover, it is feasible to resolve the mechanical phonon number using electromagnetic signals, as described in [62].

This is further evidence that, in the single-photon strong cooperativity regime, the impact of one average intracavity photon on the mechanical resonator is adequate to facilitate cooling [104], prepare mechanical systems in quantum superposition states [62], and achieve critical quantum fluctuations (a critical regime characterized by nonlinear interactions between optical and mechanical fluctuations) [110, 111] and photon antibunching in optomechanical systems [111]. Investigating the classical-to-quantum transition is of particular interest in the single-photon strong coupling regime with mechanical resonators of large mass and long coherence time, as discussed in [9].

In current experiments, optomechanical implementations would require significant improvements in  $g_0$ , mechanical quality factor  $Q_m$ , or optical finesse  $\mathcal{F}$  to approach single-photon strong coupling. Single-photon strong cooperativity has been achieved by coupling mechanical resonators to microwave qubits [15, 60, 61, 103, 104, 112–114]. Recently, this regime was achieved in optomechanical systems with optical photons [115, 116], as well as with microwave photons [113].

## 2.4.2 Strong Coupling

The strong coupling regime refers to the regime in which  $g/\kappa \gg 1$ . In this regime, the optical mode and the mechanical mode mix to form two hybridized modes whose splitting is  $2g$ . The exact result is described by solving the linearized equations of motion, Eq. (2.31a) and (2.31b). In the red-detuned regime ( $\Delta \approx -\omega_m$ ), by applying the RWA on Eq. (2.31a) and (2.31b), the simplified linearized coupled equations of motion are:

$$\begin{pmatrix} \dot{\langle \hat{a} \rangle} \\ \dot{\langle \hat{b} \rangle} \end{pmatrix} = -i \begin{pmatrix} -\Delta - i\frac{\kappa}{2} & -g \\ -g & \omega_m - i\frac{\gamma_m}{2} \end{pmatrix} \begin{pmatrix} \langle \hat{a} \rangle \\ \langle \hat{b} \rangle \end{pmatrix}. \quad (2.72)$$

The frequencies of the hybridized modes are

$$\omega_{\pm} = \omega_m + \frac{\delta}{2} - i\frac{\kappa + \gamma_m}{4} \pm \sqrt{g^2 + \left(\frac{\delta + i(\gamma_m - \kappa)/2}{2}\right)^2}, \quad (2.73)$$

where  $\delta = -\Delta - \omega_m$ . When the drive is exactly at the red-detuned sideband ( $\Delta = -\omega_m$ ), we have

$$\omega_{\pm} = \omega_m - i\frac{\kappa}{4} \pm \sqrt{g^2 - \left(\frac{\kappa}{4}\right)^2}. \quad (2.74)$$

The transition threshold for the square root to switch from purely imaginary to purely real is  $g = \kappa/4$ . Once this threshold is surpassed, two well-resolved peaks appear, indicating the coupling of the mechanical mode and optical mode in the strong-coupling regime [44]. Such a coupling is a prerequisite for various quantum applications, including high-fidelity quantum-state transfer. The photon statistics of an optomechanical system in the strong-coupling regime also exhibit intriguing antibunching behavior and other types of correlation [117].

#### 2.4.2.1 Single Photon Strong Coupling

The five dimensionless combinations listed below can encompass all the parameters of a standard optomechanical setup:

$$\frac{\kappa}{\omega_m}, \quad \frac{\omega_m}{\gamma_m}, \quad \frac{\Delta}{\omega_m}, \quad \frac{g}{\kappa}, \quad \frac{g_0}{\kappa}. \quad (2.75)$$

The first four parameters are unrelated to the value of Planck's constant  $\hbar$ . Only the ratio  $g_0/\kappa$  is affected by it, and it's considered a "quantumness" parameter [118] or referred to as the "granularity parameter" [119]. To illustrate, one can keep the first four parameters fixed and increase  $g_0/\kappa$ , which is equivalent to increasing the value of Planck's constant. Thus, as  $g_0/\kappa$  increases, we can observe more quantum signatures in the experiment. The regime in which  $g_0/\kappa > 1$  is referred to as the single-photon strong coupling regime. Some features predicted for larger values of  $g_0/\kappa$  differ qualitatively from classical predictions [120]. Additionally, it also has been demonstrated that probing mechanical energy quantization necessitates  $g_0/\kappa \gg 1$  [62].

Another way to appreciate the single-photon strong coupling criteria is by comparing the average displacement  $\delta x$  produced by a single photon with the zero-point fluctuation. That is

$$\frac{\delta x}{x_{ZPF}} = 2 \frac{g_0}{\omega_m}. \quad (2.76)$$

$g_0 > \omega_m$  is needed to resolve the displacement  $\delta x$ . It should be noted that  $n_{\text{cav}}$  refers to the average photon number inside the cavity. In order to truly observe this effect, the lifetime of a single photon should be longer than the mechanical oscillation period ( $\omega_m \gg \kappa$ ).

In a similar manner, the ratio of momentum kick to momentum zero-point fluctuations, also known as the Lamb-Dicke parameter, can be defined to express the uncertainty of

momentum:

$$\eta_{\text{Lamb-Dicke}} \equiv \delta p x_{\text{ZPF}} / \hbar = \delta p / (2p_{\text{ZPF}}) = g_0 / \kappa. \quad (2.77)$$

In both cases, the condition for strong coupling of single photons appears, *i.e.*,  $g_0 \gg \kappa$ .

### 2.4.3 Photon Blockade Parameter

Another important parameter is the photon blockade parameter. A single photon can induce a cavity frequency shift  $\Delta\omega_{\text{cav}}$  due to its radiation pressure exerting on the mechanic oscillator. This effect is captured by the effective photon-photon interaction mediated by the mechanics

$$\Delta\omega_{\text{cav}} = \frac{g_0^2}{\omega_m}. \quad (2.78)$$

If the shift caused by a single photon is larger than the cavity linewidth  $\kappa$ , then a second photon is prevented from entering the cavity due to the resonance shift. This phenomenon is referred to as photon blockade. Thus, the photon blockade parameter is defined as

$$\mathcal{D} \equiv g_0^2 / (\omega_m \kappa). \quad (2.79)$$

It is evident that you have single-photon strong coupling  $g_0 / \kappa > 1$  when you have strong photon blockade parameter  $\mathcal{D} > 1$ . The maximal (when the limit is not caused by a shifted cavity resonance but the absorption of the first intracavity photon in the cavity sideband) degree of suppression of two photons absorption process scales as  $(\kappa / \omega_m)^2$ , making sideband resolution an additional necessity for achieving single-photon blockade.

One of the predicted experimental observations of the optomechanically induced photon blockade is the strong antibunching in photon-photon correlations ( $g^{(2)}(0) < 1$ ) [121]. Further analysis has extended the study of photon-photon correlations to include the full temporal evolution of  $g^{(2)}(t)$ , Fano factors, as well as high-order moments of photon counting statistics [122].

The nonlinear quantum optomechanical regime would be a significant advancement in manipulating mechanical resonators at the quantum level. Research has demonstrated the possibility of preparing the mechanical resonator into states of non-Gaussian Wigner densities or of non-Poissonian phonon distributions in this regime[118]. In addition, it has been found that in this regime, the optomechanical system can produce mechanical states with partially negative Wigner densities for given appropriate parameters [123].

## 2.5 Relevant Optomechanical Regimes

The optomechanical system studied in this work is well-described by a single high- $Q$  optical mode unitarily coupled to a single high- $Q$  mechanical mode. The input optical power ( $\sim \mu\text{W}$ , corresponding to  $n_{\text{cav}} \sim 10^6$ ) is sufficiently large to apply the linearization approximation mentioned in Eq. (2.29). Thus the linearized coupled dynamical equations in Sec. 2.1.4 can well describe the system's evolution.

The mechanical mode has the frequency  $\omega_m/2\pi \approx 315.3 \text{ MHz}$  and linewidth  $\gamma_m/2\pi \approx 3.12 \text{ kHz}$ . The optical mode of the empty cavity has wavelength  $\lambda_{\text{cav}} \approx 1548.3 \text{ nm}$  and linewidth  $\kappa/2\pi \approx 47.2 \text{ MHz}$ . Both resonators are cooled to  $\sim 20 \text{ mK}$ . So the optical mode is very close to its ground state, and the mechanical mode is thermal equilibrium to a thermal state with a mean occupancy  $n_{m,\text{th}} \sim 1$ . The system satisfies the resolved-sideband condition ( $\omega_m \gg \kappa$ ). The discussion about the sideband-resolved regime in Sec. 2.3 is also relevant to this system.

The single-photon coupling strength  $g_0/2\pi \approx 4.6 \text{ kHz}$ . The single-photon cooperativity is  $\mathcal{C}_0 \approx 5.7 \times 10^{-4} \ll 1$ . The single-photon strong coupling parameter  $g_0/\omega \approx 1.4 \times 10^{-5}$ , which requires  $P \approx 2.5 \text{ mW}$  to achieve the strong coupling regime. Hence, these non-trivial quantum effects cannot be accessed directly in this system.

The relevant equations derived in this chapter are mainly used in Chapter 6.

“Facts are stubborn things, but statistics are pliable.”

– Mark Twain

# CHAPTER 3

## Quantum Statistics

In the universe outlined by Isaac Newton, it is usually understood that the past and future are entirely determined by the present. In accordance with this deterministic principle, Pierre-Simon Laplace later introduced “Laplace’s demon” in his 1814 publication, *A Philosophical Essay on Probabilities* [124]. This hypothetical creature is a “vast intelligence” that possesses knowledge of the complete physical state of the present universe at one instance, and so can, in principle, learn its full history and future.<sup>1</sup>

One hundred years later, quantum mechanics upended this worldview. Like classical mechanics, quantum theories tell you how the system evolves over time based on the information of the system at present. This evolution can be described by the Schrödinger equation, which represents the state of the system as a complex-valued wave on the system’s configuration space. Although this equation is deterministic, the laws of quantum mechanics are usually formulated with additional rules that govern the behavior of systems when they are under observation or measurement. The most striking difference is that measurement outcomes cannot be predicted with absolute certainty, even in principle. The square modulus of the wave function was identified as the probability density by Max Born. This is the interpretation of quantum mechanics that is used by the overwhelming majority of physicists. However, it is important to note that there are other interpretations in which fundamental plays a different role or is even entirely absent. A recent review is in Ref. [127].

In addition to the apparently fundamental uncertainty inherent to quantum mechanics, it is also important to be able to describe situations in which “classical uncertainty” (*i.e.*, the describer’s ignorance about the quantum state in which the system was prepared) is in presence. In this chapter, we discuss the theories which incorporate classical probability into the quantum description and show theoretical results that are used in later chapters.

---

<sup>1</sup>The status of determinism in Newtonian mechanics is actually more subtle. See examples in Refs. [125, 126].

## 3.1 Photon Statistics

In quantum mechanics, the idea of wave-particle duality suggests that any quantum entity or particle can be characterized as either a wave or a particle, highlighting the limitation of classical concepts such as ‘wave’ or ‘particle’ in completely accounting for the behavior of objects at the quantum scale. As Einstein wrote [128]:

*It seems as though we must use sometimes the one theory and sometimes the other, while at times we may use either. We are faced with a new kind of difficulty. We have two contradictory pictures of reality; separately neither of them fully explains the phenomena of light, but together they do.*

For optics, these discrete particles are referred to as photons. Photon counting statistics can fully reveal information about the quantum state of the light, which also exhibits a wave-like feature. As described below, certain statistics can distinguish quantum features from those obtained by any classical theory.

### 3.1.1 Photon Counting Distribution

Assume the set of eigenstates of a system is  $\{\psi_i\}$ . A general “mixed state” of this system can be represented by a density matrix  $\hat{\rho}$  in the basis of  $\{\psi_i\}$  as

$$\hat{\rho} = \sum_i \rho_i |\psi_i\rangle\langle\psi_i|, \quad (3.1)$$

where  $\rho_i$  is the probability (in the classical sense) that the system is in the quantum state  $|\psi_i\rangle$ . The probability to find  $n$  photons in a measurement in a measurement of a system characterized by  $\hat{\rho}$  is

$$P_n = \text{Tr}\hat{\rho}|n\rangle\langle n| = \sum_i \rho_i |\langle\psi_i|n\rangle|^2. \quad (3.2)$$

For a harmonic oscillator, the eigenstate basis is the Fock state basis or number state basis. It turns out that this basis is useful for evaluating the photon count statistics as we have  $P_n = \rho_n$  in Eq. (3.2).

A thermal state is a mixed state, and its density matrix can be expressed in the Fock state basis as [129]

$$\hat{\rho}_{\text{th}} = \sum_{n=0}^{\infty} \frac{n_{\text{th}}^n}{(1+n_{\text{th}})^{n+1}} |n\rangle\langle n|, \quad (3.3)$$

where  $n_{\text{th}} = \langle n \rangle = \sum_n \rho_n n$  is the expectation occupancy of the thermal state. The

probability follows the Bose-Einstein distribution. The variance of a thermal state is

$$(\Delta n)_{\text{th}}^2 = n_{\text{th}}^2 + n_{\text{th}}. \quad (3.4)$$

A coherent state is a pure state and can be expressed as

$$|\alpha\rangle = e^{-\frac{1}{2}|\alpha|^2} \sum_{n=0}^{\infty} \frac{\alpha^n}{\sqrt{n!}} |n\rangle. \quad (3.5)$$

Its photon number distribution is given by

$$P_{|\alpha\rangle}(n) = \exp(-|\alpha|^2) \cdot \frac{|\alpha|^{2n}}{n!}, \quad (3.6)$$

which is a Poisson distribution. The variance of a coherent state is

$$(\Delta n)_{|\alpha\rangle}^2 = |\alpha|^2. \quad (3.7)$$

In practice, classical measurement inefficiency impacts the information that can be extracted about the photon number distribution. Assuming the detection efficiency is such that the probability of measuring a single photon when the state of the system is  $|1\rangle$  is  $\eta$ , then the probability  $P_m^{(n)}$  of observing  $m$  photons of the state  $|n\rangle$  is given by [129]

$$P_m^{(n)} = C_n^m \eta^m (1 - \eta)^{n-m}. \quad (3.8)$$

This is Bernoulli's distribution for  $m$  successful events in  $n$  trials in which each individual event has identical independent success probability  $\eta$ . Thus, the measured photon counting distribution reads

$$P_m = \sum_{n=m}^{\infty} C_n^m \eta^m (1 - \eta)^{n-m} \rho_n. \quad (3.9)$$

Clearly, in the case  $\eta = 1$ , we have  $P_n = \rho_n$ , *i.e.*, we can obtain the  $\rho_i$  from the measured photon counting probability distribution. For  $\eta < 1$ , if the density matrix element truncates at  $n'$ , then  $\rho_i$  can be inversely solved exactly from measurements of  $P_m$ .

It is also worth pointing out that this probability could be reexpressed by the  $P$ -function (discussed in Sec. 3.4.1.1) as

$$P_m = \int d^2\alpha \sum_{n=m}^{\infty} C_n^m P(\alpha, \alpha^*) \frac{|\alpha|^{2n}}{n!} e^{-|\alpha|^2} \eta^m (1 - \eta)^{n-m}. \quad (3.10)$$

This can be further simplified by changing  $n$  to  $l + m$ , giving

$$P_m = \int d^2\alpha P(\alpha, \alpha^*) \frac{(\eta|\alpha|^2)^m}{m!} e^{-\eta|\alpha|^2}. \quad (3.11)$$

Therefore, it is also possible to invert Eq. (3.11) to derive the  $P$ -function. Detailed discussion on quasi-probability functions (such as the  $P$ -function) will be provided in Sec. 3.4.

### 3.1.2 Photon Correlations and Coherences

In statistics, correlation or dependence refers to any statistical relationship between two random variables or bivariate data, regardless of whether this relationship is causal or not. Photon correlations make it possible to unravel the wave-like behavior of light from particle-like measurements. Nonclassical correlations (discussed below) are explicit examples of the quantum nature of light.

Formally, the correlation can be defined as the expectation value of the product of variables  $\langle ABCD \rangle$ . In quantum mechanics,  $A, B, C$ , and  $D$  are not  $c$ -numbers but operators, and in general do not commute. In the optical domain, detectors usually measure the local optical field in an absorptive way by the photoelectric effect or photothermal effect. Therefore, only annihilation operators  $\hat{a}$  contribute to the measurement probability. In terms of Fermi's golden rule, the transition rate satisfies

$$\Gamma_{i \rightarrow f} \propto |\langle f | H_{\text{int}} | i \rangle|^2, \quad (3.12)$$

where  $|i\rangle$  and  $|f\rangle$  are initial and final states, respectively, and the completeness relation gives  $\sum_f |f\rangle\langle f| = 1$ . Hence, the transition probability of absorptively measuring a photon from the initial state of the light field  $|i\rangle$  at time  $t$  and position  $\mathbf{r}$  is proportional to

$$p_1(\mathbf{r}, t) = |\langle f | \hat{a}(\mathbf{r}, t) | i \rangle|^2 = \text{Tr}[\hat{\rho}\hat{a}^\dagger\hat{a}] = \langle \hat{a}^\dagger(\mathbf{r}, t)\hat{a}(\mathbf{r}, t) \rangle. \quad (3.13)$$

In general, the initial state is not a pure state, and so must be described by a density matrix  $\hat{\rho}$ .

Therefore, we define the first-order correlation function of the field  $\hat{a}$  by normally ordered creation and annihilation operators as the following

$$G^{(1)}(\mathbf{r}_1, \mathbf{r}_2; t_1, t_2) = \langle \hat{a}^\dagger(\mathbf{r}_1, t_1)\hat{a}(\mathbf{r}_2, t_2) \rangle. \quad (3.14)$$

For a statistically stationary optical state and identical detectors, the correlation functions  $G^{(1)}(\mathbf{r}_1, \mathbf{r}_2; t_1, t_2)$  only depends on the time difference  $\tau = t_2 - t_1$  as shown below:

$$G^{(1)}(\mathbf{r}_1, \mathbf{r}_2; t_1, t_2) \equiv G^{(1)}(\tau). \quad (3.15)$$

Photon detectors only measure the individual photon arrival time and the photon count rates. In this case, the first-order correlation reduces to the number operator up to an overall measurement efficiency prefactor  $\eta$  as

$$G^{(1)}(0) \equiv \eta \langle \hat{a}^\dagger \hat{a} \rangle. \quad (3.16)$$

Now consider a joint measurement at two different times  $t_1$  and  $t_2$ . Similar to the discussion above, the joint probability of two-photon coincidence measurement is thus governed by the second-order correlation function, which is defined as

$$G^{(2)}(\mathbf{r}_1, \mathbf{r}_2; t_1, t_2) = \langle \hat{a}^\dagger(\mathbf{r}_1, t_1) \hat{a}^\dagger(\mathbf{r}_2, t_2) \hat{a}(\mathbf{r}_2, t_2) \hat{a}(\mathbf{r}_1, t_1) \rangle, \quad (3.17)$$

where not only the creation and annihilation operators are normally ordered but also are time-ordered as  $t_2 \geq t_1$ . This is apparent by considering the final state is a result of a series of measurements that strictly obey time ordering.

This definition can be generalized to the  $n$ th-order correlation function as

$$\begin{aligned} G^{(n)}(\mathbf{r}_1, \mathbf{r}_2, \dots, \mathbf{r}_n; t_1, t_2, \dots, t_n) \\ = \langle \hat{a}^\dagger(\mathbf{r}_1, t_1) \hat{a}^\dagger(\mathbf{r}_2, t_2) \dots \hat{a}^\dagger(\mathbf{r}_n, t_n) \hat{a}(\mathbf{r}_n, t_n) \dots \hat{a}(\mathbf{r}_2, t_2) \hat{a}(\mathbf{r}_1, t_1) \rangle. \end{aligned} \quad (3.18)$$

Notice that in the definitions above, we always have equal numbers of creation and annihilation operators. This is because for typical measurements, only such Hermitian operators contribute to the measurement results.

Coherences are correlation functions that are normalized to remove the experiment-dependent measurement efficiency  $\eta$ . We define the second-order coherence as

$$g^{(2)}(r_1, r_2; t_1, t_2) = \frac{\langle \hat{a}^\dagger(\mathbf{r}_1, t_1) \hat{a}^\dagger(\mathbf{r}_2, t_2) \hat{a}(\mathbf{r}_2, t_2) \hat{a}(\mathbf{r}_1, t_1) \rangle}{\langle \hat{a}^\dagger(\mathbf{r}_1, t_1) \hat{a}(\mathbf{r}_1, t_1) \rangle \langle \hat{a}^\dagger(\mathbf{r}_2, t_2) \hat{a}(\mathbf{r}_2, t_2) \rangle}. \quad (3.19)$$

For a stationary state measured by identical detectors, the coherence reads

$$g^{(2)}(\tau) = \frac{\langle \hat{a}^\dagger(t) \hat{a}^\dagger(t + \tau) \hat{a}(t + \tau) \hat{a}(t) \rangle}{\langle \hat{a}^\dagger \hat{a} \rangle^2}. \quad (3.20)$$

In this case, the first-order coherence is always  $g^{(1)} = 1$ . As discussed in Sec. 3.4.1.1, the expectation value of normally ordered operators is associated with the  $P$ -function of the state, which is a correspondence between classical and quantum coherence theory. We thus can calculate the coherence of the state by using its corresponding  $P$ -function.

Similar to the high-order correlation functions shown in Eq. (3.18), the second-order

coherence shown in Eq. (3.20) can be extended to high-order coherences as

$$g^{(n)}(\boldsymbol{\tau}) = \frac{\langle \hat{a}^\dagger(t) \cdots \hat{a}^\dagger(t + \cdots \tau_{n-1}) \hat{a}(t + \cdots \tau_{n-1}) \cdots \hat{a}(t) \rangle}{\langle \hat{a}^\dagger \hat{a} \rangle^n}, \quad (3.21)$$

where the elements of  $\boldsymbol{\tau} = \{\tau_1, \tau_2, \dots, \tau_{n-1}\}$  are the delay times between each two consecutive counts. All delaying times are nonnegative (*i.e.*,  $\forall \tau_i \geq 0$ ) to satisfy the time ordering requirement.

### 3.1.3 Bunching and Anti-Bunching

Literally, bunching is the tendency of photons (or other particles) to distribute themselves preferentially in bunches rather than randomly. Oppositely, anti-bunching photons tend to be more evenly spread than for a random sequence. Before we reach that part, I will discuss the definition of the Poisson, sub-Poisson and super-Poisson distributions. And eventually, I will discuss the confusing relations between these concepts.

#### 3.1.3.1 Poisson, Sub-Poisson and Super-Poisson Distributions

The photon counting problem is part of the general counting problem, which has its roots in queue theory [130]. Let's first quickly review what a Poisson distribution is.

The validity of the Poisson distribution is restricted to the following assumptions:

**Independence** All events are independent;

**Identity** The average rate at which events occur is constant;

**Exclusion** Two events cannot occur at exactly the same instant.

Assume the average rate of photons is  $\lambda$ . In a unit of time  $dt$ , the probability of finding a photon in that time interval is  $dt\lambda$ . Based on the independence assumption, the probability of finding  $m$  photons in a time interval  $T$  is given by

$$P_{\Delta t=T}(m) = \lim_{dt \rightarrow 0} \binom{T/dt}{m} (1 - dt\lambda)^{T/dt} (dt\lambda)^m = \frac{(\lambda T)^m e^{-\lambda T}}{m!}. \quad (3.22)$$

In a special case,  $\lim \lambda T \rightarrow 0$ , the Poisson distribution reduces into the Binomial distribution. In other words, the Poisson distribution is the continuous limit of identical independent binomial distributions (*i.i.d.*). The Poisson distribution generating function is given by

$$\Pi_X(s) = e^{-\lambda T(1-s)} \quad (3.23)$$

and the probability of the separation time between two consecutive photons  $t$  satisfies  $\sim e^{-\lambda t}$ .

Particularly, the expectation value and the variance of the photon number in a time interval  $T$  are identical, given by

$$\text{E}(n) = \text{Var}(n) = \lambda T. \quad (3.24)$$

Along this spirit, the super-Poisson and the sub-Poisson distributions are defined as distributions satisfying the following conditions [131]:

$$\text{Super-Poisson: } \text{Var}(n) > \text{E}(n); \quad (3.25a)$$

$$\text{Sub-Poisson: } \text{Var}(n) < \text{E}(n). \quad (3.25b)$$

### 3.1.3.2 The Second-Order Coherences of Bunching and Anti-Bunching

In Sec. 3.1.3. we briefly mentioned the conceptual definition of bunching and anti-bunching effects. In this section, we show rigorous mathematical restrictions on the second-order coherences  $g^{(2)}(t)$  for bunching, anti-bunching and random photons to clarify what we mean [131]:

<b>Bunching:</b>	$g^{(2)}(\tau_1) > g^{(2)}(\tau_2)$	$\forall \tau_1 < \tau_2, \quad \tau_1, \tau_2 \in [0, T]$
<b>Anti-bunching:</b>	$g^{(2)}(\tau_1) < g^{(2)}(\tau_2)$	$\forall \tau_1 < \tau_2, \quad \tau_1, \tau_2 \in [0, T]$
<b>Random:</b>	$g^{(2)}(\tau_1) = g^{(2)}(\tau_2)$	$\forall \tau_1 < \tau_2, \quad \tau_1, \tau_2 \in [0, T]$

An important message to address is that these restrictions on  $g^{(2)}(t)$  are specified within a time interval  $T$ . In other words, it describes a local monotonicity rather than a global behavior.

### 3.1.3.3 Relations between Super-/Sub-Poisson Distributions and Bunching/Anti-Bunching Effects

One might ask about relations between sub-Poisson, super-Poisson & Poisson distribution and bunching & anti-bunching effects. In this section, we clarify that these definitions are not identical. However, in certain circumstances, they might fall into the same category. Perhaps, the confusion among these concepts originates from this coincidence as described in the following quote [131]:

*“Perhaps because the effects often tend to occur together, there has been a widespread tendency in the literature to mix them up or even to regard them as one and the same.”*

The relation between the sub-/super-Poisson distribution and the anti-bunching/bunching

effect is subtle. For brevity, we introduce the relative coherence function  $\lambda(\tau)$ :

$$\lambda(\tau) \equiv g^{(2)}(\tau) - 1. \quad (3.26)$$

For a stationary state which satisfies  $R^{-1} \ll \tau_c$  ( $R$  is the count rate,  $\tau_c$  is the decoherence time (for  $t \gg \tau_c$ ,  $\lambda(t) = 0$ )), the probability  $P_{\Delta t=T}(m)$  that the detector registers  $m$  photons in the time interval  $T$  is readily given in Refs. [131, 132]. From this, the variance of the measured photon number is [131]

$$\langle (\Delta n)^2 \rangle - \langle n \rangle = \langle n \rangle^2 \frac{1}{T^2} \int_{-T}^T d\tau (T - |\tau|) \lambda(\tau). \quad (3.27)$$

Since  $T - |\tau| \geq 0$ , the sign of  $\lambda(\tau)$  is crucial in determining whether the variance exceeds the mean or not, *i.e.*, whether photon-counting statistics are super- or sub-Poissonian. For a negatively correlated state ( $\lambda(\tau) < 0$ ,  $\forall \tau < T$ ), its counting statistics is sub-Poissonian. Similar steps can relate a positively correlated state ( $\lambda(\tau) > 0$ ,  $\forall \tau < T$ ) to super-Poissonian photon-counting statistics. It is worth addressing that only the integral, not the sign of  $\lambda$  of a given delay, determines whether photon-counting statistics are super- or sub-Poissonian.

Especially for an infinitesimal time interval  $T \rightarrow 0$ , we have the following relations which seem to be familiar:

$$\text{Super-Poisson: } g^{(2)}(0) > 1; \quad (3.28a)$$

$$\text{Sub-Poisson: } g^{(2)}(0) < 1; \quad (3.28b)$$

$$\text{Poisson: } g^{(2)}(0) = 1. \quad (3.28c)$$

If  $g^{(2)}(\tau)$  always monotonically approaches one, which is true for certain states, we can treat super-Poissonian (sub-Poissonian) photon statistics and the bunching (anti-bunching) phenomena of photons as the same manifestation of the state. Confusion among the definitions of these phenomena is previously caused by the result of this special case.

Regrettably, a direct and unequivocal relationship between Poissonian statistics and the bunching effect does not exist. A counter-example presented in Ref. [131] demonstrates a state of sub-Poissonian photon-counting statistics while the photons themselves exhibit bunching over time. If the field is in the superposition of Fock states of two modes,  $|n_{\omega_1}\rangle + |n_{\omega_2}\rangle$ , where  $n_{\omega_1} = n_{\omega_2} = \frac{1}{2}n_{\omega}$ , then we find its relative correlation is given by

$$\lambda(\tau) = \frac{1}{2} \cos(\omega_1 - \omega_2)\tau - 1/n_{\omega}, \quad (3.29)$$

and from Eq. (3.27), we have

$$\langle(\Delta n)^2\rangle - \langle n \rangle = \langle n \rangle^2 \left[ \frac{1}{2} \left( \frac{\sin((\omega_1 - \omega_2)T/2)}{(\omega_1 - \omega_2)T/2} \right)^2 - \frac{1}{n_\omega} \right]. \quad (3.30)$$

Such photon-counting statistics show sub-Poissonian behavior for specific counting intervals, such as  $T = 2\pi/|\omega_1 - \omega_2|$ . However, the function  $\lambda(\tau)$  decreases as  $\tau$  increases from  $\tau = 0$ , indicating that photons are more likely to be found in close proximity, resulting in short-term bunching rather than anti-bunching.

### 3.1.3.4 Compound Poisson Distribution

For a state which has a time-dependent coherence  $g^{(2)}(\tau)$  with a decoherence time  $\tau_c$  ( $g^{(2)}(\tau) = 1$  for  $\tau \gg \tau_c$ ), if the time interval  $T \gtrsim \tau_c$ , its photon-counting statistic is no longer Poissonian. In the discussion above, we simply categorize them into super-/sub-Poissonian distributions. This section provides a mathematical description of the photon-counting statistics of such a state.

The probability  $P_n(t, t + T)$  of the detector registering  $n$  photons in the time interval from  $t$  to  $t + T$  is given by [132].

$$P_n(t, t + T) = \int_0^\infty \frac{\nu^n}{n!} e^{-\nu} W(\nu) d\nu, \quad (3.31a)$$

$$G(u) = \int_0^\infty e^{(u-1)\nu} W(\nu) d\nu, \quad (3.31b)$$

$$\langle n^{[m]} \rangle \equiv \langle n(n-1) \cdots (n-m+1) \rangle = \int_0^\infty \nu^m W(\nu) d\nu, \quad (3.31c)$$

where

$$W(\nu) = \int \delta(\nu - \mathfrak{N}_{\alpha\alpha}) P(\{\alpha\}) \prod_k d^2\alpha_k, \quad (3.31d)$$

$$\mathfrak{N}_{\beta\alpha} = \int_t^{t+T} dt' \mathcal{A}^*(\{\beta\}, t') \mathcal{A}(\{\alpha\}, t'), \quad (3.31e)$$

where  $P(\{\alpha\})$  is the corresponding  $P$ -function. Here, we also show the corresponding generating function  $G(u)$  and the factorial  $m$ -th order mean value  $\langle n^{[m]} \rangle$  of the state. As you can see,  $P_n(t, t + T)$  is a linear superposition of independent Poissonian distributions  $\text{Pois}(\nu)$ , each with a weight  $W(\nu)$ . Thus,  $P_n(t, t + T)$  is known as the compound Poisson distribution. The weight function  $W$  evaluates the probability of each coherent state  $|\alpha\rangle$  in a  $P$ -representation with an effective intensity  $\mathfrak{N}_{\alpha\alpha}$ .  $\mathfrak{N}_{\alpha\beta}$  generally calculates the effective detected intensity between coherent states  $|\alpha\rangle$  and  $|\beta\rangle$ . Detailed derivations are shown in Ref. [132]. In the special case, considering a coherent state, we have  $W(\nu) = \delta(\nu - \mathfrak{N}_{\alpha\alpha})$ .  $P_n(t, t + T)$  becomes simply the Poisson distribution with mean value  $\mathfrak{N}_{\alpha\alpha}$ .

## 3.2 Coherence Functions of Various States

This section outlines the step-by-step process of determining values of zero-delay coherences of various quantum states, such as thermal states, coherent states, photon-added/subtracted states, and displaced thermal states. Furthermore, by utilizing the input-output formalism, we illustrate the time dependence of certain states.

### 3.2.1 Zero-Delay Second-Order Coherence

Zero-delay coherences are especially important because their values are directly linked to the initial state. All expected values in both the numerator and denominator can be expressed as integrals over the  $P$ -function of the initial state. Therefore, it is feasible to use coherence values to evaluate the quasi-probability functions of the state.

In the case  $\tau = 0$ , the second-order coherence  $g^{(2)}(\tau)$  in Eq. (3.20) reduces to

$$g^{(2)}(0) = \frac{\langle \hat{a}^\dagger \hat{a}^\dagger \hat{a} \hat{a} \rangle}{\langle \hat{a}^\dagger \hat{a} \rangle^2} = \frac{\langle n^2 \rangle - \langle n \rangle}{\langle n \rangle^2} = 1 + \frac{\langle \Delta n \rangle^2 - \langle n \rangle}{\langle n \rangle^2}. \quad (3.32)$$

Here, the commutation relation  $[\hat{a}^\dagger, \hat{a}] = 1$  has been used. With this, it is straightforward to calculate the zero-delay second-order coherences by evaluating the mean and the variance of the photon number.

**Thermal State** As shown in Eq. (3.3), the second-order coherence is

$$g^{(2)}(0) = \frac{2\langle n^2 \rangle + \langle n \rangle - \langle n \rangle}{\langle n \rangle^2} = 2. \quad (3.33)$$

**Coherent State** We have  $\langle n^2 \rangle = \langle n \rangle^2 + \langle n \rangle$ , and its second-order coherence reads

$$g^{(2)}(0) = \frac{\langle n^2 \rangle + \langle n \rangle - \langle n \rangle}{\langle n \rangle^2} = 1. \quad (3.34)$$

**Fock State** The Fock state  $|n\rangle$  is an eigenstate of the number operator. Thus we have

$$\langle n^2 \rangle = \langle n \rangle^2, \quad (3.35)$$

Its second-order coherence is

$$g^{(2)}(0) = \frac{\langle n \rangle^2 - \langle n \rangle}{\langle n \rangle^2} = 1 - \frac{1}{\langle n \rangle}. \quad (3.36)$$

**Displaced Thermal state** A displaced thermal state  $|n_{\text{th}}, \alpha\rangle$  is initially a thermal state and displaced in the coherent basis by a displacement operator  $\hat{D}(\alpha)$ . Its associated

density matrix  $\hat{\rho}$  is

$$\rho(\alpha) = \hat{\mathcal{D}}(\alpha)\rho_{\text{th}}\hat{\mathcal{D}}^\dagger(\alpha). \quad (3.37)$$

It is straightforward to calculate the mean and the variance of the photon number, which are

$$\langle n \rangle = |\alpha|^2 + n_{\text{th}} \quad (3.38)$$

$$\langle n^2 \rangle = |\alpha|^2 (2n_{\text{th}} + 1) + n_{\text{th}}^2 + n_{\text{th}} \quad (3.39)$$

Hence, its second-order coherence is

$$g^{(2)}(0) = \frac{2|\alpha|^2/n_{\text{th}} + 1}{(1 + |\alpha|^2/n_{\text{th}})^2} = 1 + \frac{2\xi^{-1} + 1}{(1 + \xi^{-1})^2}, \quad (3.40)$$

where  $\xi = n_{\text{th}}/|\alpha|^2$  is the ratio of the mean thermal photon number  $n_{\text{th}}$  over the displacement amplitude square.

**General Single-Mode Gaussian State** The most general single-mode Gaussian state is described as the displaced squeezed thermal state [133]. The density matrix of this state is given by

$$\hat{\rho}_{n_{\text{th}},\alpha,\zeta} \equiv \hat{\mathcal{D}}(\alpha)\hat{\rho}_{n_{\text{th}},\zeta}\hat{\mathcal{D}}^\dagger(\alpha) = \hat{\mathcal{D}}(\alpha)\hat{\mathcal{S}}(\zeta)\hat{\rho}_{n_{\text{th}}}\hat{\mathcal{S}}^\dagger(\zeta)\hat{\mathcal{D}}^\dagger(\alpha), \quad (3.41)$$

where  $\hat{\mathcal{D}}(\alpha) \equiv \exp(\alpha\hat{a}^\dagger - \alpha^*\hat{a})$  is the displacement operator,  $\hat{\mathcal{S}}(\zeta) \equiv \exp[\frac{1}{2}(\zeta^*\hat{a}^2 - \zeta\hat{a}^{\dagger 2})]$  is the squeezing operator and  $\hat{\rho}_{n_{\text{th}}}$  is the density operator of a thermal state with a mean occupancy  $n_{\text{th}}$ .

The corresponding two-time coherence is [133]

$$g^{(2)}(0) = 1 + \frac{2|\alpha|^2(n - \cos(\theta - 2\phi)s) + s^2 + n^2}{(|\alpha|^2 + n)^2}, \quad (3.42a)$$

$$n_{\text{tot}} \equiv \langle \hat{a}^\dagger \hat{a} \rangle = |\alpha|^2 + n, \quad (3.42b)$$

with

$$\theta = \arg(\alpha); \quad \phi = \arg(\zeta), \quad (3.43a)$$

$$n \equiv \text{Tr} [\hat{\rho}_{n_{\text{th}},\zeta}\hat{a}^\dagger \hat{a}] = \left(n_{\text{th}} + \frac{1}{2}\right) \cosh 2|\zeta| - \frac{1}{2}, \quad (3.43b)$$

$$s \equiv |\text{Tr} [\hat{\rho}_{n_{\text{th}},\zeta}\hat{a}\hat{a}^\dagger]| = \left(n_{\text{th}} + \frac{1}{2}\right) \sinh 2|\zeta|, \quad (3.43c)$$

where  $n_{\text{tot}}$  is the total photon number.

These specific examples show that using the number state basis as an expansion basis is highly advantageous when calculating photon-counting statistics. This is because number states are eigenstates of the number operator and are also the preferred basis for creation and annihilation operators.

### 3.2.2 High-Order Coherence

The calculation of high-order coherence functions is similar to the approach used in evaluating the second-order coherence function Eq. (3.20). The zero-delay  $m$ th-order coherence  $g^{(m)}(0)$  is

$$g^{(m)}(0) = \frac{\langle n(n-1)\cdots(n-m+1) \rangle}{\langle n \rangle^m}. \quad (3.44)$$

Both the numerator and the denominator can be calculated by  $\langle f(n) \rangle = \sum P_m f(m)$ . The following example explicitly demonstrates this approach.

For a thermal state  $|n_{\text{th}}\rangle$  whose occupancy is  $n_{\text{th}}$ ,  $\rho_n$  (the probability of the state  $|n\rangle$ ) follows the geometric progression. The summation over the numerator in Eq. (3.44) yields

$$\langle n \times \cdots \times (n-m+1) \rangle = \sum_{n=0}^{\infty} \frac{n_{\text{th}}^n}{(1+n_{\text{th}})^{n+1}} \times n \times \cdots \times (n-m+1) = m! n_{\text{th}}^m. \quad (3.45)$$

Therefore, the zero-delay  $m$ th-order coherence  $g^{(m)}(0)$  reads

$$g^{(m)}(0) = m! \quad (3.46)$$

which is independent of the thermal occupancy  $n_{\text{th}}$ .

An alternative way to calculate the coherence of Gaussian states is using Wick's theorem or Isserlis's theorem. In probability theory, Isserlis' theorem or Wick's probability theorem is a formula that allows one to compute high-order moments of the multivariate normal distribution in terms of its covariance matrix.

**Theorem 1 (Wick's Theorem)** *If  $(X_1, X_2 \cdots X_n)$  is a zero-mean multivariate normal random vector, then*

$$\mathbb{E}[X_1 X_2 \cdots X_n] = \sum_{p \in P_n^2} \prod_{\{i,j\} \in p} \mathbb{E}[X_i X_j] = \sum_{p \in P_n^2} \prod_{\{i,j\} \in p} \text{Cov}(X_i, X_j), \quad (3.47)$$

where the sum is over all the pairings of  $\{1, 2 \cdots n\}$ , i.e. all distinct ways of partitioning  $\{1, 2 \cdots n\}$  into pairs  $\{i, j\}$  and the product is over the pairs contained in  $p$ .  $P_n$  is the permutation group of  $\{1, 2 \cdots n\}$ .

Note that this theorem only applies to Gaussian states. For non-Gaussian random vari-

ables, the moment-cumulants formula replaces the role of Wick's probability formula [134].

The thermal state is a Gaussian state. The following shows how to apply Wick's theorem to get its high-order coherence. The numerators in the second-order coherence Eq. (3.32) can be evaluated by

$$\langle \hat{a}_0^\dagger \hat{a}_1^\dagger \hat{a}_1 \hat{a}_0 \rangle = \langle \hat{a}_0^\dagger \hat{a}_0 \rangle \langle \hat{a}_1^\dagger \hat{a}_1 \rangle + \langle \hat{a}_0^\dagger \hat{a}_1 \rangle \langle \hat{a}_1^\dagger \hat{a}_0 \rangle, \quad (3.48)$$

where  $\hat{a}_0 = \hat{a}(t)$  and  $\hat{a}_1 = \hat{a}(t + \tau_1)$ . Thus, this yields the value of  $g^{(2)}(0)$  for a thermal state as  $g^{(2)}(0) = 2$ . Applying the theorem to the numerator in Eq. (3.44) yields

$$\langle \hat{a}_0^\dagger \hat{a}_1^\dagger \cdots \hat{a}_{m-1}^\dagger \hat{a}_{m-1} \cdots \hat{a}_1 \hat{a}_0 \rangle = \sum_{p \in P_n^2} \prod_{\{i,j\} \in p} \langle \hat{a}_i^\dagger \hat{a}_j \rangle. \quad (3.49)$$

There are  $m!$  possible permutations for the group  $\{0, \dots, m-1\}$ . Hence, the value of the  $m$ th-order coherence is  $g^{(m)}(0) = m!$ .

The anti-normally ordered coherence  $h^{(m)}(\tau_1, \dots, \tau_{m-1})$  is defined as

$$h^{(m)}(\tau_1, \dots, \tau_{m-1}) = \frac{\langle \hat{a}(t) \cdots \hat{a}(t + \cdots \tau_{m-1}) \hat{a}^\dagger(t + \cdots \tau_{m-1}) \cdots \hat{a}^\dagger(t) \rangle}{\langle \hat{a} \hat{a}^\dagger \rangle^m}. \quad (3.50)$$

These are used in Sec. 7.3 and Sec. 7.4. We can evaluate the anti-normally ordered coherence of a thermal state in the same manner, which gives

$$h^{(m)}(\tau_1, \dots, \tau_{m-1}) = \frac{\sum_{p \in P_n^2} \prod_{\{i,j\} \in p} \langle \hat{a}_i \hat{a}_j^\dagger \rangle}{\prod_{i \in \{0, \dots, m-1\}} \langle \hat{a}_i \hat{a}_i^\dagger \rangle} = m!. \quad (3.51)$$

### 3.2.3 Post-Selected States

Post-selected states are states conditionally selected based on measurement results. They are out of thermal equilibrium with their thermal reservoir. These post-selected states exhibit different photon-counting statistics and have different energies than the original states (*i.e.*, prior to the post-selection).

In quantum optics, one can conditionally subtract or add quanta of thermal energy even with imperfect single-photon detectors. More explicitly, photon addition always results in a non-classical state [87, 135, 136], whereas photon subtraction produces a non-classical field only if the original state was already non-classical [137, 138]. Moreover, a sequence of photon creation and annihilation operators creates more interesting states [87, 139]. Notice that the creation and annihilation operations do not commute [88, 140], so a sequence of operators of different orderings produces yet another distinct state.

For certain non-classical post-selected states, their negative quasi-probabilities enable

post-selected experiments to outperform optimal post-selection-free experiments, yielding high information-cost rates impossible in any classical theories [89]. A preparation-and-postselection procedure has been proposed to achieve an arbitrarily large Fisher information, benefiting quantum-enhanced metrological advantage [3].

In the following, I derive and discuss the statistical properties of certain post-selected states. For brevity, I restrict the discussion to the case of an ensemble of identical quantum particles, such as photons in a single-mode radiation field.

The bosonic creation or annihilation operators are used to describe the addition or subtraction of a single photon to/from the light field. For a thermal state  $|n_{\text{th}}\rangle$ , the addition of a single photon is achieved by operating the creation operator  $\hat{a}^\dagger$  on the initial state. Thus we have a *single*-photon-added thermal state (SPAS), denoted as  $|n_{\text{th}}^{+1}\rangle$ . The density matrix  $\hat{\rho}_{+1}$  of a SPAS can be derived by Bayesian updating of the density matrix of the original thermal state  $\hat{\rho}_{\text{th}}$  in Eq. (3.3). More explicitly, With the addition of one photon, we have

$$\hat{\rho}_{\text{th}} \rightarrow \alpha \hat{a}^\dagger \hat{\rho}_{\text{th}} \hat{a}, \quad (3.52)$$

so that

$$\rho_m |m\rangle\langle m| \rightarrow \alpha \rho_m m |m-1\rangle\langle m-1| \quad (3.53)$$

up to an overall normalization factor chosen to satisfy  $\alpha \sum_{m=1}^{\infty} m \rho_m = 1$ . Thus,  $\alpha = 1 / \text{Tr}[\hat{a}^\dagger \hat{\rho}_{\text{th}} \hat{a}]$ . The density matrix  $\hat{\rho}_{+1}$  is

$$\hat{\rho}_{+1} = \sum_{n=0}^{\infty} \frac{n+1}{(1+n_{\text{th}})^2} \left(\frac{n_{\text{th}}}{1+n_{\text{th}}}\right)^n |n+1\rangle\langle n+1|. \quad (3.54)$$

Substituting Eq. (3.54) into Eq. (3.44) yields the second-order coherence of a SPAS, which is

$$g^{(2)}(0) = \frac{6n_{\text{th}}^2 + 4n_{\text{th}}}{(2n_{\text{th}} + 1)^2}. \quad (3.55)$$

Similarly, the density matrix  $\hat{\rho}_{-1}$  of a *single*-photon-subtracted thermal state (SPSS) is given by

$$\hat{\rho}_{-1} = \frac{\hat{a} \hat{\rho}_{\text{th}} \hat{a}^\dagger}{\text{Tr}[\hat{a} \hat{\rho}_{\text{th}} \hat{a}^\dagger]}. \quad (3.56)$$

That is,

$$\hat{\rho}_{-1} = \sum_{n=0}^{\infty} \frac{(1+n)}{(1+n_{\text{th}})^2} \left( \frac{n_{\text{th}}}{1+n_{\text{th}}} \right)^n |n\rangle\langle n|. \quad (3.57)$$

The second-order coherence of a SPSS is

$$g^{(2)}(0) = \frac{6n_{\text{th}}^2}{4n_{\text{th}}^2} = \frac{3}{2}. \quad (3.58)$$

This result is also independent of the initial phonon occupancy, similar to the result of a thermal state. The underlying reason for this independence will be explained in Sec. 3.4.4.

### 3.2.3.1 Multi-Photon-Added/Subtracted States

The same procedure can be iteratively applied to the density matrix of the thermal state  $k$  times to obtain  $k$ -photon-subtracted/added thermal states, which are

$$\hat{\rho}_{-k} = \frac{\hat{a}\hat{\rho}_{k-1}\hat{a}^\dagger}{\text{Tr}[\hat{a}\hat{\rho}_{k-1}\hat{a}^\dagger]} = \frac{\hat{a}^k\hat{\rho}_{\text{th}}\hat{a}^{\dagger k}}{\langle \hat{a}^k\hat{a}^k \rangle}, \quad (3.59a)$$

$$\hat{\rho}_{+k} = \frac{\hat{a}^\dagger\hat{\rho}_{k-1}\hat{a}}{\text{Tr}[\hat{a}^\dagger\hat{\rho}_{k-1}\hat{a}]} = \frac{\hat{a}^{\dagger k}\hat{\rho}_{\text{th}}\hat{a}^k}{\langle \hat{a}^k\hat{a}^{\dagger k} \rangle}. \quad (3.59b)$$

More explicitly, the probability  $\rho_m|_{\pm k}$  of having  $m$  photons after addition/subtraction of  $k$  photons is updated as

$$\rho_m|_{-k} = \frac{1}{k!(n_{\text{th}})^k} \frac{(m+k)!}{m!} \frac{1}{(n_{\text{th}}+1)} \left( \frac{n_{\text{th}}}{n_{\text{th}}+1} \right)^{(m+k)}; \quad (3.60a)$$

$$\rho_m|_{+k} = \begin{cases} 0 & , m < k \\ \frac{1}{k!(n_{\text{th}}+1)^k} \frac{(m+k)!}{m!} \frac{1}{(n_{\text{th}}+1)} \left( \frac{n_{\text{th}}}{n_{\text{th}}+1} \right)^{(m-k)} & , m \geq k \end{cases} \quad (3.60b)$$

The mean photon number of  $k$ -photon-subtracted/added states are

$$\langle n \rangle|_{-k} = \frac{\langle \hat{a}^{\dagger(k+1)}\hat{a}^{(k+1)} \rangle}{\langle \hat{a}^{\dagger(k)}\hat{a}^{(k)} \rangle} = (k+1)n_{\text{th}}, \quad (3.61a)$$

$$\langle n \rangle|_{+k} = \frac{\langle \hat{a}^k\hat{a}^{\dagger}\hat{a}\hat{a}^{\dagger k} \rangle}{\langle \hat{a}^k\hat{a}^{\dagger k} \rangle} = (k+1)n_{\text{th}} + k. \quad (3.61b)$$

The corresponding second-order moments are

$$\langle \hat{a}^\dagger \hat{a}^\dagger \hat{a} \hat{a} \rangle|_{-k} = \frac{\langle \hat{a}^{\dagger(k+2)} \hat{a}^{(k+2)} \rangle}{\langle \hat{a}^{\dagger(k)} \hat{a}^{(k)} \rangle} = (k+1)(k+2)n_{\text{th}}, \quad (3.62\text{a})$$

$$\langle \hat{a}^\dagger \hat{a}^\dagger \hat{a} \hat{a} \rangle|_{+k} = \frac{\langle \hat{a}^k \hat{a}^\dagger \hat{a}^\dagger \hat{a} \hat{a} \hat{a}^\dagger \rangle}{\langle \hat{a}^k \hat{a}^\dagger \rangle} = (k+1)(k+2)n_{\text{th}}^2 + 2k(k+1)n_{\text{th}} + k^2 - k. \quad (3.62\text{b})$$

Therefore, the second-order coherences of these states are

$$g^{(2)}(0)|_{-k} = \frac{k+2}{k+1}, \quad (3.63\text{a})$$

$$g^{(2)}(0)|_{+k} = \frac{(k+1)(k+2)n_{\text{th}}^2 + 2k(k+1)n_{\text{th}} + k^2 - k}{((k+1)n_{\text{th}} + k)^2}. \quad (3.63\text{b})$$

### 3.2.3.2 High-Order Coherence of a SPSS/SPAS

It is also interesting to show the high-order coherence of some post-selected states.

**SPSS** The  $m$ th-order moment of a SPSS is

$$\langle \hat{a}^{\dagger m} \hat{a}^m \rangle|_{-1} = \frac{\langle \hat{a}^{\dagger(m+1)} \hat{a}^{(m+1)} \rangle}{\langle \hat{a}^\dagger \hat{a} \rangle} = (m+1)!n_{\text{th}}^m, \quad (3.64)$$

and its corresponding coherence is

$$g^{(m)}(0)|_{-1} = \frac{(m+1)!n_{\text{th}}^m}{(2n_{\text{th}})^m} = \frac{(m+1)!}{2^m}. \quad (3.65)$$

**SPAS** The  $m$ th-order moment of a SPAS is

$$\langle \hat{a}^{\dagger m} \hat{a}^m \rangle|_{+1} = \sum_{n=0}^{\infty} n(n-1) \cdots (n-m+1) \rho_n|_{-1} = m![(m+1)n_{\text{th}} + m]n_{\text{th}}^{m-1}, \quad (3.66)$$

and its corresponding  $m$ th-order coherence is

$$g^{(m)}(0)|_{+1} = \frac{m![(m+1)n_{\text{th}} + m]n_{\text{th}}^{m-1}}{(2n_{\text{th}} + 1)^m}. \quad (3.67)$$

**2PAS/2PSS** The  $m$ th-order coherences of a 2-photon-added/subtracted state (2PAS)

/2PSS) is

$$g^{(m)}(0)|_{-2} = \frac{(m+2)!}{2 \times 2^m}; \quad (3.68a)$$

$$g^{(m)}(0)|_{+2} = \frac{m! n_{\text{th}}^{m-2} \left[ \left( \frac{m(m-1)}{2} + 2m + 1 \right) n_{\text{th}}^2 + m(m+1)n_{\text{th}} + \frac{m(m-1)}{2} \right]}{(3n_{\text{th}} + 2)^m}. \quad (3.68b)$$

As you might have noticed, the results of post-selected states are closely related to high-order coherences of a thermal state, which will be discussed in Sec. 3.3.2.

### 3.2.3.3 Different Ordered Coherences of a SPAS/SPSS

Besides the conventional normally ordered coherence functions, we show all other ordered second-order coherences of a SPAS/SPSS in the following.

For a SPAS, we have

$$\left| \frac{\langle \hat{a}\hat{a}\hat{a}^\dagger\hat{a}^\dagger \rangle}{\langle \hat{a}\hat{a}^\dagger \rangle \langle \hat{a}\hat{a}^\dagger \rangle} \right|_{+1} = \frac{3}{2}; \quad (3.69a)$$

$$\left| \frac{\langle \hat{a}\hat{a}^\dagger\hat{a}\hat{a}^\dagger \rangle}{\langle \hat{a}\hat{a}^\dagger \rangle \langle \hat{a}^\dagger\hat{a} \rangle} \right|_{+1} = \frac{(3n_{\text{th}} + 1)(n_{\text{th}} + 2)}{(2n_{\text{th}} + 1)(n_{\text{th}} + 1)}; \quad (3.69b)$$

$$\left| \frac{\langle \hat{a}^\dagger\hat{a}\hat{a}^\dagger\hat{a} \rangle}{\langle \hat{a}\hat{a}^\dagger \rangle \langle \hat{a}^\dagger\hat{a} \rangle} \right|_{+1} = \frac{6n_{\text{th}}^2 + 6n_{\text{th}} + 1}{(2n_{\text{th}} + 2)(2n_{\text{th}} + 1)}; \quad (3.69c)$$

$$\left| \frac{\langle \hat{a}^\dagger\hat{a}^\dagger\hat{a}\hat{a} \rangle}{\langle \hat{a}^\dagger\hat{a} \rangle \langle \hat{a}^\dagger\hat{a} \rangle} \right|_{+1} = \frac{(6n_{\text{th}} + 4)n_{\text{th}}}{(2n_{\text{th}} + 1)^2}; \quad (3.69d)$$

For a SPSS, we have

$$\left| \frac{\langle \hat{a}\hat{a}\hat{a}^\dagger\hat{a}^\dagger \rangle}{\langle \hat{a}\hat{a}^\dagger \rangle \langle \hat{a}\hat{a}^\dagger \rangle} \right|_{-1} = \frac{2(3n_{\text{th}} + 1)(n_{\text{th}} + 1)}{(2n_{\text{th}} + 1)(2n_{\text{th}} + 1)}; \quad (3.70a)$$

$$\left| \frac{\langle \hat{a}\hat{a}^\dagger\hat{a}\hat{a}^\dagger \rangle}{\langle \hat{a}\hat{a}^\dagger \rangle \langle \hat{a}^\dagger\hat{a} \rangle} \right|_{-1} = \frac{6n_{\text{th}}^2 + 6n_{\text{th}} + 1}{2n_{\text{th}}(2n_{\text{th}} + 1)}; \quad (3.70b)$$

$$\left| \frac{\langle \hat{a}^\dagger\hat{a}\hat{a}^\dagger\hat{a} \rangle}{\langle \hat{a}\hat{a}^\dagger \rangle \langle \hat{a}^\dagger\hat{a} \rangle} \right|_{-1} = \frac{3n_{\text{th}} + 1}{2n_{\text{th}} + 1}; \quad (3.70c)$$

$$\left| \frac{\langle \hat{a}^\dagger\hat{a}^\dagger\hat{a}\hat{a} \rangle}{\langle \hat{a}^\dagger\hat{a} \rangle \langle \hat{a}^\dagger\hat{a} \rangle} \right|_{-1} = \frac{3}{2}; \quad (3.70d)$$

These quantities can be used to reveal the nonclassical nature of post-selected states by violating certain classical bounds discussed in Sec. 3.5.1.

### 3.2.3.4 Interpretation of the Post-Selected Photon Number

In this section, we discuss on the mean photon occupancy of post-selected states. In particular, we explain how the mean occupancy increases by  $(k + 1)$ -fold after subtracting  $k$  photons. The increase of the mean photon number after subtraction seems to be counter-intuitive at first glance, that can be understood as a Bayesian update on the probabilities, as elaborated below.

Any measurement that consists of a sequence of random variables  $\{X_n, n = 1, 2, 3, \dots\}$  ( $X_n$  means state at time  $n$ ) satisfies

$$P(x_{n+1}) = \sum_{x_1 \dots x_n \in \mathcal{S}} P(x_{n+1}|x_n, x_{n-1}, \dots x_1)P(x_n, x_{n-1}, \dots x_1), \quad (3.71)$$

where  $P(x_n, x_{n-1}, \dots x_1)$  is the probability of the first  $n$  variables  $\{X_n, X_{n-1}, \dots, X_1\}$  being  $\{x_n, x_{n-1}, \dots x_1\}$ ,  $P(x_{n+1})$  is the probability of  $X_n = x_n$  and  $P(x_n|x_{n-1}, x_{n-2}, \dots x_1)$  is the corresponding conditional probability.  $\mathcal{S} = \{s_1, s_2, \dots, s_m\}$  is the set of all possible comes of each variable  $X_i$ .

If this process is memoryless (*i.e.*, the future state  $X_{n+1}$  is independent of the past states and depends only on the present state  $X_n$ ), then Eq. (3.71) is reduced into a Markov chain process, given by

$$P(x_{n+1}) = \sum_{x_n \in \mathcal{S}} P(x_{n+1}|x_n)P(x_n). \quad (3.72)$$

Let  $\mathbf{M}$  be an  $m \times m$  matrix (where  $m$  is the maximal number of possible values of each  $X_i$ ), which denotes the transition matrix of this Markov chain process, so that  $M_{ji} = P(x_{n+1} = s_j | x_n = s_i)$ .

The reversed process is described by

$$P(x_n) = \sum_{x_{n+1} \in \mathcal{S}} P(x_n|x_{n+1})P(x_{n+1}), \quad (3.73)$$

with the inversion matrix  $\mathbf{N}$  where  $N_{ji} = P(x_n = s_j | x_{n+1} = s_i)$ . Using Bayes' theorem, we have the following relation between  $\mathbf{M}$  and  $\mathbf{N}$ :

$$N_{ji} = P(x_n = s_j | x_{n+1} = s_i) = P(x_{n+1} = s_i | x_n = s_j) \frac{P(x_n = s_j)}{P(x_{n+1} = s_i)} = M_{ij} \frac{P(x_n = s_j)}{P(x_{n+1} = s_i)}. \quad (3.74)$$

Consider a stationary Markov chain  $X_i$  whose probability satisfies

$$\begin{cases} P(X_i = 1) = \epsilon \\ P(X_i = 0) = 1 - \epsilon. \end{cases} \quad (3.75)$$

So we have  $E[X_i] = \epsilon$ . If this is a stochastic process of photons released by a thermal state, we have  $P(x_i = 1|x_{i-1} = 1) = 2\epsilon$  which is equivalent to  $g^{(2)}(0) = 2$ . In addition,  $\mathbf{M}$  satisfies the stationary condition: the stationary probability distribution  $P^* = \begin{pmatrix} \epsilon \\ 1 - \epsilon \end{pmatrix}$  is invariant after the Markov transition

$$P^* = \mathbf{M} \cdot P^*. \quad (3.76)$$

Thus, the transition matrix  $\mathbf{M}$  can be

$$\mathbf{M} = \begin{bmatrix} 2\epsilon & \frac{\epsilon - 2\epsilon^2}{1-\epsilon} \\ 1 - 2\epsilon & 1 - \frac{\epsilon - 2\epsilon^2}{1-\epsilon} \end{bmatrix}. \quad (3.77)$$

Substituting  $\mathbf{M}$  into Eq. (3.74), we have  $\mathbf{N} = \mathbf{M}$ .

The expected value  $E[X_i]$  (*i.e.*, the mean photon number  $\langle n \rangle$  in this experiment) of a post-selected state is thus twice the selection-free state. That is

$$\frac{E[X_{\text{Post-Selected}}]}{E[X]} = \frac{P(x_{n+1} = 1|x_n = 1)}{P(x_{n+1} = 1)} = 2. \quad (3.78)$$

We denote  $X_{\text{Pre-Selected}}$  for any  $X_{n-1}$  if  $X_n = 1$  (“Pre-Selected” means the selected events are prior to the selection condition). Similarly, we have

$$\frac{E[X_{\text{Pre-Selected}}]}{E[X]} = \frac{P(x_{n-1} = 1|x_n = 1)}{P(x_{n-1} = 1)} = 2. \quad (3.79)$$

This result indicates that these conditional results are time reversible, which stems from Bayes’s theorem.

Under the same Markov chain process assumption, we can generalize this result to  $k$ -photon-conditioned states. Consider a stationary Markov chain  $X_i$  whose values are in  $\{0, 1, \dots, m\}$  ( $m \geq k$ ). The ratio of the mean occupancy between a post-selected state by conditioning  $x_n = k$  and a selection-free state is

$$\frac{E[X_{\text{Post-Selected}}]}{E[X]} = \frac{\sum_{j=0}^m j \cdot P(x_{n+1} = j|x_n = k)}{\sum_{j=0}^m j \cdot P(x_{n+1} = j)}. \quad (3.80)$$

Similarly, we have the time-reversible relation between the post- and pre-selected states as

$$\frac{E[X_{\text{Post-Selected}}]}{E[X_{\text{Pre-Selected}}]} = \frac{\sum_{j=0}^m j \cdot P(x_{n+1} = j|x_n = k)}{\sum_{j=0}^n j \cdot P(x_{n-1} = j|x_n = k)} = 1. \quad (3.81)$$

### 3.3 Decoherence of Different states

This section presents calculations of time-dependent coherence functions for a thermal state, a post-selected state, and a displaced thermal state. These functions are directly utilized in the experiment. The decoherence of a quantum system can be modeled by coupling to a thermal reservoir, which can be evaluated in the input-output formalism. Here, two different approaches are taken to calculate the decoherence of a Gaussian state.

#### 3.3.1 Decoherence of a Thermal State

Thermal states are the simplest but very important Gaussian states as they are in thermal equilibrium with the reservoir. We calculate the decoherence of a thermal state using two different approaches: multi-mode interference [100] and input-output formalism [98]. These two approaches are different in their mathematical formalisms, but both use Gaussianity to simplify the calculation.

##### 3.3.1.1 Multi-Mode Interference

In multi-mode quantum optics [100], the basis of the state is

$$\{|n_{k_1}\rangle \otimes \cdots |n_{k_i}\rangle \cdots \otimes |n_{k_m}\rangle\} \quad (3.82)$$

where  $k_m$  is the wavenumber vector,  $i \in \{1, 2 \dots m\}$  is the mode index and  $|n_{k_i}\rangle$  is the corresponding  $|n\rangle$  Fock state of mode  $k_i$ . For brevity, let's denote this basis as  $|\{\mathbf{n}_k\}\rangle$ , with  $\mathbf{k} = \{k_1, k_2 \dots, k_m\}$ .

##### The First-Order Coherence

In the Fock state basis, the expectation value of the intensity  $\langle \hat{E}^-(t) \hat{E}^+(t) \rangle$  of a Gaussian state satisfies

$$\langle \hat{E}^-(t) \hat{E}^+(t) \rangle \propto \sum_{\{\mathbf{n}_k\}} \rho_{n_{k_i}, n_{k_i}} \langle n_{k_i} | \hat{E}^-(t) \hat{E}^+(t) | n_{k_i} \rangle \propto \sum_{k_i \in \mathbf{k}} \omega_{k_i} \langle n_{k_i} \rangle, \quad (3.83)$$

where  $\omega_{k_i}$  is the frequency of mode  $k_i$ , and we only keep the diagonal terms  $\rho_{n_{k_i}, n_{k_i}}$  in the density matrix because the state is Gaussian. Thus, the first-order coherence is

$$g^{(1)}(\tau) = \frac{\langle \hat{E}^-(t) \hat{E}^+(t + \tau) \rangle}{\langle \hat{E}^-(t) \hat{E}^+(t) \rangle} = \frac{\sum_{k_i \in \mathbf{k}} \omega_{k_i} \langle n_{k_i} \rangle e^{-i\omega_{k_i}\tau}}{\sum_{k_i \in \mathbf{k}} \omega_{k_i} \langle n_{k_i} \rangle}. \quad (3.84)$$

Consider a resonance at  $\omega_0$  with a linewidth  $\kappa$ . When this resonance is in thermal equilibrium (*i.e.*, a thermal state driven by a frequency-independent input), the power spectrum

satisfies

$$S_{\hat{E}^- \hat{E}^+}(k_i) \propto \omega_{k_i} \langle n_{k_i} \rangle \propto \frac{\kappa/2\pi}{(\omega_0 - \omega_{k_i})^2 + \kappa^2/4}. \quad (3.85)$$

In the continuous mode approximation, which is accurate for chaotic light that excites a large number of modes, the summation over  $\mathbf{k}$  in Eq. (3.84) is converted into an integral. Therefore, Eq. (3.84) can be reexpressed as

$$g^{(1)}(\tau) = \int_0^\infty d\omega_k \frac{(\kappa/2\pi) \exp(-i\omega_k \tau)}{(\omega_k - \omega_0)^2 + \kappa^2/4}. \quad (3.86)$$

This integral can be done using a contour over the lower half complex plane with only one simple pole at  $\omega_0 - i\kappa/2$ . That is

$$g^{(1)}(\tau) = \int_{-\infty}^\infty d\omega_k \frac{(\kappa/2\pi) \exp(-i\omega_k \tau)}{(\omega_k - \omega_0)^2 + \kappa^2/4} = 2\pi i \cdot (-1) \cdot \mathcal{R}es(\omega_0 - i\kappa/2) = e^{-i\omega_0 \tau - \kappa|\tau|/2}. \quad (3.87)$$

Here, the lower limit of this integral is approximated as  $-\infty$  (highlighted in red) for a resonance  $\omega_0 \gg \kappa$  without significant change in its value.

### The Second-Order Coherence

For a Gaussian state, the field operator product in the second-order coherence generally contains operators of the form  $\hat{a}_k^\dagger \hat{a}_l^\dagger \hat{a}_m \hat{a}_n$ , where there are only two terms having non-zero expectation values in the Fock state basis for :

$$\hat{a}_k^\dagger \hat{a}_l^\dagger \hat{a}_k \hat{a}_l; \quad \hat{a}_k^\dagger \hat{a}_l^\dagger \hat{a}_l \hat{a}_k. \quad (3.88)$$

Hence the average in the numerator reduces to

$$\left\langle \hat{E}^-(t) \hat{E}^-(t+\tau) \hat{E}^+(t+\tau) \hat{E}^+(t) \right\rangle \propto \iint \omega_k \langle n_k \rangle \omega_l \langle n_l \rangle (1 + e^{-i(\omega_l - \omega_k)\tau}) d\omega_k d\omega_l, \quad (3.89)$$

where we have replaced the summation by the integral in a continuous mode limit. Substituting Eq. (3.85) into this equation yields

$$g^{(2)}(\tau) = \iint d\omega_k d\omega_l \frac{(\kappa/2\pi)^2 (1 + e^{-i(\omega_k - \omega_l)\tau})}{[(\omega_0 - \omega_k)^2 + \kappa^2/4] [(\omega_0 - \omega_l)^2 + \kappa^2/4]}. \quad (3.90)$$

The pole for  $\omega_k$  is at  $\omega_0 - i\kappa/2$  and the pole for  $\omega_l$  is at  $\omega_0 + i\kappa/2$ . Applying contour integrals for both  $\omega_k$  and  $\omega_l$ , we have the time-dependent second-order coherence  $g^{(2)}(\tau)$

$$g^{(2)}(\tau) = 1 + e^{-\kappa\tau/2} e^{-i(\omega_0 - \omega_0 - i\kappa/2)\tau} = 1 + e^{-\kappa\tau} = 1 + |g^{(1)}(\tau)|^2. \quad (3.91)$$

The same procedure can be extended to get higher-order coherence functions of thermal states.

### 3.3.1.2 Input-Output Formalism

This section presents calculations of coherence functions using the input-output formalism.

For any Gaussian state, Wick's theorem implies that high-order moments can be evaluated in terms of the second-order moments. For example, the numerators in the second-order coherence

$$g^{(2)}(\tau_1) = \frac{\langle \hat{a}_0^\dagger \hat{a}_1^\dagger \hat{a}_1 \hat{a}_0 \rangle}{\langle \hat{a}_0^\dagger \hat{a}_0 \rangle \langle \hat{a}_1^\dagger \hat{a}_1 \rangle}, \quad (3.92)$$

where  $\hat{a}_0 = \hat{a}(0)$  and  $\hat{a}_1 = \hat{a}(\tau_1)$ , can be evaluated by

$$\langle \hat{a}_0^\dagger \hat{a}_1^\dagger \hat{a}_1 \hat{a}_0 \rangle = \langle \hat{a}_0^\dagger \hat{a}_0 \rangle \langle \hat{a}_1^\dagger \hat{a}_1 \rangle + \langle \hat{a}_0^\dagger \hat{a}_1 \rangle \langle \hat{a}_1^\dagger \hat{a}_0 \rangle. \quad (3.93)$$

These first-order correlations can be calculated by solving the cavity's quantum Langevin equation [99, 133]

$$\dot{\hat{a}} = -\left(\frac{\kappa}{2} - i\omega\right)\hat{a} + \sqrt{\kappa_{\text{ex}}}\hat{a}_{\text{in}}, \quad (3.94)$$

where  $\hat{a}_{\text{in}}$  is the thermal noise input with  $\langle \hat{a}_{\text{in}} \rangle = 0$ . The correlations of  $\hat{a}_{\text{in}}$  are given by  $\langle \hat{a}_{\text{in}}^\dagger(\tau) \hat{a}_{\text{in}}(0) \rangle = n_{\text{th}}\delta(\tau)$  and  $\langle \hat{a}_{\text{in}}(\tau) \hat{a}_{\text{in}}^\dagger(0) \rangle = (n_{\text{th}} + 1)\delta(\tau)$ , where  $\tau \geq 0$ . The formal integral of Eq. (3.94) yields

$$\hat{a}(\tau) = \sqrt{\kappa} \int_{-\infty}^{\infty} dt' e^{-(\kappa/2-i\omega)(\tau-t')} \hat{a}_{\text{in}}(t'). \quad (3.95)$$

Substituting the correlations of  $\hat{a}_{\text{in}}$  into Eq. (3.95), we obtain the first-order normally/anti-normally ordered correlation functions of a thermal state

$$\langle \hat{a}^\dagger(\tau) \hat{a}(0) \rangle = n_{\text{th}} e^{-(\kappa/2+i\omega)\tau}, \quad (3.96a)$$

$$\langle \hat{a}(\tau) \hat{a}^\dagger(0) \rangle = (n_{\text{cav}} + 1) e^{-(\kappa/2-i\omega)\tau}. \quad (3.96b)$$

Notice that Eq. (3.96a) and (3.96b) only work for  $\tau \geq 0$ . The value of the second moment for  $\tau \leq 0$  is obtained by simply taking the conjugation of Eq. (3.96a) and (3.96b).

Combining Eq. (3.92) and (3.96a) results in the time-dependent second-order coherence function of a thermal state

$$g^{(2)}(\tau) = 1 + e^{-\kappa\tau}. \quad (3.97)$$

### 3.3.1.3 Higher-Order Coherence

In the following, we will use the similar scheme to generalize the calculation of the coherence functions to a higher order.

For example, the third-order coherence function is defined as

$$g^{(3)}(\tau_1, \tau_2) = \frac{\langle \hat{a}_0^\dagger \hat{a}_1^\dagger \hat{a}_2^\dagger \hat{a}_2 \hat{a}_1 \hat{a}_0 \rangle}{\langle \hat{a}_0^\dagger \hat{a}_0 \rangle \langle \hat{a}_1^\dagger \hat{a}_1 \rangle \langle \hat{a}_2^\dagger \hat{a}_2 \rangle}, \quad (3.98)$$

where  $\hat{a}_2 = \hat{a}(\tau_1 + \tau_2)$ . Applying Wick's theorem, its numerator can be decomposed into

$$\begin{aligned} \langle \hat{a}_0^\dagger \hat{a}_1^\dagger \hat{a}_2^\dagger \hat{a}_2 \hat{a}_1 \hat{a}_0 \rangle &= \langle \hat{a}_0^\dagger \hat{a}_0 \rangle \langle \hat{a}_1^\dagger \hat{a}_1 \rangle \langle \hat{a}_2^\dagger \hat{a}_2 \rangle \\ &+ \langle \hat{a}_0^\dagger \hat{a}_0 \rangle \langle \hat{a}_1^\dagger \hat{a}_2 \rangle \langle \hat{a}_2^\dagger \hat{a}_1 \rangle + \langle \hat{a}_0^\dagger \hat{a}_1 \rangle \langle \hat{a}_1^\dagger \hat{a}_0 \rangle \langle \hat{a}_2^\dagger \hat{a}_2 \rangle \\ &+ \langle \hat{a}_0^\dagger \hat{a}_1 \rangle \langle \hat{a}_1^\dagger \hat{a}_2 \rangle \langle \hat{a}_2^\dagger \hat{a}_0 \rangle + \langle \hat{a}_0^\dagger \hat{a}_2 \rangle \langle \hat{a}_1^\dagger \hat{a}_0 \rangle \langle \hat{a}_2^\dagger \hat{a}_1 \rangle \\ &+ \langle \hat{a}_0^\dagger \hat{a}_2 \rangle \langle \hat{a}_1^\dagger \hat{a}_1 \rangle \langle \hat{a}_2^\dagger \hat{a}_0 \rangle. \end{aligned} \quad (3.99)$$

Substituting Eq. (3.96a) into Eq. (3.99), we have

$$g^{(3)}(\tau_1, \tau_2) = 1 + e^{-\kappa\tau_1} + e^{-\kappa\tau_2} + 3e^{-\kappa(\tau_1+\tau_2)}. \quad (3.100)$$

Similarly, we have the fourth-order coherence function

$$\begin{aligned} g^{(4)}(\tau_1, \tau_2, \tau_3) &= 1 + e^{-\kappa\tau_1} + e^{-\kappa\tau_2} + e^{-\kappa\tau_3} + \dots \\ &3e^{-\kappa(\tau_1+\tau_2)} + 3e^{-\kappa(\tau_2+\tau_3)} + e^{-\kappa(\tau_1+\tau_3)} + 9e^{-\kappa(\tau_1+\tau_2+\tau_3)} + 4e^{-\kappa(\tau_1+2\tau_2+\tau_3)}. \end{aligned} \quad (3.101)$$

The expressions of the anti-normally ordered coherence functions can be obtained in the same method.

We will discuss some results of these high-order coherences that can be easily interpreted using intuition via the following. The fourth-order photon coherence function  $g^{(4)}(\tau_1, \tau_2, \tau_3)$  can be reduced into results of the lower-order coherence functions  $g^{(3)}(\tau_1, \tau_2)$ . The subset of fourth-order coherence  $g^{(4)}(\tau_1, \infty, \tau_3)$  is equivalent to the product of two one-dimensional  $g^{(2)}(\tau)$  functions. If the third photon arrives with delay  $\tau_2 = \infty$ , then the arrivals of the third and the fourth photons are uncorrelated with the arrival of the first pair of photons. That is,  $g^{(4)}(\tau_1, \infty, \tau_3)$  is proportional to the product of the probability of measuring a pair of photons separated by a delay  $\tau_1$  and the probability of measuring another pair of photons separated by a delay  $\tau_3$ . This can be seen from the expression for  $g^{(4)}(\tau_1, \tau_2, \tau_3)$  given in Eq. (3.101), where setting  $\tau_2 = \infty$  results in

$$g^{(4)}(\tau_1, \infty, \tau_3) = 1 + e^{-\kappa\tau_1} + e^{-\kappa\tau_3} + e^{-\kappa(\tau_1+\tau_3)} = g^{(2)}(\tau_1)g^{(2)}(\tau_3).$$

Similarly, the subset  $g^{(4)}(\tau_1, \tau_2, \infty)$  is equivalent to  $g^{(3)}(\tau_1, \tau_2)$ . If the fourth photon

arrives with delay  $\tau_3 = \infty$ , then its arrival is uncorrelated with the arrivals of the first three photons. Therefore,  $g^{(4)}(\tau_1, \tau_2, \infty)$  is proportional to the probability of measuring a triplet of photons with a delay  $\tau_1$  between the first and second and a delay  $\tau_2$  between the second and third. We can also see this by setting  $\tau_3 = \infty$  in Eq. (3.101), which yields

$$g^{(4)}(\tau_1, \tau_2, \infty) = 1 + e^{-\kappa\tau_1} + e^{-\kappa\tau_2} + 3e^{-\kappa(\tau_1+\tau_2)} = g^{(3)}(\tau_1, \tau_2). \quad (3.102)$$

### 3.3.2 Decoherence of Post-Selected States

The decoherence of post-selected states can be evaluated by the combination of different coherence functions of a thermal state. By way of illustration, consider the second-order coherence of a SPSS,

$$g^{(2)}(\tau)|_{-1} = \frac{\langle \hat{a}^\dagger(0)\hat{a}^\dagger(\tau)\hat{a}(\tau)\hat{a}(0) \rangle_{\hat{\rho}_{-1}}}{\langle \hat{a}^\dagger(0)\hat{a}(0) \rangle_{\hat{\rho}_{-1}} \langle \hat{a}^\dagger(\tau)\hat{a}(\tau) \rangle_{\hat{\rho}_{-1}}}, \quad (3.103)$$

where  $\hat{\rho}$  labels the initial state and  $\hat{\rho}_{-1}$  marks the an *single*-photon-subtracted state. The numerator is

$$\frac{\langle \hat{a}^\dagger(0)\hat{a}^\dagger(0)\hat{a}^\dagger(\tau)\hat{a}(\tau)\hat{a}(0)\hat{a}(0) \rangle_{\hat{\rho}}}{\langle \hat{a}^\dagger(0)\hat{a}(0) \rangle_{\hat{\rho}}} = g^{(3)}(0, \tau) \langle \hat{a}^\dagger(0)\hat{a}(0) \rangle_{\hat{\rho}}^2, \quad (3.104)$$

and the denominator is

$$\frac{\langle \hat{a}^\dagger(0)\hat{a}^\dagger(0)\hat{a}(0)\hat{a}(0) \rangle_{\hat{\rho}}}{\langle \hat{a}^\dagger(0)\hat{a}(0) \rangle_{\hat{\rho}}} \frac{\langle \hat{a}^\dagger(0)\hat{a}^\dagger(\tau)\hat{a}(\tau)\hat{a}(0) \rangle_{\hat{\rho}}}{\langle \hat{a}^\dagger(0)\hat{a}(0) \rangle_{\hat{\rho}}} = g^{(2)}(0) g^{(2)}(\tau) \langle \hat{a}^\dagger(0)\hat{a}(0) \rangle_{\hat{\rho}}^2. \quad (3.105)$$

So we have

$$g^{(2)}(\tau)|_{-1} = \frac{g^{(3)}(0, \tau)}{g^{(2)}(0) g^{(2)}(\tau)}. \quad (3.106)$$

The normally ordered second-order coherence function of a *single*-photon-subtracted thermal state is

$$g^{(2)}(\tau)|_{-1,\text{th}} = \frac{1 + 2e^{-\kappa t}}{1 + e^{-\kappa t}}. \quad (3.107)$$

It is straightforward to show that

$$g^{(2)}(\tau)|_{-1,\text{th}} = h^{(2)}(\tau)|_{+1,\text{th}}. \quad (3.108)$$

More generally, the subtraction (addition) of  $k$  photons at time  $t = 0$  from a state described by density matrix  $\hat{\rho}$  yields the state with density matrix  $\hat{\rho}_{-k}$  ( $\hat{\rho}_{+k}$ )

$$\hat{\rho}_{-k} = \frac{(\hat{a}(0))^k \hat{\rho} (\hat{a}^\dagger(0))^k}{\langle (\hat{a}^\dagger(0))^k (\hat{a}(0))^k \rangle_{\hat{\rho}}}, \quad (3.109a)$$

$$\hat{\rho}_{+k} = \frac{(\hat{a}^\dagger(0))^k \hat{\rho} (\hat{a}(0))^k}{\langle (\hat{a}(0))^k (\hat{a}^\dagger(0))^k \rangle_{\hat{\rho}}}. \quad (3.109b)$$

Through an *ab-initio* evaluation similar to that illustrated above, the  $n$ th-order coherence of a  $k$ -photon-subtracted (added) state is evaluated in terms of the coherences of the steady state  $\hat{\rho}$  to be

$$g^{(n)}(\boldsymbol{\tau})|_{-k} = \frac{g^{(k+n)}(\mathbf{0}^{\otimes k}, \boldsymbol{\tau}) (g^{(k)}(\mathbf{0}))^{n-1}}{g^{(k+1)}(\mathbf{0}) [\prod_{p=1}^{n-1} g^{(k+1)}(\mathbf{0}^{\otimes(k-1)}, t_p)]}, \quad (3.110)$$

where  $\boldsymbol{\tau} = (\tau_1, \tau_2, \dots, \tau_{n-1})$ ,  $\mathbf{0}^{\otimes k} = (0, 0, \dots k \text{ times})$ , and  $t_p = \sum_{j=1}^p \tau_j$  is the  $(p+1)^{\text{th}}$  time. (Recall that  $\tau_k$  is the delay between the  $k^{\text{th}}$  and  $(k+1)^{\text{th}}$  time.)

Note that the derivation and discussion above imply that the coincidences and normalization required to evaluate the  $n$ th-order coherences of  $k$ -photon heralded states occur as various subsets in the higher-dimensional  $(n+k)$ -photon detection record. While the record, viewed as a whole, corresponds to that of the equilibrium state (which, for this work, is a thermal state), the post-selection extracts the non-equilibrium (non-thermal) heralded state coherences.

For a thermal state  $\hat{\rho}_{\text{th}}$ , we have

$$g^{(2)}(\tau)|_{-k} = \frac{g^{(k+2)}(\mathbf{0}^{\otimes k}, \tau) g^{(k)}(\mathbf{0})}{g^{(k+1)}(\mathbf{0}) g^{(k+1)}(\mathbf{0}^{\otimes(k-1)}, \tau)}, \quad (3.111a)$$

$$g^{(2)}(\tau)|_{-k, \text{th}} = \frac{1 + (k+1)e^{-\kappa\tau}}{1 + ke^{-\kappa\tau}}. \quad (3.111b)$$

### Mean Photon Numbers

Using Eq. 3.109a), we obtain the mean photon number of a  $k$ -photon-subtracted state at delay time  $\tau$

$$n^{-k}(\tau) = \langle b^\dagger(\tau) b(\tau) \rangle_{\hat{\rho}_{-k}} = \frac{\langle (b^\dagger(0))^k b^\dagger(\tau) b(\tau) (b(0))^k \rangle_{\hat{\rho}}}{\langle (b^\dagger(0))^k (b(0))^k \rangle_{\hat{\rho}}}. \quad (3.112)$$

Dividing both sides by  $n(0) = \langle b^\dagger(0) b(0) \rangle_{\hat{\rho}}$  yields

$$\frac{n^{-k}(\tau)}{n(0)} = \frac{g^{(k+1)}(\mathbf{0}^{\otimes(k-1)}, \tau)}{g^{(k)}(\mathbf{0})} \quad (3.113)$$

Eq. 3.113 indicates that the mean photon number of a  $k$ -photon-subtracted state can be measured by the ratio of its high-order coherence functions.

Similarly, the mean photon number of a  $k$ -photon-added state at delay time  $\tau$  is (using Eq. 3.109b)

$$n^{+k}(\tau) + 1 = \langle b^\dagger(\tau) b(\tau) \rangle_{\hat{\rho}_{+k}} + 1 = \frac{\langle (b(0))^k b(\tau) b^\dagger(\tau) (b^\dagger(0))^k \rangle_{\hat{\rho}}}{\langle (b(0))^k (b^\dagger(0))^k \rangle_{\hat{\rho}}}. \quad (3.114)$$

Dividing both sides by  $n(0) + 1 = \langle b(0)b^\dagger(0) \rangle_{\hat{\rho}}$  yields

$$\frac{n^{+k}(\tau) + 1}{n(0) + 1} = \frac{h^{(k+1)}(\mathbf{0}^{\otimes(k-1)}, \tau)}{h^{(k)}(\mathbf{0})}. \quad (3.115)$$

### 3.3.3 Decoherence of a Displaced Thermal State

The dynamics of  $\hat{a}(t)$  is governed by Eq. (2.10). This evolution is characterized by the damping rate  $\kappa$  in a standard input-output formalism. In the rotating frame of the input frequency  $\omega_{\text{in}}$ , we have

$$\partial_t \hat{d}(t) = -\frac{1}{2}\kappa \hat{d}(t) - \sqrt{\kappa_{\text{ex}}} \hat{d}_{\text{in}}(t), \quad (3.116)$$

where we define the quantum fluctuation  $\hat{d} = \hat{a} - \alpha$ ,  $\alpha = \langle \hat{a} \rangle$ , the operator  $\hat{d}_{\text{in}} = \hat{a}_{\text{in}} - \alpha_{\text{in}}$  is the input noise, which satisfies the following relations

$$\langle \hat{d}_{\text{in}}(t) \rangle = 0, \quad (3.117a)$$

$$\langle \hat{d}_{\text{in}}^\dagger(t) \hat{d}_{\text{in}}(0) \rangle = n_{\text{th}} \delta(t), \quad (3.117b)$$

$$\alpha_{\text{in}} = -\frac{\sqrt{\kappa_{\text{ex}}}}{2} \alpha, \quad (3.117c)$$

where  $n_{\text{th}}$  is the equivalent occupancy of the input thermal fluctuation. The Langevin equation (3.116) is formally integrated to give

$$\hat{d}(t) = -\sqrt{\kappa_{\text{ex}}} \int_{-\infty}^t dt' e^{-(1/2)\kappa(t-t')} \hat{d}_{\text{in}}(t'). \quad (3.118)$$

Thus, the second-order correlation of the fluctuation is

$$\langle \hat{d}^\dagger(t) \hat{d}(0) \rangle = n_{\text{th}} e^{-(1/2)\kappa t}. \quad (3.119)$$

Applying Wick's theorem to the Gaussian quantum field  $\hat{d}$ , we have

$$\langle \hat{d}^\dagger(t) \hat{d}^\dagger(t+\tau) \hat{d}(t+\tau) \hat{d}(t) \rangle = 2n_{\text{th}}^2 e^{-\kappa t}. \quad (3.120)$$

Combining Eq. (3.119) and (3.120), the second-order coherence function of the field  $\hat{a} = \hat{d} + \alpha$  reads

$$g^{(2)}(t) = 1 + \frac{2n_{\text{th}}|\alpha|^2 e^{-\kappa t/2} + n_{\text{th}}^2 e^{-\kappa t}}{(|\alpha|^2 + n_{\text{th}})^2}. \quad (3.121)$$

In the small displacement limit, *i.e.*,  $|\alpha|^2 \ll n_{\text{th}}$ , the coherence function reduces into

the well-known decoherence of a thermal state. In the large displacement limit  $|\alpha|^2 \gg n_{\text{th}}$ , the correlation Eq. (3.121) approximates as

$$g^{(2)}(t) \approx 1 + \frac{2n_{\text{th}}e^{-\kappa t/2}}{|\alpha|^2}. \quad (3.122)$$

The result in Eq. (3.122) indicates such a displaced thermal state has a decoherence time twice of a thermal state.

The decoherence of general states should be calculated by solving the evolution of the state and evaluating the correlations accordingly.

## 3.4 Quasi-Probability Distributions

To incorporate classical uncertainty and quantum uncertainty, the density operator is typically used to describe a mixed state, as mentioned in 3.1. Instead of the density operator, one can also use distribution functions that in many respects are similar to classical probability distributions. Nonetheless, the quantum nature of these distributions distinguishes them from classical ones, and this distinction will be explained in the following.

Since the essential quantum features of these distributions can be measured experimentally, they are often used to verify the quantumness of the state. This makes them a valuable tool for understanding and analyzing quantum systems, particularly in the context of quantum information and computation.

### 3.4.1 Quantum Distribution Theory

Quasi-probability functions can be utilized to depict quantum states (both pure and mixed). Unlike classical probability distributions, which are always positive, quasi-probability functions can display negative values and can be extended beyond the range of 0 to 1.

In classical physics, the definite state corresponding to position  $x_0$  and momentum  $p_0$  can be represented as a Dirac delta distribution  $\delta(x - x_0, p - p_0)$  over the phase space. If instead we want to represent a statistical ensemble or a lack of knowledge about the state, we can replace this delta distribution with a positive-definite probability density function  $f(x, p)$ . The statistical average  $\langle o \rangle$  of any observable quantity  $o(x, p)$  is given by:

$$\langle o \rangle = \int f(x, p)o(x, p)dxdp. \quad (3.123)$$

The extension of this approach to represent quantum states is the quasi-probability distribution that will be discussed in this section.

In this section, we introduce the three most used quasi-probability distribution functions: the Glauber-Sudarshan  $P$ -function or coherent state representation, which is often

used to evaluate normally ordered correlation functions; the Wigner function or position-momentum representation; and the Husimi  $Q$ -function which is associated with the anti-normally ordered correlation functions. Each function has its unique characteristics and can be utilized to portray different facets of quantum mechanical systems. The difference between these quasi-probability functions emerges due to the non-commutative relationship of operators.

### 3.4.1.1 The Glauber-Sudarshan $P$ -function

Since coherent states are considered the most classical quantum states, using them as a basis facilitates exploring the interface of quantum-classical transition.

Like the definition in Eq. (3.1), the density matrix  $\hat{\rho}$  can be expanded in terms of coherent states as

$$\hat{\rho} = \iint \frac{d^2\alpha}{\pi} \frac{d^2\beta}{\pi} |\alpha\rangle\langle\alpha| \hat{\rho} |\beta\rangle\langle\beta|. \quad (3.124)$$

For a normally ordered operator  $\hat{O}_N(\hat{a}, \hat{a}^\dagger)$ , the expectation value can be written as

$$\langle \hat{O}_N(\hat{a}, \hat{a}^\dagger) \rangle = \text{Tr}[\hat{\rho} \hat{O}_N(\hat{a}, \hat{a}^\dagger)]. \quad (3.125)$$

Notice that

$$\delta(\alpha^* - \hat{a}^\dagger) \delta(\alpha - \hat{a}) = \frac{1}{\pi^2} \int \exp[-i\beta(\alpha^* - \hat{a}^\dagger)] \exp[-i\beta^*(\alpha - \hat{a})] d^2\beta. \quad (3.126)$$

Eq. (3.125) can then be reexpressed in terms of Eq. (3.126) as

$$\langle \hat{O}_N(\hat{a}, \hat{a}^\dagger) \rangle = \int d^2\alpha P(\alpha, \alpha^*) O_N(\alpha, \alpha^*), \quad (3.127)$$

where

$$P(\alpha, \alpha^*) = \text{Tr}[\hat{\rho} \delta(\alpha^* - \hat{a}^\dagger) \delta(\alpha - \hat{a})] = \frac{e^{|\alpha|^2}}{\pi^2} \int \langle -\beta | \hat{\rho} | \beta \rangle e^{|\beta|^2} e^{-\beta\alpha^* + \beta^*\alpha} d^2\beta. \quad (3.128)$$

The function  $P(\alpha, \alpha^*)$  is known as the Glauber-Sudarshan  $P$ -function. Due to the Hermiticity of the density operator  $\hat{\rho}$ , the  $P$ -function is real everywhere. Moreover,  $\text{Tr}(\hat{\rho}) = 1$  leads to the normalization of  $P(\alpha, \alpha^*)$

$$\int P(\alpha, \alpha^*) d^2\alpha = 1. \quad (3.129)$$

Reversely, the density operator can be represented in terms of the  $P$ -function:

$$\hat{\rho} = \int P(\alpha, \alpha^*) |\alpha\rangle\langle\alpha| d^2\alpha. \quad (3.130)$$

Notice that the coherent state basis  $\{|\alpha\rangle\}$  is an over-complete set, hence the orthogonality condition can not be applied in the calculation.

The  $P$ -function is not nonnegative definite. For instance, the  $P$ -function of the Fock state  $|n\rangle$  is given by

$$P(\alpha, \alpha^*) = \frac{|\alpha|^2}{n!} \frac{\partial^{2n}}{\partial \alpha^n \partial \alpha^{*n}} \delta^{(2)}(\alpha), \quad (3.131)$$

which is neither a nonnegative definite nor well-defined for any  $n \geq 1$ .

Another equivalent procedure to generate  $P(\alpha, \alpha^*)$  is by its kernel function, which will be covered in Sec. 3.4.2.

### 3.4.1.2 The Husimi $Q$ -function

Just as the  $P$ -function is associated with the evaluation of normally ordered operators, the Husimi  $Q$ -function is defined in terms of the evaluation of anti-normally ordered operators

$$Q(\alpha, \alpha^*) = \text{Tr} [\hat{\rho} \delta(\alpha - \hat{a}) \delta(\alpha^* - \hat{a}^\dagger)]. \quad (3.132)$$

Similarly, using Eq. (3.126), we have

$$Q(\alpha, \alpha^*) = \frac{1}{\pi} \langle \alpha | \hat{\rho} | \alpha \rangle, \quad (3.133)$$

which is proportional to the diagonal element of the density operator in the coherent state representation. The expectation value of the anti-normally ordered operators thus is given by

$$\langle \hat{O}_A (\hat{a}, \hat{a}^\dagger) \rangle = \int Q(\alpha, \alpha^*) O_A(\alpha, \alpha^*) d^2\alpha. \quad (3.134)$$

The  $Q$ -function is nonnegative definite and bounded, which can be seen by

$$Q(\alpha, \alpha^*) = \frac{1}{\pi} \sum_{\psi} P_{\psi} |\langle \psi | \alpha \rangle|^2. \quad (3.135)$$

Because  $|\langle \psi | \alpha \rangle|^2 \leq 1$ , so we have

$$0 \leq Q(\alpha, \alpha^*) \leq \frac{1}{\pi}. \quad (3.136)$$

### 3.4.1.3 The Wigner-Weyl Function

This approach can be used to derive distribution functions for arbitrary orderings. The Wigner-Weyl distribution is one of them, which is associated with symmetric ordering. Interestingly, the formula for the Wigner function has been independently discovered multiple times in different contexts. In fact, Wigner was unaware that even within the context of quantum theory, it had been introduced previously by Heisenberg and Dirac, *albeit* purely formally. They only regarded it as an approximation to the complete quantum depiction of a system like an atom, without recognizing its negative values and its significance.

The motivation behind the Wigner function is naturally from the extension of classical Hamiltonian physics. In classical Hamiltonian physics, a state can be described by a point in the phase space (e.g., the space spanned by position  $x$  and momentum  $p$ ). However, due to the Heisenberg uncertainty principle, we have a quasi-probability distribution to describe a quantum state in the phase space even in the absence of any statistical indeterminacy. In other words, a fundamental quantum blurring adds to any classical uncertainties. The goal is to construct a formalism of quantum-mechanics-based state description in terms of a phase space distribution, which is known as the Wigner-Weyl function.

To construct such a distribution, we first introduce the Weyl-transform, which maps the operator  $\hat{A}$  into a function  $\tilde{A}$  in the phase space in the following way [141]:

$$\tilde{A}(x, p) = \int dy e^{\frac{-ipy}{\hbar}} \left\langle x + \frac{y}{2} | \hat{A}(\hat{x}, \hat{p}) | x - \frac{y}{2} \right\rangle. \quad (3.137)$$

This transform preserves the product relation as

$$\text{Tr}[\hat{A}\hat{B}] = \frac{1}{2\pi\hbar} \iint dx dp \tilde{A}(x, p) \tilde{B}(x, p). \quad (3.138)$$

Therefore, the Wigner-Weyl function is defined as the Weyl-transformed density matrix  $\hat{\rho}$ ,

$$W(x, p) = \frac{\tilde{\rho}}{2\pi\hbar} = \frac{1}{2\pi\hbar} \int dy e^{-\frac{ipy}{\hbar}} \psi \left( x + \frac{y}{2} \right) \psi^* \left( x - \frac{y}{2} \right), \quad (3.139)$$

so that the expectation value of an operator  $\hat{A}$  is

$$\langle \hat{A} \rangle = \iint dx dp W(x, p) \tilde{A}(x, p), \quad (3.140)$$

which is similar to the form of the classical probability distribution in Eq. (3.123).

The expectation values of  $x$  and  $p$  are given by

$$\langle \hat{x} \rangle = \iint dx dp W(x, p) x, \quad (3.141a)$$

$$\langle \hat{p} \rangle = \iint dx dp W(x, p) p. \quad (3.141b)$$

Thus, the Wigner function is also known as the generating function for the probability distribution of position and momentum by simply integrating over either  $x$  or  $p$ .

The Wigner function is always real due to the Hermiticity of the density matrix  $\hat{\rho}$ . In this aspect, the Wigner function looks like a classical probability distribution. However, the Wigner function is not nonnegative definite, which is easily seen by considering  $\iint dx dp W_a(x, p) W_b(x, p) = 0$  of two orthogonal states. This negativity is hidden when the Wigner function corresponds to a physical property. Because of the uncertainty principle, it is forbidden to determine the momentum and position in the phase space simultaneously. The negative-valued regions are provable to be small (by showing the relation between nonnegative  $Q$ -function and the Wigner function), usually covering an area of phase space of a few  $\hbar$ , and therefore are shielded from detection in most of the experiments [142].

Lastly, likewise, the value of the Wigner function is also bounded, which is easily shown by the following

$$W(x, p) = \frac{1}{2\pi\hbar} \int dy e^{-\frac{ipy}{\hbar}} \psi\left(x + \frac{y}{2}\right) \psi^*\left(x - \frac{y}{2}\right) \leq \frac{1}{\pi\hbar}. \quad (3.142)$$

The time evolution of the Wigner function is based on the evolution of the density matrix  $\hat{\rho}$ , which is given by

$$\frac{\partial W}{\partial t} = \frac{-p}{m} \frac{\partial W(x, p)}{\partial x} + \sum_{s=0}^{\infty} (-\hbar^2)^s \frac{1}{(2s+1)!} \left(\frac{1}{2}\right)^{2s} \frac{\partial^{2s+1} U(x)}{\partial x^{2s+1}} \frac{\partial^{2s+1} W(x, p)}{\partial p^{2s+1}}, \quad (3.143)$$

where  $U$  is the potential and is assumed to be expandable in a power series. Without higher-order terms ( $s > 2$ ) in the expansion, the evolution reduces to the familiar form

$$\frac{\partial W(x, p)}{\partial t} = \frac{-p}{m} \frac{\partial W(x, p)}{\partial x} + \frac{\partial U(x)}{\partial x} \frac{\partial W(x, p)}{\partial p} = -\{W(x, p), H\}, \quad (3.144)$$

where  $\{A, B\}$  is the Poisson bracket. This is exactly the classical Liouville equation. Therefore, in a purely harmonic potential, the dynamics of the Wigner function is identical to that of the classical distribution which is governed by the classical Liouville equation under the same harmonic potential. In the limit  $\hbar \rightarrow 0$ , the distinction between the classical and the quantum dynamics also vanishes. Therefore, an anharmonic potential of order  $n$

will result in quantum corrections of order  $\hbar^{n-2}$  over the prediction made by the classical theory.

The physical meaning of the Wigner function can be treated as the expectation value of the parity around  $(x, p)$  of the given state [143]. The Wigner function can be represented as

$$W(x, p) = \frac{2}{\hbar} \langle \Psi | \Pi_{xp} | \Psi \rangle, \quad (3.145)$$

where the parity operator is

$$\Pi_{xp} = \int dk e^{-2ikx/\hbar} |p+k\rangle \langle p-k| = \int dy e^{-2ipy/\hbar} |x-y\rangle \langle x+y| = D(x, p) \Pi D(x, p)^{-1}. \quad (3.146)$$

Therefore the Wigner function can be expressed by

$$W(x, p) = \frac{1}{\hbar\pi} \left( \|\psi_{xp}^+\|^2 - \|\psi_{xp}^-\|^2 \right). \quad (3.147)$$

The Wigner function also corresponds to the probability distribution of the expectation value of symmetrically ordered operators, represented by

$$W(\alpha, \alpha^*) = \frac{1}{\pi^2} \int d^2\beta e^{-i\beta\alpha^* - i\beta^*\alpha} \text{Tr} \left( e^{i\beta a^\dagger + i\beta^* a} \hat{\rho} \right). \quad (3.148)$$

This result is more obvious and general in the discussion in Sec. 3.4.2.

### 3.4.2 General Representation of Quasi-Probability Distributions

In the following section, we introduce a generalized method to generate different types of quasi-probability functions.

Different quasi-probability functions correspond to different orderings. We can write them in terms of the characteristic functions or so-called kernels. As shown in Eq. (3.128), (3.133) and (3.148), the Wigner,  $P$ - and  $Q$ -functions are the Fourier transforms of three different characteristic functions [144, 145]:

$$C_S^{[\hat{\rho}]}(\lambda) = \text{Tr} \left[ \hat{\rho} e^{\lambda \hat{a}^\dagger - \lambda^* \hat{a}} \right], \quad (3.149)$$

$$C_N^{[\hat{\rho}]}(\lambda) = \text{Tr} \left[ \hat{\rho} e^{\lambda \hat{a}^\dagger} e^{-\lambda^* \hat{a}} \right], \quad (3.150)$$

$$C_A^{[\hat{\rho}]}(\lambda) = \text{Tr} \left[ \hat{\rho} e^{-\lambda^* \hat{a}} e^{\lambda \hat{a}^\dagger} \right], \quad (3.151)$$

respectively. The general representation is given by

$$F_i(\alpha, \alpha^*) = \frac{1}{\pi^2} \int d^2\lambda C_i(\lambda) e^{-\alpha\lambda^* + \alpha^*\lambda}, \quad (3.152)$$

where  $\{i\}$  denotes the specific orderings.

Note that the symmetric characteristic function  $C_S^{[\hat{\rho}]}(\lambda)$  is related to the quantum average of the displacement operator  $\hat{D}(\lambda) = e^{\lambda\hat{a}^\dagger - \lambda^*\hat{a}}$ . Thus, three different characteristic functions correspond to the quantum average of the three simplest orderings that can be used in the expansion of  $\hat{a}$  and  $\hat{a}^\dagger$ : symmetric ordering, normal ordering, and anti-normal ordering,

$$C_{\{i\}}^{[\hat{\rho}]}(\lambda) = \langle : \hat{D}(\lambda) :_i \rangle, \quad (3.153)$$

where  $::_i$  stands for different orderings. These functions are closely related by the Baker–Campbell–Hausdorff (BCH) formula or the Glauber identity:

$$e^{\hat{A}} e^{\hat{B}} = e^{\hat{A} + \hat{B}} e^{[\hat{A}, \hat{B}]/2}, \quad (3.154)$$

which holds when  $\hat{A}$  and  $\hat{B}$  commute with  $[\hat{A}, \hat{B}]$ . So we immediately have

$$C_N^{[\hat{\rho}]}(\lambda) = e^{|\lambda|^2/2} C_S^{[\hat{\rho}]}(\lambda); \quad C_A^{[\hat{\rho}]}(\lambda) = e^{-|\lambda|^2/2} C_S^{[\hat{\rho}]}(\lambda). \quad (3.155)$$

Eq. (3.152) can be further reduced by substituting Eq. (3.126) to

$$F_i(\alpha, \alpha^*) = \text{Tr}[\hat{\rho} : \delta(\alpha - \hat{a})\delta(\alpha^* - \hat{a}^\dagger) :_i]. \quad (3.156)$$

The relation between the correlation of operators with different orderings and different quasi-probability functions is made clear by the following [129]

$$\begin{aligned} \langle \hat{O}_i \rangle &= \text{Tr} [\hat{\rho} \hat{O}_i] = \int d^2\alpha O_i(\alpha, \alpha^*) \text{Tr} [\hat{\rho} : \delta(\alpha - \hat{a})\delta(\alpha^* - \hat{a}^\dagger) :_i] \\ &= \int d^2\alpha O_i(\alpha, \alpha^*) F_i(\alpha). \end{aligned} \quad (3.157)$$

The relation among characteristic functions also leads to the direct relation between quasi-probability functions. For example,

$$Q(\alpha, \alpha^*) = \frac{1}{\pi} \int P(\alpha', \alpha'^*) e^{-|\alpha - \alpha'|^2} d^2\alpha'. \quad (3.158)$$

More generally, we can rewrite the expression for the Wigner function Eq. (3.152) as

$$\begin{aligned}
W(\alpha, \alpha^*) &= \frac{1}{\pi^2} \int d^2 \lambda C_S(\lambda) e^{\alpha \lambda^* - \alpha^* \lambda} \\
&= \frac{1}{\pi^2} \int d^2 \lambda e^{-|\lambda|^2/2} C_N(\lambda) e^{\alpha \lambda^* - \alpha^* \lambda} = (F_1 * P)(\alpha, \alpha^*) \\
&= \frac{1}{\pi^2} \int d^2 \lambda e^{+|\lambda|^2/2} C_A(\lambda) e^{\alpha \lambda^* - \alpha^* \lambda} = (F_2 * Q)(\alpha, \alpha^*), \tag{3.159}
\end{aligned}$$

where  $(f * g)$  is the convolution product over the phase space  $\{\alpha, \alpha^*\}$ ,  $F_1(\alpha, \alpha^*) = 2\pi e^{-2|\alpha|^2}$  and  $F_2(\alpha, \alpha^*) = 2\pi e^{+2|\alpha|^2}$ .

### 3.4.3 Reconstructing the Wigner Function

One of the motivations to measure the high-order correlations  $\langle (\hat{a}^\dagger)^n \hat{a}^m \rangle$  is that knowing all orders of correlations specifies the quantum state of the field mode  $\hat{a}$ . Therefore, it is interesting and useful to connect the phase space representations (such as the Wigner, the Glauber-Sudarshan  $P$ -, or the Husimi  $Q$ -functions) to correlations. Especially, in practice, many unique experimental techniques exist to measure the quantities  $\langle (\hat{a}^\dagger)^n \hat{a}^m \rangle$ . These measured correlations can potentially be used to reconstruct the quasi-probability functions experimentally [146–148].

The measured normally ordered correlations can be used reconstruct the Wigner function in the following manner [146, 148]:

$$W(\alpha) = \sum_{n,m} \int d^2 \lambda \frac{\langle (\hat{a}^\dagger)^n \hat{a}^m \rangle (-\lambda^*)^m \lambda^n}{\pi^2 n! m!} e^{(-1/2)|\lambda|^2 + \alpha \lambda^* - \alpha^* \lambda}. \tag{3.160}$$

This expression is obvious by expanding the characteristic function  $C_N^{[\hat{\rho}]}(\lambda)$  in Eq. (3.159) as

$$C_N^{[\hat{\rho}]}(\lambda) = \text{Tr} \left[ \hat{\rho} e^{\lambda \hat{a}^\dagger} e^{-\lambda^* \hat{a}} \right] = \sum_{n,m} \text{Tr} \left[ \hat{\rho} \frac{(\hat{a}^\dagger)^n \hat{a}^m (-\lambda^*)^m \lambda^n}{n! m!} \right]. \tag{3.161}$$

Similarly, we have

$$P(\alpha) = \sum_{n,m} \int d^2\lambda \frac{\langle (\hat{a}^\dagger)^n \hat{a}^m \rangle (-\lambda^*)^m \lambda^n}{\pi^2 n! m!} e^{+\alpha\lambda^* - \alpha^*\lambda}, \quad (3.162a)$$

$$\begin{aligned} Q(\alpha) &= \sum_{n,m} \int d^2\lambda \frac{\langle (\hat{a}^\dagger)^n \hat{a}^m \rangle (-\lambda^*)^m \lambda^n}{\pi^2 n! m!} e^{-|\lambda|^2 + \alpha\lambda^* - \alpha^*\lambda} \\ &= \sum_{n,m} \int d^2\lambda \frac{\langle \hat{a}^m (\hat{a}^\dagger)^n \rangle (-\lambda^*)^m \lambda^n}{\pi^2 n! m!} e^{+\alpha\lambda^* - \alpha^*\lambda} \end{aligned} \quad (3.162b)$$

Thus, correlations of the state play the role of an expansion coefficient in this expansion.

For a state whose Wigner function is rotationally symmetric around the origin ( $x = 0, p = 0$ ), only  $\langle (\hat{a}^\dagger)^m \hat{a}^m \rangle$  terms are non-zero. The value at the origin  $W(0, 0)$  is given by

$$\begin{aligned} W(0, 0) &= \sum_m \int_0^\infty d|\lambda| 2|\lambda| \frac{\langle (\hat{a}^\dagger)^m \hat{a}^m \rangle (-|\lambda|^2)^m}{\pi(m!)^2} e^{(-1/2)|\lambda|^2} \\ &= \sum_m \int_0^\infty d|\lambda| 2|\lambda| \frac{\langle \hat{a}^m (\hat{a}^\dagger)^m \rangle (-|\lambda|^2)^m}{\pi(m!)^2} e^{(+1/2)|\lambda|^2}. \end{aligned} \quad (3.163)$$

In this simplified scenario, I will now show a few examples by evaluating  $W(0, 0)$  for different states.

For a thermal state, we have

$$\begin{aligned} W(0, 0) &= \int d^2\lambda \frac{n_{\text{th}}^m (-|\lambda|^2)^m}{\pi^2 m!} e^{(-1/2)|\lambda|^2} \\ &= \frac{1}{\pi^2} \int d^2\lambda e^{-|\lambda|^2 n_{\text{th}}} e^{(-1/2)|\lambda|^2}. \end{aligned} \quad (3.164)$$

For a single-photon-added thermal state, in terms of Eq. (3.163), we have

$$\begin{aligned} W(0, 0) &= \sum_m \int d^2\lambda \frac{(m+1)!(n_{\text{th}}+1)^m (-|\lambda|^2)^m}{\pi^2 (m!)^2} e^{(+1/2)|\lambda|^2} \\ &= \frac{1}{\pi^2} \int d^2\lambda e^{-(n_{\text{th}}+1)|\lambda|^2} (1 - (n_{\text{th}}+1)|\lambda|^2) e^{(+1/2)|\lambda|^2}. \end{aligned} \quad (3.165)$$

It is straightforward to prove this value is always negative.

Notice that in the first line of Eq. (3.165), if you take the integration before the summation, each integral does not converge. Hence, the derivation above is only formally correct. Consequently, in practice, if we just use the first few terms in anti-normally ordered moments, we can't approach the desired Wigner function.

More generally, Eq. (3.163) can be represented as

$$\begin{aligned}
W(0, 0) &= \sum_m \frac{\langle (\hat{a}^\dagger)^m \hat{a}^m \rangle}{\pi(m!)^2} \int_0^\infty d|\lambda| 2|\lambda| (-|\lambda|^2)^m e^{(-1/2)|\lambda|^2} \\
&= \sum_m \frac{\langle (\hat{a}^\dagger)^m \hat{a}^m \rangle}{\pi(m!)^2} (-1)^m 2^{m+1} \Gamma(m+1) \\
&= \sum_m \frac{\langle (\hat{a}^\dagger)^m \hat{a}^m \rangle (-1)^m 2^{m+1}}{\pi m!} \\
&= \sum_m \frac{2(-1)^m (2 \times \langle n \rangle)^m g^{(m)}(0)}{\pi m!},
\end{aligned} \tag{3.166}$$

where  $\Gamma(n)$  is the Gamma function. This expansion can be truncated at  $m$ -th order as a good approximation if the condition  $(2 \times \langle n \rangle)^{m-1} g^{(m)}(0) \ll m!$  is satisfied.

For example, if the coherence  $g^{(m)}(0)$  of the state scales as  $m!$  (such as for thermal states or photon-added/subtracted thermal states), Eq. (3.166) can be simplified as

$$W(0, 0) \approx \sum_m \frac{2(-1)^m (2 \times \langle n \rangle)^m}{\pi}. \tag{3.167}$$

This series converges only when  $\langle n \rangle < \frac{1}{2}$ .

### 3.4.4 Relation between Moments and Cumulants of the Quasi-Probability Distribution

In probability and statistics, the cumulants  $\kappa_n$  offer an alternative approach for characterizing a probability distribution, as opposed to the moments (the correlations discussed previously). Cumulants are more straightforward and intuitive than moment-based representations. The first, second, and third cumulants correspond to the mean, variance, and third central moment, respectively. Notably, for a Gaussian distribution, the third and all higher-order cumulants are all zero. Additionally, for multiple independent random variables, the sum of their  $n$ th-order cumulants equals the  $n$ th-order cumulant of their sum.

The cumulants of a random variable  $X$  are defined using the cumulant-generating function  $K_X(t)$  in the following manner:

$$K_X(t) = \log E[e^{tX}] = \sum_{n=1}^{\infty} \kappa_n \frac{t^n}{n!}. \tag{3.168}$$

Notice that the cumulant-generating function  $K_X(t)$  is the natural logarithm of the moment-

generating function

$$M_X(t) = \mathbb{E}[e^{tX}] = \sum_{n=1}^{\infty} \mu_n \frac{t^n}{n!}. \quad (3.169)$$

Both expansions are Maclaurin series, so the value of the  $n$ th-order can be generated by differentiating the above expansion  $n$  times and evaluating the result at zero.

The relation in Eq. (3.168) and (3.169) explicitly expresses the relation between cumulants and moments as

$$\kappa_n = K_X^{(n)}(0) = \left. \frac{d^n \log M_X(t)}{dt^n} \right|_{t=0}. \quad (3.170)$$

The explicit expression can be obtained by using Faá di Bruno's formula for higher derivatives of composite functions, given by

$$\kappa_n = \sum_{k=1}^n (-1)^{k-1} (k-1)! B_{n,k} (0, \mu_2, \dots, \mu_{n-k+1}), \quad (3.171)$$

where  $\mu_n$  is the  $n$ -th central moment with  $\mu_1 = 0$  and  $B_{n,k}$  are incomplete (or partial) Bell polynomials.

The first few orders of cumulants  $\kappa_n$  ( $n > 1$ ) as functions of the corresponding central moments  $\mu_n$  are

$$\kappa_2 = \mu_2, \quad (3.172a)$$

$$\kappa_3 = \mu_3, \quad (3.172b)$$

$$\kappa_4 = \mu_4 - 3\mu_2^2, \quad (3.172c)$$

$$\kappa_5 = \mu_5 - 10\mu_3\mu_2, \quad (3.172d)$$

$$\kappa_6 = \mu_6 - 15\mu_4\mu_2 - 10\mu_3^2 + 30\mu_2^3, \quad (3.172e)$$

$$\kappa_8 = \mu_8 - 35\mu_4^2 - 28\mu_6\mu_2 + 420\mu_2^2\mu_4 - 630\mu_2^4. \quad (3.172f)$$

Now let's consider the measured normally ordered moments  $\langle (\hat{a}^\dagger)^m \hat{a}^m \rangle$ . The expectation value is given by integrating the  $P$ -function over phase space, as shown in Eq. (3.127). Without losing generality, we assume the  $P$ -function is centered at the origin, *i.e.*,  $\mu_1 = 0$  and is symmetric between the momentum and position. That is

$$P(x) = \int P(\alpha) d\Re(\alpha) = \int P(\alpha) d\Im(\alpha) = P(y), \quad (3.173a)$$

$$P(x+iy) = P(x)P(y), \quad (3.173b)$$

where we decompose  $\alpha = x+iy$ , and  $P(x)$  and  $P(y)$  are marginal probability distributions

on  $\Re(\alpha)$  and  $\Im(\alpha)$ , respectively. Therefore, the expectation value of such a state can be evaluated by

$$\langle (\hat{a}^\dagger)^m \hat{a}^m \rangle = \int d^2\alpha |\alpha|^{2m} P(\alpha, \alpha^*) = \int dx dy (x^2 + y^2)^m P(x, y). \quad (3.174)$$

So we have

$$\langle \hat{a}^\dagger \hat{a} \rangle = \int dx x^2 P(x) + \int dy y^2 P(y) = 2\mu_2, \quad (3.175)$$

where we have used the Eq. (3.173) to project the joint distribution into the marginal probability distribution. Likewise, we have

$$\langle (\hat{a}^\dagger)^2 \hat{a}^2 \rangle = 2\mu_4 + 2\mu_2^2, \quad (3.176a)$$

$$\langle (\hat{a}^\dagger)^3 \hat{a}^3 \rangle = 2\mu_6 + 6\mu_2\mu_4, \quad (3.176b)$$

$$\langle (\hat{a}^\dagger)^4 \hat{a}^4 \rangle = 2\mu_8 + 8\mu_2\mu_6 + 6\mu_4. \quad (3.176c)$$

Due to the symmetry that we assumed, all odd order moments  $\mu_{2n+1} = 0$ . Combining Eq. (3.172a) and (3.176a) yields the relation between the measured high-order coherence functions and the high-order cumulants, shown as:

$$\kappa_2 = \frac{1}{2} \langle n \rangle, \quad (3.177a)$$

$$\kappa_4 = \frac{3}{8} (g^{(2)} - 2) \langle n \rangle^2, \quad (3.177b)$$

$$\kappa_6 = \frac{5}{16} (g^{(3)} - 9g^{(2)} + 12) \langle n \rangle^3, \quad (3.177c)$$

$$\kappa_8 = \frac{35}{128} (g^{(4)} - 18(g^{(2)})^2 - 16g^{(3)} + 144g^{(2)} - 144) \langle n \rangle^4. \quad (3.177d)$$

For a thermal state, inserting  $g^{(n)}(0) = n!$  into these equations yields

$$\kappa_2 = \frac{1}{2} \langle n \rangle, \quad (3.178a)$$

$$\kappa_4 = 0, \quad (3.178b)$$

$$\kappa_6 = 0, \quad (3.178c)$$

$$\kappa_8 = 0, \quad (3.178d)$$

which aligns with our expectations of a Gaussian state. Even in this case, higher-order coherences are necessary to demonstrate the Gaussianity of the state of higher degrees of statistical confidence.

Note that for  $\langle n \rangle > 1$ , the expression of higher-order cumulant will not converge

unless the coefficient of  $\kappa_m$  shrinks faster than  $1/\langle n \rangle^m$ . This result is more obvious for a single-photon subtracted thermal state. Substituting Eq. (3.64) into Eq. (3.177), we have

$$\kappa_2 = \frac{1}{2}(2n_{\text{th}}), \quad (3.179\text{a})$$

$$\kappa_4 = -\frac{3}{16}(2n_{\text{th}})^2, \quad (3.179\text{b})$$

$$\kappa_6 = \frac{15}{32}(2n_{\text{th}})^3, \quad (3.179\text{c})$$

$$\kappa_8 = \dots \quad (3.179\text{d})$$

where  $n_{\text{th}}$  is the original thermal occupancy. If  $\langle n_{\text{th}} \rangle$  is not very small, *i.e.*,  $\langle n_{\text{th}} \rangle \not\ll 1$ , then the higher-order cumulant  $\kappa_n$  generally does not tend to zero. Consequently, in such cases, the first few primary coherence functions cannot provide an accurate description of the state. This result matches the discussion in Sec. 3.4.3. The Gaussianity of the thermal state  $P$ -function also implies the result discussed in Sec. 3.2.2.

## 3.5 Classical Bounds and Nonclassical Criteria

The quantum quasi-probability distribution behaves like a classical distribution in several aspects, as discussed in Sec. 3.4. Some general principles of quantum mechanics imprint features in these distributions and eventually distinguish them from any classical descriptions.

In the field of quantum optics, a “nonclassical state” refers to a quantum state that cannot be represented as a classical probability distribution over all possible states. Such a state is usually associated with uniquely quantum phenomena such as superposition, entanglement, or interference, which do not occur in any classical theories. Examples of nonclassical states include squeezed states, entangled states, cat states, and Fock states. Nonclassical states are significant in the study of quantum mechanics and are essential to achieving quantum advantages in applications [3, 4].

In the following, some criteria in observable statistics that can be used to distinguish a quantum state from a classical state are derived. Furthermore, we describe a hierarchy of “increasingly quantum” states [149–152].

### 3.5.1 Nonclassical States and Nonclassical Criteria

The  $P$ -function is a quantum probability distribution expanded in a coherent state basis. As discussed in Sec. 3.4.1.1, the  $P$ -function exhibits a key distinction from classical probability distributions in that its probability density can take negative values or be otherwise “badly behaved”. While this may be seen as a drawback resulting from the attempt to represent quantum phenomena within a classical framework, it can serve as a useful criterion

for identifying nonclassicality.

The nonclassical states are defined as quantum states associated with  $P$ -functions having negative values. It is impossible to explain such states as any classical ensemble of coherent states.

The  $P$ -function negativity is the lowest member of the hierarchy characterizing quantum states [152]. A detailed discussion about the hierarchy of quantum states is given in Sec. 3.5.2. A typical example is the squeezed state, for which we express the variance of either quadrature  $(\Delta X_i)^2$  in terms of the  $P$ -function

$$(\Delta X_i)^2 = \frac{1}{4} \left\{ 1 + \int d^2\alpha P(\alpha, \alpha^*) [(\alpha + \alpha^*) - (\langle \alpha \rangle + \langle \alpha^* \rangle)]^2 \right\}. \quad (3.180)$$

The squeezing condition  $(\Delta X_i)^2 < \frac{1}{4}$  requires  $P(\alpha, \alpha^*)$  to be negative for at least some values of  $\alpha$ . However, for such a state, the Wigner function is positive definite.

It is challenging to directly measure the  $P$ -function as it is not bounded and not well-defined in certain cases. Fortunately, normally ordered quantum correlations directly map to the relevant properties of the  $P$ -function. Restricting the  $P$ -function to be nonnegative definite yields restrictions in the coherence functions, which is known as a classical bound. Violating these restrictions verifies the  $P$ -function negativity of the state, proving the nonclassicality of the state.

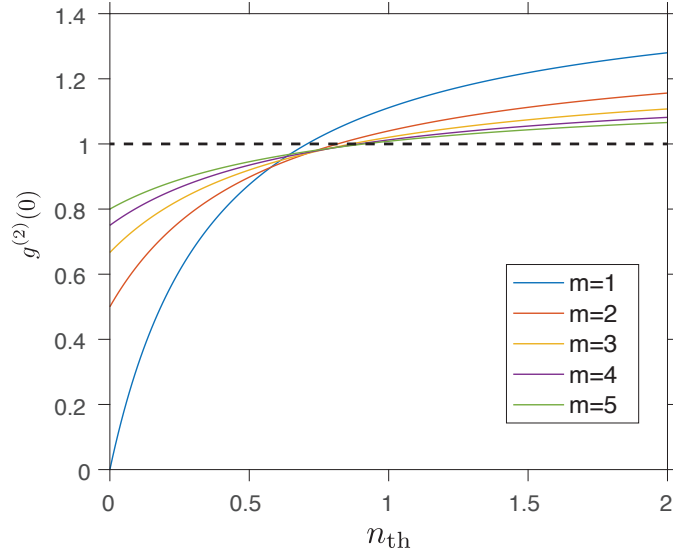


Figure 3.1: The second-order coherence  $g^{(2)}(0)$  of a  $m$ -photon-added thermal state for various initial thermal occupancies  $n_{\text{th}}$ . The black dashed line represents the classical bound given in Sec. 3.5.1.1.

### 3.5.1.1 Photon Blockade Inequality

**Inequality 1 (Photon Blockade Inequality)** *For any state having a nonnegative  $P$ -function, we have [129]*

$$g^{(2)}(0) \geq 1. \quad (3.181)$$

To see this explicitly, Eq. (3.181) can be expressed as

$$\langle \hat{a}^\dagger \hat{a}^\dagger \hat{a} \hat{a} \rangle - \langle \hat{a}^\dagger \hat{a} \rangle^2 \geq 0, \quad (3.182)$$

which can be expressed as an integral of the  $P$ -function

$$\int d^2\alpha P(\alpha, \alpha^*) (|\alpha|^4 - 2|\alpha|^2 \langle \hat{a}^\dagger \hat{a} \rangle + \langle \hat{a}^\dagger \hat{a} \rangle^2) \geq 0. \quad (3.183)$$

Notice that the second term ( $|\alpha|^2 - \langle \hat{a}^\dagger \hat{a} \rangle$ )<sup>2</sup> is nonnegative for any  $\alpha$ . Violation of Eq. (3.181) is satisfied if and only if  $P(\alpha, \alpha^*)$  is negative for some values of  $\alpha$ . Thus violating this classical bound is a sufficient condition (not a necessary condition) to prove the state is nonclassical.

This inequality is also known as photon blockade inequality. For instance, the second-order coherence of a Fock state  $|1\rangle$  is  $g^{(2)}(0) = 0$ , which means two photons cannot arrive at the same time. Therefore, it is often regarded as the criterion to test a single photon source.

Next, we evaluate  $g^{(2)}(0)$  of a  $m$ -photon-added thermal state of an initial thermal occupancy  $n_{\text{th}}$ , which is given in Eq. (3.63b). The numerical result is shown in Fig. 3.1. Despite the nonclassicality of such states for any  $m$  and  $n_{\text{th}}$ , the nonclassical criterion  $g^{(2)}(0) < 1$  is satisfied only for small  $n_{\text{th}}$ . More specifically, for a single-photon-added thermal state,  $n_{\text{th}} < \sqrt{2}/2$  is required to violate this classical bound.

### 3.5.1.2 Chebyshev Inequality

Eq. (3.181) can be generalized to inequality of high-order coherence functions, dating back to R. J. Glauber's original discussion in 1965 [153]. This generalized classical bound utilizes the less well-known Chebyshev inequality (other than the famous one used in statistics) to set the inequality between high-order coherence functions of nonnegative probability distributions.

**Inequality 2 (Chebyshev Inequality)** *If  $f, g : [a, b] \rightarrow \mathbb{R}$  are two monotonic functions of the same monotonicity, then*

$$\frac{1}{b-a} \int_a^b f(x)g(x)dx \geq \left[ \frac{1}{b-a} \int_a^b f(x)dx \right] \left[ \frac{1}{b-a} \int_a^b g(x)dx \right]. \quad (3.184)$$

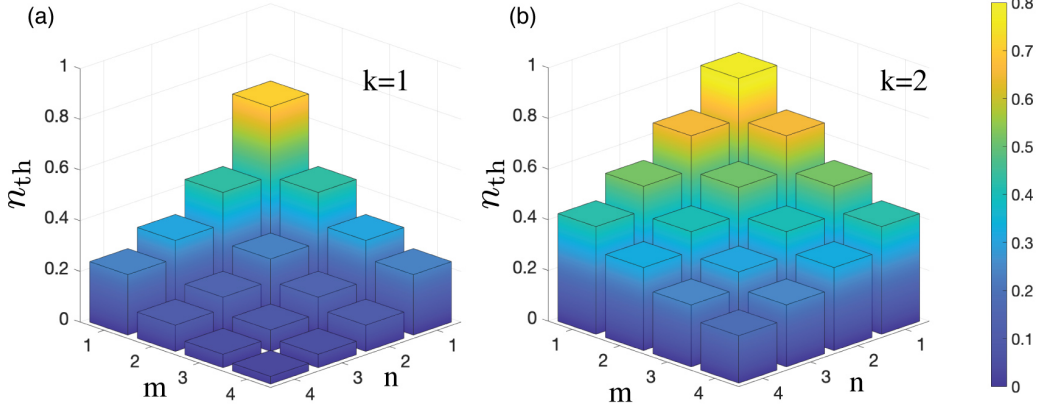


Figure 3.2: The critical initial thermal photon  $n_{\text{th}}$  for various  $m$  and  $n$ , below which  $g^{(m)}(0)$ ,  $g^{(n)}(0)$  of a  $k$ -photon-added thermal state violate the Chebyshev inequality Eq. (3.186). (a) and (b) show the results of  $k = 1$ ,  $k = 2$ , respectively.

If  $f(x)$  and  $g(x)$  are of opposite monotonicity, then the above inequality works in a reverse way.

This inequality is also known as the rearrangement inequality. It is straightforward to reexpress inequality (3.184) in the following form:

$$\int d^2\alpha P(\alpha)f(\alpha)g(\alpha) \geq \int d^2\alpha P(\alpha)f(\alpha) \int d^2\alpha P(\alpha)g(\alpha), \quad (3.185)$$

where we simply replace  $\frac{1}{b-a}dx$  by a weighted average  $d^2\alpha P(\alpha)$ . If we choose  $f(\alpha) = (|\alpha|^2)^m$  and  $g(\alpha) = (|\alpha|^2)^n$ , which are obviously two monotonic functions of the same monotonicity, then after rearrangements and normalization, we have

$$g^{(m+n)}(0) \geq g^{(m)}(0)g^{(n)}(0). \quad (3.186)$$

By choosing  $m = n = 1$ , we easily reproduce the classical bound Eq. (3.181).

To demonstrate this result more explicitly, let us consider the case of a  $k$ -photon-added thermal state ( $k = 1, 2$  in this discussion) with an initial thermal occupancy  $n_{\text{th}}$ . The higher-order coherences of such states are given in Sec. 3.2.3.2. Figure 3.2 shows the critical  $n_{\text{th}}$  for  $g^{(m)}(0)$  and  $g^{(n)}(0)$ , below which the Chebyshev inequality Eq. (3.186) is violated. Even though all such states are nonclassical, this particular witness of nonclassicality is rendered to be unobservable by the initial thermal occupancy.

### 3.5.1.3 Cauchy-Schwarz Inequality

Another nonclassical bound that is frequently discussed in the literature arises from the Cauchy-Schwarz inequality.

**Inequality 3 (Cauchy-Schwarz Inequality)** If  $\mathbf{u}, \mathbf{v} \in \mathcal{R}^n$ , then

$$\left( \sum_{i=1}^n u_i v_i \right)^2 \leq \left( \sum_{i=1}^n u_i^2 \right) \left( \sum_{i=1}^n v_i^2 \right), \quad (3.187)$$

or equivalently, for any nonnegative probability distribution

$$|\langle \mathbf{u}, \mathbf{v} \rangle|^2 \leq \langle \mathbf{u}, \mathbf{u} \rangle \cdot \langle \mathbf{v}, \mathbf{v} \rangle, \quad (3.188)$$

where  $\langle \mathbf{a}, \mathbf{b} \rangle$  is the expectation value of the inner product between  $\mathbf{a}$  and  $\mathbf{b}$ .

In the continuous case, the expectation value can be evaluated by integrating the corresponding probability distribution, in this case, the  $P$ -function. That is

$$\left( \int d^2\alpha d^2\beta P(\alpha, \beta) |\alpha|^2 |\beta|^2 \right)^2 \leq \left( \int d^2\alpha d^2\beta P(\alpha, \beta) |\alpha|^4 \right) \left( \int d^2\alpha d^2\beta P(\alpha, \beta) |\beta|^4 \right), \quad (3.189)$$

where  $P(\alpha, \beta)$  is the joint  $P$ -function for two separate states. Rewriting these averages in terms of the expectation values of normally ordered operators gives

$$\langle \hat{a}^\dagger \hat{b}^\dagger \hat{b} \hat{a} \rangle^2 \leq \langle \hat{a}^\dagger \hat{a}^\dagger \hat{a} \hat{a} \rangle \langle \hat{b}^\dagger \hat{b}^\dagger \hat{b} \hat{b} \rangle. \quad (3.190)$$

After certain rearrangements, this is equivalent to:

$$\left[ g_{a,b}^{(2)}(0) \right]^2 \leq g_{a,a}^{(2)}(0) g_{b,b}^{(2)}(0), \quad (3.191)$$

where  $g_{a,b}^{(2)}$  is the cross coherence function between states  $\hat{a}$ ,  $\hat{b}$ , and  $g_{a,a}^{(2)}$  and  $g_{b,b}^{(2)}$  are the auto coherence functions for states  $\hat{a}$  and  $\hat{b}$ , respectively. This inequality holds for any probability distribution whose values are nonnegative definite. Violating this inequality proves the joint  $P$ -function negativity at some  $\alpha$  and  $\beta$ , and so demonstrates the nonclassicality of this joint state.

This inequality is widely deployed in quantum communication [154] to verify the joint state in a quantum repeater or to verify the fidelity of the quantum information stored in a quantum memory [74] for future scalable and long-distance quantum communication.

In a special case, where  $\mathbf{v} = \mathbf{I}$ , this inequality also leads to

$$1 = \left[ g_a^{(1)}(0) \right]^2 \leq g_{a,a}^{(2)}(0), \quad (3.192)$$

which is exactly the aforementioned photon blockade inequality.

### Two-Mode Squeezed State

For concreteness, let us consider a joint state generated by a two-mode squeezing op-

erator  $\hat{a}^\dagger \hat{b}^\dagger + \text{H.C.}$  on a thermal state  $|0\rangle_a |n_{\text{th}}\rangle_b$ . This is exactly the state generated in the DLCZ protocol, where  $g_{a,b}^{(2)}(0)$  is given by [98]

$$g_{a,b}^{(2)}(0) = 2 + \frac{1}{n_{\text{th}}} > \sqrt{g_{a,a}^{(2)}(0)g_{b,b}^{(2)}(0)} = 2. \quad (3.193)$$

This cross-coherence always violates the classical bound that is set by the product of two auto-coherences. The violation margin is reduced for increasing thermal occupancy, as you can expect.

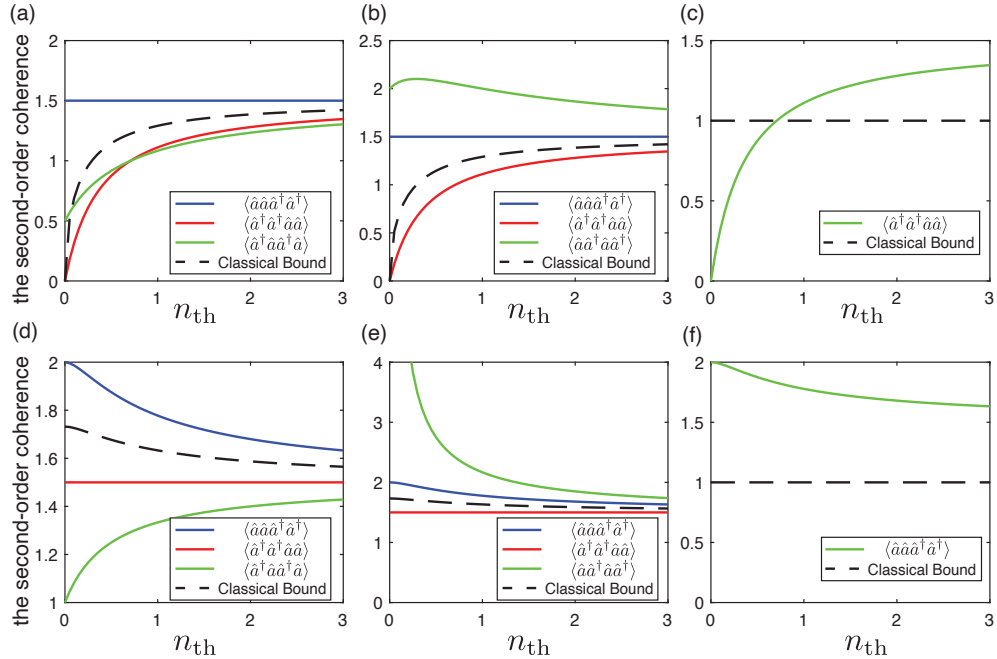


Figure 3.3: The cross-coherences and the auto-coherences of a single-photon-added/subtracted thermal state for various initial photon occupancy  $n_{\text{th}}$ . The solid green lines represent the cross-coherences. The blue and red solid lines are the corresponding auto-coherences. The classical bounds are determined by the Cauchy-Schwarz inequality in Eq. (3.191), which are shown in dashed black lines. Top: (a)(b)(c) show the results of a single-photon-added thermal state  $|n_{\text{th}}^{+1}\rangle$ . Bottom: (d)(e)(f) show the results of a single-photon-subtracted thermal state  $|n_{\text{th}}^{-1}\rangle$ .

### Post-Selected State

We also further investigate the violation of the Cauchy-Schwarz inequality for a single-photon-added or -subtracted thermal state.

For a single-photon-added thermal state, let us consider the case that each of two operators  $\hat{a}$  and  $\hat{a}^\dagger$  act on this state a total of two times. Thus, we have four possible outcomes in its correlations:  $\langle \hat{a}\hat{a}\hat{a}^\dagger\hat{a}^\dagger \rangle$ ,  $\langle \hat{a}\hat{a}^\dagger\hat{a}\hat{a}^\dagger \rangle$ ,  $\langle \hat{a}^\dagger\hat{a}\hat{a}^\dagger\hat{a} \rangle$ , and  $\langle \hat{a}^\dagger\hat{a}^\dagger\hat{a}\hat{a} \rangle$ . The expressions of these coherences are given in Eq. (3.69).

For example, for  $\langle \hat{a}\hat{a}^\dagger\hat{a}\hat{a}^\dagger \rangle$ , the test of the Cauchy-Schwarz inequality is achieved by comparing the values of  $(\langle \hat{a}^\dagger\hat{a}\hat{a}^\dagger\hat{a} \rangle)^2$  and  $(\langle \hat{a}^\dagger\hat{a}\hat{a}^\dagger\hat{a} \rangle \cdot \langle \hat{a}\hat{a}\hat{a}^\dagger\hat{a}^\dagger \rangle)$ , or their corresponding second-order coherences. These numerical values are shown in Fig. 3.3(a), where the second-order cross-coherences and two auto-coherences are shown in a solid green line and blue/red lines, respectively. By comparing the cross-coherence (green solid) with the classical bound determined by Eq. (3.191) (dashed black), we see that the Cauchy-Schwarz inequality is violated for small  $n_{\text{th}}$ .

Figures 3.3(b,c) show the results of a single-photon-added thermal state with different orderings. Similarly, the results of a single-photon-subtracted state are shown in Fig. 3.3(d-f).

### 3.5.1.4 Hölder's Inequality

The Cauchy-Schwarz inequality can also be extended to a more general case, which is known as the Hölder inequality.

**Inequality 4 (Hölder's Inequality)** *For any nonnegative definite probability distributions, if  $\mathbf{u}, \mathbf{v} \in \mathcal{R}^n$ , then*

$$|\langle \mathbf{u}, \mathbf{v} \rangle| \leq \|\mathbf{u}\|_p \cdot \|\mathbf{v}\|_q \quad \text{with } 1 \leq p, q \quad \text{and} \quad \frac{1}{p} + \frac{1}{q} = 1, \quad (3.194)$$

where  $\|\mathbf{x}\|_p$  is the  $p$ -norm or  $L^p$ -norm, defined by

$$\|\mathbf{x}\|_p = (|x_1|^p + |x_2|^p + \cdots + |x_n|^p)^{1/p}. \quad (3.195)$$

This is a direct result of the convexity of the linear space in its dimension. As you can see, the Cauchy-Schwarz inequality is the special case where  $p = q = 2$ .

Likewise, we have inequalities of coherence functions for any classical probability distributions

$$g_{a,b}^{(2)}(0) \leq \sqrt[p]{g_{a,a}^{(p)}(0)} \sqrt[q]{g_{b,b}^{(q)}(0)} \quad \text{with} \quad \frac{1}{p} + \frac{1}{q} = 1. \quad (3.196)$$

When this inequality applies to the same state, we have

$$g^{(2)}(0) \leq \sqrt[p]{g^{(p)}(0)} \sqrt[q]{g^{(q)}(0)} \quad \text{with} \quad \frac{1}{p} + \frac{1}{q} = 1. \quad (3.197)$$

Moreover, we can set  $\mathbf{u}$  and  $\mathbf{v}$  in Eq. (3.194) to be  $(|\alpha|^2)^m$  and  $(|\alpha|^2)^n$ , respectively. Thus, the inequality yields

$$g^{(m+n)}(0) \leq \sqrt[p]{g^{(mp)}(0)} \sqrt[q]{g^{(nq)}(0)} \quad \text{with} \quad \frac{1}{p} + \frac{1}{q} = 1. \quad (3.198)$$

### 3.5.1.5 CHSH Inequality

So far we have only discussed nonclassicality condition based on  $P$ -function negativity. There are other types of inequalities that result from the non-local character of quantum mechanics. More specifically, Bell type inequalities identify certain results that are excluded by local hidden-variable theories. As these inequalities are violated, quantum mechanics predicts situations in which the non-local character is in presence. The CHSH inequality is a type of Bell inequality, named after John Clauser, Michael Horne, Abner Shimony, and Richard Holt, who described it in a much-cited paper published in 1969 [155]. The inequality is fulfilled by two postulates about macrorealism (macroscopic realism) [156]:

**Macrorealism:** “A macroscopic object, which has available to it two or more macroscopically distinct states, is at any given time in a definite one of those states.”

**Noninvasive measurability:** “It is possible in principle to determine which of these states the system is in without any effect on the state itself, or on the subsequent system dynamics.”

Thus we have

**Inequality 5 (CHSH Inequality)** *For any classical theory satisfying macrorealism*

$$|S| = |E(a, b) - E(a, b') + E(a', b) + E(a', b')| \leq 2, \quad (3.199)$$

where  $E(a, b)$  etc. are the quantum correlations of the two observables  $a, b$ .

Without loss generality, assume all events have outcome  $f = \{-1, 1\}$ . Then the correlation is defined as

$$E(a, b) = \langle f(a)f(b) \rangle = \frac{n_{11} + n_{-1,-1} - n_{1,-1} - n_{-1,1}}{n_{11} + n_{-1,-1} + n_{1,-1} + n_{-1,1}}. \quad (3.200)$$

If we can arbitrarily assign  $+1$  or  $-1$  to each observable without considering the consistency, the upper bound of  $S$  is 4.

If the measurement is conducted on a qubit (*i.e.*, or any two-level system), the maximum value of  $|S|$  is the Tsirelson bound [157],

$$S < 2\sqrt{2}V < 2\sqrt{2}, \quad (3.201)$$

where the visibility  $V$  is defined as the maximum quantum correlation, *i.e.*, [76]:

$$V = |E(a, b)|_{\max}. \quad (3.202)$$

Therefore,  $V > 1/\sqrt{2} \approx 70.7\%$  is a necessary condition for violating the CHSH inequality.

In the low measurement efficiency case (also the case in this work),  $V$  is related to  $g^{(2)}(0)$  and we have the necessary condition for  $g^{(2)}(0)$  to violate the CHSH inequality. In this case, the visibility  $V$  can be approximated by [76]

$$V \simeq \frac{\sum_i p_{a_i, b_i} - \sum_{i \neq j} p_{r_i} p_{b_j}}{\sum_i p_{a_i, b_i} + \sum_{i \neq j} p_{r_i} p_{b_j}} = \frac{g_{a,b}^{(2)} - 1}{g_{a,b}^{(2)} + 1}. \quad (3.203)$$

The necessary condition for the system to violate the CHSH inequality becomes

$$g_{a,b}^{(2)} > \frac{\sqrt{2} + 1}{\sqrt{2} - 1}. \quad (3.204)$$

There has been tremendous progress in the achievable value of  $g_{a,b}^{(2)}$ , and large  $g_{a,b}^{(2)}$  is crucial for the high-fidelity, long-distance quantum network applications [76].

### 3.5.1.6 Inequality for Wigner Function Negativity

Additionally, we require an inequality to deduce the negativity of the Wigner function. To achieve this, we employ the well-known Chebyshev inequality from statistics that restricts the likelihood of a random variable deviating from its anticipated value by a specific margin.

**Inequality 6 (Statistical Chebyshev Inequality)** *Let  $\mathbf{X} \in \mathcal{R}^N$  with expected value  $\mu = E[\mathbf{X}]$  and covariance matrix  $\mathbf{V}$ . If  $\mathbf{V}$  is a positive-definite matrix, for any real number  $t$  and nonnegative joint probability  $P(\mathbf{X}) \geq 0$ , we have*

$$\Pr \left( \sqrt{(\mathbf{X} - \mu)^T \mathbf{V}^{-1} (\mathbf{X} - \mu)} > t \right) \leq \frac{N}{t^2} \quad (3.205)$$

For a single particle state, we have the joint probability distribution  $W(x, p)$  in the phase space and their covariance matrix is always positive definite. Therefore, if the inequality Eq. (3.205) is violated, then it proves the Wigner function negativity of this state.

## 3.5.2 Hierarchy in Quantum States

A given “quantum effect” may require only a portion of quantum mechanics for its explanation. There is no such a universal measure of “quantumness” of a given effect. However, the complexity of realizing distinctive quantum phenomena is related to their quantum characteristics, which can be used to define a hierarchy of quantum witnesses and their associated quantum advantages, *e.g.* in communication and computation [73, 151, 152].

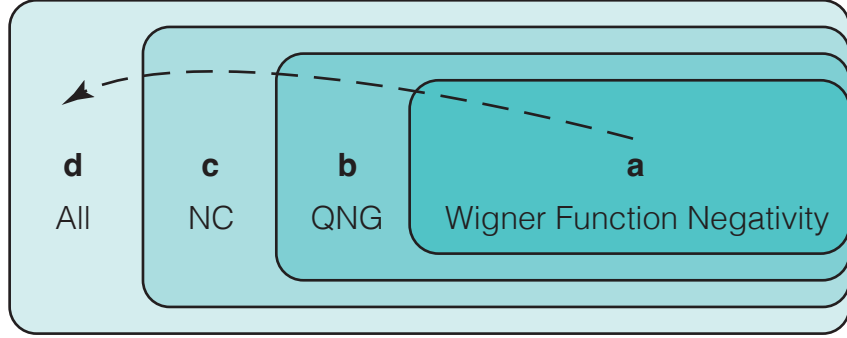


Figure 3.4: The quantum state classification discussed in Sec. 3.5.2. **a** is the set of states with negative Wigner functions. **b** is the set of states that can not be represented by a classical mixture of Gaussian states, known as quantum non-Gaussian states (QNG). **c** is a set of states with the  $P$ -function negativity, known as non-classical states (NC). **d** contains all states in general. These sets satisfy  $a \subset b \subset c \subset d$ . The black dashed arrow represents a possible trajectory of a state with a negative Wigner function to a general state without any quantum witnesses owing to the presence of classical factors, such as loss and classical fluctuations.

The lowest member of this hierarchy are the nonclassical (NC) states, which has been discussed in Sec. 3.5.1 [158]. They are states with  $P$ -function negativity, which rules out them being statistical mixtures of coherent states. The “bad behaved”  $P$ -function of NC states is proven to be associated with quantum information and metrology advantages [3].

The second category is the quantum non-Gaussian (QNG) state, which cannot be represented as a statistical mixture of pure Gaussian states [149, 150, 159]. QNG states are a subset of NC states. This can be easily obtained by noticing that any coherent state is also a Gaussian state [133]. Therefore, a QNG state is considered to be “more quantum” than an NC state. Similarly, there are experimental criteria to verify the non-Gaussianity [152, 160].

The last category is those states having a negative Wigner function. This category is a subset of QNG states. This is obvious by noticing the Wigner function of any Gaussian state must be positive definite. Hence a state with the Wigner function negativity can not be represented by a mixture of Gaussian states. However, a QNG state can still have a positive definite Wigner function [160]. Wigner function negativity is proven to be vital in quantum computational advantages [4].

In conclusion, the aforementioned quantum features divide quantum states into four sets, each being a subset of the previous one offering different quantum advantages. Figure 3.4 shows these sets in relation to each other. The dashed black line schematically represents how quantum features are lost due to the presence of dissipation.

*“Quantum mechanics has shown us that the world is far stranger than we ever imagined, and that the behavior of even macroscopic objects can be unpredictable and non-intuitive.”*

– Sean Carroll

## Quantum Macroscopicity

The spooky features of quantum mechanics are not limited to the microscopic world of subatomic particles, atoms, and molecules. In principle, they should also be exhibited by the macroscopic objects that we encounter in our daily life. However, it is intriguing why macroscopic objects never exhibit quantum effects.

One often-used explanation is the smallness of Planck’s constant. As explained in Sec. 3.4.1.3, when  $\hbar$  approaches 0, the dynamics of quantum probability become identical to those predicted by the classical Liouville equation. The de Broglie wavelength  $\lambda = h/p$  shows that as an object becomes more macroscopic, its quantum wavelength becomes shorter, and thus the features associated with the wave-like features of quantum mechanics are less visible.

Alternatively, decoherence theory suggests that a system loses its quantum features when interacting with a sufficiently large classical environment. However, the formalism of decoherence is still based on the unitary quantum interaction (*i.e.*, with a thermal reservoir). More precisely, the process of decoherence arises when a quantum system becomes entangled with its environment, such as when it interacts with other particles [161]. The quantum system together with the environment that it couples to is a closed system. Such a closed system should be restricted to the quantum description as all interactions are unitary. The origin of the quantum decoherence in this case is unclear and needs to be further explained [161, 162].

Many take it for granted that quantum theory can be applied to macroscopic scales. But there are good reasons to consider the possibility of its failure beyond a certain scale. One compelling reason is that quantum theory allows for a massive object to be in a superposition of locations, which according to general relativity results in a superposition of spacetime geometry. Such a superposition is not well-defined in the framework of general relativity [34–36]. A sketch of this conflict is shown in Fig. 4.1.

Another reason is related to what happens at the Planck length scale  $l_P$ , which can be

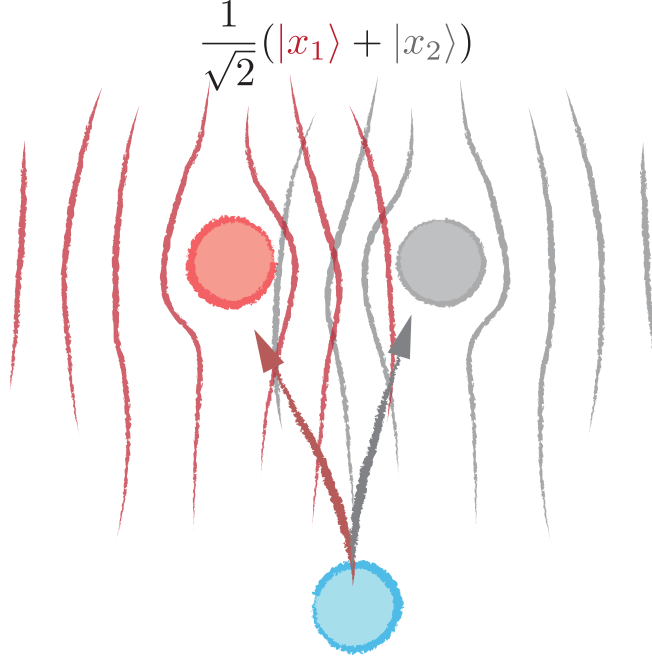


Figure 4.1: A sketch of a debatable spacetime in superposition caused by a massive object in a superposition state. Colored lines represent curved spacetime.

defined in the following equations

$$2 \frac{GM_{\text{eff}}}{c^2} = l_P, \quad (4.1a)$$

$$M_{\text{eff}} = \frac{1}{2} \frac{\hbar c}{l_P} \frac{1}{c^2}, \quad (4.1b)$$

where LHS of eq. (4.1a) is the Schwarzschild radius of a mass  $M_{\text{eff}}$  and  $M_{\text{eff}}$  is the effective mass of the quantum fluctuation energy of wavelength  $l_P$ . This means, at this scale, quantum fluctuations generate enough energy to produce black holes. The fact that both quantum and gravitational effects are equally significant at the Planck length scale causes problems in observing physics and interpreting causality at that scale. This is often described as “spacetime becomes a foam at the Planck scale” [163]. Some quantum gravity theories propose that there exists a minimum observable length scale, or that spacetime is discrete [164–167]. The granularity of spacetime would result in non-unitary time evolution of quantum systems and an intrinsic decoherence process [168, 169]. One way to incorporate this phenomenologically in (the non-relativistic limit of) quantum theory is to postulate modified commutator relations [1, 170–172], or to have a nonlinear Schrödinger equation [1, 5, 34, 173].

Experimental tests confirm quantum mechanics impressively so far. Especially the past decade has witnessed so-called the second quantum revolution, *i.e.*, Quantum 2.0.

The growing capabilities in carefully controlled experiments can extend the observation of quantum phenomena to increasingly macroscopic objects, such as entangled massive mechanical resonators [59, 60, 97], nonclassical quantum mechanical resonators [52, 53, 61, 62, 75, 92, 174, 175], and matter-wave interference [8, 176–178]. Experiments on macroscopic quantum phenomena may help theorists to build new frameworks [1, 9, 37–39] or even lead to new scientific discoveries. In recent years, there have been emerging proposals and experiments to test the effect of gravity on quantum systems, such as atomic interferometry [8, 177, 179–184], atomic clocks [185, 186], and quantum optics [170, 187]. Particularly, massive and macroscopic optomechanical systems are well-suited to achieve this goal [1, 171, 172, 187–190].

In this section, we first describe one way to quantify macroscopicity across different experiments. Then we describe two approaches to modifying standard quantum theory to account for quantum gravity effects phenomenologically.

## 4.1 Macroscopicity

Various experiments in different systems have been suggested to demonstrate quantum features at macroscopic scales. This raises the question of how to objectively assess the degree of macroscopicity reached in different experiments. Such an approach should allow us to compare different systems, for example: oscillating micromirrors [191], oscillating membranes [81], levitated nanospheres [52, 53], and even atomic interferometers [178] in an unbiased way.

To see this problem more explicitly, in interferometric experiments with atoms, molecules, or Bose-Einstein condensates, the wave nature of objects with more than  $10^4$  atomic mass units has been confirmed, with state-of-the-art delocalization achieved over a length of meters and a time scale of seconds [7, 8, 178–180]. Meanwhile, mechanical devices exhibit high mass compared to other quantum systems, and recent experiments have demonstrated nonclassical states in various mechanical resonators [13, 61, 62, 75, 92, 175], involving a truly macroscopic number of atoms, up to  $10^{16}$ . However, the quantum delocalization associated with these resonators' vibrational state is limited to about one picometer in conceivable setups. Therefore, some matter-wave experiments might surpass the macroscopicity of a mechanical resonator, raising uncertainty regarding their comparison with other macroscopic quantum effect tests.

To solve this problem, a macroscopicity assessment that is universally applicable and can evaluate the empirical parameters of a given experiment has been introduced in Ref. [2, 192]. In summary, a general modified quantum theory has been developed that accounts for the decoherence of quantum experiments at a specific macroscopic scale. The comparison between the observed decoherence and the decoherence in this modified quantum theory yields the assessment of the macroscopicity.

The proposal of Refs. [2, 192] considers a modification of the quantum theory that satisfies the following requirements:

1. Invariant under Galilean transformations, avoiding a distinguished frame of reference;
2. The exchange symmetry of identical particles is unaffected;
3. Adding an uncorrelated system leaves the reduced state unchanged;
4. Displays scale invariance with respect to the center-of-mass of a compound system.

Using the formalism of quantum dynamical semigroups and a theorem by Holevo [193] for any Galilean invariant theory, the modification to the von Neumann equation for the state  $\hat{\rho}$  of a single particle should take the form of

$$\partial_t \hat{\rho} = [\hat{H}, \hat{\rho}] / i\hbar + \hat{\mathcal{L}}_1 \hat{\rho}, \quad (4.2)$$

with an additional Lindblad generator  $\hat{\mathcal{L}}_1 \hat{\rho}$  given by

$$\hat{\mathcal{L}}_1 \hat{\rho} = \frac{1}{\tau} \int d^3q d^3p g(q, p) \mathcal{D}[\hat{L}(\mathbf{q}, \mathbf{p})] \hat{\rho}, \quad (4.3)$$

where  $\mathcal{D}[\hat{L}] \hat{\rho} = \hat{L} \hat{\rho} \hat{L}^\dagger - \{\hat{L}^\dagger \hat{L}, \hat{\rho}\} / 2$ . The operator  $\hat{L}$  displaces a single particle in the phase space by an amount  $\mathbf{q}$ ,  $\mathbf{p}$ , and is given by

$$\hat{L}(\mathbf{q}, \mathbf{p}) = e^{\frac{i}{\hbar} (\mathbf{P} \cdot \mathbf{q} - \mathbf{p} \cdot \mathbf{X})}, \quad (4.4)$$

and  $g(p, q)$  is a positive, normalized phase-space distribution. The modified von Neumann equation Eq. (4.2) reduces to the normal equation when the standard deviation of  $g(p, q)$  statistics  $\sigma_q = \sigma_p = 0$  (*i.e.*,  $g(p, q)$  is a delta function). This modified term can be interpreted as the classicalizing of a delocalized state. The parameter  $\tau$  in Eq. (4.3) estimates the time scale for the decoherence of the state whose delocalization is greater than critical length scale  $\hbar/\sigma_p$  in position or greater than  $\hbar/\sigma_q$  in momentum. Remarkably, if one takes  $\sigma_q = 0$ , the special form of Eq. (4.3) describes the results of the continuous spontaneous localization (CSL) theory [5, 6, 194], which is the best studied nonlinear modification of quantum mechanics. Within this theoretical framework, the superposition of macroscopically distinct positions is predicted to collapse rapidly.

Usually, we use the electron as the reference particle with decoherence time  $\tau_e$  and take  $g_e(q, p)$  to be a Gaussian distribution with standard deviations  $\sigma_p$  and  $\sigma_q$ , respectively. With this, Eq. (4.4) can be extended as a weighted sum of single particle operators in the

form of

$$\hat{L}_N(\mathbf{q}, \mathbf{p}) = \sum_{n=1}^N \frac{m_n}{m_e} e^{\frac{i}{\hbar} (\mathbf{P}_n \cdot \frac{m_e}{m_n} \mathbf{q} - \mathbf{p} \cdot \mathbf{x}_n)}, \quad (4.5)$$

with

$$\hat{\mathcal{L}}_N \hat{\rho} = \frac{1}{\tau_e} \int d^3 q d^3 p g_e(q, p) \mathcal{D}[\hat{L}_N(\mathbf{q}, \mathbf{p})] \hat{\rho}. \quad (4.6)$$

The center-of-mass motion of a mechanical resonator of total mass  $M$  can be approximated by treating the single degree of freedom as a single-particle, using Eq. (4.3). The rate  $\tau$  and the phase-space distribution  $g(q, p)$  in this form can be represented by

$$\frac{1}{\tau} = \frac{1}{\tau_e} \frac{1}{m_e^2} \int d^3 q d^3 p g_e(q, p) |\tilde{\varrho}(\mathbf{p})|^2, \quad (4.7)$$

$$g(q, \mathbf{p}) = \frac{\tau M^3}{\tau_e m_e^5} g_e \left( \frac{M}{m_e} q, p \right) |\tilde{\varrho}(\mathbf{p})|^2, \quad (4.8)$$

where  $\tilde{\varrho}(\mathbf{p}) = \int d^3 x \varrho(\mathbf{x}) e^{-i\mathbf{p}\cdot\mathbf{x}/\hbar}$  is the Fourier transform of the mass density  $\varrho(\mathbf{x})$  of the oscillator. The effective coherence time  $\tau$  depends on the relation between the size of the mechanical resonator and the critical length scale  $\hbar/\sigma_p$  of the reference distribution  $g_e$ . Substituting the effective coherence time  $\tau$  and the effective phase distribution  $g(q, p)$  into Eq. (4.2) yields the constraint on the single electron coherence time  $\tau_e$  from various experimental results. Finally, the assessment of the macroscopicity  $\mu$  is given by

$$\mu = \log_{10} \left( \frac{\tau_e}{1 \text{ s}} \right). \quad (4.9)$$

For a massive oscillator  $m \gg m_e$ , the expression  $g_e$  in Eq. (4.7) approximates a delta function in the variable  $q$ . Therefore, the translation  $\mathbf{q}$  is negligible in the effective phase space distribution  $g(q, p)$ . As a result, Eq. (4.5) and (4.6) can be approximated as

$$\hat{\mathcal{L}}_N \hat{\rho} = \frac{1}{\tau_e} \int d^3 p g_e(\sigma_p, p) \mathcal{D}[\hat{L}_N(\mathbf{p})] \hat{\rho}, \quad (4.10)$$

$$\hat{L}_N(\mathbf{p}) = \sum_{n=1}^N \frac{m_n}{m_e} e^{\frac{-i}{\hbar} \mathbf{p} \cdot \mathbf{x}_n}, \quad (4.11)$$

where  $g_e$  is an isotropic Gaussian momentum distribution given by

$$g_e(\sigma_p, p) = \frac{e^{-p^2/2\sigma_p^2}}{(2\pi\sigma_p^2)^{3/2}}. \quad (4.12)$$

To make this example more explicit, let's consider a bulk acoustic resonator with the geometry of a Fabry-Pérot cavity [72, 174] with the acoustic mode taking the form

$$\mathbf{u}(\mathbf{r}_n) = \exp\left(-\frac{y_n^2 + z_n^2}{w_0^2}\right) \cos\left(\pi \frac{qx_n}{L}\right) \mathbf{e}_x, \quad (4.13)$$

of waist  $w_0$ , mode index  $q$ , length  $L$  and  $\mathbf{r}_n = (x_n, y_n, z_n)$  is the spatial coordinate. A single phonon excites a displacement field described by

$$\mathbf{X}_n = \mathbf{r}_n + \mathbf{u}(\mathbf{r}_n) x_0 \hat{\mathbf{X}}, \quad (4.14)$$

where  $x_0 = \sqrt{\hbar/m_{\text{eff}}\omega}$  is the zero-point fluctuation amplitude,  $m_{\text{eff}}$  is the effective mass,  $\mathbf{r}_n$  is the equilibrium position for  $n$ -th particle and  $\hat{\mathbf{X}}$  is the position operator. In a continuous limit, the Lindblad operator thus yields

$$\hat{\mathcal{L}}(\mathbf{p}) = \frac{1}{m_e} \int d^3r \varrho(\mathbf{r}) e^{-i\mathbf{p}\cdot\mathbf{r}/\hbar} e^{-i\mathbf{p}\cdot\mathbf{u}(\mathbf{r})x_0\hat{\mathbf{X}}/\hbar}, \quad (4.15)$$

where the integral is over real space. We assume a homogeneous mass density  $\varrho(\mathbf{r}) = \bar{\varrho}$  and expand the Lindblad operator Eq. (4.15) to first order in  $\hat{\mathbf{X}}$ . Thus a diffusion rate for the oscillator is given by

$$\Gamma = \frac{m_{\text{eff}}^2}{m_e^2 \tau_e} \frac{(4x_0/L)^2}{1 + \sigma_w^2} \int d\zeta \frac{e^{-\zeta^2/2\sigma_L^2}}{\sqrt{2\pi}\sigma_L} \frac{1 - (-)^q \cos \zeta}{(1 - \pi^2 q^2/\zeta^2)^2}, \quad (4.16)$$

where  $\sigma_w = w_0/(\hbar/\sigma_p)$  and  $\sigma_L = L/(\hbar/\sigma_p)$  are the ratios of the geometric lengths over the critical modification length  $\hbar/\sigma_p$ . The maximum rate  $\Gamma$  with respect to  $\sigma_p$  can be analytically solved as [174]

$$\max_{\sigma_p} \Gamma \approx \sqrt{\frac{3\pi}{2e^3}} \frac{6\hbar\bar{\varrho}}{m_e^2 \omega \tau_e} \frac{L}{q} = \sqrt{\frac{3\pi}{2e^3}} \frac{6\hbar\bar{\varrho}}{m_e^2 \tau_e} \left(\frac{L}{q}\right)^2 \frac{1}{2\pi v}. \quad (4.17)$$

In the rotating frame of the oscillator, the evolution of the density matrix  $\hat{\rho}$  is governed by the master equation, which includes the energy decay rate  $\gamma_\downarrow$ ,

$$\dot{\hat{\rho}} \approx (\Gamma + \gamma_\downarrow) \mathcal{D}[\hat{a}] \hat{\rho} + \Gamma \mathcal{D}[\hat{a}^\dagger] \hat{\rho}. \quad (4.18)$$

This coarse-grained master equation is averaged over the rapidly oscillating terms. With this equation of motion, we could compare the experimental results of such an oscillator to a single particle. More examples are calculated in Refs. [192].

To date, the most macroscopic mechanical resonator with Wigner function negativities is reported to have  $\mu = 11.3$  [174] and the most macroscopic matter-wave interferometer experiment is assessed to have  $\mu = 14.0$  [178].

## 4.2 Modified Quantum Theory

The lack of compatibility between general relativity and quantum theory indicates the possibility of modifying the quantum theory to bridge this gap. The requirement of macrorealism for a plausible description of physical reality remains a topic of debate. There are competing descriptions of nature that predict significantly different effects at macroscopic scales, despite being compatible with all microscopic experiments and astrophysical observations to date. While metaphysical arguments may be made in support of one theory over another, their empirical status is equivalent, and only future experiments can differentiate between them. Here I highlight two proposed theories that suit quantum optomechanical experiments. One approach is to introduce modified commutator relations for canonical observables, which can be tested by monitoring the quantum-level motion of massive pendulums [170–172, 195]. The other is to extend the Schrödinger equation nonlinearly to account for the possible granularity of spacetime [1, 2, 188, 189].

### 4.2.1 Deformed Commutator

It has been proposed that modified commutators could provide a phenomenological means for incorporating quantum gravitational effects (in particular, discrete spacetime) [195–197]. This motivates the idea of the so-called generalized uncertainty principles (GUPs) in the following form [171]:

$$\Delta q \Delta p \geq \frac{\hbar}{2} \left( 1 + \beta_0 \left( \frac{L_P \Delta p}{\hbar} \right)^2 \right), \quad (4.19)$$

which is equivalent to

$$[q, p] = i\hbar \left( 1 + \beta_0 \left( \frac{L_P p}{\hbar} \right)^2 \right), \quad (4.20)$$

where  $L_P$  is the Planck length and  $\beta_0$  is a dimensionless parameter. This modification indicates that the minimal uncertainty on the position is

$$\Delta q \geq \frac{\hbar}{2} \left( \frac{1}{\Delta p} + \beta_0 \left( \frac{L_P}{\hbar} \right)^2 \Delta p \right) \geq \sqrt{\beta_0} L_P, \quad (4.21)$$

If we assume  $\beta_0 \sim 1$ , the second term in Eq. (4.19) will be negligible unless the momentum fluctuation satisfies  $\hbar/\Delta p \sim L_p$ . However, the experimental constraint on the parameter  $\beta_0$  is still needed to verify or rule out this framework. By taking the usual dimensionless

coordinates  $\tilde{q}$  and  $\tilde{p}$ , we have

$$[\tilde{q}, \tilde{p}] = i(1 + \beta \tilde{p}^2); \quad (4.22)$$

$$H = \frac{\hbar\omega_0}{2} (\tilde{q}^2 + \tilde{p}^2), \quad (4.23)$$

where  $\tilde{q} = \sqrt{(m\omega_0)/\hbar}q$ ,  $\tilde{p} = p/\sqrt{\hbar m\omega_0}$  and  $\beta = \beta_0(\hbar m\omega_0/m_p^2 c^2)$  is a small dimensionless parameter. If we apply the following transform to  $\tilde{p}$

$$\tilde{p} = \left(1 + \frac{1}{3}\beta p'^2\right) p', \quad (4.24)$$

we reobtain the familiar canonical commutation relation

$$[\tilde{q}, p'] = i, \quad (4.25)$$

with a modified Hamiltonian expanded to the first order in  $\beta$

$$H = \frac{\hbar\omega_0}{2} (\tilde{q}^2 + p'^2) + \frac{\hbar\omega_0}{3} \beta p'^4. \quad (4.26)$$

Note that this Hamiltonian is equivalent to an anharmonic oscillator with Kerr nonlinearity. It implies two relevant effects: the appearance of the third harmonic and the dependence of the oscillation frequency on the amplitude. That is

$$\tilde{q} = q_0 \left[ \sin(\tilde{\omega}t) + \frac{\beta}{8} q_0^2 \sin(3\tilde{\omega}t) \right], \quad (4.27)$$

$$\tilde{\omega} = \left(1 + \frac{\beta}{2} q_0^2\right) \omega_0, \quad (4.28)$$

where  $q_0$  is the oscillating amplitude. The challenging part in practice is that all materials exhibit intrinsic Kerr nonlinearity for large oscillating amplitudes, yielding the same experimental effects. It is impossible to distinguish one from another. The best constraint on  $\beta_0$  to date is reported to be  $\beta_0 \leq 3 \times 10^7$  [171].

## 4.2.2 Nonlocal Dynamics

Another approach involves modification of the standard Schrödinger equation. This field of research seeks to develop general models of quantum gravity that can be tested via observation in the absence of a definitive quantum gravity theory. One class of models deserving special attention is those that uphold local Lorentz invariance (LLI) as a guiding principle while viewing spacetime as emerging from more fundamental discreteness [198]. Some types of nonlocal modifications of standard local dynamics are suggested

to be able to reconcile LLI with fundamental discreteness [199, 200]. Along this line, the requirement of LLI together with the avoidance of classical instabilities effectively restricts dynamics to either standard local dynamics with 1st or 2nd order in spacetime, or to nonlocal dynamics with infinite orders of derivatives according to Ostrogradsky's theorem [201].

As an example, modifying the Klein-Gordon equation for a massive free scalar field in flat spacetime involves replacing  $(\square + \mu^2)$  with  $f(\square + \mu^2)$ , where  $f$  is a nonpolynomial function to avoid the generic Ostrogradsky instabilities [201]. Additionally, the function  $f$  must satisfy three requirements:

1.  $f(k^2) = 0$  iff  $k^2 = 0$ : ensure there exist no classical runaway solutions;
2. The nonlocal QFT must be unitary: conservation of probability;
3. The nonlocal QFT must possess a global U(1) symmetry: to ensure a probabilistic interpretation can be given to the wave function.

To ensure a suitable power series expansion that characterizes deviations from standard local field theory, the definition of  $f$  must incorporate a characteristic, covariantly defined scale  $\epsilon$ . Thus a nonlocal Lagrangian for a free complex, massive, scalar field  $\phi(x)$  is

$$\mathcal{L} = \phi(x)^* f(\square + \mu^2) \phi(x) + \text{c.c.} \quad (4.29)$$

In Eq. (4.29), without losing generality, we assume  $f$  is an analytic function and can be formally expanded as a power series  $f(z) = \sum_{n=1}^{\infty} b_n \epsilon^n z^n$ . Thus, the nonlocal dynamic equation reads

$$f(\mathcal{S})\psi(t, x) = V(x)\psi(t, x), \quad (4.30)$$

where  $\mathcal{S} = i\hbar \frac{\partial}{\partial t} + \frac{\hbar^2}{2\mu} \frac{\partial^2}{\partial x^2}$  is the standard Schrödinger operator, and  $V(x)$  is the potential.

Considering the case of a 1-D harmonic oscillator with  $V(x) = \frac{1}{2}m\omega^2x^2$ , where  $m$  is its effective mass and  $\omega$  is its natural resonance frequency.  $f(\mathcal{S})$  can be expanded as

$$f(\mathcal{S}) = \mathcal{S} + \sum_{n=2}^{\infty} b_n \left( \frac{-2m}{\hbar^2} \right)^{n-1} l_k^{2n-2} \mathcal{S}^n \quad (4.31a)$$

$$= \mathcal{S} + \sum_{n=2}^{\infty} b_n (-2)^{n-1} \left( \frac{l_k}{x_{\text{ZPF}}} \right)^{2(n-1)} \mathcal{S}^n \quad (4.31b)$$

$$= \mathcal{S} + \sum_{n=2}^{\infty} b_n (-2)^{n-1} \epsilon^{n-1} \mathcal{S}^n, \quad (4.31c)$$

where  $l_k$  is the nonlocality length scale,  $x_{\text{ZPF}} = \sqrt{\hbar/m\omega}$  is the zero-point motion of the oscillator,  $\epsilon = (l_k/x_{\text{ZPF}})^2$  is a dimensionless parameter that characterizes the nonlocal

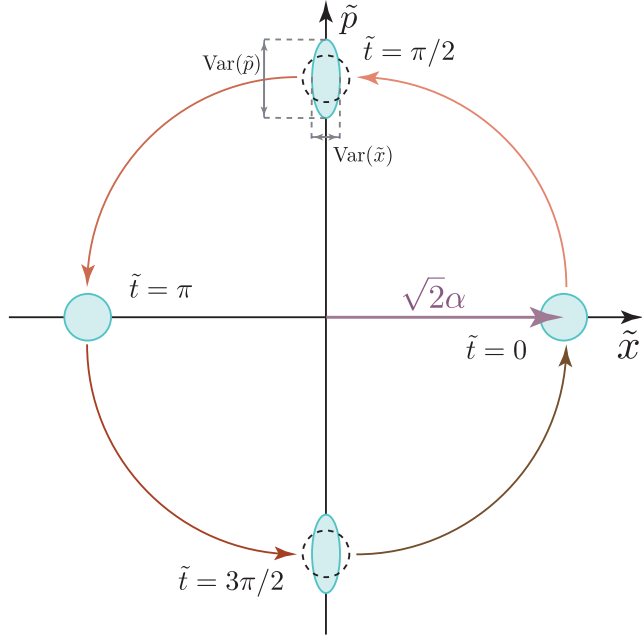


Figure 4.2: Sketch of the time evolution of a coherent state in the phase space. The solid circles represent the variance of the coherent state. The black dashed circles represent the unperturbed variances under the standard quantum theory.

dynamic deviation, and  $b_n$  (assumed to be  $\mathcal{O}(1)$ ) are the dimensionless expansion coefficients of the analytical function  $f(\mathcal{S})$ . This expression means that if the zero-point motion is comparable to  $l_k$  (*i.e.*,  $\epsilon \sim 1$ ), the higher-order nonlocal dynamical terms will be significant in the state evolution. Notably,  $l_k$  is not necessarily the same as the Planck length  $L_P$ , and so needs to be experimentally constrained.

The evolution of a displaced ground state — *i.e.*, a quantum coherent state — under Eq. (4.31a) can be solved perturbatively when  $\epsilon \ll 1$ . This assumption is intuitively correct since a physically reasonable solution of the modified Schrödinger equation should reduce to the solution of the standard Schrödinger equation in the nonrelativistic limit to meet all well-tested physics.

The results for perturbations around a coherent state  $|\alpha\rangle$  are

$$\langle \tilde{x} \rangle = \sqrt{2}|\alpha| \cos(\tilde{t}) \left\{ 1 + \frac{1}{4}\epsilon|\alpha|^2 b_2 [\cos(2\tilde{t}) - 1] \right\} + \mathcal{O}(\epsilon^2), \quad (4.32a)$$

$$\langle \tilde{p} \rangle = \sqrt{2}|\alpha| \sin(\tilde{t}) \left\{ 1 + \frac{1}{4}\epsilon b_2 [|\alpha|^2(7 + 3\cos(2\tilde{t})) - 2] \right\} + \mathcal{O}(\epsilon^2). \quad (4.32b)$$

The variances of the position and the momentum are

$$\text{Var}(\tilde{x}) = \frac{1}{2} \left\{ 1 - \epsilon b_2 \left[ (6|\alpha|^2 - 1) \sin^2(\tilde{t}) \right] \right\} + \mathcal{O}(\epsilon^2), \quad (4.33a)$$

$$\text{Var}(\tilde{p}) = \frac{1}{2} \left\{ 1 + \epsilon b_2 \left[ (6|\alpha|^2 - 1) \sin^2(\tilde{t}) \right] \right\} + \mathcal{O}(\epsilon^2), \quad (4.33b)$$

where  $\tilde{x}$ ,  $\tilde{p}$ , and  $\tilde{t}$  are dimensionless variables, defined as  $\tilde{x} \equiv x/x_{\text{ZPF}}$ ,  $\tilde{p} \equiv p/p_{\text{ZPF}}$  and  $\tilde{t} \equiv \omega t$ , respectively.  $|\alpha|$  is the displacement amplitude of the coherent state,  $b_2 \sim 1$  is the expansion coefficient of  $f$ . The position and momentum present third harmonics due to the nonlocal dynamics. More importantly, the variances of the position and the momentum in Eq. (4.33) undergo a synchronous, cyclic squeezing of order  $\epsilon$  as shown in Fig. 4.2. This spontaneous, oscillating squeezing is a highly significant phenomenon that is not likely to be generated by other effects. The amplitude of this squeezing is  $\sim 6\epsilon|\alpha|^2$ . Apparently, to better test or discover evidence of this phenomenological theory, a larger amplitude and a larger mass, which equate to a more macroscopic system in certain regards, are preferred. So far the best constraint on  $l_k$  is provided by the LHC, giving  $l_k \leq 10^{-19} \text{ m}$  [202].

*“Superfluid helium is one of the most remarkable phenomena in nature, a truly fascinating subject for scientists and physicists.”*

– Richard Feynman

# Superfluid Helium Filled Fabry-Pérot Cavity

Chapters 2-4 provided an overview of the scientific motivations and relevant theoretical backgrounds of my graduate research. This chapter focuses on the implementation of the experimental system. Specifically, we utilized a Fabry-Perot cavity filled with superfluid helium-4. In this chapter, I will describe the details of this system, including its optical and mechanical modes as well as the optomechanical interaction between them. Furthermore, I will elaborate on the unique material advantages of using superfluid helium in optomechanical applications.

## 5.1 Experiment Overview

Figure 5.1(a) shows a schematic of the device. The main part of the device is an optical Fabry-Pérot cavity. This optical cavity is formed between two fiber ends, with each being curved and coated with high-reflectivity distributed Bragg reflectors (DBR). This type of cavity is also known as a fiber cavity.

Fibers are confined in glass ferrules whose inner diameter (ID) is only  $5 \pm 3 \mu\text{m}$  larger than the fibers' outer diameter, as shown in Fig. 5.1(b). The two ferrules are aligned by threading a scrap piece of fiber through both of them. These two ferrules were positioned with  $\sim 0.5 \text{ mm}$  distance between the ferrule faces, and then they were epoxied on the top of the substrate. The detailed cavity building process can be found in Refs. [70, 71, 203, 204].

There are a number of good reasons to use a fiber cavity in this work. First, its small mode volume results in strong optomechanical coupling. In addition, the traveling light in each fiber couples to the cavity mode without any *in situ* alignment optics (albeit with coupling efficiency  $\eta_\kappa \sim 0.3$  in the present devices). Last but not least, such construction and alignment are robust to thermal expansion during cooldown and are resilient after several thermal cycles.

The optical modes are confined by the two high-reflectivity coatings, and achieve an

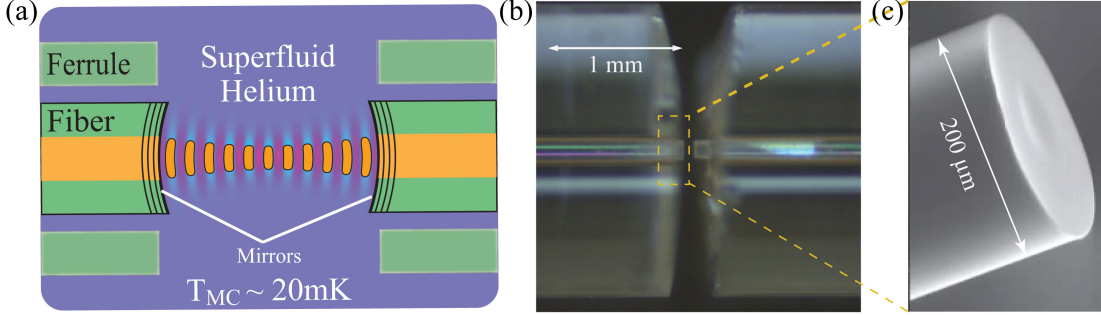


Figure 5.1: (a) A schematic of the main experiment device. The orange represents the optical intensity contour. The purple and blue area stands for the liquid helium density wave. Several black lines on each fiber end represent the optical DBR coating. (b) A photo of the empty cavity in the experiment. The inner brighter cylinders are the fiber, and the outer wider cylinders are glass ferrules. (c) A zoom-in view of the fiber end (dashed orange box in (b)). The center of the fiber end is a curved smooth surface.

optical finesse  $\mathcal{F} \sim 4.36(1) \times 10^4$ . The empty space of the cavity is filled with superfluid helium, which serves as the host of the mechanical resonator. The density wave of the helium acts as the mechanical resonator. The mechanical modes are mainly confined by the impedance mismatch between the glass and liquid helium, with a mechanical finesse  $\sim 100$  (details c.f. Sec. 5.2).

The dielectric constant of liquid helium is density-dependent. Hence, the optomechanical coupling arises from the change of the optical resonance frequency due to the presence of the density wave. In turn, the density distribution is altered by the electrostrictive force exerted by the gradient of the optical intensity. This is the so-called photoelastic coupling. As discussed in detail in Sec. 5.4, this coupling is proportional to the overlap between the optical intensity and the amplitude of the mechanical mode (*i.e.*, change of the density). Both types of modes are governed by the same wave equation and confined by the same boundaries, thus sharing the same eigenmode set. Given the geometry of the cavity, the intensity distribution of an optical Gaussian mode is approximately the same as the density profile of the mechanical Gaussian mode having twice the longitudinal index. As a result of eigenmode orthogonality, this relationship yields the single-mode coupling between any given optical Gaussian mode to one mechanical Gaussian mode, as illustrated in Fig. 5.1(a).

Lasers are sent to one side of the cavity to excite the cavity mode. The cavity mode is monitored by allowing part of the intra-cavity light to travel; back into the fiber. The input coupling efficiency  $\eta_\kappa = \kappa_{\text{ex}}/\kappa$  is measured by the heterodyne detection scheme through both phase modulation and amplitude modulation [70, 71, 203, 204], giving  $\eta_\kappa = 0.29(1)$  [205].

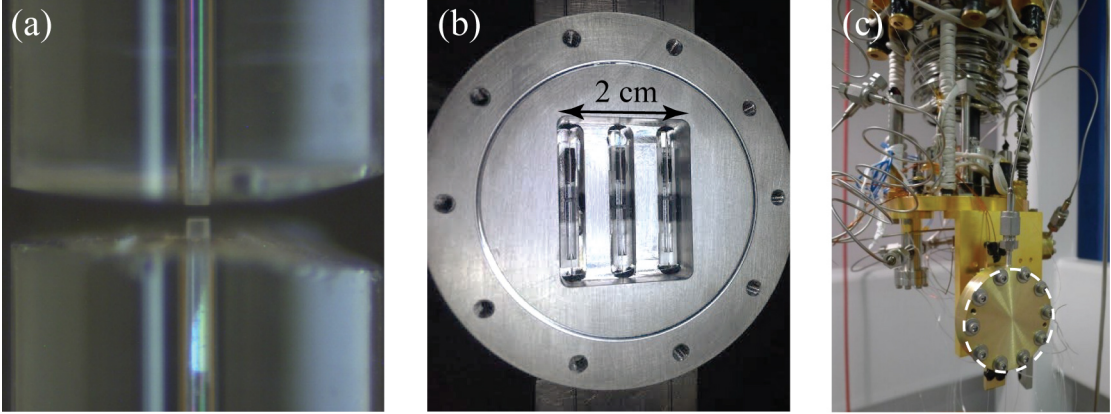


Figure 5.2: (a) The photo of the fiber cavity aligned in glass ferrules. (b) Three identical fiber cavities are assembled in one cell. This cell is indium sealed and filled with liquid helium. (c) The cell shown in (b) is attached to a gold-plated bracket. The entire device is mounted on the mixing plate of a dilution fridge. The stainless steel VCR connection is the gas feedthrough line.

Information about the mechanical state is encoded in the emitted light. In this experiment, this light is measured by two superconducting nanowire single photon detectors (SNSPDs). Details of this measurement are presented in Sec. 6.1.

Three almost identical fiber cavities are mounted in an invar cell, which is attached to a gold-plated copper bracket, as shown in Fig. 5.2. The entire device is mounted on the mixing chamber of the dilution refrigerator and can be cooled down to  $\sim 20$  mK.

## 5.2 Fiber Fabrication and Device Description

The fibers (IVGfiber; Cu1300 and Cu1300/200) used in this study are 200  $\mu\text{m}$  in diameter. They are copper coated with an inner carbon coating. Copper coating, as opposed to plastic, is preferred by the mirror coating company. Further information about the fiber manufacturing process can be found in Refs. [70, 71, 203, 204]. Pictures of the fiber cavity and fiber ends are shown in Figs. 5.1(b,c).

To get a high-finesse optical cavity, one key engineering challenge is creating smooth curved surfaces. This is achieved by laser machining the ends of the fibers at Prof. Jakob Reichel's group (Laboratoire Kastler Brossel, ENS Université) [206–208]. The laser ablation process technique was pioneered by Prof. Reichel to achieve a sweet spot where the glass flows if pulses are of the optimal duration and power. This flow is essential to attain the required surface roughness of  $\sim 200$  pm RMS, enabling the production of cavities with  $\mathcal{F}_{\text{cav}} \sim 2 \times 10^5$ . This is close to the roughness obtained through super-polishing or chemical etching methods ( $\sim 50$  pm) [206]. In addition, laser ablation removes some material and creates a concavity with radii of curvature (RoC)  $\sim 1 \mu\text{m}$ -1 mm [206]. Such

a small RoC was not previously possible using super-polishing techniques. These small RoCs make it possible to achieve very low mode volumes, which is crucial for some applications requiring strong coupling and compact packaging. Furthermore, the ability to create mirrors on fibers is an achievement in itself since fibers offer the integrated transport of light to hybrid systems of interest (e.g., atoms) that can be trapped or placed inside a fiber cavity.

The two fiber mirrors used in this study have radii of curvature (RoC)  $r_1 \approx 324.5 \mu\text{m}$  and  $r_2 \approx 496.7 \mu\text{m}$ , respectively. The fiber ends are coated with a high-reflectivity dielectric DBR mirror coating consisting of alternating layers of  $\text{SiO}_2$  and  $\text{Ta}_2\text{O}_5$ . This coating provides  $\mathcal{F}_{\text{cav}} \approx 4.36(1) \times 10^4$ . Two fiber ends are separated by  $L_{\text{cav}} = 69.7(1) \mu\text{m}$ , which is determined from the optical and mechanical resonance measurement in Sec. 6.2.

Beneath the layers that are designed to give high optical reflection are additional layers of  $\text{SiO}_2$  and  $\text{Ta}_2\text{O}_5$  that are designed to give high mechanical reflectivities. However, these layers fail to improve the mechanical mode quality factor to the expected value. The major reason is the huge acoustic velocity difference between the glass fiber and liquid helium, which significantly reduces the mechanical wavenumber in the fiber. As a result, the paraxial approximation  $k^2 w_0^2 \gg 1$  is not valid in the fiber, with the result that the mechanical wave propagates nearly spherically rather than paraxially, and its wavefront mismatches the DBR layers. This precludes the constructive interference that is necessary to provide high reflection. A detailed discussion can be found in Refs. [203, 204].

As a result, the reflectivity of mechanical waves is primarily determined by the impedance mismatch between liquid helium and fiber,

$$R = \left| \frac{Z_{\text{fiber}} - Z_{\text{He}}}{Z_{\text{fiber}} + Z_{\text{He}}} \right|^2, \quad (5.1)$$

where  $Z_{\text{fiber}} = \rho_{\text{fiber}} v_{\text{fiber}} = 1.298 \times 10^7 \text{ kg m}^{-2} \text{s}^{-1}$  and  $Z_{\text{He}} = \rho_{\text{He}} v_{\text{He}} \approx 3.4 \times 10 \text{ kg m}^{-2} \text{s}^{-1}$  are sound wave impedances in the fiber core and the superfluid helium, respectively. This impedance mismatch, if we suppose it is the only source, would yield a reflectivity of 0.9896 for mechanical waves and a mechanical finesse  $\mathcal{F}_{\text{m}} \approx 295$  assuming no internal loss. The measured finesse is 537(3), which indicates the additional DBR layers increase the mechanical quality factor by roughly a factor of 2 instead of the designed factor of 50 [70, 203, 204].

### 5.3 Optical Mode and Mechanical Mode

In this section, I will describe the modes of a Fabry-Pérot cavity. Under the paraxial approximation, the solutions of the paraxial wave equation are presented for both the optical and mechanical modes [209].

### 5.3.1 Optical Mode

This section explores the optical mode in liquid helium, where liquid helium is treated as a linear and isotropic non-dispersive medium. The mathematics of monochromatic waves in such a medium is nearly identical to the one in vacuum.

For a non-dispersive, simple medium, the constitutive relations are

$$\mathbf{D} = \epsilon \mathbf{E}, \quad \text{and} \quad \mathbf{B} = \mu \mathbf{H}. \quad (5.2)$$

The source-free Maxwell equations in such a medium are

$$\nabla \cdot \mathbf{E} = 0, \quad \nabla \cdot \mathbf{H} = 0, \quad (5.3a)$$

$$\nabla \times \mathbf{E} = -\mu \frac{\partial \mathbf{H}}{\partial t}, \quad \nabla \times \mathbf{H} = \epsilon \frac{\partial \mathbf{E}}{\partial t}. \quad (5.3b)$$

Thus, one can obtain the wave equation for the electric field in liquid helium:

$$\nabla^2 \mathbf{E}(\vec{r}, t) = \frac{n_{\text{He}}^2}{c^2} \frac{\partial^2 \mathbf{E}}{\partial t^2}. \quad (5.4)$$

Assume the wave propagates along the z-axis. Electromagnetic plane waves are transverse, *i.e.*,  $E_z = 0$ . The wave's polarization can be chosen either along the x- or y-axis. For brevity, we reduce Eq. (5.4) into a scalar field of a particular polarization, such as  $E_x$  (denoted as  $E$  in the following), given by:

$$\nabla^2 E(\vec{r}, t) = \frac{n_{\text{He}}^2}{c^2} \frac{\partial^2 E(\vec{r}, t)}{\partial t^2}. \quad (5.5)$$

Under the paraxial approximation  $k^2 w_0^2 \gg 1$ , where  $k$  is the wave number and  $w_0$  is the beam waist (details c.f. Appendix B.1), the paraxial wave equation yields a set of eigenmodes given by

$$E^{(m,n)}(\vec{r}, z) \propto \frac{w_0}{w(z)} H_n \left( \frac{\sqrt{2}x}{w(z)} \right) H_m \left( \frac{\sqrt{2}y}{w(z)} \right) \times \exp \left( -\frac{r_\perp^2}{w(z)^2} \right) \exp \left( i \left[ kz + \frac{kr^2}{2R(z)} - \phi_G^{(n,m)}(z) \right] \right). \quad (5.6)$$

Here,  $(m, n)$  are the transverse mode indexes (eigenvalues associated with the x- and y-axes),  $w(z)$  and  $R(z)$  are the beam radius and the radius of curvature (RoC) at point z measured from the beam center, respectively.  $H_i$  is the Hermite polynomial of order  $i$ .

Particularly,  $\phi_G^{(n,m)}(z)$  is the Guoy phase shift

$$\phi_G^{(n,m)}(z) = (1 + n + m) \arctan \left( \frac{z\lambda}{\pi w_0^2} \right). \quad (5.7)$$

These modes are called the Hermite-Gaussian modes.

Two curved high reflectivity mirrors at  $z_1$  and  $z_2$  confine the optical mode. For a perfect DBR structure (the thickness of each layer precisely satisfies  $nd = \lambda/4$ ) with a large number layers, the unit reflection on the boundary comes along with a  $\pi$  phase shift, *i.e.*,  $r = -1$ . As a result, the optical field is required to have nodes at the boundary surfaces ( $E(z_1) = 0$ ,  $E(z_2) = 0$ ), and the two end mirrors' radii of curvature match the curvatures of the modes' wavefront ( $R(z_1) = r_1$ ,  $R(z_2) = r_2$ ).

Eigenmodes can be solved by matching the general solution Eq. (5.6) with these boundary conditions. Thus, we have  $(\phi(z_2) - \phi(z_1)) = q\pi$  with an integer  $q$  as the longitudinal mode index, where  $\phi$  is the total phase given in Eq. (5.6). The wavenumber  $k^{(q,m,n)}$  of mode  $(q, m, n)$

$$k^{(q,m,n)} = \pi q / L_{\text{cav}} + (m + n + 1) \arccos(\pm \sqrt{g_1 g_2}) / L_{\text{cav}}, \quad (5.8)$$

with  $g_1$  and  $g_2$  defined as  $g_i = 1 - L_{\text{cav}}/r_i$ . A detailed discussion of the Hermite-Gaussian modes in a Fabry-Pérot cavity can be found in Appendix B.2. Fundamental transverse modes ( $m = n = 0$ ) are evenly distributed in frequency with the free spectral range given by  $\Delta\omega_{\text{FSR}} = \pi c / n_{\text{He}} L_{\text{cav}}$ . For any given longitudinal mode index  $q$ , transverse modes are split by the same spacing  $\arccos(\pm \sqrt{g_1 g_2}) c / (L_{\text{cav}} n_{\text{He}})$  and modes of the same value ( $m + n$ ) are degenerate. In the ideal case, modes of the two polarizations are also degenerate. However, in practice, boundary conditions might vary for different polarizations, which results in polarization splitting.

Particularly, we are interested in modes (Gaussian modes) whose transverse mode indexes are  $(m = 0, n = 0)$ . This is because most of the single-mode fibers only support the Gaussian mode, so only these cavity modes couple to the input and output modes efficiently. The Gaussian mode can be derived from Eq. (5.6), and is given by

$$E^{(q,0,0)}(\vec{r}) = E_0 \frac{w_0}{w(z)} e^{-\frac{r^2}{w(z)^2}} \sin \left( k^{(q,0,0)} z + \frac{k^{(q,0,0)} r^2}{2R(z)} - \phi_G^{(0,0)}(z) + \theta^{(q,0,0)} \right). \quad (5.9)$$

Here,  $\theta^{(q,0,0)}$  is a constant phase shift to match the boundary conditions. The wavenumber for different  $q$  is given by

$$k^{(q,0,0)} = \pi q / L_{\text{cav}} + \arccos(\pm \sqrt{g_1 g_2}) / L_{\text{cav}}. \quad (5.10)$$

For  $R \gg L_{\text{cav}}$  or  $q \gg 1$ , the second term in Eq. (5.10) can be dropped. In this limit, the profile along the z-axis can be approximated as a plane wave. This picture is useful to

understand the single-mode coupling discussed in Sec. 5.4.1.

### 5.3.2 Mechanical Mode

The wave equation for the mechanics is derived from the linearized Navier-Stokes equations with zero viscosity in Eq. (A.14a), represented as

$$\nabla^2 \psi + (\omega^2/v_{\text{He}}^2) \psi = 0, \quad (5.11)$$

where  $\psi$  is the helium density function defined in Eq. (A.14a). This wave equation is equivalent to

$$\nabla^2 \Delta p + (\omega^2/v_{\text{He}}^2) \Delta p = 0, \quad (5.12)$$

where  $\Delta p = p - p_0$  is the pressure fluctuation in the liquid helium. The mechanical wave is also confined by the same two mirrors (via the impedance mismatch between fiber and superfluid helium). So it requires the velocity field (the component perpendicular to the surface) to have nodes at the mirror surfaces because the fiber ends are supposed to be fixed. From Eq. (A.1b), it is easy to obtain that

$$\left. \frac{\partial \tilde{\rho}}{\partial \hat{s}} \right|_{\vec{r}=\text{Boundary}} = 0, \quad (5.13)$$

where  $\hat{s}$  is the unit vector perpendicular to the boundary, and  $\tilde{\rho} = (\rho(\vec{r}) - \rho_0)/\rho_0$  is the normalized change of the density. Therefore, the density fluctuation must have antinodes at the mirror surfaces. Thus, both density waves and optical modes are governed by the same wave function and confined by the same boundary conditions except for a  $\pi/2$  phase shift. The mechanical eigenmode corresponding to the fundamental transverse Gaussian mode is described by

$$\tilde{\rho}^{(q,0,0)}(\vec{r}) = \tilde{\rho}_{\max} \frac{w_0}{w(z)} e^{-\frac{r^2}{w(z)^2}} \cos \left( k^{(q,0,0)} z + \frac{k^{(q,0,0)} r^2}{2R(z)} - \phi_G^{(0,0)}(z) + \theta^{(q,0,0)} \right), \quad (5.14)$$

where  $\tilde{\rho}_{\max}$  is the maximum fractional change in the density. Compared to the wavefunction of the optical mode Eq. (5.9), sin is replaced by cos to compensate for the  $\pi/2$  phase shift on boundary conditions. A general representation of the mode  $(q, m, n)$  is provided in Eq. (5.6).

The effective mass of the mechanical oscillator is defined as Eq. (2.16) to normalize its energy to an oscillator of amplitude  $\tilde{\rho}_{\max}$ :

$$m_{\text{eff}} = \int d^3 \vec{r} \frac{\tilde{\rho}(\vec{r})^2}{\tilde{\rho}_{\max}^2} \rho(\vec{r}) \approx \rho_{\text{He}} \frac{\pi w_0^2 L_{\text{cav}}}{4} \approx 1 \text{ ng}. \quad (5.15)$$

## 5.4 Optomechanical Coupling

An intuitive picture of optomechanical coupling is that, as a dielectric material, helium is attracted to regions of high optical intensity by the electrostrictive force. Therefore, the optical intensity changes the distribution of the superfluid helium density. In turn, the density wave changes the local refractive index and thus changes the propagation speed of the optical mode. This coupling mechanism is named photoelastic coupling.

To obtain the value of the single photon coupling strength  $g_0$ , we need to know the zero-point fluctuation amplitude of the mechanical mode and the change of an optical mode frequency due to this fluctuation.

The dimensionless zero-point density fluctuation  $\tilde{\rho}_0$  is obtained by using Eq. (A.17)

$$\tilde{\rho}_0(\vec{r}) = \sqrt{\frac{\hbar\omega_m}{2\rho_0 v_{He}^2}} \psi(\vec{r}), \quad \text{with } \int_V |\psi(\vec{r})|^2 d^3\vec{r} = 1. \quad (5.16)$$

The change of a mode's optical frequency can be evaluated by using perturbation theory, given by [203, 204]:

$$\delta\omega = -\omega_{cav} \frac{\int_V \delta n_{He}(\vec{r}) |E(\vec{r})|^2 d^3\vec{r}}{\int_V \bar{n}_{He} |E(\vec{r})|^2 d^3\vec{r}}, \quad (5.17)$$

where  $\bar{n}_{He}$  is the average refractive index of the superfluid helium, and  $E(\vec{r})$  is the spatial profile of the optical mode. The refractive index is directly related to the density via the Clausius-Mossotti relation defined in Eq. (A.12)

$$\tilde{\rho} = \frac{\delta\rho}{\rho_0} = \frac{\delta n_{He}}{\bar{n}_{He} - 1}. \quad (5.18)$$

Substituting Eq. (5.18) into Eq. (5.17), we have

$$\delta\omega = -\omega_{cav} \frac{\bar{n}_{He} - 1}{\bar{n}_{He}} \frac{\int_V |E(\vec{r})|^2 \tilde{\rho}(\vec{r}) d^3\vec{r}}{\int_V |E(\vec{r})|^2 d^3\vec{r}}. \quad (5.19)$$

Plugging  $\tilde{\rho}_0$  in Eq. (5.16) into Eq. (5.19), we obtain the single photon coupling strength

$$\begin{aligned} g_0 &= \omega_{cav} \frac{\bar{n}_{He} - 1}{\bar{n}_{He}} \sqrt{\frac{\hbar\omega_m}{2\rho_0 v_{He}^2}} \sqrt{\frac{\int_V |E(\vec{r})|^2 d^3\vec{r}}{(\int_V |E(\vec{r})|^2 d^3\vec{r})^2}} \frac{\int_V |E(\vec{r})|^2 \tilde{\rho}(\vec{r}) d^3\vec{r}}{\sqrt{\int_V |E(\vec{r})|^4 d^3\vec{r}} \sqrt{\int_V |\tilde{\rho}(\vec{r})|^2 d^3\vec{r}}} \\ &= \omega_{cav} \frac{\bar{n}_{He} - 1}{\bar{n}_{He}} \sqrt{\frac{\hbar\omega_m}{2\rho_0 v_{He}^2}} \frac{1}{\sqrt{V_{eff}}} \alpha_{ovlp}, \end{aligned} \quad (5.20)$$

where  $V_{eff} = (\int I dV)^2 / \int I^2 dV$  is the effective mode volume, and  $\alpha_{ovlp} \leq 1$  is the nor-

malized dimensionless overlap function between  $E(\vec{r})$  and  $\tilde{\rho}(\vec{r})$ . The effective mode volume can be approximated by  $V_{\text{eff}} \approx L_{\text{cav}} w_0^2 \pi / 4$ . Notice that, if  $r_i \gg L_{\text{cav}}$ , we have

$$w_0 = \sqrt{\frac{2L_{\text{cav}}}{k^{(q,n,m)}}} \left( \frac{g_1 g_2 (1 - g_1 g_2)}{(g_1 + g_2 - 2g_1 g_2)^2} \right)^{1/4} \approx \sqrt{\frac{2L_{\text{cav}}}{k^{(q,n,m)}}} \left( \frac{L_{\text{cav}}}{r_1} + \frac{L_{\text{cav}}}{r_2} \right)^{-1/4} \quad (5.21)$$

(see Appendix B.2). Therefore, the coupling strength  $g_0$  scales as

$$g_0 \sim \frac{1}{r^{1/4} L_{\text{cav}}^{3/4}}. \quad (5.22)$$

If the entire system is scaled up by a factor  $\alpha_{\text{scale}}$ , then  $g_0 \sim 1/\alpha_{\text{scale}}$ .

Beyond linear coupling, the nonlinear coupling that originates from the nonlinear dispersion relation in Eq. (A.10) describes the coupling between the optical intensity and the mechanical wave intensity. However, its single phonon coupling strength is smaller than the linear coupling strength by a factor of  $10^{10}$ . This mechanism and the second quantization of the linear and nonlinear optomechanical couplings are discussed in detail in Appendix A.5.

### Photothermal Coupling

The discussion above only involves photoelastic coupling via radiation pressure. Though superfluid helium does not absorb light, the mirror substrates and mirror coatings do, and their temperature is coupled to mechanical motion. This effect is called photothermal coupling. There are two mechanisms related to this coupling,

- The thermal expansion of the fiber mirrors due to laser heating,
- Thermal phonons radiated from the hot mirror into the helium result in flows of the superfluid.

This process modifies the dynamic equation Eq. (2.30b) into

$$\dot{\hat{b}} = -i \left( \omega_m \hat{b} + g_0 \hat{a}^\dagger \hat{a} + g_T \delta T \right) - \frac{\gamma_m}{2} \hat{b} + \sqrt{\gamma_m} \hat{b}_{\text{in}}, \quad (5.23)$$

where  $g_T$  is the coupling rate between the mechanical modes and the temperature fluctuations. The change of the temperature  $\delta T$  depends on the intracavity photon number as

$$\dot{\delta T} = g_{\text{ta}} \hat{a}^\dagger \hat{a} - \kappa_{\text{th}} \delta T, \quad (5.24)$$

where  $g_{\text{ta}}$  is the single photon heating rate, and  $\kappa_{\text{th}}$  is the relaxing rate. Together we have the dynamical equation of the mechanical mode

$$\dot{\hat{b}} = - \left( \frac{\gamma_m}{2} + i\omega_m \right) \hat{b} - i(g_0 + g_{\text{pt}}) \hat{a}^\dagger \hat{a} + \sqrt{\gamma_m} \hat{b}_{\text{in}}, \quad (5.25)$$

where  $g_{\text{pt}} = g_T g_{\text{ta}}/\omega_m + i\kappa_{\text{th}}$  is the single-photon photothermal coupling rate. Note that the photothermal coupling is not symmetric, as the equation of motion for the optical mode remains unchanged. The photothermal coupling changes the optomechanical dynamic backactions, but it does not affect the output field spectrum (Eq. (2.61)) [204]. Details of this coupling can be found in Refs. [203, 204].

### 5.4.1 Single-Mode Coupling

One practical hurdle in most optomechanical devices is that any given optical mode couples to multiple mechanical modes, making the readout of such optomechanical systems complicated. This often requires the use of complex filtering systems for extracting the desired information. To overcome this challenge, one possible approach is to meticulously design phononic band gap structures that only allow one mechanical mode in its bandgap. This way, this “defect” mode can be exclusively selected to couple to optical modes [51, 210]. However, this exclusive coupling between one optical mode and one mechanical mode, namely single-mode coupling, is a natural feature in our superfluid helium-filled Fabry-Pérot cavity optomechanical system.

The optical mode of particular interest is the Gaussian mode, described in Eq. (5.9). As demonstrated in Eq. (5.20), the coupling strength is proportional to an overlap integral between the optical mode intensity and the mechanical wave amplitude  $\alpha_{\text{ovlp}}$ , where the optical intensity of the Gaussian mode is given by

$$I^{(q,0,0)} = \frac{E_0^2}{2} \frac{w_0^2}{w(z)^2} e^{-\frac{2r^2}{w(z)^2}} \left( 1 - \cos \left( 2k^{(q,0,0)} z + \frac{2k^{(q,0,0)} r^2}{2R(z)} - 2\phi_G^{(0,0)}(z) + 2\theta^{(q,0,0)} \right) \right). \quad (5.26)$$

#### Plane Wave Approximation

In the case of  $q \gg 1$  and  $r_1, r_2 \gg L_{\text{cav}}$ , the cavity is close to being formed by two flat mirrors. Thus, the mode profile along the z-axis approximates plane waves. The wavenumber for modes of longitudinal index  $2q$  defined in Eq. (B.13) can be approximated as:

$$\begin{aligned} \lim_{q \gg 1, r_1, r_2 \gg L_{\text{cav}}} k^{(2q,n,m)} &= \pi 2q / L_{\text{cav}} + (n + m + 1) \arccos(\pm \sqrt{g_1 g_2}) / L_{\text{cav}} \\ &\approx \pi 2q / L_{\text{cav}} \approx 2k^{(q,n,m)}. \end{aligned} \quad (5.27)$$

The beam radius defined in Eq. (B.15) can be approximated as:

$$\lim_{q \gg 1, r_1, r_2 \gg L_{\text{cav}}} w_0|_{2q} = \sqrt{\frac{2L_{\text{cav}}}{k^{(2q,n,m)}}} \left( \frac{g_1 g_2 (1 - g_1 g_2)}{(g_1 + g_2 - 2g_1 g_2)^2} \right)^{1/4} \approx \frac{w_0|_q}{\sqrt{2}}, \quad (5.28)$$

$$w(z)|_{2q} = \frac{w(z)|_q}{\sqrt{2}}. \quad (5.29)$$

The Guoy phase shift  $\phi_G \approx 0$  and the Rayleigh range  $z_R \gg L_{\text{cav}}$ . Therefore, the optical intensity of mode index  $q$  can be approximated as

$$I^{(q,0,0)} \approx \frac{E_0^2}{2} e^{-\frac{r^2}{(w(z)|_{2q})^2}} \cos \left( k^{(2q,0,0)} z + \frac{k^{(2q,0,0)} r^2}{2R(z)} + \theta^{(2q,0,0)} \right). \quad (5.30)$$

Here, we drop the constant term (*i.e.*, a constant equal to 1) in Eq. (5.26) as this term will vanish in the overlap integral. Under these approximations, the profile of the optical intensity  $I^{(q,0,0)}$  is identical to the mechanical mode profile  $\tilde{\rho}^{(2q,0,0)}$ .

The orthogonality between different eigenmodes results in the following selection rule for the overlap integral

$$\alpha_{\text{ovlp}} = \frac{\int_V I^{(q,0,0)}(\vec{r}) \tilde{\rho}^{(q',m,n)}(\vec{r}) d^3\vec{r}}{\sqrt{\int_V (I^{(q,0,0)}(\vec{r}))^2 d^3\vec{r}} \sqrt{\int_V |\tilde{\rho}^{(q',m,n)}(\vec{r})|^2 d^3\vec{r}}} \propto \delta_{2q,q'} \delta_{0,m} \delta_{0,n}, \quad (5.31)$$

where  $\delta_{i,j}$  is the Kronecker delta function. This means that the optical Gaussian mode of mode index  $(q, 0, 0)$  only couples to the mechanical Gaussian mode of mode index  $(2q, 0, 0)$ , whose wavelengths satisfy  $\lambda_{\text{cav}} = 2\lambda_m$ .

## 5.4.2 Beyond Single-Mode Coupling

Note that this single-mode coupling feature is an approximate result. In this section, I will discuss a few possible mechanisms for the coupling between the optical Gaussian mode  $(q_0, 0, 0)$  and mechanical modes that don't obey the relation Eq. (5.31).

- **Orthogonality:** As discussed in Sec. 5.4.1, only in the case of  $q \gg 1$  and  $r_1, r_2 \gg L_{\text{cav}}$ , does an optical Gaussian mode intensity have approximately the same spatial profile of one of the mechanical eigenmodes. More precisely, the optical intensity profile is not equal to any eigenmode of this Fabry-Pérot cavity (it is the optical field, not the intensity, that is an eigenmode). This always leads to some small but non-zero overlaps with other mechanical modes.

Notably, any optical transverse mode other than the fundamental transverse mode is well-coupled to a set of mechanical modes, as its intensity profile is not close to any eigenmode. Details are shown in Sec. 5.4.3.

- **Hermiticity:** The orthogonality of normal modes is exact only in a truly Hermitian system. Non-Hermiticity due to losses in optical and mechanical modes causes the profile to deviate from the eigenmodes of the Hermitian system. Such states are described by quasi-normal modes [85], whose profiles can be approximated by using perturbation theory. To see this, assume  $|a\rangle$  and  $|b\rangle$  are right quasi-normal modes of a non-Hermitian operator  $\hat{o}$  with eigenvalues  $\lambda_a$  and  $\lambda_b$ , respectively. The overlap between  $|a\rangle$  and  $|b\rangle$  is

$$\langle b|a\rangle = \frac{1}{\lambda_a - \lambda_b^*} \langle b|\hat{o} - \hat{o}^\dagger|a\rangle \neq 0, \quad (5.32)$$

where we use the relation  $\hat{o} \neq \hat{o}^\dagger$ .

The generic lossy wave equation is

$$\left[ \nabla^2 + \frac{\omega^2}{v^2} - \frac{i}{Q} \frac{2\omega^2}{v^2} \right] u(\vec{r}, \omega) = 0, \quad (5.33)$$

where the first two terms are the Hermitian part of the operator, and the last term is the non-Hermitian part with  $Q = \omega/\gamma$  the quality factor.

In a simplified 1-D model, in which we ignore the profile in the transverse plane, the overlap between quasi-normal modes for Eq. (5.33) of indexes  $q$  and  $q'$  ( $q \neq q'$ ) can be expressed as

$$\lim_{|q+q'| \gg |q-q'|} \alpha_{\text{ovlp}} \approx \left| \frac{((-1)^{(q-q'+1)} + 1)}{\pi} \frac{q+q'}{Q} \frac{1}{(q-q')^2} \right|. \quad (5.34)$$

Notice that there is a simple selection rule:  $\alpha_{\text{ovlp}} \neq 0$  if and only if  $q, q'$  have different parities. The overall overlap scales as  $\alpha_{\text{ovp}} \propto 1/(q - q')^2$ .

In general, the overlap between two quasi-normal modes  $|a\rangle = (q, m, n)$  and  $|b\rangle = (q', m', n')$  can be approximated by

$$\langle a|b\rangle \approx \frac{2\gamma}{\omega_{a'} - \omega_{b'}} \langle a'|i|b'\rangle, \quad (5.35)$$

where  $|a'\rangle, |b'\rangle$  and  $\omega_{a'}, \omega_{b'}$  are corresponding normal modes and eigenvalues of  $|a\rangle$  and  $|b\rangle$ . The factor of  $i = \sqrt{-1}$  provides a  $\pi/2$  phase shift and leads to nonzero overlaps between different normal modes. The orthogonality between modes of different transverse indexes is still valid, *i.e.*,  $\langle q, m, n|i|q, m', n'\rangle = 0$ , which can be seen through the point that the paraxial assumption guarantees no transverse momentum in its solution. It is also straightforward to show that this overlap is also

bounded by

$$\langle a|b\rangle \approx \frac{2\gamma}{\omega_{a'} - \omega_{b'}} \langle a'|i|b'\rangle \leq \frac{2}{Q} \frac{\omega}{\Delta\omega}, \quad (5.36)$$

with  $\Delta\omega = \omega_{a'} - \omega_{b'}$ .

The estimation of the overlap  $\alpha_{\text{ovlp}}$  between the profile of the optical intensity  $|a\rangle$  and the mechanical mode profile  $|b\rangle$  (defined Eq. (5.31)) is similar to the discussion above, and is

$$\alpha_{\text{ovlp}} = \langle a|b\rangle \approx (\langle a'| + \delta\langle a'|)(\langle b'| + \delta\langle b'|), \quad (5.37)$$

where  $|a'\rangle$ ,  $|b'\rangle$  are corresponding normal modes, and  $\delta|a'\rangle$ ,  $\delta|b'\rangle$  are corresponding perturbation term. Because  $Q_{\text{opt}} \gg Q_{\text{m}}$  (*i.e.*, optical modes are more Hermitian), the correction of the optical mode intensity can be omitted. Thus, we have

$$\alpha_{\text{ovlp}} \approx \frac{\gamma_{\text{m}}}{\omega_{a'} - \omega_{b'}} \langle a'|i|b'\rangle. \quad (5.38)$$

Here,  $\omega_{b'}$  is the eigenfrequency of the mechanical mode  $|b'\rangle$ , and  $\omega_{a'}$  is the eigenfrequency of the mechanical mode that has a similar profile of the intensity of  $|a'\rangle$ . Compared to Eq. (5.35), a factor of 2 is removed to account for this neglected correction on optical mode.

- **Geometrical Symmetry:** Not all orthogonality relations results solely from Hermiticity. Some of the orthogonality relations are protected by the symmetry of the mode. The geometry of the boundaries in our Fabry-Pérot holds the following spatial symmetries:

- Reflection symmetry along the longitudinal plane, *i.e.*, zx- or zy-plane (black dash-dotted line shown in Fig. 5.3),
- Reflection symmetry along the center transverse plane (purple dashed line shown in Fig. 5.3).

Note that the optical intensity is proportional to the square of its spatial eigenmode. As a result, the profiles of any optical intensity should exhibit even reflection symmetry with respect to the aforementioned geometric reflection planes. On the other hand, the profile of the mechanical mode  $(q, m, n)$  exhibits odd reflection symmetry with respect to one of the geometric reflection planes when the corresponding mode index is odd. Therefore, the overlap coefficient  $\alpha_{\text{ovlp}}$  is zero between the intensity of any given optical mode and any mechanical mode of odd mode indexes. This geometrical symmetry leads to certain selection rules (odd mechanical modes are more

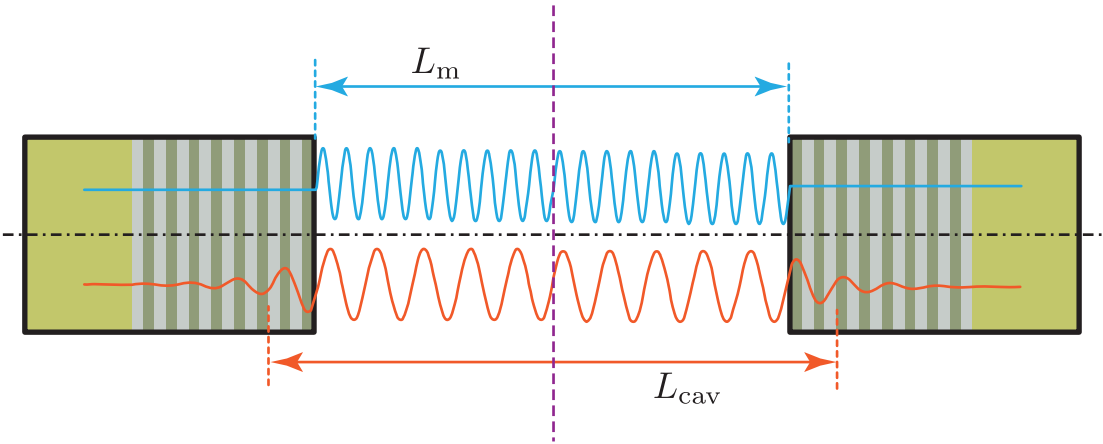


Figure 5.3: A schematic of optical waves (shown in red) and mechanical waves (shown in blue) in the cavity. The alternating green and grey layers represent the optical DBR coatings. The effective cavity length of the optical mode  $L_{\text{cav}}$  is different than the mechanical wave's  $L_m$ . The black dash-dotted line represents the longitudinal reflection symmetric plane, and the purple dashed line represents the transverse reflection symmetric plane in the middle of the cavity.

difficult to be coupled) independent of all of the approximations in the single-mode coupling discussion in Sec. 5.4.1.

- **Boundary:** In Sec. 5.4.1, boundaries of optical and mechanical modes are treated on the exact same surface, *i.e.*, the end faces of the mirrors. However, the mechanisms of defining boundaries for both modes are not exactly the same. For mechanical modes, boundaries are determined by the impedance mismatch between the fiber and liquid helium at the fiber end face. For optical modes, the impedance mismatch (the reflection) is achieved by layers of DBR coatings. The phase of the optical mode on the innermost surfaces may deviate from 0 (node) by a phase  $\theta$ , which is defined as

$$\theta = 2(L_{\text{cav}} - L_m)k_{\text{cav}}. \quad (5.39)$$

A schematic of different boundaries is shown in Fig. 5.3.

In a simplified 1D model, the overlap coefficient  $\alpha_{\text{ovlp}}$  between the intensity of an optical mode  $(q, 0, 0)$  and a mechanical mode  $(q', 0, 0)$  is

$$\lim_{q,q' \gg 1} \alpha_{\text{ovlp}} \approx \left| \frac{2}{(2q - q') - \theta} \sin\left(\frac{\theta}{2}\right) \right|, \quad q' \text{ is even.} \quad (5.40)$$

Notably, each factor contributes a coupling rate with a sign. These signed factors must be

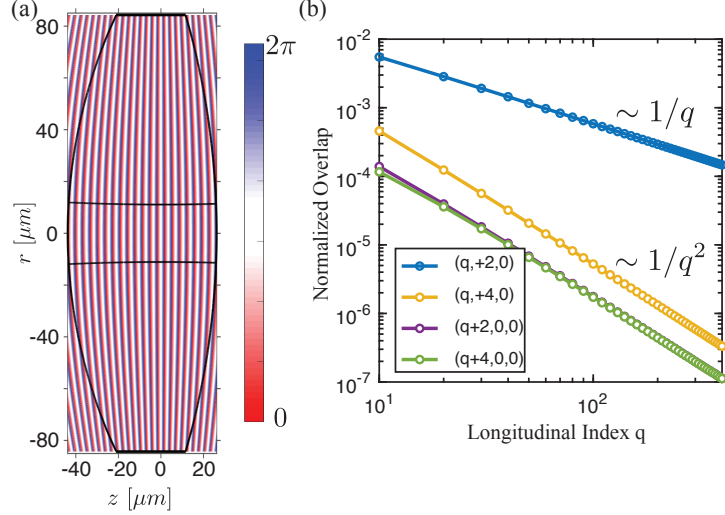


Figure 5.4: (a) The phase plot of the mode  $(20, 0, 0)$ . The phase is indicated by the color-bar on the right. The outer black solid line represents the integral volume in the numerical simulation. The two curved lines are two fiber ends with radii and a separation of the experiment device, given in Sec. 5.2. The inner black line is the beam diameter  $w(z)$ . (b) The plot of normalized overlap integral  $\alpha_{\text{ovlp}}$  between a Hermite Gaussian mode  $(q, 0, 0)$  and a mode given in the legend. For the mode  $(q, +2, 0)$ , the overlap scales as  $1/q$ , and for the rest three modes in the plot, the overlap scales as  $1/q^2$ .

summed together to find the net coupling rate between any given optical Gaussian mode and all other mechanical modes.

### 5.4.3 Numerical Simulation

To evaluate the coupling between an optical mode and a mechanical mode, we numerically calculate the overlap coefficient between different modes without making the approximations described in Sec. 5.4.1. The geometrical boundaries take the measurement results ( $r_1 = 324.5 \mu\text{m}$ ,  $r_2 = 496.7 \mu\text{m}$ ,  $L_{\text{cav}} = 69.7 \mu\text{m}$ ), which are given in Sec. 5.2. We implement the so-called Gauss-Hermite quadrature instead of the general random/uniform nodes to make the integral converge faster. The description of the Gauss-Hermite quadrature can be found in Appendix C. Instead of solving the eigenmodes of this cavity, I used the Hermite-Gaussian modes defined in Eq. (5.6) to approximately describe the eigenstates of this cavity.

We first numerically demonstrate that the Hermite-Gaussian modes shown in Eq. (5.26) are not the exact eigenmodes of a Fabry-Pérot cavity but are approximate descriptions of the eigenmodes under the paraxial approximation with approximated boundaries.

Regarding approximation boundaries, it is straightforward to see this by checking the wavefront geometry of the optical mode described by Eq. (5.9). Its wavefront is not a

dome of a sphere but rather closer to a parabolic shape determined by

$$\frac{r^2}{2R} + z \approx \text{CONST}, \quad (5.41)$$

whose radius of curvature is  $R$ . The larger the longitudinal index  $q$ , the smaller the beam radius  $w$  is, which leads to a smaller deviation from a spherical boundary condition. This deviation is shown in Fig. 5.4(a), where the spherical boundary (curved black lines) does not exactly match the equal phase surface of a Hermite-Gaussian mode for  $r \gtrsim w$ .

The paraxial approximation requires  $k^2 w_0^2 \gg 1$ . For a Hermite-Gaussian mode  $(q, 0, 0)$ , this value scales as  $k^2 w_0^2 \sim q$ . Therefore, the validity of this approximation is better with a larger  $q$ . The deviation of this approximated solution from the exact solution can be expanded as a polynomial function of  $q^{-1}$ . Therefore, the orthogonality, defined by the overlap integral, between different Hermite-Gaussian modes should scale as  $\alpha_{\text{ovlp}} \sim q^{-n}$ . Figure 5.4 shows the overlap integral  $\alpha_{\text{ovlp}}$  between a Hermite-Gaussian mode  $(q, 0, 0)$  and another mode that is given in the legend. The linear fitting in the logarithmic coordinates yields slopes  $k = -0.986(3)$  and  $k = -1.974(5)$  for the upper blue data and the lower data, respectively, which correspond to scaling rule  $\sim 1/q$  and  $\sim 1/q^2$ . For  $q = 182$ , the Hermite-Gaussian mode should be accurate in evaluating  $\alpha_{\text{ovlp}}$  in the order of  $3 \times 10^{-4}$ .

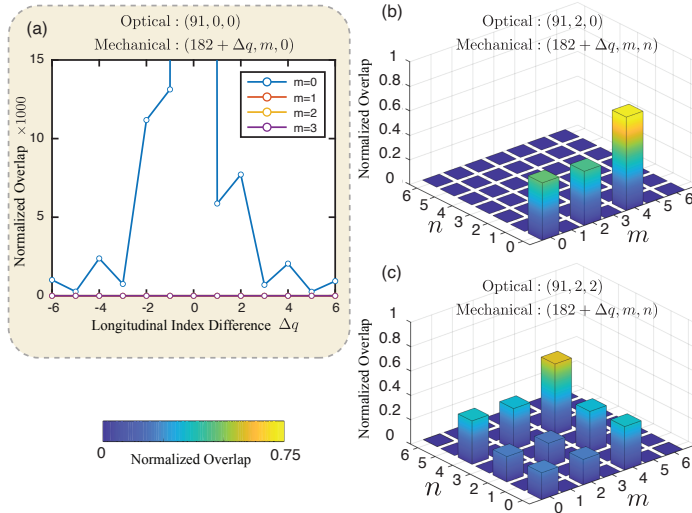


Figure 5.5: (a) The overlap between the intensity of optical mode  $(91, 0, 0)$  and mechanical modes  $(182 + \Delta q, m, 0)$ . The values for modes  $m \neq 0$  are all very close to 0. (b) The normalized overlap between the intensity of optical mode  $(91, 2, 0)$  and mechanical modes  $(182, m, n)$ . (c) The normalized overlap between the intensity of optical mode  $(91, 2, 2)$  and mechanical modes  $(182, m, n)$ .

### 5.4.3.1 Orthogonality

As mentioned in Sec. 5.4.2, the optical intensity of a Gaussian mode  $(q_0, 0, 0)$  has roughly the same spatial profile as a mechanical mode  $(2q_0, 0, 0)$  if  $q_0 \gg 1$  and  $r_1, r_2 \gg L_{\text{cav}}$ . Here, we present the deviation from this approximation by numerically evaluating the overlap between the optical intensity of mode  $(91, 0, 0)$  and mechanical modes  $(182 + \Delta q, m, 0)$ , as shown in Fig. 5.5(a). This overlap has been normalized to the overlap between the optical Gaussian mode  $(91, 0, 0)$  and the mechanical Gaussian mode  $(182, 0, 0)$ , which yields  $\alpha_{\text{ovlp}} = 0.566$ .

Furthermore, we evaluate the overlap between the profile of the optical intensity of mode  $(91, 2, 0)$  (which is not anywhere close to a mechanical mode profile) and the profile of other mechanical modes  $(182, m, n)$ . As shown in Fig. 5.5(b), this optical mode is well coupled to a number of mechanical modes. A similar result for the optical mode  $(91, 2, 2)$  is shown in Fig. 5.5(c).

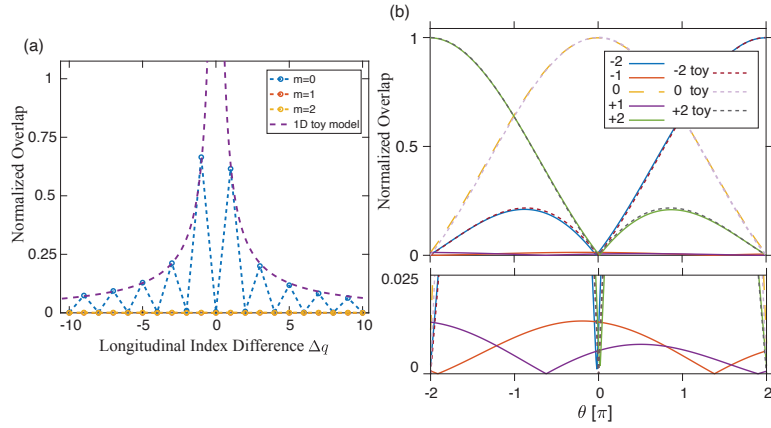


Figure 5.6: (a) The numerical results of the overlap in the first-order perturbation term, *i.e.*,  $\langle a | i | b \rangle$  with  $\langle a |$  being the intensity of optical mode  $(91, 0, 0)$  and  $| b \rangle$  being the mechanical mode  $(182 + \Delta q, m, 0)$ . The purple dashed line represents the result of the 1-D toy model, given in Eq. (5.34). (b) The numerical results of the normalized overlap between the intensity of the optical mode  $(91, 0, 0)$  and the mechanical mode  $(182 + \Delta q, 0, 0)$  ( $\Delta q$  is shown in the legend) for various  $\theta$ . Dashed lines represent the result of the 1-D toy model, given in Eq. (5.40). Bottom: a zoom-in view for Gaussian modes of odd  $q$ . These nonzero values are discussed in Sec. 5.4.3.1.

### 5.4.3.2 Hermiticity

Non-Hermiticity is not captured in the Hermite-Gaussian mode descriptions as they are still a complete orthogonal basis. We deploy the perturbation result in Eq. (5.35) and numerically evaluate the overlap in the perturbative term  $\langle a' | i | b' \rangle$  between the intensity of the optical mode  $(91, 0, 0)$  and the mechanical mode  $(182 + \Delta q, m, 0)$ . Figure 5.6(a)

shows the results of the numerical simulation. They are well captured by the 1-D toy model (purple dashed line) derived in Eq. (5.34). The overlap  $\langle a'|i|b' \rangle$  is further scaled by a factor  $\omega/(Q\Delta\omega)$  to yield  $\alpha_{\text{ovlp}}$  in Eq. (5.38).

#### 5.4.3.3 Boundary Conditions

If the boundary of the optical mode is shifted by a given phase  $\theta$  (defined in Eq. (5.39)), we show that the normalized overlaps between the intensity of the optical mode (91, 0, 0) and the mechanical mode ( $182 + \Delta q, 0, 0$ ) for various  $\theta$  in Fig. 5.6(b). As can be seen, the optical mode mainly couples to the mechanical mode of even longitudinal index  $q$  for all  $\theta$  because of the spatial symmetries of modes (details c.f. Sec. 5.4.2). The results of the 1-D toy model for mechanical Gaussian modes of even indexes  $q$  (given in Eq. (5.40)) are shown in dashed lines, which agree well the numerical result.

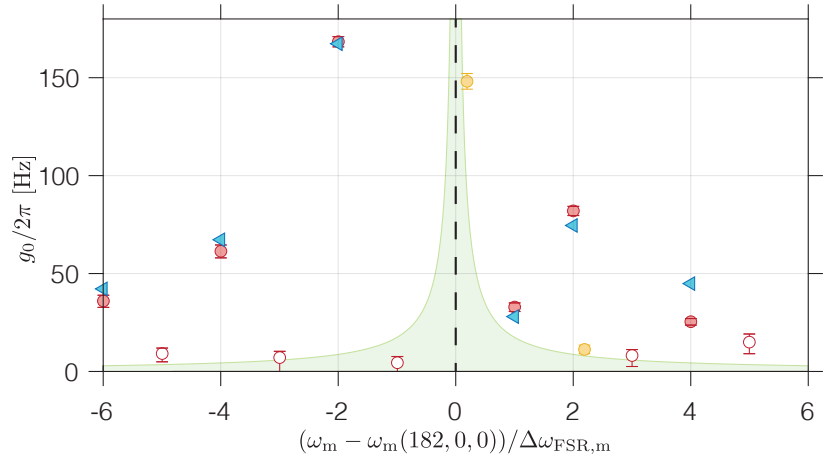


Figure 5.7: All measured coupling rates  $g_0$  between the mechanical mode other than  $(182, 0, 0)$  to the given optical mode  $(91, 0, 0)$ . Red circles represent measured coupling rates for all Gaussian modes (filled circles mean we identify a mechanical mode, and empty circles mean we cannot identify the mode but we used the acquired data to constrain the coupling strength). Yellow circles represent measured coupling rates to transverse Gaussian mode with  $m + n = 1$ . Blue triangles are the numerical simulation results in which the boundary condition  $\theta$  is a free parameter. The best-fit give  $\theta = 0.15(\text{rad})$ . Green shaded area is the allowed coupling rate due to the non-Hermiticity discussed in Sec. 5.4.3.2.

#### 5.4.3.4 Net Effect

Finally, we combine all of these factors and evaluate the coupling rate between the optical mode  $(91, 0, 0)$  and the mechanical mode  $(182 + \Delta q, m, n)$ . We compare these numerical results to the measured coupling rates in Fig. 5.7 (details of the measurement are discussed

in Sec. 6.4). Here, the phase  $\theta$  discussed in Sec. 5.4.3.3 is a fitting parameter to minimize the summed squared error between the results of the numerical model and the measured coupling rates, which gives  $\theta = 0.15\text{ rad}$ .

Overall, this numerical model captures most of the coupling rates accurately. However, we also observed that two mechanical transverse modes ( $m+n=1$ ) coupled to the optical Gaussian mode in the experiment. This is not expected in our numerical model. One possible explanation is that the description of the cavity geometry is not accurate enough. Notice that the mechanical mode (182, 1, 0) is coupled relatively well to this given optical mode. It is close in frequency to the mainly coupled mechanical resonance, which would lead to increase the effect of weak perturbations.

## 5.5 Superfluid Helium in Optomechanics

The existence of a phase transition in helium-4 at  $T_\lambda = 2.17\text{ K}$  was first discovered by Heike Kamerlingh Onnes in 1924 and the remarkable phenomenon of superfluidity was then discovered in 1938 by Pyotr Kapitsa, John F. Allen, and Don Misener. It was later shown that superfluidity was related to the Bose-Einstein condensation of helium-4 atoms at low temperatures.

In Sec. 2.4, we discussed figures of merit for an optomechanical system. Several unique material properties of superfluid helium make it stand out as an ideal material:

**Low Optical Absorption** The remarkable optical properties of superfluid helium arise from its large electronic excitation energy of 19.9 eV [211], zero chemical impurities (as all impurities freeze to a chamber wall of temperature  $T < 100\text{ mK}$ ), and zero structural defects (such as interstitial defects, dislocations, or vacancies) owing to the superfluidity. These factors give rise to an ultra-low optical absorption, which is predicted to be less than  $10^{-12}/\text{mm}$  for 1550 nm light at  $T < 300\text{ mK}$  [211–213]. The low absorption also allows for high circulating photon numbers without significant heating effects. However, light can be absorbed in the mirrors that bound the liquid helium, which could indirectly heat up the system.

**Low Mechanical Loss** The absence of chemical impurities and structural impurities is crucial to achieving ultra-low mechanical loss. In addition, superfluidity is needed to remove the viscous damping that is present in a normal fluid. At temperatures  $T < 600\text{ mK}$ , at which the thermal energy is far below roton excitation energy, the dominant loss mechanism is the three-phonon process, which scales as  $T^4$  [214–216]. The mechanical quality factor ( $Q_m$ ) of superfluid helium sound waves has been experimentally demonstrated to reach up to  $10^8$  [63]. Further details on the mechanical loss mechanism are discussed in Sec. 5.5.1.

**High Thermal Conductivity** Liquid helium also has large thermal conductivity among insulators even at the dilution fridge temperature  $\sim 20\text{ mK}$  (comparable to brass) [217].

**Liquid** In contrast to conventional solid-based optomechanical devices, the mechanical mode frequency of liquids can be tuned over a wide range by pressurization, as demonstrated in [218]. The liquid is also homogeneous and isotropic, eliminating polarization dependence of wave propagation. Since superfluid helium is a fluid with non-trivial dynamical properties, it is also interesting to study unique kinds of excitations, such as quantized vortices [219–222], or second- and third-sound waves [223–225].

Several superfluid-helium-based optomechanical systems have emerged in recent years with different geometries and focusing on different mechanical excitation. [218, 221, 226–229].

The dynamical properties of superfluid helium have been studied thoroughly, and can be well-predicted. In the following two sections, I discuss two relevant aspects of superfluid helium: the mechanical dissipation and the nonlinearity of its mechanical modes.

### 5.5.1 Mechanical Dissipation in Helium

This section provides a brief explanation of the mechanical loss mechanism in superfluid helium. Landau proposed that the normal fluid component can be modeled as a gas consisting of weakly interacting elementary excitations [230–232]. These quasiparticles move through the superfluid component, which serves as their background. Hence at  $T < 600\text{ mK}$ , where rotons are hardly excited, the primary internal loss mechanism for mechanical waves in the superfluid is controlled by three-phonon interactions, namely the Landau-Beliaev process. This process is also discussed in Appendix A.

For a phonon frequency much smaller than the typical thermal phonon frequency, that is,  $\hbar\omega_m \ll k_B T$  [227], a phonon is absorbed by a thermal phonon, resulting in the production of a second thermal phonon, known as the Landau process [214–216]. This process can be characterized by an amplitude attenuation coefficient  $\alpha_{3pp}$ , represented by

$$\alpha_{3pp}(\omega_m) = \frac{\pi^2 k_B^4 (u + 1)^2}{30 \hbar^3 \rho_{He} v_{He}^6} \omega_m T^4 \left( \arctan(\omega_m \tau) - \arctan\left(\frac{3}{2} \gamma_3 \bar{p}^2 \omega_m \tau\right) \right), \quad (5.42)$$

where  $\omega_m$  is the mechanical wave frequency,  $T$  is the temperature,  $\mu = 2.84$  is the Grüneisen constant,  $\tau = \xi T^{-5}$  is the thermal phonon lifetime with  $\xi = -1.11 \times 10^{-7} \text{ s} \cdot \text{K}^5$  and  $\bar{p} = 3k_B T / v_{He}$  is the average thermal phonon momentum. Finally,  $\gamma_3 = -8 \times 10^{47} \text{ kg}^{-2} \text{ m}^{-2} \text{ s}^2$  is the coefficient for the cubic term in the phonon dispersion. Hence, in

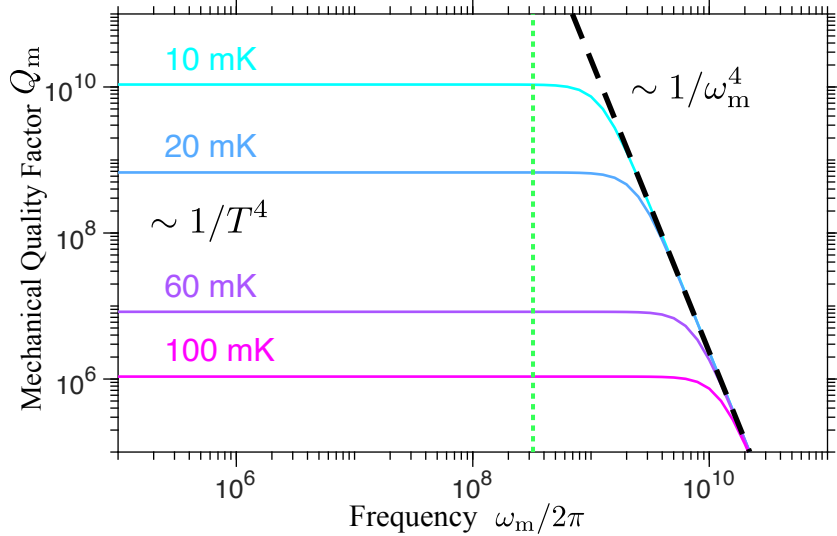


Figure 5.8: Mechanical Quality factor  $Q_m$  of superfluid helium as a function the frequency  $\omega_m/2\pi$  at various temperatures. These values are computed by using the result in Ref. [227]. The black dashed line indicates the Beliaev processes at high frequency ( $\hbar\omega_m \gg k_B T$ ), which scales as  $1/\omega_m^4$ . The green dotted line represents the frequency of the mechanical mode we studied.

the collisionless regime ( $\omega_m\tau \gg 1$ ), the sound attenuation can be reexpressed as

$$\alpha_{3pp}(\omega_m) = \frac{\pi^3 k_B^4 (u+1)^2}{30 \hbar^3 \rho_{He} v_{He}^6} \omega_m T^4, \quad (5.43)$$

which leads to a simple relation between the mechanical quality factor  $Q_m$  and the temperature  $T$ , given by

$$Q_m = \frac{\omega_m}{2v_{He}\alpha_{3pp}} \approx \frac{118}{T^4}. \quad (5.44)$$

This relation has been experimentally demonstrated in various systems [63, 70]. The attenuation for the full range ( $0 \text{ K} < T < 2 \text{ K}$ ) is given in Refs. [216, 233].

At higher frequencies,  $\hbar\omega_m \gg k_B T$ , Beliaev processes, for which a phonon can decay into two phonons, become significant [227, 234]. The damping rate is

$$\lim_{T \rightarrow 0} \Gamma_q^{\text{Bel}} \approx \frac{(u+1)^2}{8\pi} \frac{(k_B T)^5}{\rho_{He} \hbar^4 v_{He}^5} \tilde{\Gamma}_q^{\text{Bel}}(\tilde{q}), \quad (5.45)$$

where  $\tilde{q} = q/q_{\text{th}}$  is the dimensionless wave number normalized by the typical thermal phonon wave number  $q_{\text{th}} \approx k_B T / \hbar v_{He}$ . The functions  $\tilde{\Gamma}_q^{\text{Bel}}$  are universal functions of  $\tilde{q}$

given by [234]

$$\tilde{\Gamma}^{\text{Bel}}(\tilde{q}) = \frac{\tilde{q}^5}{30} - \frac{4\pi^4}{15}\tilde{q} + 48 [\zeta(5) - g_5(e^{-\tilde{q}})] - 24\tilde{q}g_4(e^{-\tilde{q}}) + 4\tilde{q}^2 [\zeta(3) - g_3(e^{-\tilde{q}})], \quad (5.46)$$

where  $g_\alpha$  are the Bose functions and  $\zeta(\alpha)$  are the Riemann zeta functions ( $\zeta(\alpha) = g_\alpha(1)$ ). Therefore in the high frequency limit,  $\tilde{q} \gg 1$ , this damping rate Eq. (5.46) simplifies to

$$\lim_{\omega_m \gg q_{\text{th}}, v_{\text{He}}, T \rightarrow 0} \Gamma^{\text{Bel}}(\omega_m) \approx \frac{(u+1)^2}{8\pi} \frac{(k_B T)^5}{\rho_{\text{He}} \hbar^4 v_{\text{He}}^5} \frac{\tilde{q}^5}{30} = \frac{(u+1)^2}{240\pi} \frac{\hbar}{\rho_{\text{He}}} \left( \frac{\omega_m}{v_{\text{He}}} \right)^5. \quad (5.47)$$

In this limit the mechanical quality factor  $Q_m = \omega_m / \Gamma^{\text{Bel}}$  is independent of the temperature and scales as  $1/\omega_m^4$ .

Figure. 5.8 shows the mechanical quality factor as a function of  $\omega_m$  at various temperatures (10 mK, 20 mK, 60 mK, 100 mK). For the mechanical frequency ( $\sim 315$  MHz) studied in this work, the mechanical quality factor is dominated by the Landau process ( $\sim 1/T^4$ ) at typical dilution fridge temperature ( $> 10$  mK).

### 5.5.2 Mechanical Nonlinearity

The mechanical wave of superfluid helium is represented by the superfluid density  $\rho$  and the velocity  $\mathbf{v}$  (which is taken to be curlless in the absence of vortices). The dynamics of this hydrodynamic wave are governed by the Navier-Stokes equations with zero viscosity [235],

$$\frac{\partial \rho}{\partial t} + \nabla \cdot (\rho \mathbf{v}) = 0, \quad (5.48)$$

$$\frac{\partial}{\partial t}(\rho \mathbf{v}) + \nabla \cdot \overleftrightarrow{T} = 0, \quad (5.49)$$

where the stress tensor  $\overleftrightarrow{T}$  is

$$T_{ij} = p\delta_{ij} + \rho v_i v_j. \quad (5.50)$$

Here  $p$  is the pressure. The intrinsic nonlinearity of these equations and the material nonlinear response (*i.e.*, in the form of  $p(\rho)$ ) together yield higher-order anharmonic effects in the mechanical waves.

We can expand the pressure in terms of the normalized density deviation  $\tilde{\rho} = (\rho -$

$\rho_0)/\rho_0$  as

$$\begin{aligned} p - p_0 &= \left( \rho \frac{\partial p}{\partial \rho} \right) \tilde{\rho} + \frac{1}{2} \left( \rho^2 \frac{\partial^2 p}{\partial \rho^2} \right) \tilde{\rho}^2 + \frac{1}{6} \left( \rho^3 \frac{\partial^3 p}{\partial \rho^3} \right) \tilde{\rho}^3 + \mathcal{O}(\tilde{\rho}^4) \\ &= (\rho_0 v_{\text{He}}^2) \tilde{\rho} + \frac{1}{2} A_2 \tilde{\rho}^2 + \frac{1}{6} A_3 \tilde{\rho}^3 + \mathcal{O}(\tilde{\rho}^4), \end{aligned} \quad (5.51)$$

where  $A_2 = \partial^2 p / \partial \rho^2$  and  $A_3 = \partial^3 p / \partial \rho^3$ . Here, we use the relation  $v_{\text{He}} = \sqrt{\partial p / \partial \rho} = 238 \text{ m/s}$ , and the parameter  $A_2 / (2\rho_0 v_{\text{He}}^2) = 2.84$  is the Gruneisen constant. The dimensionless parameter  $A_3 / (6\rho_0 v_{\text{He}}^2)$  is also of order 1. Defining the dimensionless parameter

$$C \equiv \frac{1}{24} \frac{-10\rho_0 v_{\text{He}}^2 - 2A_2 + A_3}{\rho_0 v_{\text{He}}^2}, \quad (5.52)$$

the shift of the eigenenergy in first-order perturbation theory is (details c.f. Appendix A.4.2)

$$\Delta E_n^{(1)} = \hbar \omega_m \varsigma (6n^2 + 6n + 3), \quad \text{with } \varsigma \approx C \frac{\hbar \omega_m}{4\rho_0 v_{\text{He}}^2} \frac{1}{V_{\text{eff}}}, \quad (5.53)$$

where  $V_{\text{eff}}$  is the mode volume. The first term is the nonlinear correction of the phonon energy. The second term is equivalent to increasing the frequency by a factor of  $6\varsigma$ . The last term is the trivial overall energy shifting.

For the device in this thesis, the mode volume  $V \sim 1 \times 10^{-15} \text{ m}^3$ , the mode frequency  $\omega_m / 2\pi \sim 315 \text{ MHz}$ , and  $\rho_0 v_{\text{He}}^2 \approx 8,213,380 \text{ J} \cdot \text{m}^{-3}$ . The relative perturbation strength  $\varsigma$  is estimated to be  $\varsigma \sim 6 \times 10^{-18}$ . Since the mechanical quality factor is  $10^5$ , to have a noticeable nonlinear effect ( $\Delta E_n > \hbar \gamma_m$ ) would require the mechanical resonator to be driven to  $n_m \approx 7 \times 10^6$ . Quantization of the Navier-Stokes equations and implementation of the perturbation theory to evaluate the nonlinear effect are discussed in Appendix A.

*“Not only is the Universe  
stranger than we think, it is  
stranger than we can think.”*

– Werner Heisenberg

# CHAPTER 6

## Experiment Setup and System Characterization

In this chapter, we elucidate the measurement schemes employed in the experiment. We commence by outlining the experimental protocols and the optical setups. Subsequently, we provide an in-depth discussion of two pivotal components of this experiment: the filter cavity and the superconducting nanowire single photon detector (SNSPD). Furthermore, we measure the optical modes and the mechanical modes of the superfluid-filled cavity, as well as the dynamical backaction that results from the optomechanical coupling. Lastly, we present the measurement results of the thermal state of this optomechanical system, as a proof-of-principle demonstration of the measurement scheme used in this thesis.

### 6.1 Measurement Setups

In the experiments, we have used two optical setups. The basic optical setup described in Sec. 6.1.1 suits both continuous and pulsed optical input schemes. The second optical setup, as described in Sec. 6.1.3, includes an acousto-optic modulator (AOM), which allows for generating an optical beat note to drive the mechanical motion.

#### 6.1.1 Basic Optical Setup

A schematic of the basic optical setup is shown in Fig. 6.1. The basic idea underlying this setup is: Two input lasers (the red shaded area) are stabilized in frequency and intensity (the light pink shaded area), and then are sent into the optomechanical cavity (OMC) in a dilution fridge (the bottom light blue shaded area). The scattered light from the OMC is further filtered by the two cascaded filter cavities (the beige shaded area) to reject the input laser. Finally, the transmitted light is measured by two single-photon detectors (the top light blue shaded area). The light green shaded area covers the optics that are used in locking various frequencies. Details of the optics are discussed in the following.

In this setup, two input lasers<sup>1</sup> are either blue-detuned or red-detuned from the OMC optical resonance frequency  $\omega_{\text{cav}}$  by one mechanical resonance frequency ( $\omega_m$ ). These two lasers are always locked to a tunable laser (TL)<sup>2</sup>. This is accomplished by combining each input laser with the TL (shown in grey shaded areas on the upper left corner of Fig. 6.1) and monitoring the frequency of the resulting beat note on a photodetector (PD)<sup>3</sup>.

Each input laser passes through a narrowband filter cavity<sup>4</sup> ( $\kappa_{\text{NBFC}}/2\pi \approx 30$  MHz) whose resonance frequency is locked by monitoring the intensity of the laser (measured in a PD<sup>5</sup>) after the corresponding narrowband filter cavity. The intensity of each laser is then locked through a variable optical attenuator (VOA)<sup>6</sup> by monitoring the output laser intensity (the feedback signal is generated by a PID module<sup>7</sup>). The optical path for this part is shown in blue or red lines in the light pink shaded area.

Then two lasers are combined via a 50/50 fiber coupler. The polarization and the intensity of the combined beam are controlled before being sent into the OMC. The part of the optical path that is common to the two input beams is shown in orange. A pair of optical shutters<sup>8</sup> (Shutter1 and Shutter2) just before the 50/50 coupler are used to determine whether the blue-detuned laser or the red-detuned laser drives the OMC. They have a response time  $< 60$  ns, and are also implemented to set the desired pulse sequence for pulsed measurements.

Scattered sideband photons that are optically resonant with the OMC exit the cavity and pass through two fiber cascade filter cavities: FC1<sup>9</sup> and FC2<sup>10</sup> with linewidth  $\kappa_{\text{FC1}}/2\pi = 1.21(5)$  MHz and  $\kappa_{\text{FC2}}/2\pi = 1.71(2)$  MHz, respectively. By using Pound–Drever–Hall (PDH) technique, these two filter cavities are independently locked to the TL via their piezo and thermal tunings<sup>11</sup>. A fiber isolator<sup>12</sup> is placed in between the two FCs to avoid forming a cavity between the adjacent end mirrors of the two FCs. The maximal transmission of the two filter cavities are  $\eta_{\text{FC1}} = 40\%$  and  $\eta_{\text{FC2}} = 17\%$ , respectively. This part is highlighted in the beige shaded area in Fig. 6.1.

Finally, photons emitted from the OMC arrive at a pair of superconducting nanowire single-photon detectors (SNSPDs)<sup>13</sup>. Details of SNSPD characterization are discussed in Sec. 6.1.4. We note that the coherence times of the mechanical mode in this thesis

<sup>1</sup>Toptica grating stabilized tunable single-mode diode laser; Model: DLPro.

<sup>2</sup>ID Photonics CoBrite DX1; Model: PPCL200.

<sup>3</sup>Thorlabs photodetector DET 01CFC; Maximum bandwidth 1.2 GHz.

<sup>4</sup>Micron Optics FFPI.

<sup>5</sup>All photodetectors used in our setup are Thorlabs PDA10CS series unless otherwise specified.

<sup>6</sup>Thorlabs electronic variable optical attenuator; Model: V1550A; Max attenuation 30 dB.

<sup>7</sup>Liquid Instruments Moku-Lab; Instrument: PID controller.

<sup>8</sup>BATi's NanonaTM ultra-fast optical switch; Model: FOS 3220.

<sup>9</sup>Micron Optics FFP-SI FF24U7.

<sup>10</sup>Micron Optics FFP-SI FF24U7.

<sup>11</sup>Stanford Research Systems programmable temperature controller PTC10.

<sup>12</sup>Thorlabs fiber isolator; Model: IO-F-1550APC.

<sup>13</sup>Quantum Opus 1550 nm superconducting nanowire single-photon detectors.

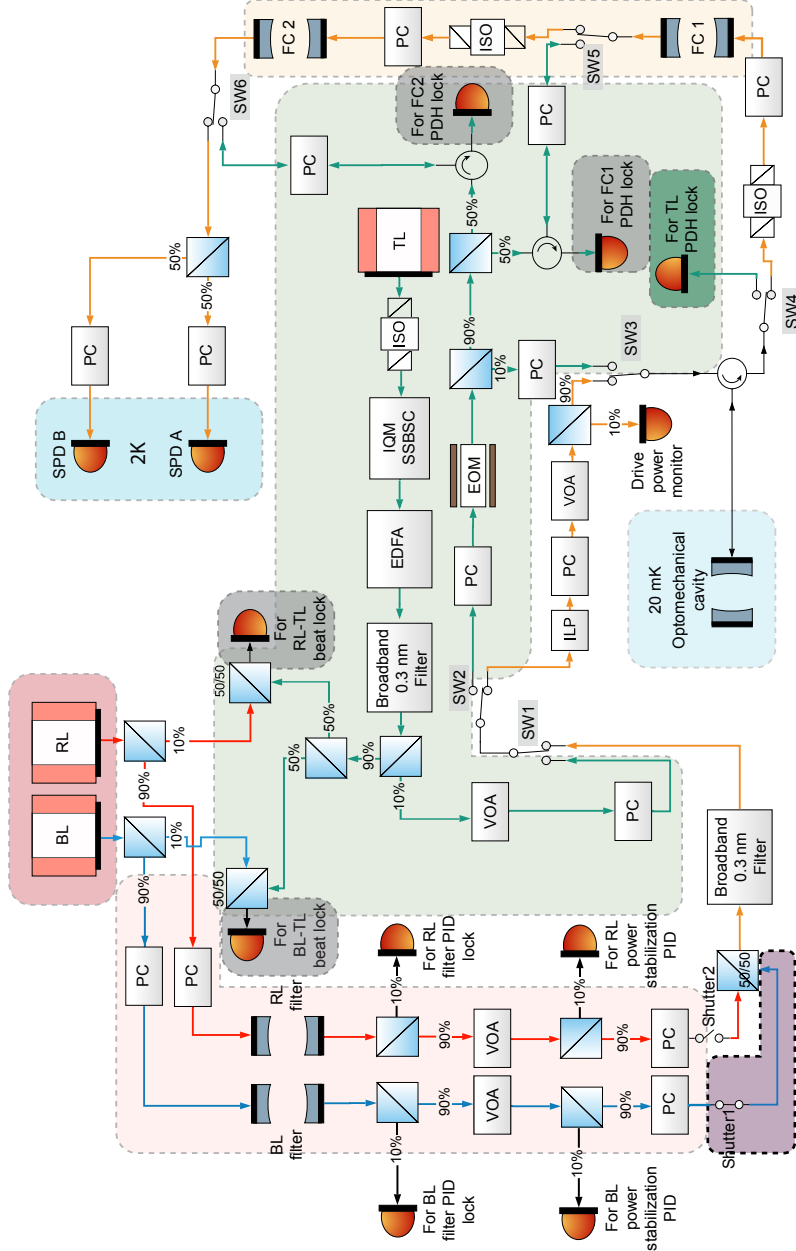


Figure 6.1: This figure shows the schematic of the basic optical setup of the experiment. The setup is switched between the “lock” and “hold” configurations during the experiment, as described in Sec. 6.1.2. The TL is locked to the OMC during the lock configuration. The blue (BL) and red (RL) input lasers are always locked to the TL with a frequency offset  $\sim \pm \omega_m$ . A total of six  $1 \times 2$  MEMS switches are used to switch between the lock configuration (green optical path) and the drive configuration (orange optical path) every 100 ms, such that the optical components are either locked to their desired frequency or free running. PC: polarization controller. VOA: variable optical attenuator. EDFA: erbium-doped fiber amplifier. EOM: electro-optic modulator. ILP: in-line polarizer. ISO: isolator. FC: filter cavity.

	Input coupling efficiency $\eta_{\kappa}$	29%
$\eta_{\text{det}}$	Filter cavity 1 efficiency $\eta_{\text{FC1}}$	40%
	Filter cavity 2 efficiency $\eta_{\text{FC2}}$	17%
	All other efficiency $\eta_{\text{misc}}$	40%
	SNSPD measurement efficiency $\eta_{\text{SNSPD}}$	90%

Table 6.1: Summary of different measurement efficiencies

(10-100  $\mu\text{s}$ ) are much longer than the dead (recovery) time of the SNSPDs ( $< 50 \text{ ns}$ ). Multiple distinguishable scattering events that occur within these coherence times are thus detectable by each of the SNSPDs. The maximal measurement efficiency of the SNSPD is around  $\eta_{\text{SNSPD}} \approx 90\%$ , which is highly polarization sensitive.

Several VOAs are used to adjust the optical power, and the polarization controllers (PCs)<sup>14</sup> are used to align the polarization of light entering polarization-sensitive components such as the FCs, the EOM, and the SNSPDs.

We now describe the frequency-locking optics (the light green shaded area in Fig. 6.1). The TL is used as an optical reference for the entire setup. The TL enters an IQ modulator (IQM)<sup>15</sup> operating in the single-sideband suppressed-carrier mode. The IQM serves as a frequency shifter to lock the TL to the OMC. The output light from the IQM is amplified by an Erbium-doped fiber amplifier (EDFA)<sup>16</sup> and filtered by a broadband ( $\Delta\lambda \approx 0.3 \text{ nm}$ ) filter<sup>17</sup> to suppress the EDFA's amplified spontaneous emission noise. The beam then passes through an electro-optic modulator (EOM)<sup>18</sup>, producing a pair of sidebands used for standard PDH locking. Finally, this beam is sent to the OMC and can be locked to the OMC via the IQM control voltage.

This optical setup can be deployed in either a continuous or pulsed input scheme by programming the control optical shutters (Shutter1,2). The entire optical setup is fiber-based and is covered by black optical curtains. Particularly, the optical fiber, starting from the output of the second filter cavity to the vacuum fiber feedthrough on the cryostat ( $\sim 10 \text{ m}$ ), is wrapped by layers of black tape to shield the room light from leaking into the fiber.

The overall maximal measurement efficiency is given by

$$\eta_{\text{det}} = \eta_{\text{FC1}}\eta_{\text{FC2}}\eta_{\text{SNSPD}}\eta_{\text{misc}} \approx 2.5\%, \quad (6.1)$$

where  $\eta_{\text{misc}}$  includes insertion and connection losses of fibers and all other optics. This efficiency depends on the polarization of the light before filter cavities and SNSPDs and

---

<sup>14</sup>Thorlabs 3-paddle polarization controllers; Model: FPC032.

<sup>15</sup>EOspace QPSK modulator; Model: IQ-ODKS-25.

<sup>16</sup>Thorlabs Erbium-doped fiber amplifier; Model: EDFA100S.

<sup>17</sup>OZ Optics tunable filter; Model: TF-100-11.

<sup>18</sup>EO Space phase modulator; Model: PM-OKS-10.

thus usually drifts down by 10 - 20% in a long measurement ( $>10$  hours).

Other details of the optical setup can be found in Ref. [205].

### 6.1.2 Measurement Scheme

This section describes the timing sequence and the optics settings of two configurations. During the experiment, the setup is alternated between two configurations: the “lock” and the “hold”, each lasting 100 ms. This alternating scheme is applied to avoid the lock laser being mixed up with the signal and heating up the system.

All control signals are triggered by a master transistor-to-transistor logic (TTL) signal so that various instruments are synchronized with precise control of their timing. Specifically, this master TTL is 5 Hz square wave, which is used as the trigger for an FPGA device. The FPGA is programmed to send out trigger/control signals to various instruments upon being triggered by the master TTL. The “hold” configuration corresponds to the high state of the trigger signal in this work.

One type of control signal is a lock-hold (LH) trigger sent to the PID controllers used for locking the FCs and the TL. Other control signals trigger six optical  $1 \times 2$  MEMS switches<sup>19</sup> (SW1-6) to switch the optical path between the two configurations. The control signal for the two optical shutters (Shutter1,2) can be independently programmed for either continuous drive or pulsed drive experiments. The last type of control signal is used to gate the SNSPDs, and is only enabled during the high state of the trigger.

The exact time sequence of each control is shown in Fig. 6.2.

#### “Lock” Configuration

In the “lock” configuration, the six optical switches are switched (SW1-6) from the orange optical path to the green optical path (in the light green shaded area in Fig. 6.1).

The optical resonance of the OMC is slightly drifting for various reasons, such as temperature fluctuation, pressure fluctuations, and cavity length fluctuation. The TL is locked to the OMC in a PDH locking scheme. Part of the TL is sent to the OMC via SW3 and SW4. The PDH error signal is obtained from the reflection off the OMC of a phase-modulated lock tone (the dark green shaded area). This error signal is sent to a PID controller<sup>20</sup> which converts it into a voltage feedback signal to shift the TL frequency via the IQM.

A part of the locked TL is sent into FC1 and FC2 (via SW5 and SW6). They are individually locked to the TL by the similar PDH locking scheme. The corresponding PDH error signals (measured in the PDs shown in the right grey shaded areas in Fig. 6.1) are sent to PID modules<sup>21</sup> to generate feedback signals which drive the piezo of the FCs. This way two FCs are thus indirectly locked to the OMC.

---

<sup>19</sup>Thorlabs  $1 \times 2$  MEMS fiber-optic switches; Model: OSW12-1310-SM.

<sup>20</sup>New Focus PI controller; Model: LB1005.

<sup>21</sup>New Focus PI controller; Model: LB1005.

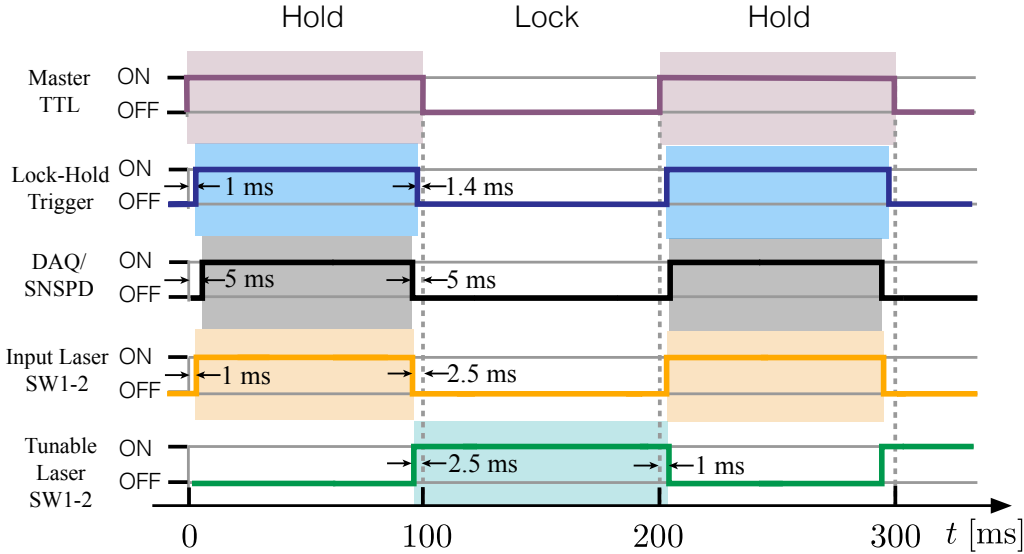


Figure 6.2: The time sequence of switching between the “lock” and the “hold” configurations. Each colored area stands for the “ON” status. Photon counts are only recorded during the central 90 ms of the DAq “ON” status.

Another part of TL is always (in both “lock” and “hold” configurations) combined with the input laser to generate a beat note (measured in the left top grey shaded areas). This beat note is mixed with a local oscillator to generate reference signals, which are further used to generate a frequency-dependent error signal via a frequency-to-voltage (FTV) converter. The error signal is sent to a PID module<sup>22</sup> that generates the feedback signals to the drive laser piezo. This way the input lasers are locked to the TL with a given frequency offset, typically  $\pm\omega_m$ .

The SNSPDs are disabled during the “lock” configuration via the control signal from FPGA.

### “Hold” Configuration

In the “hold” configuration, the six optical switches (SW1-6) are switched back to the orange optical path in Fig. 6.1.

During the “hold” configuration, the feedback signals that are used to lock the TL frequency and the two FC resonance frequencies are held constant. The PID controllers are triggered to stop performing feedback and hold their current states so that the lock is preserved as it was at the end of the “lock” configuration.

SW3-6 are triggered 780  $\mu$ s after SW1-2 are triggered (orange line in Fig. 6.2). This lag ensures that the TL does not enter the SNSPDs.

The two SNSPDs are triggered by the master TTL signal. Each photon’s arrival time is labeled by its relative time with respect to the master TTL trigger. We only use the photon

---

<sup>22</sup>Liquid Instruments Moku-Lab; Instrument: PID controller.

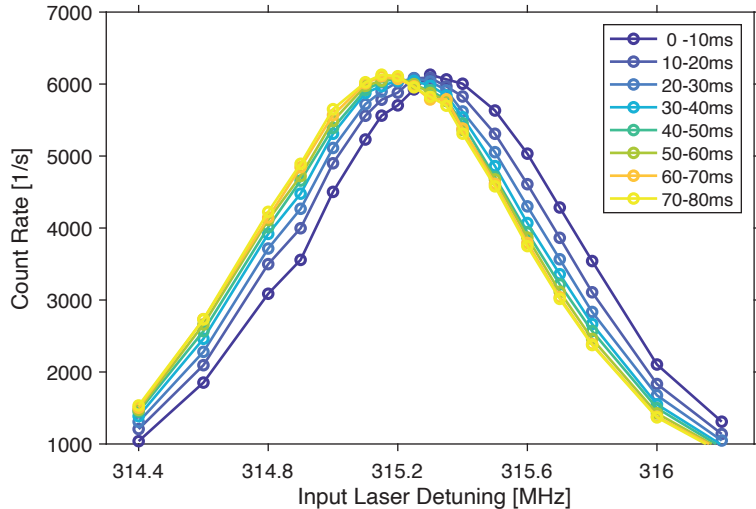


Figure 6.3: The count rate spectrum at different time intervals during the “hold” configuration.

collected during the middle 90 ms of the 100 ms “hold” period. This time period is called data acquisition time (DAq). This helps us get rid of the thermal transient behavior after switching off the TL or the leaked TL laser during the switching time. The detailed time sequence of the “hold” configuration is shown in Fig. 6.2.

The FC resonance frequency drifts away from the TL laser frequency during the “hold” configuration. This can be seen through the scattered count rate spectrum at different time intervals during the “hold” configuration as shown in Fig. 6.3. As given in Eq. (6.11), the count rate depends on the input laser detuning  $\Delta$  from the cavity resonance with respect to the filter cavities resonance frequency. The shifted shape during the “hold” configuration over time indicates a shifted filter cavity resonance frequency. Further details of the “lock” and “hold” schemes can be found in Ref. [205].

### 6.1.3 Second Optical Setup

The second optical setup is obtained by replacing the purple shaded area in Fig. 6.1 with the purple shaded area shown in Fig. 6.4. This optical setup involves utilizing two input lasers with distinct roles: one as the probe laser (PL) and the other as the drive laser (DL).

The probe laser is locked to the TL with a detuning of either  $\omega_m$  or  $-\omega_m$ . The drive laser is red-detuned by  $\Delta = -\omega_m/2$  (locked to the TL) and sent to the additional optics shown in Fig. 6.4. This beam is split into two arms by a 90/10 fiber coupler. The optical intensity in the 10% arm is further adjusted by a VOA, and the remaining 90% of the light is directed to an AOM<sup>23</sup>. The AOM is controlled by an RF signal which is generated in

---

<sup>23</sup>Brimrose IPF-315-30-1550-2FP; Serial No.: 2009-SY-19865.

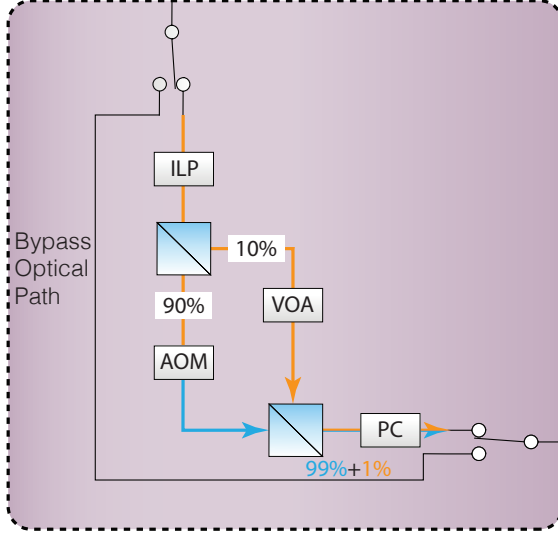


Figure 6.4: The additional optics allow for generating the optical beat note. These optics are inserted in the purple shaded area in Fig. 6.1. If switching to the bypass optical path, the optical setup is identical to the basic optical setup.

a lock-in amplifier (LIA)<sup>24</sup> and then amplified by an amplifier<sup>25</sup>. The two beams are then combined using a 50/50 fiber beam coupler to generate an optical beat note. The maximal transmission efficiency of the VOA is approximately 80%, and the maximum transmission efficiency of the AOM is around 10%. Thus, the net efficiency of each arm is comparable, which allows for achieving the strongest optical beat note. The polarization of the optical beat note is further controlled by a PC.

Furthermore, an additional bypass optical fiber is incorporated into this setup, which allows the drive laser to bypass all amplitude modulation components. In this case, the setup is identical to the basic optical setup elucidated in Sec. 6.1.1.

The measurement scheme alternates between the “lock” configuration and the “hold” configuration in the same way as described in Sec. 6.1.2.

#### 6.1.3.1 AOM Characterization

The AOM is the most crucial component in generating the optical beat note. This AOM is customized for 1550 nm with an expected peaking frequency at 315.0 MHz, which has a designed insertion loss of 3.9 dB and maximum allowed RF drive power of 1.25 W (31.0 dBm). In the following, I present the characterization results of the AOM.

- **Frequency Response:** We measured the optical output power after the AOM at various RF drive frequencies. For each measurement, the power is maximized by

---

<sup>24</sup>Zurich UHFLI lock-in amplifier.

<sup>25</sup>Mini Circuit ZHL-2-8-S; 34 dB Gain.

optimizing the input laser polarization. In all measurements, the RF power is fixed at 25.7 dBm and the optical input power is fixed at 36.1  $\mu$ W.

As shown in Fig. 6.5(a), this response is fit to a Gaussian shape, which gives a center frequency 314.2(1) MHz and a FWHW 27.6(2) MHz. The fit has a sum of squares due to errors (SSE) of 0.00102, indicating the good Gaussianity of the frequency response. The peak efficiency  $P_{\text{out}}/P_{\text{in}} \approx 6.5\%$  at this RF power.

- **Power Response:** We also measured the optical output power after the AOM at various RF drive powers. The drive frequency is set at 314.2 MHz, and the RF input power is varied from -4.3 dBm to 28.3 dBm. Within this RF input power range, the efficiency is linear with the RF drive power, as shown in Fig. 6.5(b). The extrapolated converting efficiency at 31.0 dBm (the maximal allowed RF power) is 20.8%, *i.e.*, an insertion loss of 6.8 dB.
- **Thermal Transient:** In practice, besides the electro response, the quartz crystal is slowly heated by the RF input, which also influences its efficiency. We measured the time response of the optical output power to a pulsed RF drive, as shown in Fig. 6.5(c). Fitting to an exponentially decaying function ( $I(t) = a + b \times \exp(-t/\tau_{\text{AOM,th}})$ ) yields the thermal transient time  $\tau_{\text{AOM,th}} = 0.612 \pm 0.015$  s and a transient amplitude  $b/a = 2.5\%$ . We also mimic the experiment operating scheme by alternating between the “lock” and “hold” configurations for each 100 ms. In this case, the thermal transient amplitude is around 0.66% compared to the stabilized intensity.

#### 6.1.4 Single-Photon Detector

The single-photon detector plays a pivotal role in this experiment beyond a highly sensitive sensor. It can reveal the discrete nature of light and further facilitates the construction of photon counting distributions and photon statistics.

The type of single-photon detector we used in the experiment is the superconducting nanowire single-photon detector (SNSPD). SNSPDs offer a number of advantages over conventional photon detectors, including high detection efficiency ( $\geq 80\%$ ), low dark photon count rate ( $< 100$  Hz), high time resolution ( $< 100$  ps), short recovery time ( $< 50$  ns), and large maximum count rate ( $> 1$  MHz) [236]. They are characterized by their broadband detection capability (with a FWHM of approximately 200 nm). They can be engineered for detecting single photons across a wide range of wavelengths, spanning from visible to near-infrared and beyond, making them well-suited for diverse applications, including quantum communication and quantum computing. In addition to their spectral versatility, SNSPDs are also advantageous due to their compact size, which allows for integration into complex systems. SNSPDs can be coupled to fibers, which can be easily integrated

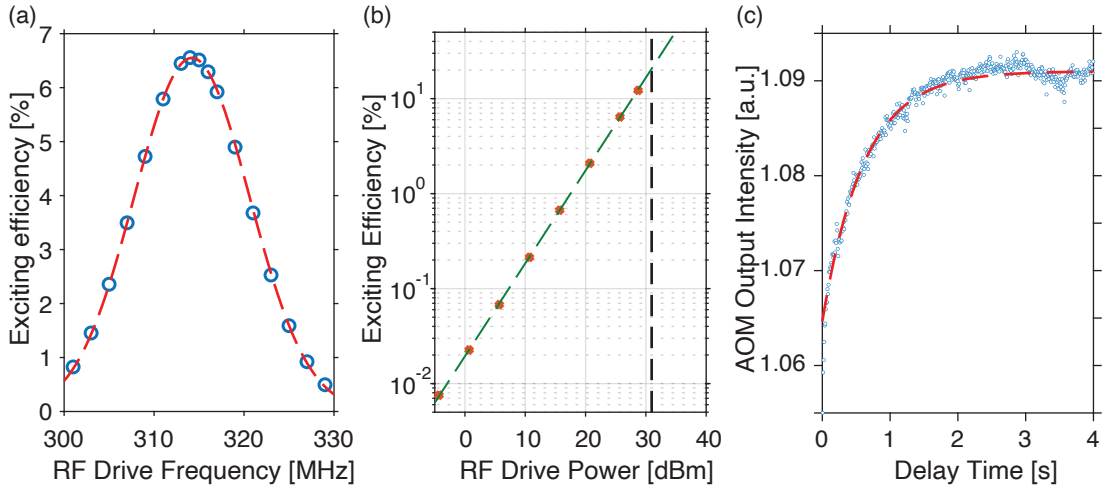


Figure 6.5: Characterization Results of the AOM. (a) The exciting efficiency of the AOM as a function of the RF drive frequency. Blue solid circles represent measured results. The red dashed line is a fit to a Gaussian function. (b) The exciting efficiency of the AOM as a function of the RF drive power. The green dashed line is a linear fit. The black dashed represents the maximal allowed RF power. (c) The AOM optical output power as a function of the time right after turning on the RF drive. The red dashed line is the fit to an exponentially saturating line, as described in the thermal transient measurement.

into practical, closed-cycle cryostat systems, expanding the range of applications for these detectors.

Some recent progress in developing SNSPDs has pushed the dark photon count rate down to sub-Hz, maximum count rate up to 10 MHz, and maximum efficiency up to >90%. Moreover, polarization-insensitive SNSPDs [237–239] and number-resolved SNSPDs [240, 241] are becoming commercially available<sup>26</sup>. As next-generation SNSPDs become accessible, the significance of these detectors is anticipated to further escalate in the fields of quantum information and quantum computing.

The SNSPD is composed of a meandering thin (100 nm) nanowire patterned from a thin film of superconducting material using electron-beam lithography (EBL). This pattern expands the receiving surface area of SNSPDs, enabling it to collect almost the entire optical output while providing a single pathway for the electric signal. The detectors are operated at cryogenic temperatures (1.5 K-4.0 K) and are biased with a constant current that is below the critical current of the superconductor. Due to the nanoscale cross-section, the SNSPD exhibits exceptionally high sensitivity, capable of detecting a single photon upon absorption. Moreover, the superconducting material used in the SNSPD is carefully chosen with fast photoresponsive properties. When a single photon is absorbed by the nanowire, the local superconductivity is temporarily disrupted (*i.e.*, the wire becomes re-

<sup>26</sup>Such as IDQ (<https://www.idquantique.com>)

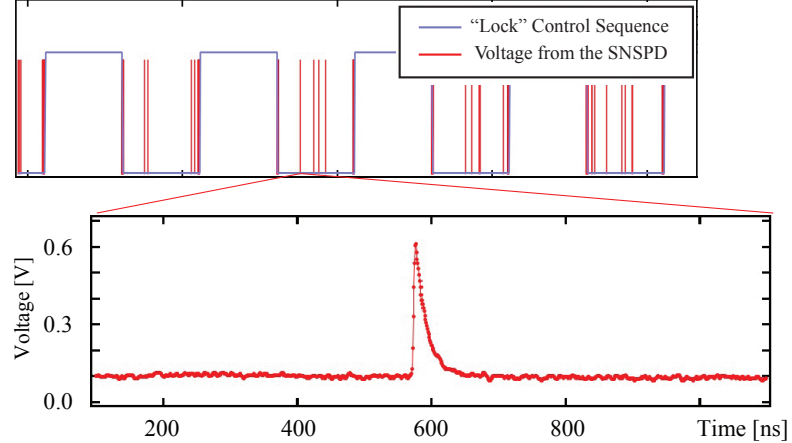


Figure 6.6: The measured voltage from the SNSPD. The blue solid line represents the control signal of the “lock” configuration. The red solid line is the measured voltage from the SNSPD. Bottom: a zoom-in plot of one of the photon arrival events. The sharp edge on the left is used to record the arrival time.

sistive), generating a voltage pulse. The edge of the voltage pulse determines the time resolution of the SNSPD. The superconductivity in the nanowire quickly recovers after the absorption by passive cooling, allowing the SNSPD to be ready for the next photon detection event. Therefore, the recovery time of the SNSPD relies on this cooling process, which constrains the maximum counting rate. Finally, the pulse signal is amplified by an electronic amplifier and the arrival time of the photon is recorded by digital time-tagging electronics.

The two SNSPDs<sup>27</sup> used in this thesis are from Quantum Opus (denoted as SNSPD1 and SNSPD2, respectively). They are designed to detect 1550 nm photons. Both SNSPDs are mounted on the 1 K plate of the dilution fridge at temperatures ranging from 1.7 K to 2.0 K. The input fiber is connected to a bare 1550 nm single-mode optical fiber, which is sent into the vacuum chamber of the cryostat via a vacuum fiber feedthrough and is connected to one of the two SNSPDs. The output electric cable is microwave-shielded and is sent out from the cryostat via a vacuum electrical feedthrough.

The electrical signal from the SNSPD is amplified by low-noise electronic amplifiers<sup>28</sup>. We found that properly grounding the output RF cables (by multi-layers of folded, compressed aluminum foils surrounding the vacuum electrical feedthrough) is crucial to lowering the dark photon count rates. The cable is not wound in loops to avoid receiving unwanted microwave signals. Figure 6.6 shows the measured voltage from the SNSPD after amplification. The photon absorption triggers a  $\sim 0.5$  V voltage pulse with a very sharp rising edge. It is followed by a  $\sim 20$  ns relaxing time. This electrical signal is then

<sup>27</sup>Quantum Opus, 1550 nm superconducting nanowire single-photon detectors.

<sup>28</sup>QO-SIM module, Quantum Opus

sent to a digital time tagger<sup>29</sup> which has two independent input channels. The rising edge that is greater than the threshold voltage (typically 150 mV) triggers a photon arrival event, whose arrival time with respect to the TTL trigger signal is recorded. Each channel has a 250 ps resolution and a 25 ns dead time.

The detection efficiency depends on the photon polarization, with a maximum  $\approx 90\%$ . Its maximum count rate is around 2 MHz.

#### 6.1.4.1 False Counts

Not every count registered by the SNSPDs corresponds to the detection of a photon. Here we consider three types of false counts: (i) afterpulses, (ii) rapid bursts of counts in a short duration (10 - 100  $\mu$ s), and (iii) dark counts. This section also describes the filtering protocols which is used to prevent false counts of types (i) and (ii) from compromising the coherence measurements. False counts of type (iii) cannot be identified or filtered, given that they occur at random times and are uniformly distributed in time; however, their effect on measured coherences can be accounted for, as is detailed in the following. This section also includes the measurement results of the effect of the bias currents on these false counts.

**Afterpulses** It is known that reflection of the voltage pulses generated by SNSPDs can cause false counts [242–244]. Following a detection event at time  $t = 0$ , an afterpulse can occur at a delay  $\tau_{ap}$  set by the time it takes for the voltage reflection to reach the SNSPD.

The signature of afterpulses is illustrated in Fig. 6.7(a). It shows the second-order coherence  $g^{(2)}(\tau)$  of a power-stabilized laser, measured with a bin size of 2 ns. The peak at delay  $\tau_{ap} \approx 24$  ns is caused by the afterpulses. For  $\tau > 50$  ns,  $g^{(2)}(\tau) \approx 1$ , as expected for laser light.

To reduce the impact of these afterpulses in the experiments described here, any count that is registered within 100 ns of a preceding count (on a given SNSPD) is tagged as an afterpulse and discarded. This also removes any true counts that occur within 100 ns of each other; however, the error that this step introduces in coherence measurements is to effectively shorten the bin at the smallest delay by 100 ns. This can easily be compensated for since the shortest delays used in this work are  $\tau \geq \mu$ s.

**Rapid Bursts** There occur rare instances ( $< 0.01\%$  of most 90 ms DAq configuration intervals, c.f. Sec. 6.1.2) in which the SNSPDs register a periodic train of counts with an abnormally high rate ( $\gtrsim 10^3 \times$  expected count rate) for a short duration (10 – 100  $\mu$ s). It is not clear whether these false counts are associated with the SNSPD or not. Indeed, we observed less rapid bursts of counts when we entirely

---

<sup>29</sup>PicoQuant, TimeHarp260 PICO model

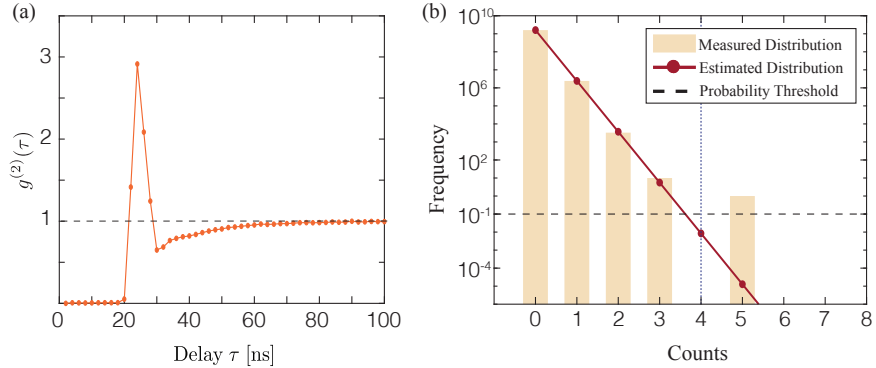


Figure 6.7: Characterization of two types of false counts. (a) Afterpulses in the SNSPDs. The second-order coherence of a coherent laser shows a sharp feature in the first 50 ns due to the afterpulsing effect. The flat region before 20 ns is the deadtime of the SNSPDs. For delays  $\tau > 30$  ns,  $g^{(2)}(\tau)$  gradually approach 1 as expected for a coherent state. (b) Distribution of counts. Number of intervals as a function counts measured in the interval. We binned data into 3  $\mu\text{s}$  intervals. The beige bars are the histogram of counts in the intervals. The red solid line is the estimated distribution of counts in the narrow interval limit (*i.e.*,  $\Delta t \ll \tau_c$ , where  $\tau_c$  is the coherence time). The black dashed line is the threshold (corresponds to a count threshold  $k_{\text{thr}}$ ) that we choose to filter unlikely events  $k > k_{\text{thr}}$ . In this data, one interval with 5 counts is rejected by this protocol.

blocked the input light. While the underlying cause of these spurious counts is unknown, such events can be identified as outliers and discarded. This is done using a statistical model that tags events with an extremely low probability of occurring, as described below.

Suppose the mean count rate during an experiment is measured to be  $I$ . The average number of counts received in a time interval  $\Delta t$  is thus  $\lambda = I\Delta t$ . The probability of receiving  $k$  photons in this interval can be estimated using a  $P(k, \lambda)$  statistical model. Thus, for a total DAq time  $T$ , among the  $N = T/\Delta t$  number of  $\Delta t$ -intervals, the mean number of intervals in which  $k$  counts are recorded is expected to be  $N \times P(k, \lambda)$ . To reject outliers, we set a threshold  $\epsilon \ll 1$  and search for all  $\Delta t$ -intervals that receive  $\geq k_{\text{thr}}$  counts, where  $k_{\text{thr}}$  is the smallest value of  $k$  for which  $N \times P(k_{\text{thr}}, \lambda) < \epsilon$ . For each  $\Delta t$ -interval that is identified as an outlier in this way, we discard the entire 90 ms DAq record containing this interval.

For instance, figure 6.7(b) illustrates this protocol. It shows the experimentally measured frequency with which  $k$ -counts were detected in  $\Delta t = 3 \mu\text{s}$  intervals for  $T \approx 4800$  s ( $N \sim 1.6 \times 10^9$ ) and  $I \approx 2500$  counts/s ( $\lambda \sim 1.51 \times 10^{-3}$ ). The red solid line represents the statistical model  $P(k, \lambda)$  (see below). For  $k \geq 4$ ,  $N \times P(k, \lambda) < 0.1$ , so that  $k_{\text{thr}} = 4$ . As such, the 90 ms DAq intervals that included any  $\Delta t = 3 \mu\text{s}$  intervals that registered  $\geq 4$  counts were discarded from the dataset.

In this instance, 1 out of 53421 DAq intervals was discarded.

The best apriori statistical guess for  $P(k, \lambda)$  depends on the choice of  $\Delta t$ , the measured count rate  $I$ , and the coherence timescale  $\tau_c$  of the photon source. For  $\Delta t \gg \tau_c$  and  $I^{-1} \ll \tau_c$ , the photons detected within the interval  $\Delta t$  can be approximated as uncorrelated, and we model  $P(k, \lambda)$  as a Poissonian,  $\text{Pois}(k, \lambda) = \lambda^k e^{-\lambda} / k!$  [132]. However, if  $\Delta t \lesssim \tau_c$  or  $I^{-1} \gtrsim \tau_c$ ,  $P(k, \lambda)$  is best modeled by accounting for the coherence of the source. For a thermal state,  $P(k, \lambda)$  is well modeled by  $P_{\text{th}}(k, \lambda) = \lambda^k / (1 + \lambda)^{k+1}$  for  $\Delta t \ll \tau_c$ . For  $\Delta t \sim \tau_c$ ,  $P(k, \lambda)$  can be estimated to be between these two limiting cases of  $\Delta t \gg \tau_c$  and  $\Delta t \ll \tau_c$ . To avoid making an apriori guess for  $\tau_c$ , we chose to model  $P(k, \lambda)$  with  $P_{\text{th}}(k, \lambda)$  for all  $\Delta t$ . This achieves a more conservative filtering of the data as it allows for more frequent occurrences of a higher number of counts within any  $\Delta t$ -interval ( $P_{\text{th}}(k, \lambda) > P(k, \lambda)$  for  $k > 2, \lambda < 1$ ).

**Dark Photons** Dark photons refer to false counts without receiving any photons. We found that these false counts are random and independent. Therefore their photon count distribution follows the Poissonian distribution as discussed in Sec. 3.1.3.1 and the second-order coherence function  $g^{(2)}(\tau) = 1$ . Dark photons cannot be identified or filtered. However, we can characterize the dark photon count rate and remove their effects in the measured coherences. This is a sort of background subtraction treatment and inevitably harms the statistical confidence of the result. Details of this subtraction are discussed in Sec. 8.4.3.

#### 6.1.4.2 Bias Current

As you can expect, the bias current would significantly influence the dark photon count rate and measurement efficiency. In the measurements, the voltage threshold is fixed at 150 mV. We measured dark photon count rates and signal photon count rates at different bias currents. This is achieved by blocking the fiber input via a fiber terminator and by directly sending a laser beam of fixed power to SNSPDs. As shown in Fig. 6.8, both the measurement efficiency and the dark count rate increase with the bias current for both SNSPDs. The sharper slope in the dark count rates indicates that the dark count ratio to the total count rate also increases with the bias current.

The bias current also influences the first two types of false counts: afterpulses and rapid bursts of counts (described in Sec. 6.1.4.1). To characterize these effects, we fixed the temperature of the SNSPD and sent a power-stabilized laser into the SNSPD at various bias currents with a fixed voltage threshold (150 mV).

Figure 6.9 shows the measurement results of SNSPD2. From the top row, we can see the afterpulsing effect is getting more significant with an increasing bias current. These afterpulsing counts can be removed based on the protocol described in Sec. 6.1.4.1. We

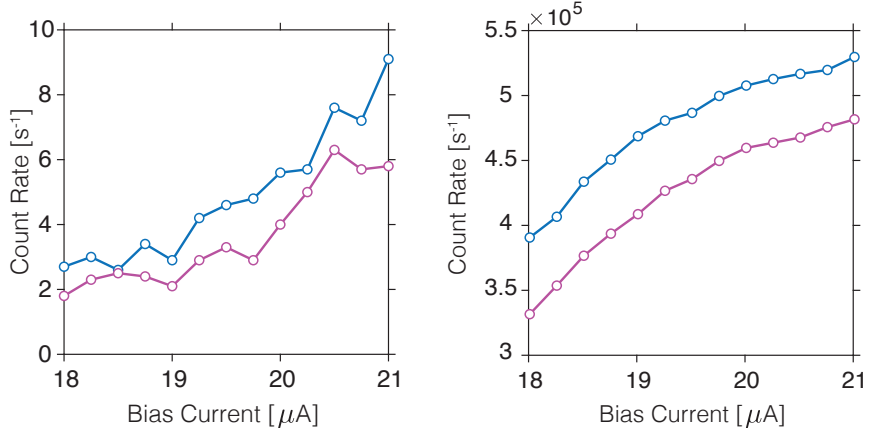


Figure 6.8: Characterization of the performance of the SNSPDs at different bias currents. Left: dark count rates at various bias currents. Right: signal count rates at various bias currents. Blue and purple circles represent the measured results of SNSPD1 and SNSPD2, respectively.

also show the second-order coherence from 100 ns to 4  $\mu$ s in the middle row to see their residual effects in the measured coherence. Clearly,  $g^{(2)}(\tau)$  at 22  $\mu$ A bias current has a long residual tail which lasts for more than 4  $\mu$ s. Rapid bursts of counts are shown in the bottom row. For an increasing bias current, there are more unexpected high-count events. Especially at 22  $\mu$ A bias current, a bunch of unexpected events appear in the measurement. This is because when the bias current is close to the critical current (in this case 22  $\mu$ A), the superconducting nanowire is unstable and vulnerable to any environmental turbulence, and hence triggers unwanted false counts.

To balance the dark photon count rate, the detection efficiency and the false count rates, in most experiments the bias currents of SNSPD1 and SNSPD2 are chosen at 19.0  $\mu$ A and 19.8  $\mu$ A, respectively, unless otherwise specified.

## 6.2 System Characterization

In this section, we present the experimental characterization of the resonance frequencies and linewidths of the optical modes and the mechanical modes.

### 6.2.1 Optical Resonance

In the experiment, we determine the optical resonance by sweeping the laser frequency across the cavity resonance, which is achieved by modulating the IQM with a 5 Hz triangular signal. By measuring the reflectivity of the optical cavity (filled with liquid helium), we can identify the optical resonance and further extract the corresponding linewidth  $\kappa$  and input coupling efficiency  $\eta_\kappa$ .

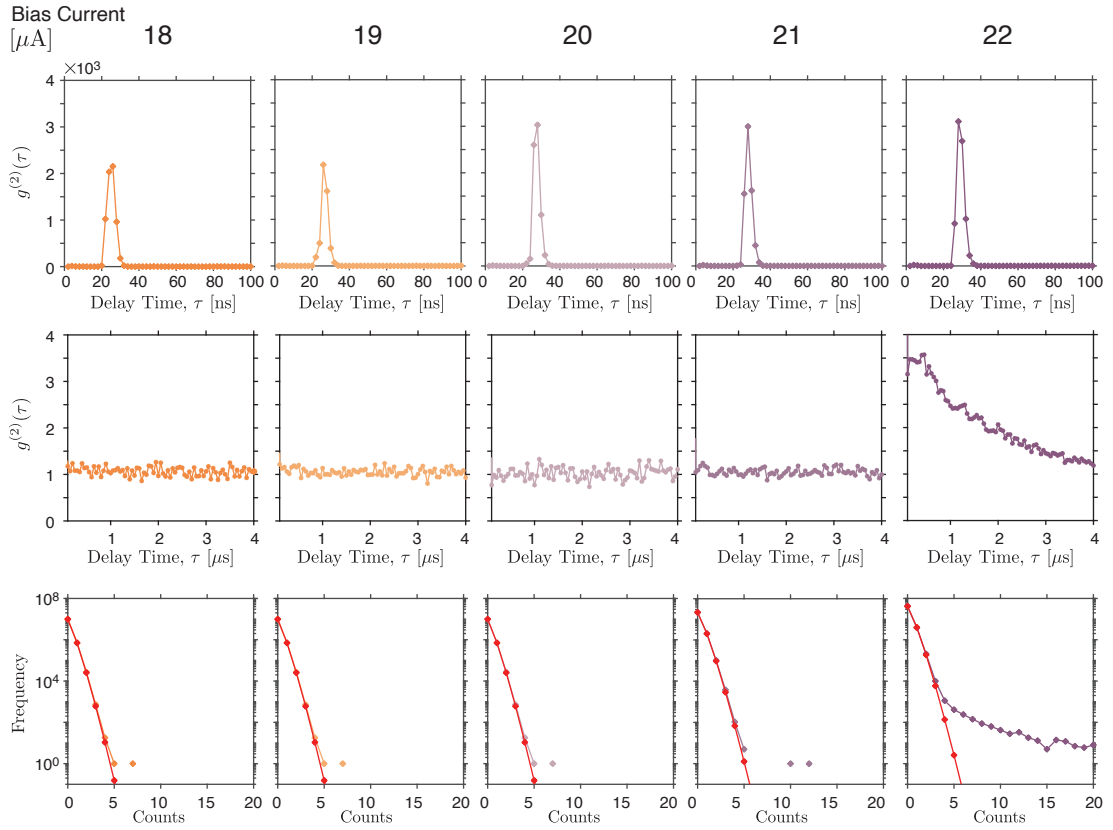


Figure 6.9: False counts at different bias currents. From left to right are the measurement results of SNSPD2 at bias currents ranging from  $18 \mu\text{A}$  to  $22 \mu\text{A}$ . Top row: measured  $g^{(2)}(\tau)$  for various bias currents. Each spike is the result of the afterpulsing effect. Middle row:  $g^{(2)}(\tau)$  for a longer delay time. Bottom row: the count distributions at various bias currents. The red dots represent the expected Poisson distribution for light in a coherent state.

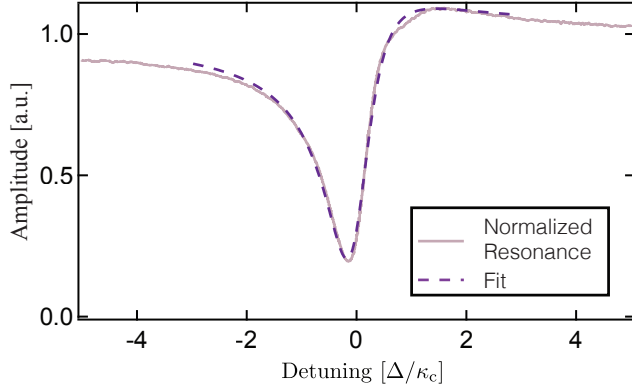


Figure 6.10: The measured normalized optical intensity as a function of the relative detuning. The dark purple dashed line represents the fit to extract the linewidth and the input coupling efficiency.

Figure 6.10 shows the measured reflected optical intensity across the optical mode we are particularly interested in. We fit this data to a reflection of an optical cavity with an asymmetric Fano background, which is given by

$$R_{\text{Fano}}[\Delta] = 1 - \frac{\eta_\kappa [(\cos \phi + 2 \sin \phi (\Delta/\kappa)) - \eta_\kappa] \kappa}{(\kappa/2)^2 + \Delta^2}, \quad (6.2)$$

where  $\phi$  is a fitting parameter to account for the asymmetric Fano shape. The best fit (the purple dashed line) yields  $\kappa/2\pi = 47.2(5)$  MHz and  $\eta_\kappa = 0.29$ .

As described in Sec. 5.3.1, the optical mode eigenfrequency of mode  $(q, m, n)$  is

$$\omega_{\text{cav}}(q, m, n) \approx \left( q + (m + n + 1) \frac{\cos^{-1}(\sqrt{g_1 g_2})}{\pi} \right) \Delta\omega_{\text{FSR,cav}}. \quad (6.3)$$

All the Gaussian modes are evenly separated by  $\Delta\omega_{\text{FSR,cav}}$  and for a given longitudinal mode index  $q$ , its corresponding transverse modes are evenly separated by

$$\delta\omega_{\text{Trans,cav}} = (\cos^{-1}(\sqrt{g_1 g_2})/\pi) \Delta\omega_{\text{FSR,cav}}.$$

A wider frequency sweep determines a number of distinct optical modes, as shown in Fig. 6.11. The fit to Eq. 6.3 gives  $\Delta\omega_{\text{FSR,filledcav}}/2\pi = 2.087(3)$  THz and the splitting between transverse modes  $\delta\omega_{\text{Trans,filledcav}}/2\pi = 0.3971(1)$  THz. Thus, the ratio between these two is  $\cos^{-1}(\sqrt{g_1 g_2})/\pi = 0.1903(3)$ .

The optical spectrum of an empty cavity has  $\Delta\omega_{\text{FSR,emptycav}}/2\pi = 2.1496(4)$  THz, the transverse mode splitting  $\delta\omega_{\text{Trans,emptycav}}/2\pi = 0.4088(6)$  THz, and the ratio between these two 0.1902(3). Compare  $\Delta\omega_{\text{FSR,cav}}$  of two scenarios, we can extract the refractive index of superfluid helium  $n_{\text{He}} = 1.030(2)$ . The perfect agreement on the ratio

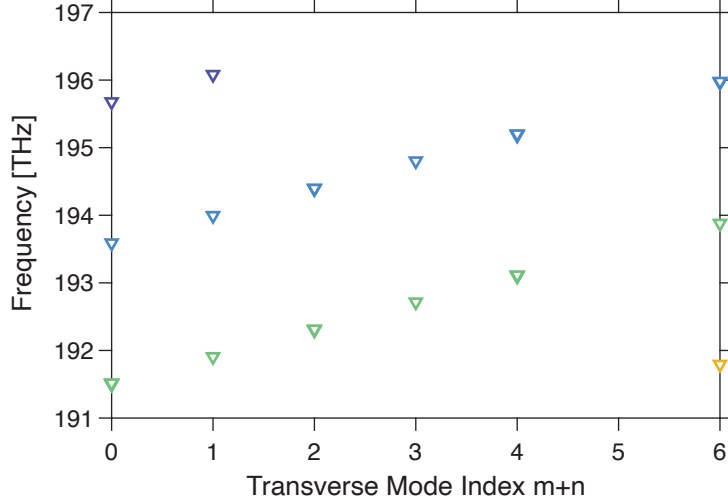


Figure 6.11: Measured optical resonance of a filled cavity. Different colors represent different longitudinal mode index  $q$ .

$\cos^{-1}(\sqrt{g_1 g_2})/\pi$ , which is fully determined by the geometry, indicates the cavity does not expand or shrink after being filled with liquid helium. This value is also comparable to the value (0.193(1)) determined from the measured geometrical parameters (given in Sec. 5.2). The length of the filled cavity can be determined by  $L_{\text{cav}} = c\pi/(\Delta\omega_{\text{FSR,filledcav}} n_{\text{He}}) = 69.7(1) \mu\text{m}$ .

### 6.2.2 Mechanical Resonance

The mechanical mode can be characterized by the scattered optical output. In previous works, the mechanical mode was measured in OMIT/A experiments [70, 71, 203, 204]. In this work, we take advantage of the SNSPDs to measure the mechanical mode by its scattered sideband photons. In the following, I will briefly discuss how we measured the mechanical mode via photon counts and show the results of these measurements. Details of the photon count spectrum can be found in Sec. 6.4, and details of the experimental procedures can be found in Sec. 6.4 and Sec. 8.2.

The optical output spectrum of this optomechanical system in the resolved-sideband regime is described in Eq. (2.61). The red-/blue-shifted sideband spectrum ( $\omega = \mp\omega_m$ ) of a blue/red detuned input ( $\Delta = \pm\omega_m$ ) reveals the mechanical susceptibility as the following

$$S_{\hat{a}_{\text{out}}^\dagger \hat{a}_{\text{out}}}(\omega \approx -\omega_m) \Big|_{\Delta=+\omega_m} \propto g_0^2 S_{\hat{b}\hat{b}^\dagger}(\omega) = g_0^2(n_m + 1)|\chi_m[-\omega]|^2, \quad (6.4)$$

$$S_{\hat{a}_{\text{out}}^\dagger \hat{a}_{\text{out}}}(\omega \approx +\omega_m) \Big|_{\Delta=-\omega_m} \propto g_0^2 S_{\hat{b}^\dagger \hat{b}}(\omega) = g_0^2 n_m |\chi_m[\omega]|^2. \quad (6.5)$$

In the schematic shown in Figs. 6.12(a,b) (corresponding to the second optical setup in

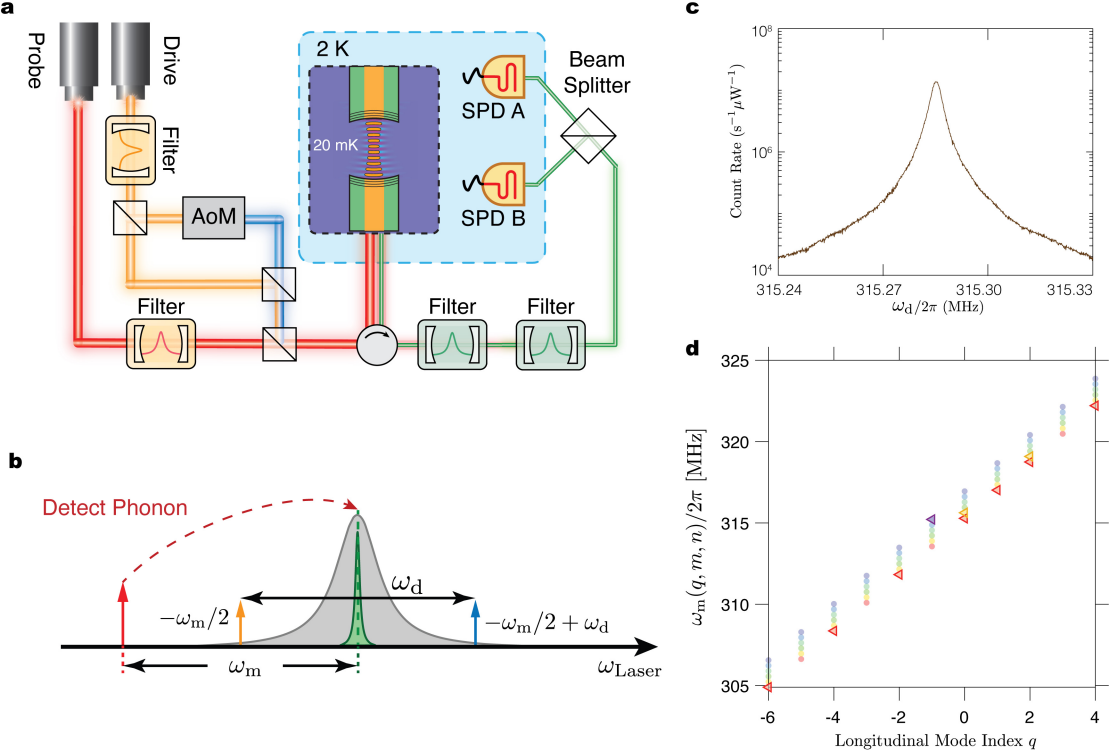


Figure 6.12: (a) Schematic of the experiment setup (details c.f. Sec. 6.1.3). (b) The optical input frequency setup. The red arrow is the probe tone. The drive tone (orange arrow) together with the AOM output (blue arrow) generates the optical beat note, which drives the mechanical mode. (c) The photon counts response for various  $\omega_d$ . (d) All measured mechanical mode frequencies (triangles) for different longitudinal mode indexes  $q$  and transverse mode indexes  $(m + n)$ . Dots represent the expected mechanical mode frequencies based on their optical mode spectrum, according to the relation described in Sec. 5.3.2. Different colors represent different transverse mode indexes (color: red to purple  $\rightarrow m+n: 0$  to 5).

Sec. 6.1.3), a weak continuous input laser ( $P_{\text{in}} = 0.2 \mu\text{W}$ ) is red-detuned by  $\sim -\omega_m$ , and we measured its blue-shifted photons ( $\omega = +\omega_m$ , resonant with the optical cavity). This photon count rate is proportional to the phonon number  $n_m$  (details c.f. Sec. 6.3.1).

A beat note at frequency  $\omega_d$  is generated by combining the second laser at  $-\omega_m/2$  and the AOM output at  $\omega_m/2 + \omega_d$  (details c.f. Sec. 6.1.3). The driven phonon number of this mechanical mode satisfies

$$n_{m,d}(\omega_d) \propto |\chi_m[\omega_d]|^2. \quad (6.6)$$

By sweeping the drive frequency  $\omega_d$ , the response in the photon count rate can reveal the mechanical susceptibility  $\chi_m$  (*i.e.*,  $\omega_m$  and  $\gamma_m$ ).

In the experiment, the vacuum optical wavelength is  $\lambda_{\text{cav}} = 1548.3(1) \text{ nm}$ , and thus the

mechanical mode that is mainly studied in this thesis has the wavelength  $\lambda_m = \lambda_{\text{cav}}/2n_{\text{He}} = 751.6(1)$  nm. The measured response count rate as a function of  $\omega_d$  is shown in Fig. 6.12(c). By fitting this response to a Lorentzian, we found  $\omega_m/2\pi = 315.2807(2)$  MHz and  $\gamma_m/2\pi = 3.12(2)$  kHz, which corresponds to a mechanical quality factor  $Q_m = 1.01(1) \times 10^5$ .

From six repeated measurements in a day, we found that the mechanical resonance frequency fluctuates with a variance  $\text{Var}(\omega_m/2\pi) \sim 160$  Hz. The frequency drift is possibly a result of: (i) the change of the temperature ( $\sim 0.4$  mHzmK, by considering the temperature dependence of the speed of sound in liquid helium); (ii) the change of the cavity length  $L_{\text{cav}}$  ( $\sim 25$  Hz/nm); or (iii) different optomechanical spring effects (arising from the probe beam) due to drifts of the optical resonance ( $< 120$  Hz $\mu$ W).

Beyond this mainly coupled mechanical mode, this beat drive can significantly enhance the visibility of some weakly coupled mechanical modes as discussed in Sec. 5.4.2 (experimental details c.f. Sec. 6.4). The mechanical resonance frequency of mode  $(q, m, n)$ , as discussed in Sec. 5.3.2, is

$$\omega_m(q, m, n) = \frac{n_{\text{He}} v_{\text{He}}}{c} \omega_{\text{cav}}(q, m, n). \quad (6.7)$$

The measured mechanical modes are triangles shown in Fig. 6.12(d). Their distributions agree with normalized optical mode frequencies (dots) as predicted in Eq. (6.3) and (6.7), where the sound velocity in liquid helium  $v_{\text{He}}$  is treated as a free parameter.

By fitting mechanical frequencies to a linear model  $\omega_m(q, p \equiv (m+n)) = q\Delta\omega_{\text{FSR},m} + (1+p)\delta\omega_{\text{Trans},m}$ , we can extract  $\Delta\omega_{\text{FSR},m}/2\pi = 1.7307(4)$  MHz and  $\delta\omega_{\text{Trans},m}/2\pi = 0.3324(8)$  MHz and determine the mode index of the mainly coupled mechanical mode is  $(182, 0)$ . The ratio between these two values is  $0.192(1)$ , which is very close to the ratio of the optical modes ( $0.1902(3)$ ) or the ratio determined from the cavity geometry ( $0.193(1)$ ). The sound velocity in liquid helium at that temperature is thus given by

$$v_{\text{He}} = \frac{c}{n_{\text{He}}} \frac{\Delta\omega_{\text{FSR},m}}{\Delta\omega_{\text{FSR,filledcav}}} = 234.3(4) \text{ m/s}. \quad (6.8)$$

This similarity between the optical and mechanical spectra verifies the discussion in Sec. 5.3.2 and Sec. 5.3.1.

### 6.3 Characterizing the Optomechanical Coupling

The theoretical framework of optomechanical coupling is covered in Sec. 2.1.3. This section presents the basic framework of the experiment and the experiment results of the optomechanical coupling characterizations. More specifically, we measured the optical output spectrums, which are different scattered photon count rates for different optical input detunings. Furthermore, the optomechanical damping rates, optomechanical cooling

effect, and parametric amplification are measured to elucidate the optomechanical dynamics. We also experimentally demonstrate the quantum sideband asymmetry, as discussed in Sec. 2.3.2.

### 6.3.1 Spectrum of Photon Counts

A schematic of the basic optical setup is shown in Fig. 6.13(a) (corresponding to the basic optical setup in Sec. 6.1.1). Two lasers are either blue-detuned (blue color) or red-detuned (red color) from the cavity resonance by  $|\Delta| \sim \omega_m$ , which are always locked to the TL. Each laser then goes through a corresponding narrowband filter cavity and then a VOA to have a phase-noise-suppressed and power-stabilized optical input before Shutter1/Shutter2.

The experiment is conducted in the “Lock-Hold” measurement scheme described in Sec. 6.1.2. During the “hold” period, either Shutter1 or Shutter2 is connected to the optical path to the optomechanical cavity. Thus, one of the two detuned lasers sends beams to the optomechanical cavity continuously during the “hold” period. The scattered photons together with the reflected input photons are sent to two filter cavities ( $\kappa_{FCi}/2\pi \sim 1$  MHz), which reject most of the unscattered photons. These transmitted photons are then received by the two SNSPDs. In the “lock” period, both two shutters are opened and both SNSPDs are disabled. The TL and two FCs are locked to the optomechanical cavity, as described in Sec. 6.1.2. The detuning of the input laser can be swept by setting different target frequency offsets during the “lock” periods. For each long measurement, we always manually optimize the polarization of the light before each polarization sensitive optical component (such as the two FCs, and the two SNSPDs) to maximize the measurement efficiency. This efficiency usually drifts down by 10 – 20% due to the drift of the polarization and the quality of various frequency lockings in the course of one day.

The optical mode studied in this thesis has wavelength  $n_{He}\lambda_{cav} = 1548.3(1)$  nm, and the frequency of the mainly coupled mechanical mode is  $\omega_m/2\pi = 315.2807(2)$  MHz.

#### 6.3.1.1 Filter Cavity

In the resolved-sideband regime, the output photon spectrum is given in Eq. (2.61) (in a frame rotating at  $\omega_L$ ). Apart from the trivial optical input at  $\omega = 0$ , Eq. (2.61) has two scattered sidebands at  $\omega \approx \pm\omega_m$ , which are what we are interested in. So the unscattered photons must be filtered before they reach the SPD. This approach has been demonstrated by groups at Caltech (Painter) [91], Delft/Vienna (Groblacher/Aspelmeyer) [12, 75, 92, 97], Neils Bohr Institute (Polzik) [57], Australian National University (Lam) [245, 246], Oxford (Walmsley) [247], and Lausanne (Galland) [248]. In this work, the optical output is filtered by two cascaded filter cavities. In the following, we will discuss the optical field after the filter cavities, and the measured count rate spectrum.

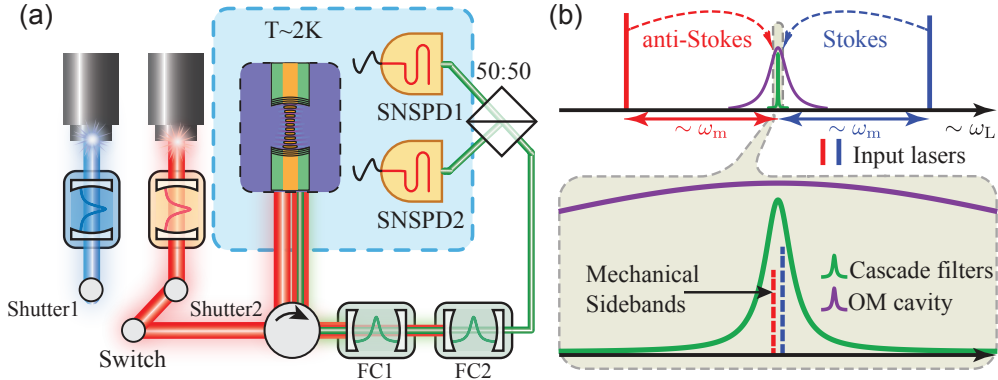


Figure 6.13: (a) Optical schematic of the continuous drive scheme showing the two input lasers (red and blue paths), optomechanical cavity (black dashed box) inside the cryostat (light blue dashed box), scattered photons (green paths), two on-resonance cascaded filter cavities (FC1, FC2, green boxes), and the two SNSPDs. (b) Optical spectrum showing the input laser tones and their scattered photons (blue/red dashed lines) with respect to the optomechanical cavity (purple solid line) and two filter cavities (green solid line).

### 6.3.1.1.1 Rejection Efficiency of the Filter Cavities

The two SNSPDs used in this thesis are broadband detectors that cannot distinguish input photons from scattered photons. With the scattering probability as low as  $\sim 10^{-5}$ , sideband photons are much less than the measured unshifted photons. To overcome this problem, photons leaving the optomechanical cavity (both the unshifted input photons and the scattered photons) are then incident on two filter cavities which are arranged in series. Both filter cavities are locked to the optomechanical cavity resonance  $\omega_{\text{cav}}$  during the “lock” configuration. This in-series filter cavity configuration is widely implemented in recent works [28, 57, 75, 92, 245, 246, 249], and provides a high-level of rejection of unwanted photons while also providing a moderate transmission coefficient for the sideband photons.

The suppression of input photons with detuning  $\Delta$  is

$$\eta_{\text{supp,tot}}(\Delta) = \prod_{i=1}^2 \frac{\kappa_{\text{FCi}}^2/4}{\kappa_{\text{FCi}}^2/4 + (|\Delta|)^2}. \quad (6.9)$$

Here, I used the simplified well-known Airy-formula for the transmission spectrum of a Fabry-Pérot cavity, details c.f. Sec. B.3.

In the case that the detuning is set at  $\Delta \sim \pm\omega_m$ , we have

$$\eta_{\text{supp,tot}}(\Delta) \approx \prod_{i=1}^2 \frac{\kappa_{\text{FCi}}^2/4}{\omega_m^2}, \quad (6.10)$$

where the approximation  $\omega_m \gg \kappa_{FCi}$  is taken. The overall suppression factor is polynomially dependent on the number of filters as  $\eta_{\text{supp,tot}} \propto \eta_{\text{supp,single}}^{n_{\text{filter}}}$ . Besides the fact that it is challenging to have a narrow linewidth filter cavity, the main reason not to reduce the linewidth to increase the suppression is that the linewidth of each filter cavity should satisfy  $\kappa_{FCi} \gg \gamma_m$  to pass most of on-resonance scattered photons. In the experiment, filter cavities have linewidths  $\kappa_{FC1}/2\pi = 1.21(5)$  MHz and  $\kappa_{FC2}/2\pi = 1.71(2)$  MHz, respectively, which can provide a suppression factor  $\sim 95$  dB (normalized to the maximum in-resonance transmission).

### 6.3.1.1.2 Transmitted Optical Field of the Filter Cavity

The transfer function  $f_{\text{filter}}(\omega)$  of the two cascaded filter cavities is given by

$$f_{\text{filter}}(\omega) = \frac{\sqrt{\eta_{FC1}}\kappa_{FC1}/2}{\kappa_{FC1}/2 + i(\omega + \Delta)} \frac{\sqrt{\eta_{FC2}}\kappa_{FC2}/2}{\kappa_{FC2}/2 + i(\omega + \Delta)}. \quad (6.11)$$

The transmission coefficients for FC1 and FC2 are  $\eta_{FC1} \approx 40\%$  and  $\eta_{FC2} \approx 17\%$ , respectively. The field  $\hat{p}$  detected by the SNSPDs is the cavity output field  $\hat{a}_{\text{out}}$  passed through the filter cavities, which is described by a Fourier transform of the transfer function  $f_{\text{filter}}(\omega)$ ,

$$\hat{p}(t) = \int_{-\infty}^{\infty} \frac{d\omega}{2\pi} e^{-i\omega t} f_{\text{filter}}(\omega) \hat{a}_{\text{out}}(\omega). \quad (6.12)$$

Applying the Weiner-Khinchin relation, we have the detected normally ordered optical correlations of  $\hat{p}$

$$\langle \hat{p}^\dagger(t + \tau) \hat{p}(t) \rangle = \int_{-\infty}^{\infty} \frac{d\omega}{2\pi} e^{-i\omega\tau} |f_{\text{filter}}(\omega)|^2 S_{\hat{a}_{\text{out}}^\dagger \hat{a}_{\text{out}}}(\omega), \quad (6.13)$$

where  $f_{\text{filter}}(\omega)$  is non-zero only around the cavity resonance  $\omega = -\Delta$ . Therefore, the anti-Stokes scattered photons ( $\omega = +\omega_m$ ) of the red-detuned input ( $\Delta = -\omega_m$ ) or the Stokes scattered photons ( $\omega = -\omega_m$ ) of the blue-detuned input ( $\Delta = +\omega_m$ ) can pass through two filter cavities (allowing for an offset in the laser detuning within  $\kappa_{FC1}, \kappa_{FC2}$ ). The contribution of the optical input  $\omega = 0$  in Eq. (2.61) to this integral Eq. (6.13) is negligible due to the 95 dB suppression. As such, substituting Eq. (2.61) into Eq. (6.13), we have

$$\langle \hat{p}^\dagger(t + \tau) \hat{p}(t) \rangle = \kappa_{\text{ex}} g_0^2 n_{\text{cav}} \int_{-\infty}^{\infty} \frac{d\omega}{2\pi} e^{-i\omega\tau} |f_{\text{filter}}(\omega)|^2 |\chi_{\text{cav}}(\omega + \Delta)|^2 [S_{\hat{b}^\dagger \hat{b}}(\omega) + S_{\hat{b}\hat{b}^\dagger}(\omega)]. \quad (6.14)$$

Thus, for the case of the red-detuned input  $\Delta \approx -\omega_m$ , only the  $S_{\hat{b}^\dagger \hat{b}}$  term contributes to the integral around  $\omega = +\omega_m$  in Eq. 6.14, corresponding to the anti-Stokes scattered photons, and yields

$$\begin{aligned}\langle \hat{a}_{AS}^\dagger(t + \tau) \hat{a}_{AS}(t) \rangle &= \langle \hat{p}^\dagger(t + \tau) \hat{p}(t) \rangle \\ &= \kappa_{ex} g_0^2 n_{cav} |\chi_{cav}(\omega_m + \Delta)|^2 |f_{filter}(\omega_m)|^2 \int_{-\infty}^{\infty} \frac{d\omega}{2\pi} e^{-i\omega\tau} S_{\hat{b}^\dagger \hat{b}}(\omega) \\ &= 4\kappa_{ex} g_0^2 n_{cav} |f_{filter}(\omega_m)|^2 / \kappa^2 \langle \hat{b}^\dagger(t + \tau) \hat{b}(t) \rangle,\end{aligned}\quad (6.15)$$

where we have approximated  $f_{filter}(\omega) \approx f_{filter}(\omega_m)$  and  $\chi_{cav}(\omega + \Delta) \approx \chi_{cav}(0)$  for  $\omega \sim +\omega_m$ , because we have  $\gamma_m \ll \kappa_{FC1}, \kappa_{FC2} \ll \kappa$ .

Similarly, for the case of the blue-detuned input  $\Delta \approx +\omega_m$ , only the  $S_{\hat{b} \hat{b}^\dagger}$  term contributes to the integral around  $\omega = -\omega_m$  in Eq. 6.14, corresponding to the Stokes scattered photons, and yields

$$\begin{aligned}\langle \hat{a}_S^\dagger(t + \tau) \hat{a}_S(t) \rangle &= \langle \hat{p}^\dagger(t + \tau) \hat{p}(t) \rangle \\ &= \kappa_{ex} g_0^2 n_{cav} |\chi_{cav}(-\omega_m + \Delta)|^2 |f_{filter}(-\omega_m)|^2 \int_{-\infty}^{\infty} \frac{d\omega}{2\pi} e^{-i\omega\tau} S_{\hat{b} \hat{b}^\dagger}(\omega) \\ &= 4\kappa_{ex} g_0^2 n_{cav} |f_{filter}(-\omega_m)|^2 / \kappa^2 \langle \hat{b}(t + \tau) \hat{b}^\dagger(t) \rangle.\end{aligned}\quad (6.16)$$

Therefore, the transmitted photon count rates of these cases are given in the case  $\tau = 0$  as

$$\langle \hat{a}_{AS}^\dagger \hat{a}_{AS} \rangle = \gamma_m \mathcal{C} n_m \times \frac{\kappa_{ex}}{\kappa} \times |f_{filter}(\omega_m)|^2, \quad \text{with } \Delta \approx -\omega_m, \quad (6.17a)$$

$$\langle \hat{a}_S^\dagger \hat{a}_S \rangle = \gamma_m \mathcal{C} (n_m + 1) \times \frac{\kappa_{ex}}{\kappa} \times |f_{filter}(-\omega_m)|^2, \quad \text{with } \Delta \approx +\omega_m, \quad (6.17b)$$

where  $\mathcal{C} = 4g^2/\gamma_m \kappa$  is the cooperativity defined in Eq. (2.64). Together with the transmission efficiency  $\eta_{misc}$  and the SNSPD measurement efficiency  $\eta_{SNSPD}$ , the measured anti-Stokes and Stokes scattered photon rates at the SNSPDs are

$$\Gamma_{AS} = \gamma_{AS} \times \eta_\kappa \times \eta_{det}, \quad (6.18a)$$

$$\Gamma_S = \gamma_S \times \eta_\kappa \times \eta_{det}, \quad (6.18b)$$

with the anti-Stokes and Stokes scattering rates defined as

$$\gamma_{AS} = \gamma_m \mathcal{C} n_m, \quad (6.19a)$$

$$\gamma_S = \gamma_m \mathcal{C} (n_m + 1), \quad (6.19b)$$

respectively.

Because the linewidth of the sideband satisfies  $\gamma_m \ll \kappa_{FC} \ll \kappa$ , the entire process can be interpreted as: if either of the scattered sidebands (behaving like a single frequency output) falls in the optical resonance, scattered photons can pass through two filter cavities and subsequently be measured by the SNSPD, as shown in Fig. 6.13(b).

In the discussion above, the “linewidth” of the input laser  $\kappa_L$  is not included and is treated as a delta function  $\delta(\omega)$ . This approximation may not be valid as  $\kappa_L$  can be comparable to or even larger than the linewidth of the mechanical linewidth  $\gamma_m$ .

This relatively low transmission rate in the fiber-based Fabry-Pérot cavity is typically caused by mode mismatching. A free-space-optics-based filter cavity of the same principle can significantly improve the overall transmission rate [28, 57]. Up to 30% overall transmission rate after 4 cascaded filter cavities each having a linewidth of approximately 30 kHz has been experimentally demonstrated [57]. A similar design of the free-space-optics-based filter cavity has been built and tested in our lab.

### 6.3.1.2 Characterizing the Spectrum of Photon Counts

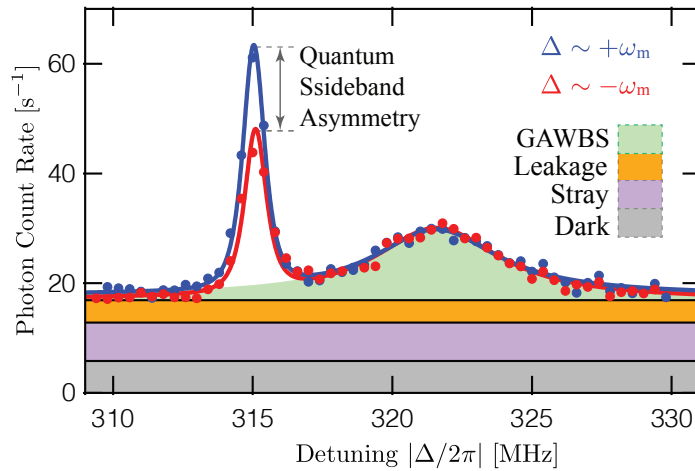


Figure 6.14: Photon count rate spectrum measured as a function of the input laser detuning  $|\Delta/2\pi|$ , with  $P_{in} = 400$  nW.

Figure 6.14 shows a measured photon detection rate as a function of the input laser detuning  $|\Delta/2\pi|$ , with  $P_{in} = 400$  nW, in which red dots represent the counts for red-detuning ( $\Delta < 0$ ) and blue dots represent the counts for blue-detuning ( $\Delta > 0$ ). The peak at  $\Delta/2\pi = \pm\omega_m/2\pi = \mp315.3(1)$  MHz corresponds to the anti-Stokes (Stokes) sidebands of the mechanical mode. This frequency is consistent with the measured  $\omega_m/2\pi = 315.2807(2)$  MHz given in Sec. 6.2.2. The broad peak at  $\Delta/2\pi = \mp322.3(1)$  MHz is a result of the input photons getting scattered by the guided acoustic wave Brillouin scattering (GAWBS) in the optical fibers [250]. The detuning-independent background is also

evident. The solid blue/red line in Fig. 6.14 is a fit to the sum of a constant (corresponding to the background counts), a broad Lorentzian (corresponding to the GAWBS signal), and the filter cavities' passband  $|f_{\text{filter}}(\omega)|^2$  (a product of two Lorentzians, corresponding to the counts from the mechanical sidebands), given in Eq. (6.23).

A detailed description of this fit is given in the following:

**Anti-Stokes/Stokes Scattered Photons** As indicated in Eq. (6.17), by sweeping the optical input detuning  $\Delta$  around  $\pm\omega_m$ , anti-Stokes/Stokes scattered photon count rates can silhouette the shape of the filter cavity transmission transfer function  $|f_{\text{filter}}(\Delta)|^2$  with different amplitudes which are characterized by the quantum sideband asymmetry.

**GAWBS** The GAWBS is the well-studied interaction between light in an optical fiber and the fiber's thermally populated transverse acoustic modes, which vibrate in the radial direction [250]. In practice, this interaction produces phase noise in the light with a spectrum determined by the fiber's acoustic modes.

The GAWBS can be characterized by a Lorentzian centered at  $\omega_{\text{GAWBS}}$  given by

$$f_{\text{GAWBS}}(\Delta) = \frac{\kappa_{\text{GAWBS}}^2/4}{\kappa_{\text{GAWBS}}^2/4 + (|\Delta| - \omega_{\text{GAWBS}})^2}. \quad (6.20)$$

The resonance frequencies  $\omega_{\text{GAWBS}}$  are determined by

$$\omega_{\text{GAWBS},m} = \frac{v_{\text{fiber}}}{r_{\text{fiber}}} y_m, \quad (6.21)$$

where  $v_{\text{fiber}} = 5996 \text{ m/s}$  is the longitudinal sound velocity and  $r_{\text{fiber}} = 62.5 \mu\text{m}$  [250, 251].  $y_m$  is the  $m$ th-order solution of

$$(1 - \alpha^2) J_0(y) = \alpha^2 J_2(y), \quad (6.22)$$

with  $\alpha = 0.624$  for fibers made of fused silica.

A more detailed characterization of the GAWBS in our system is achieved by sweeping a wider frequency spectrum. You can find a detailed description in Ref. [72].

**Background** The background photon count rate  $\Gamma_{\text{bkg}}$  is frequency-independent in the frequency range shown in Fig. 6.14 (310 MHz to 330 MHz). The frequency-independent background  $\Gamma_{\text{bkg}}$  is found to have three sources:

1. the SNSPDs' darks counts,
2. Stray light leaking into the fibers,

3. Unfiltered optical input photons leaking through the two filter cavities in the detection chain (this last contribution is polarization-dependent and so differs between the red-detuned and blue-detuned inputs).

The first two sources are independent of the optical input power  $P_{\text{in}}$ , and the last one linearly depends on the power.

Thus, for each detuning range (*i.e.*,  $\Delta \sim +\omega_m$  and  $\Delta \sim -\omega_m$ ), the count rate spectrum is fit to the form

$$\Gamma(\Delta) = \Gamma_{\text{bkg}} + |f_{\text{filter}}(\Delta)|^2 \Gamma_{\text{res}} + f_{\text{GAWBS}}(\Delta) \Gamma_{\text{GAWBS}}, \quad (6.23)$$

where  $\Gamma_{\text{bkg}}$ ,  $\Gamma_{\text{res}}(\Gamma_{\text{AS(S)}})$ ,  $\Gamma_{\text{GAWBS}}$ ,  $\omega_m$ ,  $\omega_{\text{GAWBS}}$ , and  $\kappa_{\text{GAWBS}}$  are the fit parameters.

The difference between  $\Gamma_{\text{AS}}$  and  $\Gamma_S$  is known as the quantum sideband asymmetry (QSA), and is detailedly discussed in Sec. 2.3.2. This count rate difference between blue- and red-detuned inputs is absent in the GAWBS peak.

### 6.3.1.3 The Power Dependence of the Photon Count Spectrum

Figure 6.15(a) shows the count rates as a function of the detuning at various optical input powers  $P_{\text{in}}$ . Each spectrum consistently shows a narrow peak (arising from the Stokes- and anti-Stokes-scattered photons) centered at  $\omega_m/2\pi \approx 315.3$  MHz, a broader peak centered around 322.3 MHz, and a frequency-independent background. However, these extracted fitting parameters present different power dependences, as shown in Fig. 6.15(b), which are discussed in the following.

**GAWBS** The GAWBS photon count rates  $\Gamma_{\text{GAWBS}}$  depend linearly on the power  $P_{\text{in}}$  and intersect the origin. The slopes of the red- and blue-detuned optical input are also identical. These observations align with the scattering process of a classical system ( $k_B T \gg \hbar\omega_{\text{GAWBS}}$ ).  $\Gamma_{\text{GAWBS}}(P_{\text{in}})$  is fit to the form  $k_{\text{GAWBS}} P_{\text{in}}$ . This gives  $k_{\text{GAWBS}} = 28.5 \pm 0.3 \text{ s}^{-1} \mu\text{W}^{-1}$ .

**Background** The background photon count rates  $\Gamma_{\text{bkg}}$  for the red- and blue-detuned optical input are also linearly dependent on the input power  $P_{\text{in}}$ . However, they have different slopes and intercept the y-axis above zero.

$\Gamma_{\text{bkg}}(P_{\text{in}})$  is fit to the form  $b_{\text{bkg}} + k_{\text{bkg}} P_{\text{in}}$ , which gives  $b_{\text{bkg}} = 12.4 \pm 0.8 \text{ s}^{-1}$ , and  $k_{\text{bkg}} = 9.1 \pm 0.2 \text{ s}^{-1} \mu\text{W}^{-1}$  for the red-detuned optical input, and  $k_{\text{bkg}} = 12.0 \pm 0.4 \text{ s}^{-1} \mu\text{W}^{-1}$  for the blue-detuned optical input. The power dependences of different background sources are discussed in Sec. 6.3.1.2. By acquiring the count rate while blocking the input port directly in front of the SNSPDs, it is found that  $b_{\text{bkg}}$  consists of  $7 \pm 1 \text{ s}^{-1}$  from dark counts and  $5 \pm 1 \text{ s}^{-1}$  from stray light leaking into the detection-chain fibers.  $k_{\text{bkg}}$  quantifies the number of optical input photons that pass through the filter cavities per unit optical input power.

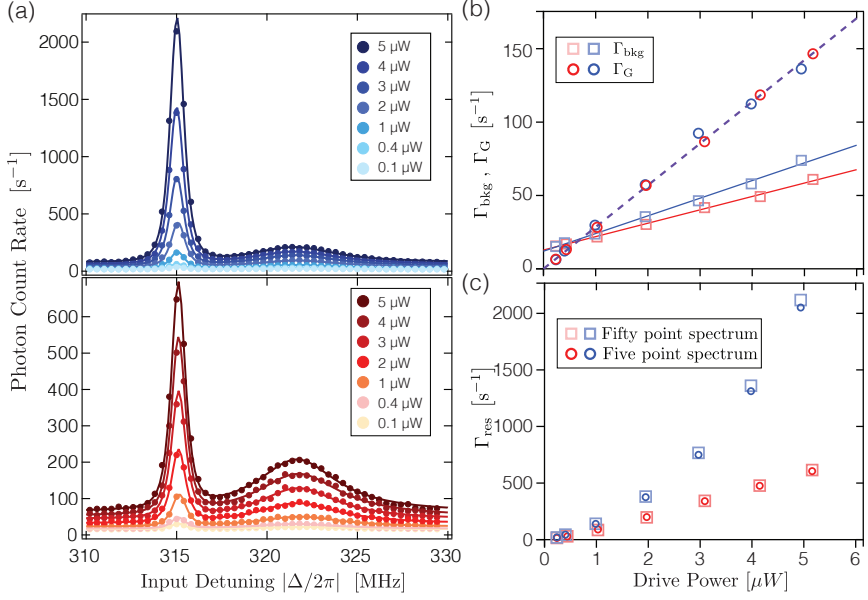


Figure 6.15: (a) Photon count rates as a function of the detuning and power of the input laser. Red and blue represents the red-detuned and the blue-detuned inputs, respectively. The narrow peak near 315.3 MHz corresponds to scattered sideband photons. The broad peak near 322 MHz is due to thermal fluctuations in the room-temperature optical fibers. Solid lines represent corresponding fit to Eq. (6.23). (b)  $\Gamma_{\text{bkg}}$  (squares) and  $\Gamma_G$  (circles) as a function of drive power. The red and blue solid lines are linear fits to  $\Gamma_{\text{bkg}}$  of the blue- and red-detuned input, respectively. The purple dashed line is the linear fit to  $\Gamma_{\text{bkg}}$ . (c)  $\Gamma_{\text{res}}$  as a function of drive power. Data are acquired in different spacings: squares are values of  $\Gamma_{\text{res}}$  extracted from a fit of a 50-frequency measurement to Eq. (6.23). Circles represent the same fit of a 5-frequency measurement.

**Anti-Stokes/Stokes Scattered Photons** The anti-Stokes- and Stokes- scattered photon count rate  $\Gamma_{\text{res}}$  are nonlinear in the input power  $P_{\text{in}}$ . They show remarkably distinct dependences with increasing power. This difference is the outcome of the standard optomechanical dynamical backaction, as well as heating (due to the absorption of photons in the fibers and mirror coatings which are in thermal contact with the superfluid), and the quantum sideband symmetry [70, 71]. A complete description of  $\Gamma_{\text{res}}$  as a function of drive power  $P_{\text{in}}$  is given in Sec. 6.3.2.

The spectra in Fig. 6.15(a) (and those used to produce Fig. 6.15(b)) are measured at 50 evenly-spaced detunings. While this is helpful in characterizing the device, the focus of the experiment is on the Stokes- and anti-Stokes-scattered photons. To measure the rates of these specific photons, we found that it was adequate to record the spectrum at just five frequencies close to  $\omega_m$  (specifically,  $|\Delta|/2\pi = 310, 312, 314.9, 315.4, 315.9$  MHz), and

then fit the results to the form

$$\Gamma(\Delta) = \Gamma_{\text{bkg}} + |f_{\text{filter}}(\Delta)|^2 \Gamma_{\text{res}}. \quad (6.24)$$

To illustrate the validity of this approach, Fig. 6.15(c) shows  $\Gamma_{\text{res}}(P_{\text{in}})$  acquired in two different approaches:

- By measuring the count rate at 50 values of  $\Delta/2\pi$  ranging from  $\pm 310$  MHz to  $\pm 330$  MHz (as in Fig. 6.15(a) and fitting the measured results to Eq. 6.23;
- By measuring the count rate at just the five values of  $\Delta/2\pi$  listed above and fitting data to Eq. 6.24.

The agreement of the fitted results shows the reliability of the five-point spectrum and the minimal influence of the GAWBS peak (which is not included in Eq. 6.24) on this analysis. The data presented in Sec. 6.3.2 were acquired using the “five frequency” approach.

### 6.3.2 Optomechanical Dynamical Backaction

This section presents the experimental demonstration of the two major forms of optomechanical dynamical backaction: optomechanical cooling/heating and optomechanical damping. The theoretical background is discussed in Sec. 2.2. These measurements provide information about the mechanical mode’s temperature and the useful range of  $P_{\text{in}}$ . They also provide a calibration of the device’s optomechanical coupling rate  $g_0$ .

#### 6.3.2.1 Optomechanical Sideband Cooling and Parametric Heating

This section describes measurements of the sideband-photon counting rates as a function of the input laser power  $P_{\text{in}}$ . As shown in Eq. (6.18a) and (6.19a), the scattered photon count rate relies on the phonon number  $n_m$  and the mechanical linewidth  $\gamma_m$ . At higher drive powers, both optical backaction and absorption-induced heating (in the fibers and mirrors) can alter  $n_m$ .

To characterize the role of backaction and heating in these devices, Fig. 6.16(a) shows  $\Gamma_{\text{AS(S)}}$  as a function of  $P_{\text{in}}$  (The data at  $P_{\text{in}} = 0$  are measured using pulsed laser excitations and then subtracting the transient heating). For sufficiently low  $P_{\text{in}}$  ( $\lesssim 300$  nW), the values of  $\Gamma_{\text{AS(S)}}$  are consistent with  $T_{\text{MC}} \approx 20$  mK, and show a splitting that is dominated by the quantum sideband asymmetry. The rest of the distinct dependences on the input power is a combined effect of the heating and, more interestingly, the dynamical backaction.

To analyze these effects quantitatively, we apply the standard theory of optomechanical backaction in Sec. 2.2 and model the heating by assuming that the device is subject to a heat load proportional to  $P_{\text{in}}$  and is thermally linked to the mixing chamber with a thermal conductance  $\sigma = bT^{k+1}$  [70–72].

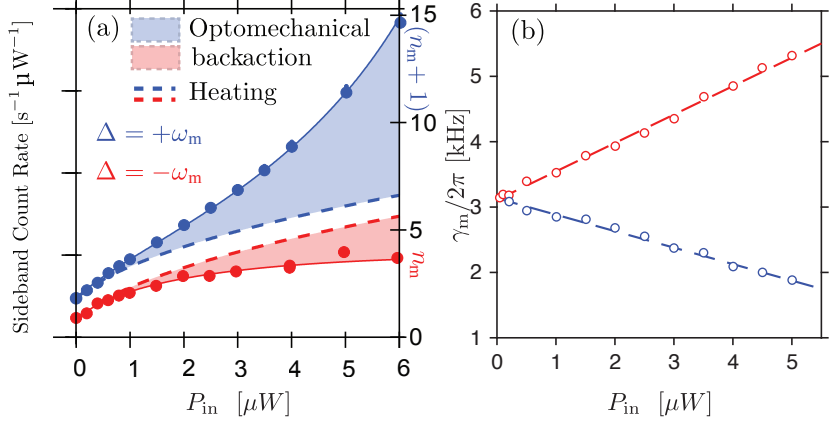


Figure 6.16: (a) Power normalized anti-Stokes (red) and Stokes (blue) photon detection rates as a function of  $P_{\text{in}}$  with  $T_{\text{MC}} \approx 20 \text{ mK}$ . Solid lines: a fit including optomechanical backaction (colored regions) and heating due to optical absorption (dashed lines) (details c.f. Sec. 6.3.2.1). Right-hand axis: the mean phonon occupancy  $n_m$  ( $n_m + 1$ ) inferred from the detection rates. (b) The measured mechanical linewidth of a blue- or red-detuned input at various  $P_{\text{in}}$ . The dashed lines are the linear fit to Eq. (6.32).

In more detail, we start with the normalized (to  $P_{\text{in}}$ ) scattering rate shown in Eq. (6.18a). In the following, all fit parameters in this model are highlighted in red. Notice that the product  $\eta_\kappa \eta_{\text{det}} \gamma_m \mathcal{C} / P_{\text{in}}$  is independent of  $P_{\text{in}}$ . The final phonon number is evaluated in Eq. (2.57), given by

$$n_m(P_{\text{in}}) = \frac{\gamma_{\text{opt}}(P_{\text{in}}) n_{\text{min}} + \gamma_m n_{m,\text{th}}(P_{\text{in}})}{\gamma_{\text{opt}}(P_{\text{in}}) + \gamma_m}, \quad (6.25)$$

with  $n_{\text{min}} = \left(\frac{\kappa}{4\omega_m}\right)^2$  and  $\gamma_{\text{opt}} = \mp \frac{4g_0^2}{\kappa} n_{\text{cav}}$ .

Here,  $n_{m,\text{th}}$  is determined by the thermal bath temperature which is subject to  $P_{\text{in}}$  due to the heating effect.

The effect of optical-absorption-induced heating in the fibers and mirrors is detailedly modeled in Refs. [70, 72, 203]. The fiber's temperature is given by

$$T_{\text{fib}} = (T_{\text{MC}}^{k+1} + \beta^{k+1} P_{\text{in}})^{1/(k+1)} \quad (6.26)$$

where  $\beta$  characterizes the amount of heat generated by a given  $P_{\text{in}}$ . In addition, we assume ballistic transport of heat (phonons) from the Helium inside the optomechanical cavity to the mixing chamber bath via the Helium channel connecting them. The effective phonon

number of the thermal bath is given by

$$n_{m,\text{th}} = \frac{n_{\text{fib}}\gamma_{m0} + n_{\text{MC}}\gamma_{3\text{pp}}}{\gamma_{m0} + \gamma_{3\text{pp}}}, \quad (6.27)$$

with

$$n_{\text{fib}} = 1/(e^{\hbar\omega_m/(k_B T_{\text{fib}})} - 1), \quad (6.28)$$

$$n_{\text{MC}} = 1/(e^{\hbar\omega_m/(k_B T_{\text{MC}})} - 1), \quad (6.29)$$

where the bare mechanical damping rate  $\gamma_m = \gamma_{m0} + \gamma_{3\text{pp}}$  includes:

1. The intrinsic mechanical damping rate  $\gamma_{m0}/2\pi = 3.2 \times 10^3$  Hz due to acoustic loss into the fibers (discussed in Sec. 5.2),
2. The three phonon loss  $\gamma_{3\text{pp}}/2\pi = 2.7 \times 10^6$   $T_{\text{MC}}^4$  Hz/K<sup>4</sup> at the base mixing chamber temperature (discussed in Sec. 5.5.1).

The solid lines in Fig. 6.16(a) show the best fit to combined model Eq. (6.25) to (6.28) while taking  $g_0$ ,  $T_{\text{MC}}$ ,  $\eta_{\text{det}}$ ,  $\beta$  and  $k$  as fit parameters. The dashed lines show the change in  $n_m$  attributable to absorption-induced heating. The best-fit value  $k = 1.05(3)$  suggests a predominantly metallic thermal conductance between the device and the mixing chamber ( $k = 1$  for metals). The fit also gives a single photon coupling rate<sup>30</sup>  $g_0/2\pi = 4.58(2)$  kHz and a net detection efficiency of  $\eta_{\text{det}} = 2.5\%$ . The best-fit value  $T_{\text{MC}} = 19(1)$  mK corresponds to a mean thermal phonon occupancy of  $n_m = 0.83(2)$ . This model also indicates that the backaction and the heating effect is negligible when the incident laser power  $P_{\text{in}} \lesssim 300$  nW.

The validity and the accuracy of the model are repeatedly verified by using it to analyze power sweep data taken on several different days over the course of ten months. Details are discussed in Ref. [72].

### 6.3.2.2 Optomechanical Damping Rates

Another intriguing optomechanical backaction is the optomechanical damping effect, as detailedly discussed in Sec. 2.2.1. This section describes the characterization of the mechanical linewidth  $\gamma_m$ 's dependence on the input power  $P_{\text{in}}$ .

In the resolved-sideband regime, the optomechanical damping rate is given in Eq. (2.43)

$$\gamma_{\text{opt}}(\Delta = \pm\omega_m)|_{\kappa \ll \omega_m} = \mp n_{\text{cav}} g_0^2 \frac{4}{\kappa}, \quad (6.30)$$

---

<sup>30</sup>More precisely, this coupling rate is the effective coupling rate by combining the photoelastic coupling  $g_0$  and the photothermal coupling  $g_{\text{pt}}$ , because the photothermal coupling  $g_{\text{pt}}$  changes the optomechanical dynamical backactions in a way by replacing  $g_0^2$  with  $g_0(g_0 + g_{\text{pt}})$  [204].

where  $n_{\text{cav}}$  is given in Eq. (2.14). Moreover, the heating in the environment due to the optical absorption may heat up the temperature of the superfluid helium in the cavity (this effect is not included in the model in Sec. 6.3.2.1). The three-phonon process contributes the mechanical loss in the following way:

$$\gamma_{3\text{pp}}(P_{\text{in}}) = \alpha T_{\text{He}}^4 = \alpha (T_{\text{MC}}^{k+1} + \beta^{k+1} P_{\text{in}})^{4/(k+1)} \Big|_{k=3} = \alpha (T_{\text{MC}}^4 + \beta^4 P_{\text{in}}), \quad (6.31)$$

where we take  $k = 3$  for superfluid helium-4 [217]. Thus, the total mechanical linewidth is

$$\begin{aligned} \gamma_m(\Delta = \pm\omega_m) &= \gamma_{m0} + \gamma_{3\text{pp}} + \gamma_{\text{opt}} \\ &= \gamma_{m0} + \alpha (T_{\text{MC}}^4 + \beta^4 P_{\text{in}}) \mp n_{\text{cav}} g_0^2 \frac{4}{\kappa}. \end{aligned} \quad (6.32)$$

The mechanical linewidth is expected to be linear with the optical input power for either sideband.

The mechanical linewidth is measured by the protocol described in Sec. 6.2.2. In the experiment, the power of the driving beat note is  $P_1 = P_2 = 100 \text{ nW}$ , and the drive frequency is changed during the “lock” period. The measured photon count is fit to a Lorentzian to extract  $\gamma_m$ . We repeat this procedure for various optical input powers  $P_{\text{in}}$  at either red- ( $\Delta = -\omega_m$ ) or blue-detuned ( $\Delta = +\omega_m$ ) sideband.

Figure 6.16(b) shows the measured linewidths for various input powers  $P_{\text{in}}$ , where red and blue dots stand for the red- and blue-detuned drives, respectively. The linear fit gives

$$\Delta = -\omega_m : \gamma_m/2\pi = (3110 \pm 8) \text{ Hz} + (435 \pm 4) P_{\text{in}} \text{ Hz}/\mu\text{W}, \quad (6.33a)$$

$$\Delta = +\omega_m : \gamma_m/2\pi = (3135 \pm 23) \text{ Hz} - (252 \pm 8) P_{\text{in}} \text{ Hz}/\mu\text{W}. \quad (6.33b)$$

This fitting results indicate the single photon coupling strength  $g_0/2\pi = 4.98(7) \text{ kHz}$  and the bare mechanical frequency  $\gamma_m/2\pi = 3.12(2) \text{ kHz}$ .

### 6.3.2.2.1 Ring-up Measurement for Parametric Amplification Effects

In the case of blue-detuned optical input, a negative mechanical linewidth is expected for input powers higher than  $13.2 \mu\text{W}$  according to Eq. (6.33b). This negative mechanical linewidth cannot be directly measured from the photon count rate response to  $\omega_d$ . Instead, the transient behavior in a ring-up measurement is used to characterize the mechanical linewidth  $\gamma_m$ .

The experimental procedure is very close to the one described in Sec. 6.3.1. The input laser is always blue-detuned by  $\omega_m$ . The major difference is that Shutter1 is controlled by a programmed trigger signal during the “hold” period, such that the input laser is sent to the optomechanical cavity for  $150 \mu\text{s}$  to  $200 \mu\text{s}$ , then it is shuttered by Shutter1 (and the

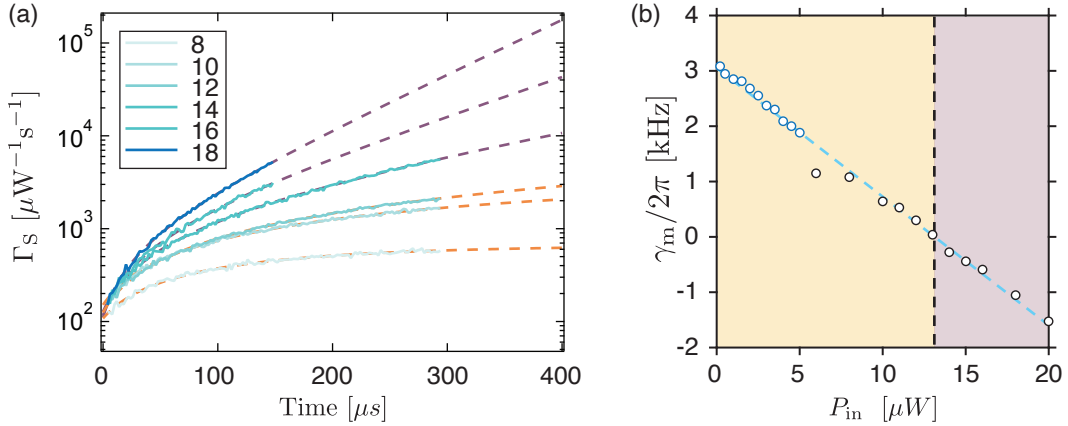


Figure 6.17: (a) The photon count rate as a function of the time right after the input is turned on for various  $P_{\text{in}}$  (shown in the legend in unit of  $\mu\text{W}$ ). The dashed lines are the fits described in the text, where purple and orange lines correspond to antidamping and damping effects, respectively. (b) The extracted linewidths  $\gamma_m$  (black circles) from the ring-up experiment as a function of  $P_{\text{in}}$ . Blue circles represent the linewidths measured in the frequency sweep measurements. The black dashed line is the instability threshold power  $P_{\text{threshold}}$ , the purple shaded area is the antidamping region, and the beige shaded area is the damping region.

VOA) for another 4 ms. This process is repeated during the entire ‘‘hold’’ period, *i.e.*, 21 times every 200 ms (including the ‘‘lock’’ time). The 4 ms waiting time is necessary to initialize the mechanical state to the thermal state of the lowest occupancy before the next drive.

Figure 6.17(a) shows the power-normalized count rates after sending the input laser to the optomechanical cavity for various input power  $P_{\text{in}}$ . We repeated  $\sim 10^5$  times such pulsed drives for each power to generate each trace in Fig. 6.17(a). The time bin we choose in this case is 2  $\mu\text{s}$ . As you can see, the photon count rate keeps exponentially increasing for  $P_{\text{in}} \geq 14 \mu\text{W}$  (purple dashed lines) in Fig. 6.17(a).

The mechanical linewidth can be extracted from the fit to the equation:  $\Gamma_S(t) = \Gamma_{\text{bkg}} + \Gamma_{\text{PA}} \exp[-2\pi\gamma_m t]$ , represented by the black circles in Fig. 6.17(b). The blue circles are the measured linewidths by the approach described in Sec. 6.3.2.2. The consistency between the two approaches in describing Eq. 6.32 proves this negative mechanical linewidth is an extension of the optomechanical-induced damping effect and the system is still well suited in the linear optomechanical regime. All measured linewidths are fit to Eq. (6.32) to extract the bare mechanical linewidth  $\gamma_m/2\pi = 3.05(4)$  kHz and the threshold power for instability  $P_{\text{threshold}} = 13.1(4)$   $\mu\text{W}$  (black dashed line in Fig. 6.17(b)). The antidamping rings up the mechanical mode to a limit cycle, a phenomenon known as the mechanical lasing [91].

## 6.4 Characterizing Weakly Coupled Mechanical Modes

For a given optical mode  $(q, 0, 0)$ , besides the mainly coupled mechanical mode  $(2q, 0, 0)$ , other mechanical modes are also weakly coupled to the optical mode, as discussed in Sec. 5.4.2. The measured frequencies of these mechanical modes are briefly described in Sec. 6.2.2. This section provides more details regarding the characterization of these weakly coupled mechanical modes and their single-photon coupling rates to this given optical mode.

In the experiment, we used the optical setup described in Sec. 6.1.3. A schematic of the optical setup is shown in Fig. 6.12(a). The expected mechanical frequency  $\hat{\omega}_m$  is determined by Eq. (6.7). The drive tone is placed at  $\Delta = -\hat{\omega}_m/2$ , which is then split into two arms in Fig. 6.4. The unshifted arm has an optical output power  $P_1 \approx 300 \text{ nW}$ . The RF signal of the frequency  $\omega_d$  from the LIA is fixed at  $-4 \text{ dBm}$ , which is then amplified to  $30.4 \text{ dBm}$  (near the maximal allowed RF power) before being sent to the AOM. The optical output power  $P_2$  of the AOM is also around  $\sim 300 \text{ nW}$  with the frequency  $-\hat{\omega}_m/2 + \omega_d$  (the optical input to the AOM is fixed, the change of the output power  $P_2$  is due to the frequency dependence of the AOM, as described in Sec. 6.1.3.1.). This way, for a fixed total input power, the modulation depth of their beat note is maximized to enhance the optical drive force. A probe laser with  $P_{in} = 4 \mu\text{W}$  (except for  $(\pm 2, 0)$  modes, where  $P_{in} = 1 \mu\text{W}$ ) is placed at detuning  $\Delta = -\hat{\omega}_m$  to monitor the mechanical mode. A schematic of the frequency spectrum is shown in Fig. 6.12(b).

The drive frequency  $\omega_d$  is swept around the expected mechanical frequency  $\hat{\omega}_m$  to search for the photons that are scattered by these other mechanical modes and which pass through the filter cavities. This sweep is achieved by changing the RF output frequency from the LIA during the “lock” period. In a typical sweep, we take 500 - 2000 steps with a step size of 100 Hz (a sweeping span of 50 - 200 kHz) near the predicted mechanical resonance frequency. The same sweep is repeated for 5-15 hours to enhance the visibility of the expected sideband. The average count rate during the “hold” for each frequency is then recorded. We discarded the data in the first 5 ms of the DAq period (during the “hold” period) to avoid the transient behavior of the driven mechanical mode.

The scattered count rate is

$$\Gamma(\omega_d, P_1, P_2)|_{\Delta=-\hat{\omega}_m} = P_{in}\gamma_{AS}\eta_\kappa\eta_{det} \propto P_{in}g_0^2n_m(\omega_d, P_1, P_2), \quad (6.34)$$

where  $g_0$  is the photoelastic coupling rate<sup>31</sup>.

The phonon number  $n_m$  can be decomposed as

$$n_m = n_{m,th} + n_{m,d}, \quad (6.35)$$

---

<sup>31</sup>The photothermal coupling doesn't change the output field spectrum [204].

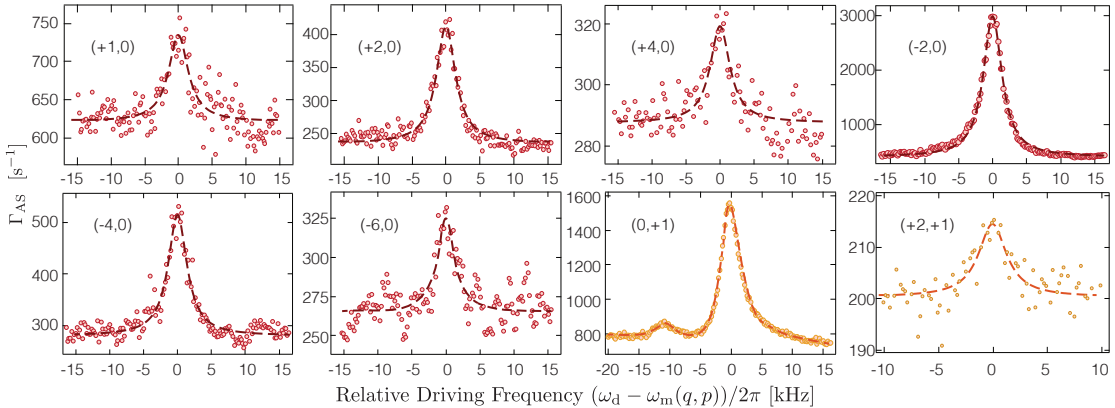


Figure 6.18: Spectrum of all weakly coupled mechanical modes. Circles represent measured results, and dashed lines are the corresponding fits to a Lorentzian. Gaussian modes are shown in red, and transverse modes ( $q = 1$ ) are shown in orange. The frequency is shifted to the corresponding resonance frequency extracted from the fit, whose values are shown in Fig. 6.12(d). The mode index shown in this figure is relative to the mainly coupled mechanical mode  $(182, 0)$ . For example,  $(+2, +1)$  represents mode  $(182+2, +1)$ .

where  $n_{m,\text{th}}$  are independent on  $\omega_d$  and the driven phonon number  $n_{m,d}$  follows

$$n_{m,d} \propto \frac{(g_0 + g_{\text{pt}})^2 P_1 P_2 \gamma_m}{(\omega_d - \omega_m)^2 + \gamma_m^2/4}, \quad (6.36)$$

where  $g_{\text{pt}}$  is the photothermal coupling rate. As discussed in Eq. (5.25),  $g_{\text{pt}}$  enters the equation for the mechanical motion by replacing  $g_0$  with  $g_0 + g_{\text{pt}}$ . In our case we have  $\omega_m \gg \kappa$ , thus  $g_{\text{pt}}$  is approximately purely imaginary.

Notably,  $g_{\text{pt}}$  is irrelevant to the discussion of the single-mode coupling in Sec. 5.4.1 due to its different coupling mechanism.  $g_{\text{pt}}$  of this system is measured to be around 1/4 of the total coupling rate in this device [203, 204]. Applying the relation  $|g_0| \ll |g_{\text{pt}}|$ , for all weakly coupled mechanical modes, Eq. (6.34) can be approximated as

$$\Gamma(\omega_d, P_1, P_2)|_{\Delta=-\omega_m} \propto P_{\text{in}} \frac{g_0^2 g_{\text{pt}}^2 P_1 P_2 \gamma_m}{(\omega_d - \omega_m)^2 + \gamma_m^2/4} + \Gamma_{\text{bkg}}, \quad (6.37)$$

where  $\Gamma_{\text{bkg}}$  includes all  $\omega_d$  independent count rates. The amplitude of the Lorentzian in this response is proportional to  $P_{\text{in}} g_0^2 g_{\text{pt}}^2 P_1 P_2 / \gamma_m$ , which can be used to determine the single photon coupling strength  $g_0$  (photoelastic). The dynamic backaction of this given input power is negligible for all weakly coupled mechanical modes. Notice that for the mainly coupled mode, this amplitude is proportional to  $P_{\text{in}} g_0^2 (g_0 + g_{\text{pt}})^2 P_1 P_2 / (\gamma_m + \gamma_{\text{opt}})$ , instead.

Figure 6.18 shows the count rate response to  $\omega_d$  of all measured weakly-coupled

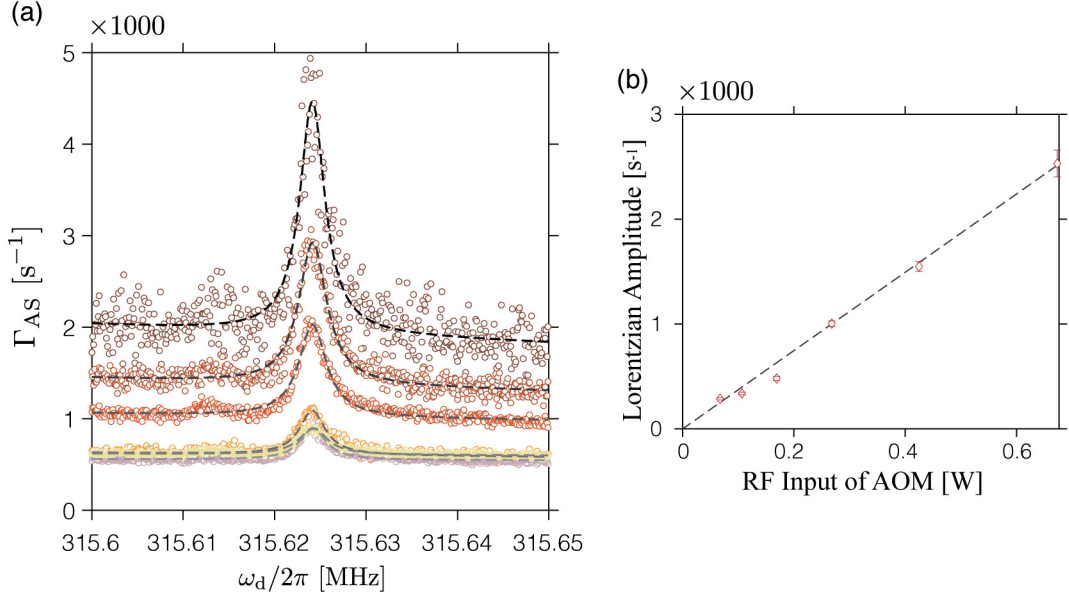


Figure 6.19: (a) The count rate response to  $\omega_d$  at various RF input powers, whose values are provided in (b). Dashed lines are the corresponding fit to a Lorentzian. (b) The extracted Lorenzian amplitudes as a function of the RF input power. The black dashed line represents a fit to a proportional function.

modes. Each count rate response is fit to a Lorentzian to extract the amplitude and the linewidth<sup>32</sup>. The extracted resonance frequencies are shown in Fig. 6.12(d). The extracted linewidth of each mechanical mode is roughly independent of the mode index. Their mean linewidth  $\bar{\gamma}_m/2\pi = 3.4(2)$  kHz is consistent with the linewidth of the mainly coupled mode (182, 0).

The extracted count rate amplitude is compared to the amplitude of the mainly coupled mode to characterize  $g_0$  of each mechanical mode. Here, we used the result  $g_{pt}/2\pi = i0.8(1)$  kHz from Refs. [203, 204] and the coupling strength  $\sqrt{|g_0(g_0 + g_{pt})|}/2\pi = 4.58$  kHz from Sec. 6.3.2.1. The extracted  $g_0$  are shown in Fig. 5.7, where those values agree with the numerical results discussed in Sec. 5.4.2.

We also characterize the drive power dependence for one of the weakly coupled mode (182, 1) by varying the RF input power to the AOM. Figure 6.19(a) illustrates the photon count rate spectra of the drive frequency  $\omega_d$  for six different AOM RF input powers, where  $P_1 = 300$  nW and the probe optical power  $P_{in} = 1$   $\mu$ W. Each trace is fit to a Lorentzian to extract the resonance frequency, the linewidth and the amplitude. The extracted resonance frequency and linewidth of this mechanical mode are independent of the drive power, whose average values are  $\bar{\omega}_m(182, 1)/2\pi = 315.624\,16(4)$  MHz and  $\bar{\gamma}_m(182, 1)/2\pi = 3.5(2)$  kHz, respectively. The extracted amplitudes are proportional to the AOM power, as

<sup>32</sup>Except for the mechanical mode (0, +1), which is fit to a sum of two Lorentzians. The splitting is caused by modes' polarization dependence.

shown in Fig. 6.19(b).

*“The ‘paradox’ is only a conflict between reality and your feeling of what reality ‘ought to be’”*

– Richard Feynman

# CHAPTER 7

## Thermal States and Phonon Added/Subtracted States

In this chapter, we demonstrate how to utilize the aforementioned knowledge of the system to optically measure the mechanical resonator. Specifically, we use statistics of the Stokes and anti-Stokes scattered light to capture the mechanical state. Rather than treating SNSPDs as ultra-sensitive photodetectors, we analyze the statistics of photon arrival times to reveal coherences of the mechanical phonons up to the fourth order. Our measurements verified with a high degree of statistical significance that the mechanical mode is in thermal equilibrium with a bath through a Markovian coupling. It should be noted that the thermal state is insignificant in revealing quantum features, as discussed in Sec. 3.5.2. This proof-of-principle demonstration shows the system’s capability to measure the mechanical mode in the quantum regime by using the quantum statistics of scattered photons.

Additionally, by post-selecting photon detection events, we are able to measure coherences in the mechanical resonator when up to three phonons have been added to or subtracted from the thermal state. This measurement-induced-backaction nonlinearity projects a Gaussian state into a non-classical state, and in principle, the observer can track measurement results to control the wavefunction trajectory [87, 88, 249, 252]. The analysis protocol presented in this chapter can also be adapted to the analysis in Chapter 8 and Chapter 9.

### 7.1 Measuring the Motional State by the Light

This section focuses on relating the measured photon arrival times to the state of the mechanical resonator. In the resolved-sideband regime, the anti-Stokes or Stokes scattering process can be selected by placing the optical input at either  $\Delta = -\omega_m$  or  $\Delta = +\omega_m$  as discussed in Sec. 2.3. The filter cavities reject almost all undesirably scattered or unscattered photons but leave only photons from the desired scattering process, as discussed in Sec. 6.3.1.2. This is the key to measuring the mechanical state faithfully.

### 7.1.1 Photon-Phonon Correspondence

In this section, we demonstrate the one-to-one correspondence between the coherences of the optical fields output by the cavity and the coherences of the phonons. The scattering Hamiltonian is given as

$$H_{\text{AS}} = -\hbar g \left( \hat{a}^\dagger \hat{b} + \hat{a} \hat{b}^\dagger \right), \quad (7.1\text{a})$$

$$H_{\text{S}} = -\hbar g \left( \hat{a}^\dagger \hat{b}^\dagger + \hat{a} \hat{b} \right). \quad (7.1\text{b})$$

As discussed in Sec. 2.3, the anti-Stokes or Stokes scattering process uniquely associates the annihilation or creation of one phonon with the creation of one on-resonance photon, respectively. The photon later exits the cavity, passes through the filter cavities, and is measured by SNSPDs.

This relation is summarized as the following:

$$\text{anti-Stokes Scattering } \Delta = -\omega_m : \hat{b} \Leftrightarrow \hat{a}_{\text{AS}}^\dagger|_{\text{cavity}} \Leftrightarrow \hat{a}_{\text{AS}}|_{\text{SNSPD}}, \quad (7.2)$$

$$\text{Stokes Scattering } \Delta = +\omega_m : \hat{b}^\dagger \Leftrightarrow \hat{a}_{\text{S}}^\dagger|_{\text{cavity}} \Leftrightarrow \hat{a}_{\text{S}}|_{\text{SNSPD}}, \quad (7.3)$$

where  $\hat{a}_{\text{AS(S)}}$  denotes the photon created by the anti-Stokes(Stokes) scattering process, and we emphasize the location in the subscript to distinguish different operations on the same state. Therefore, the measured normally ordered photon correlation  $\langle \hat{a}^\dagger \hat{a} \rangle$  corresponds to the normally ordered phonon correlation  $\langle \hat{b}^\dagger \hat{b} \rangle$  or the anti-normally ordered phonon correlation  $\langle \hat{b} \hat{b}^\dagger \rangle$  for anti-Stokes and Stokes scattering processes.

This one-to-one proportionality provides us access to unravel the statistics of the mechanical state through photon measurements. The photon acts like an instant acoustic readout because  $\gamma_m \ll \kappa$  and  $n_{\text{cav,th}} \ll 1$ . For any consecutive photon measurements with delay  $\tau \gg 1/\kappa$ , photons are not correlated by the optical cavity. On the other side, the consecutive photon measurements within  $t \lesssim 1/\gamma_m$  project the mechanics on a trajectory of its state. This mechanical state can be later read out through the anti-Stokes scattering. In this spirit, the mechanical resonator serves like a quantum memory [11].

Furthermore, we can alternate the scattering process between the anti-Stokes and Stokes processes in a pulsed input scheme and then measure the correlation of the on-resonance photons, such as  $\langle \hat{a}_{\text{AS}}^\dagger \hat{a}_{\text{S}}^\dagger \hat{a}_{\text{S}} \hat{a}_{\text{S}} \hat{a}_{\text{AS}} \rangle$ . This photon correlation is associated with the following phonon correlation:

$$\langle \hat{a}_{\text{AS}}^\dagger \hat{a}_{\text{S}}^\dagger \hat{a}_{\text{S}} \hat{a}_{\text{S}} \hat{a}_{\text{AS}} \rangle \Leftrightarrow \langle \hat{b}^\dagger \hat{b} \hat{b}^\dagger \hat{b}^\dagger \hat{b} \rangle. \quad (7.4)$$

Along this line, arbitrarily ordered phonon correlations can be measured by the scattered light.

Note that during the detection, most of the photons are lost with overall measurement

efficiency  $\eta_\kappa \eta_{\text{det}}$ . The measured photon correlation will be scaled by a factor of  $(\eta_\kappa \eta_{\text{det}})^n$  compared to the corresponding  $n$ -th order phonon correlation. The optical losses along the detection chain do not compromise any specific feature in the coherence measurements (as the coherence is the normalized correlation as discussed in Sec. 3.1.2 [75]), but simply yield larger uncertainties.

Through this discourse, it becomes clear that the term “state-swap interaction” serves as a more fitting alternative designation for the anti-Stokes scattering Hamiltonian. The normally ordered measured photon correlation is observed to be precisely congruent to the normally ordered phonon correlation.

The formal treatment is well illustrated in the results of Eq. (6.15) and (6.16). Note that high-order time-dependent correlations can be evaluated in terms of such two-time correlations using Wick’s theorem for any Gaussian state, thereby implying the correspondence of the detected optical coherences and the appropriately ordered phonon coherence as a function of the delaying time. The proportionality constant  $\gamma_m C$  in Eq. (6.15) and (6.16) is immaterial for the coherence, as it is normalized in the calculation of coherences.

### 7.1.2 Characterizing the Quantum Sideband Asymmetry

Quantum sideband asymmetry (QSA) is the difference in the amplitudes of the two mechanical sidebands. As shown in Eq. (6.15) and (6.16), this difference is associated with the zero-point fluctuation of the mechanical resonator (details c.f. Sec. 2.3.2). Thereby, this difference, which is precisely equivalent to one phonon, can be utilized as a calibration of the phonon number. This approach is known as the quantum thermometer, and has been experimentally demonstrated in Refs. [57, 72, 75, 91, 92].

The phonon number can be evaluated as

$$n_m = \frac{\Gamma_{\text{AS}}}{\Gamma_S - \Gamma_{\text{AS}}}, \quad (7.5)$$

which is independent of the measurement efficiency. The measured asymmetrical count rate  $\Gamma_{\text{QSA}} = \Gamma_S - \Gamma_{\text{AS}}$  is further used to calibrate the phonon occupancy

$$n_m = \frac{\Gamma_{\text{AS}}}{\Gamma_{\text{QSA}}}, \quad (7.6a)$$

$$n_m = \frac{\Gamma_S}{\Gamma_{\text{QSA}}} - 1, \quad (7.6b)$$

where we assume the measurement efficiency is fixed.

In the experiment discussed Sec. 6.3.2.1, the QSA is indirectly presented in the anti-Stokes and Stokes count rates. To eliminate the asymmetry caused by the optomechanical dynamical backactions, the optical input power is set to be  $P_{\text{in}} = 250 \text{ nW}$  in this experiment. This is justified by the fact that the optomechanical backactions, as well as the

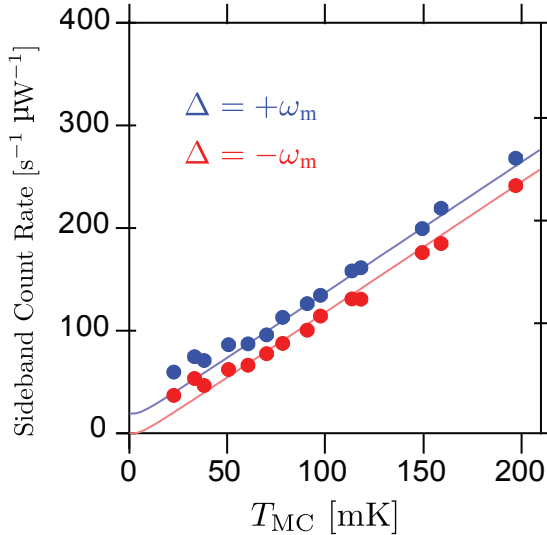


Figure 7.1: The sideband count rates as a function of  $T_{MC}$ . The constant difference in the count rate is a result of the quantum sideband asymmetry. The solid lines are corresponding fits described in the text.

heating effect, are negligible when  $P_{in} < 300 \text{ nW}$ , as shown in Fig. 6.16.

Figure 7.1 shows the experimental result for  $\Gamma_{AS}$  and  $\Gamma_S$  as a function of  $T_{MC}$ . The values of  $\Gamma_{AS}$  and  $\Gamma_S$  are extracted from fitting five-point spectra as described in Sec. 6.3.1.2. The values of  $T_{MC}$  are read from the cryostat's RuO<sub>2</sub> thermometer. Both  $\Gamma_{AS}$  and  $\Gamma_S$  increase with  $T_{MC}$  as expected, and the persistent difference between the two is consistent with the quantum sideband asymmetry. The solid lines in Fig. 7.1 show a one-parameter fit to the form  $a(e^{\hbar\omega_m/k_B T_{MC}} - 1)^{-1}$  (for the red data) and  $a(1 + (e^{\hbar\omega_m/k_B T_{MC}} - 1)^{-1})$  (for the blue data), where the fit parameter  $a = \gamma_m C \eta_\kappa \eta_{det} / P_{in}$  is the magnitude of the power-normalized QSA. The fit only uses data with  $T_{MC} > 50 \text{ mK}$ , as the calibration of the RuO<sub>2</sub> thermometer used to determine  $T_{MC}$  is uncertain at lower temperatures. The agreement between data and theory at various  $T_{MC}$  in Fig. 7.1 proves the persistent difference is the QSA instead of some unknown systematical artificial effects and indicates that the mean phonon occupancy  $n_m$  is primarily determined by  $T_{MC}$ .

We can also infer the mixing chamber base temperature from the sideband asymmetry in the pulsed experiment, where the heating effect is negligible. The measurement shown in Fig. 6.16(a) includes this data point at  $P_{in} = 0$ , which indicates  $T_{MC} \approx 20 \text{ mK}$ , consistent with our expectation.

## 7.2 Statistics from Photon Counts

In this section, we describe the method of constructing the coherences of photons from the arrival time data. The statistics of the photon arrival times possess rich information about the state of the mechanics.

### 7.2.1 Statistical Estimation of Coherence

In the experiment, the probability of a coincidence event for a given delay and the probability of a single detection event is used to determine the coherence function

$$g^{(2)}(\tau) = \frac{p(E(t) \cap E(t + \tau))}{p(E(t))p(E(t + \tau))}, \quad (7.7)$$

where  $E(t) \cap E(t + \tau)$  is the join event (coincidence), and  $E(t)$  is the marginal event (single). In the low event probability limit, *i.e.*,  $p \ll 1$ , the distribution of the coincidence events approximates as a Bernoulli distribution. Consequently, the maximum likelihood estimation (MLE) evaluates its underlying success probability for a Bernoulli distribution as  $\hat{p} = C/N$  in the case of obtaining  $C$  successes (counts) in  $N$  tries (details c.f. Appendix D). Here we use  $\hat{X}$  to denote the estimated value of  $X$ , to distinguish it from the true value  $X$ . The same notation applies to all the following. The number of tries is defined as  $N = T/\Delta t$ , where  $T$  is the total measurement time and  $\Delta t$  is the bin size. Therefore, the coherence can be reexpressed in the following way:

$$\hat{g}_{\text{ML}}^{(2)}(\tau) = \frac{\frac{C(E(t) \cap E(t + \tau))}{N}}{\frac{C(E(t))}{N} \frac{C(E(t + \tau))}{N}} = \frac{C(E(t) \cap E(t + \tau))}{C(E(t))C(E(t + \tau))} N, \quad (7.8)$$

where  $C(E)$  denotes the number of success events  $E$ . The only exception is the case when  $\tau \leq \Delta t$ , *i.e.*, considering the coincidence within the same bin (details c.f. Sec. 7.2.3.1).

In summary, a histogram of the number of coincidences for different delays  $\tau$  is sufficient to yield the estimated second-order coherence function  $\hat{g}_{\text{ML}}^{(2)}(\tau)$ . The discussion above can be extended to the higher-order coherence function straightforwardly.

### 7.2.2 Statistical Confidence of the Estimation

#### 7.2.2.1 Uncertainty of Likelihood Estimation

As we are using statistical results to interpret the phenomena, another crucial part of the analysis is to estimate their associated statistical uncertainties.

In the analysis, we use the likelihood function based on a Bernoulli distribution of

photon detection events in the limit of low probabilities to estimate the true value. Using results of the MLE for Bernoulli distribution  $\hat{p}(E) = C(E)/N$  and Slutsky's theorem, we have

$$\hat{g}_{E_1, E_2}^{(2)} \equiv \frac{C(E_1 \cap E_2)/N}{(C(E_1)/N)(C(E_2)/N)} \xrightarrow{\mathcal{P}} \frac{\langle I(E_1 \cap E_2) \rangle}{\langle I(E_1) \rangle \langle I(E_2) \rangle} \equiv g_{E_1, E_2}^{(2)}. \quad (7.9)$$

Here, the RHS is the true value we are trying to approach. The uncertainty of  $\hat{g}_{E_1, E_2}^{(2)}$  is dominated by that of the joint event probability (*i.e.*,  $\hat{p}(E_1 \cap E_2) \equiv C(E_1 \cap E_2)/N$ ) because this is the rarest event. As discussed in Appendix D, for the Bernoulli distribution in the large  $N$  limit, the confidence interval of this maximal likelihood estimator is

$$\hat{p} \pm c\sigma = \frac{C(E_1 \cap E_2)}{N} \pm c\sqrt{\frac{C(E_1 \cap E_2)(N - C(E_1 \cap E_2))}{N^2}}, \quad (7.10)$$

and the relative uncertainty is

$$\frac{\sigma}{\hat{p}} = \sqrt{\frac{(1 - \hat{p})}{\hat{p}n}} = \sqrt{\frac{(1 - \hat{p})}{C(E_1 \cap E_2)}}. \quad (7.11)$$

In the limit  $\lim \hat{p} \rightarrow 0$ , the relative uncertainty  $\sigma/\hat{p}$  approaches  $\sqrt{\frac{1}{C(E_1 \cap E_2)}}$ . This is similar to the result of the shot noise.

### 7.2.2.2 Unsymmetrical Confidence Intervals

The uncertainty evaluated above determines a symmetric Gaussian distribution in the estimator space, which is generally true if the law of large numbers (LLN) holds. Unfortunately, this interval performs poorly unless  $N$  is extremely large, and the actual coverage can be considerably less than the expected coverage ratio [253].

This symmetric confidence interval has two unfavorable features:

1. The upper/lower limit can stray outside the allowed parameter space, that is, one can get a lower limit less than 0 or an upper limit greater than 1;
2. If we happen to observe no successes ( $C = 0$ ) or no failures ( $C = N$ ), the interval becomes degenerate (has zero width) and misses the true parameter  $p$ . In practice, this event becomes quite likely when the actual  $p$  is close to 0 or 1. (Unfortunately, some of our data fall into this case)

There are a few methods to fix this issue by introducing skewed confidence intervals. In the following, I discuss a few of them:

**Nonparametric Bootstrap** The idea behind this method is to use one single set of data to generate more “independent” data sets. For the new data set, each experiment is randomly chosen from the result of the original data set till it has the same number of experiments as the original one. Numerically, you can have infinite “independent” data sets. By applying MLE to each data set, the statistic of  $\hat{p}$  appears.

**Variance-Stabilizing Transformation (VST)** The convergency of the estimated probability  $\hat{p}_n$  of a Bernoulli distribution in  $n$  trials is

$$\sqrt{n}(\hat{p}_n - p_0) \xrightarrow{\mathcal{D}} \text{Normal}(0, p_0(1 - p_0)), \quad (7.12)$$

where  $p_0$  is the true probability. The problem arises from the fact that the variance of the approached distribution depends on the true  $p_0$ , which is evaluated by the estimated  $\hat{p}_n$ . The deviation of  $\hat{p}_n$  from  $p_0$  results in different additional errors on the estimated upper and lower limits. The goal is to find a transformation that can eliminate this  $p_0$  dependence in the variance. Mathematically, we are seeking for  $h(p)$  such that

$$\sqrt{n}(h(\hat{p}_n) - h(p_0)) \xrightarrow{\mathcal{D}} \text{Normal}(0, 1). \quad (7.13)$$

For a Bernoulli distribution, this transform is

$$h(p) = \arcsin \sqrt{p},$$

and the corresponding confidence interval is

$$h(p_0) = h(\hat{p}) \pm c \frac{1}{\sqrt{n}}. \quad (7.14)$$

Therefore, the confidence intervals for parameter  $p$  is

$$p = [h^{-1}(h(\hat{p}) - c \frac{1}{\sqrt{n}}), h^{-1}(h(\hat{p}) + c \frac{1}{\sqrt{n}})]. \quad (7.15)$$

**Logistic Regression** Another point of view is that this asymmetry is caused by  $p_0$  being too close to the boundary of the parameter space. For the Bernoulli distribution, the definition domain of  $p$  is  $[0, 1]$ . However, in the confidence interval estimation, the distribution of  $p$  is approaching a Gaussian distribution, whose definition domain of  $p$  is  $(-\infty, \infty)$ .

We may be able to improve the quality of the approximation by applying a suitable reparameterization, a transformation of the parameter to a new scale. The idea behind the following transformation is that the loglikelihood function is skewed and

not very symmetric when  $\hat{p}$  is very close to 0 or 1.

The “logistic” or “logit” transformation is defined as

$$\phi = \log \frac{p}{1-p}. \quad (7.16)$$

Whereas  $p$  lies between 0 to 1,  $\phi$  maps  $p$  into  $-\infty$  to  $\infty$ . Therefore, the distribution of the reparameterized  $\phi(\hat{p})$  follows

$$\sqrt{n} (\phi(\hat{p}_n) - \phi(p_0)) \xrightarrow{\mathcal{D}} \phi'(\hat{p}_n) \text{Normal} (0, \delta(\hat{p}_n)^{-1}), \quad (7.17)$$

where  $\phi'(\hat{p}_n)$  is the Jacobian under this transformation.

For a Bernoulli distribution, this is

$$\sqrt{n} (\phi(\hat{p}_n) - \phi(p_0)) \xrightarrow{\mathcal{D}} \text{Normal} \left( 0, \frac{1}{\hat{p}(1-\hat{p})} \right). \quad (7.18)$$

Solving Eq. (7.16) for  $p$  yields the back-transformation

$$p = \frac{e^\phi}{1 + e^\phi}. \quad (7.19)$$

This back-transformation can be used to generate the corresponding confidence intervals for  $p$ .

It is worth noting that the method used in Ref. [75] lacks rigorous statistical justification. One simple argument is that  $L(\hat{p}, C, N)$  is the probability of finding  $C$  counts in  $N$  tries, which is not equivalent to the probability of  $\hat{p}$  being true in the estimator space  $\{\hat{p}\} \in [0, 1]$ .

### 7.2.2.3 Hypothesis Tests

To use statistical results to verify or violate certain assumptions, another approach is the null hypothesis test.

Suppose the null hypothesis is that photons are all uncorrelated, *i.e.*  $g^{(2)}(0) = 1$ . The actual fact is the photons are from a thermal state with  $g^{(2)}(0) = 2$ . Therefore, the  $p$ -value, the probability of observing this or more extreme results given that the null hypothesis is true, satisfies

$$p = \Pr \left( g^{(2)}(0) \geq g_{\text{act}}^2(0) = 2 | g_{\text{null}}^{(2)} = 1, N \right) \ll 1, \quad (7.20)$$

where  $N$  denotes the number of tries.

### 7.2.3 Constructing the Photon Coherences

This section introduces the protocol we used to construct the photon coherence functions from the photon arrival time data. In the analysis, the data collected from the two SNSPDs are combined to construct the coherence function unless otherwise specified. This is justified in the discussion in Sec. 7.2.3.1. Some types of unwanted data are identified prior to the analysis and removed according to the protocol described in Sec. 6.1.4.

The first-order correlation is simply counting the number of photons received in a unit of time, *i.e.*, the photon count rate. The uncertainty of the count probability can be estimated by the method discussed in Sec. 7.2.2.1.

The second-order photon coherences are constructed in the following way:

1. Track each photon's arrival time and record the time-delay  $\tau$  between this photon and all succeeding photons with a maximal delay time  $T_{\max}$  we are interested in;
2. Bin the recorded delay time with a resolution of  $\Delta t_{\text{bin}}$  and construct a histogram of the number of total coincidences within each bin (the delay time is the mean delay of each bin);
3. Normalize the histogram of the number of coincidences by the corresponding count probability, as given in Eq. (7.8);
4. Subtract some known systematic imperfections from the measured second-order coherence. (These are discussed in Sec. 7.2.4)

Note that an alternative way to construct the coincidence histogram is binning the arrival time first and then counting the delay between each bin. This method is not identical to the method above, as it effectively applies a moving average transfer function of one bin size to the final coherence function.

#### 7.2.3.1 Constructing the Coherence from a Single-photon Detector

It is relatively straightforward to calculate the correlation of photon measurements from separate photon detectors after a beam splitter. The question is: “when there is only one photon detector, can we still measure photon coherences?” In principle, the answer is “Yes, we can”, as the correlation measurement only depends on the state of the light. This section discusses the details of how to construct coherences from one SNSPD.

##### 7.2.3.1.1 Calculating Correlations from a single-photon detector

To show the difference between using one SNSPD and multiple SNSPDs in measuring coherences, let us consider the following example. When we measure  $g^{(2)}(0)$  using one

single-photon detector of a Fock number state  $|n\rangle$ , we have

$$\langle n|\hat{a}^\dagger(0)\hat{a}^\dagger(\tau)\hat{a}(\tau)\hat{a}(0)|n\rangle = n(n-1). \quad (7.21)$$

Seemingly, this result is not equal to the auto-correlation of the same bin, whose value is  $\langle I(0)I(0) \rangle = n^2$ . This contradiction is caused by the limit of the single detector: it can't measure the zero delay correlation.

The correlation is a result of the correlated consecutive measurements in the same state. Therefore, the correct way to measure  $g^{(2)}(0)$  using one ideal single-photon detector should be

$$\lim_{\delta t \rightarrow 0} \langle n(0)n(\delta t) \rangle. \quad (7.22)$$

The way to interpret results in Eq. (7.21) is: the first  $n$  is the first measurement, and the second  $(n-1)$  is the result of the second correlated measurement in zero delay time.

In the analysis, we use the same time tag to represent all counts in a bin. There could be multiple counts in the same bin if the bin size  $\Delta t_{\text{bin}} > \tau_D$ , where  $\tau_D$  is the detector dead time. Consider a sequence of signals within  $\Delta t$  in the time order of  $s_1, s_2, s_3 \dots, s_n$ . The total counting  $n$  in this time interval is  $\sum_{i=1}^n s_i$ . So the number of correlated measurements is

$$\begin{aligned} \sum_{i>j} s_i s_j &= \frac{1}{2} \left( \left( \sum_{i=1}^n s_i \right)^2 - \sum_{i=1}^n s_i^2 \right) = \frac{1}{2} (n(0)^2 - \sum_{i=1}^n s_i^2) \\ &\approx \frac{1}{2} (n(0)^2 - n(0)). \end{aligned} \quad (7.23)$$

The last approximation is achieved from the assumption that the detected photon number at each time is either zero or one, *i.e.*,  $s_i \in \{0, 1\}$ .

On the other hand, the effective bin size of the correlation measurement is modified by two factors: 1.  $\sum_{i>j} s_i s_j$  requires  $t_i > t_j$ ; and 2. The detector's dead time  $\tau_D$ . Taking account of these two correction effects, the zero-delay second-order coherence is

$$g^{(2)}(0) = \lim_{\delta t \rightarrow 0} \frac{\langle I(0)I(\delta t) \rangle}{\langle I(0) \rangle \langle I(\delta t) \rangle} = \frac{\langle n(n-1) \rangle}{\langle n \rangle^2} \cdot \frac{\Delta t}{\Delta t - \tau_D}. \quad (7.24)$$

#### 7.2.3.1.2 Limits of Single-Photon Detectors

Finally, I want to address that the discussion above is not a faithful way to measure the zero-delay correlation because we have assumed  $\lim_{\delta t \rightarrow 0} g^{(2)}(\delta t) = g^{(2)}(0)$ . In principle, there is no problem with using one detector to measure the delayed coherence  $g^{(2)}(\tau)$ .

Another problem is the inability to resolve the number of photons in single-photon detectors. For example, when measuring the correlation of a  $|2\rangle$  Fock state in a setup with two single-photon detectors as shown in Fig. 6.13(a), each detector is unable to distinguish

two photons from one photon. The measured second-coherence is expected to be

$$g_{\text{exp}}^{(2)} = \frac{4 \times 1/8}{((2 \times 1 + 4 \times 1)/8)^2} = \frac{8}{9} \neq \frac{1}{2}. \quad (7.25)$$

In general, to fully reconstruct the entire state, we need a number-resolved photon detector.

One detour is applying the source state (whose coherence time  $\tau_c \gg \tau_D$ ) to a very lossy channel before it reaches the single-photon detector. In this way, the probability of a large-number state is exponentially suppressed. Because the coherence function is independent of the measurement efficiency [75], the measured coherence will approach the true value when the efficiency approach to zero. That is

$$\lim_{\eta \rightarrow 0} g_{\text{exp}}^{(2)}(\tau) = g^{(2)}(\tau). \quad (7.26)$$

## 7.2.4 Subtracting Systematic Imperfections

Systematic imperfections compromise the measured coherence functions. In this section, we discuss four known systematic effects on the measurements and provide methods to subtract these effects.

### 7.2.4.1 Finite Acquisition Time

In each “hold” configuration as discussed in Sec. 6.1.2, we have roughly  $T_{\text{aq}} \approx 90$  ms data acquisition time to record photon arrival time. If the delay time we are interested in is  $\tau = \tau_2 - \tau_1 \ll T_{\text{aq}}$ , this finite size effect is negligible in most cases. However, for a delay  $\tau \sim T_{\text{aq}}$  or the measurement of the coherence is sensitive to the order of  $\tau/T_{\text{aq}}$ , this finite size effect should be corrected.

As shown in Fig. 7.2, for the coincidence measurement, as we require the delay  $\tau \geq 0$ , the effective measurement time is reduced by a factor of  $(T_{\text{aq}} - \tau)/T_{\text{aq}}$ . The measurement time of the single count measurement is still  $T_{\text{aq}}$ . To compensate for this finite size effect, the measured  $g^{(2)}(\tau)$  is corrected by a factor  $(T_{\text{aq}} - \tau)/T_{\text{aq}}$ . The increased uncertainty of the MLE in this process is only associated with the reduced number of tries for the coincidence with long delays  $\tau$ .

### 7.2.4.2 Background Photon Counts

This section describes the method used to correct the coherence functions for the presence of background counts in the SNSPD data. As described in Sec. 6.1.4, these background counts result from stray light, leakage through the filter cavities, and the SNSPD’s dark counts.

We characterize these background counts to have a fixed mean arrival rate over the duration of the experiments and to be uncorrelated among themselves, *i.e.*, they are Poisson

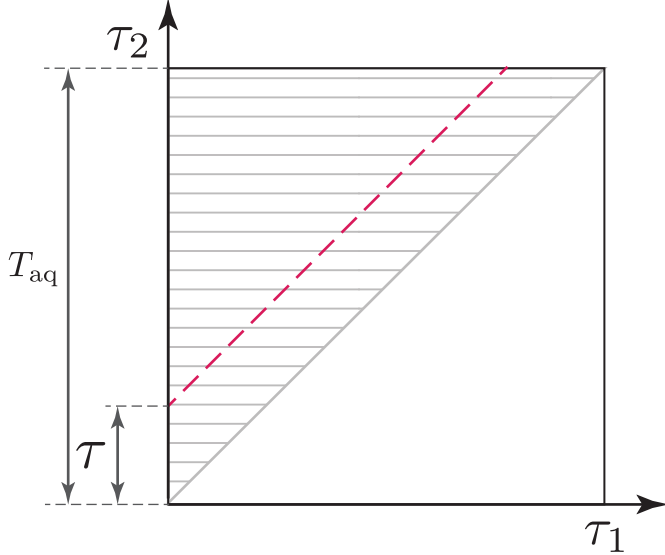


Figure 7.2: A schematic of the finite data acquisition time in the measurement.  $\tau_1$  and  $\tau_2$  represent the arrival time of the first and the second photons, respectively. Only the grey lined area is allowed, where  $\tau_2 \geq \tau_1$ . The red dashed line represents the effective measurement time if the delay is  $\tau_2 - \tau_1 = \tau$ .

distributed ( $g^{(2)}(\tau) = 1$ ). We also assume them to be independent of the sideband photons. Therefore, the measured second-order coherence function  $g_{\text{exp}}^{(2)}(\tau)$ , including the cross-coherences between the sideband photons and the background photons, is given by

$$g_{\text{exp}}^{(2)}(\tau) = \frac{\langle [\hat{a}^\dagger + \hat{\xi}^\dagger](0)[\hat{a}^\dagger + \hat{\xi}^\dagger](\tau)[\hat{a} + \hat{\xi}](\tau)[\hat{a} + \hat{\xi}](0) \rangle}{\langle [\hat{a}^\dagger + \hat{\xi}^\dagger](0)[\hat{a} + \hat{\xi}](0) \rangle \langle [\hat{a}^\dagger + \hat{\xi}^\dagger](\tau)[\hat{a} + \hat{\xi}](\tau) \rangle} = \frac{g^{(2)}(\tau) + 2\epsilon + \epsilon^2}{(1 + \epsilon)^2}, \quad (7.27)$$

where  $\hat{a}$  and  $\hat{\xi}$  correspond to the sideband and background photons, respectively, and we have used the independence relation  $\langle \hat{a}^\dagger \hat{\xi} \rangle = 0 = \langle \hat{\xi}^\dagger \hat{a} \rangle$ , and the uncorrelated relation  $\langle \hat{\xi}^\dagger(0)\hat{\xi}^\dagger(\tau)\hat{\xi}(\tau)\hat{\xi}(0) \rangle = \langle \hat{\xi}^\dagger \hat{\xi} \rangle^2 = n_{\text{bkg}}^2$ . Here,  $\epsilon = \langle \hat{\xi}^\dagger \hat{\xi} \rangle / \langle \hat{a}^\dagger \hat{a} \rangle$  is the ratio of the mean background and sideband count rates. For the optical powers used in all experiments,  $0.04 \lesssim \epsilon \lesssim 0.2$ .

The corrected second-order coherence function  $g^{(2)}(\tau)$  is thus

$$g^{(2)}(\tau) = g_{\text{exp}}^{(2)}(\tau) + 2(g_{\text{exp}}^{(2)}(\tau) - 1)\epsilon + (g_{\text{exp}}^{(2)}(\tau) - 1)\epsilon^2. \quad (7.28)$$

A similar calculation gives the corrected third-order and fourth-order coherence functions

$$g_{\text{exp}}^{(3)}(\tau_1, \tau_2) = \frac{g^{(3)}(\tau_1, \tau_2) + \epsilon (g^{(2)}(\tau_1) + g^{(2)}(\tau_2) + g^{(2)}(\tau_1 + \tau_2)) + 3\epsilon^2 + \epsilon^3}{(1 + \epsilon)^3}, \quad (7.29)$$

$$g_{\text{exp}}^{(4)}(\tau_1, \tau_2, \tau_3) = \frac{g^{(4)}(\tau_1, \tau_2, \tau_3) + \epsilon \sum_{g_i^{(3)} \in \mathbb{G}^{(3)}} g_i^{(3)} + \epsilon^2 \sum_{g_j^{(2)} \in \mathbb{G}^{(2)}} g_j^{(2)} + 4\epsilon^3 + \epsilon^4}{(1 + \epsilon)^4}, \quad (7.30)$$

where  $\mathbb{G}^{(3)}$  and  $\mathbb{G}^{(2)}$  are

$$\begin{aligned} \mathbb{G}^{(3)} &= \{g^{(3)}(\tau_1, \tau_2), g^{(3)}(\tau_1 + \tau_2, \tau_3), g^{(3)}(\tau_1, \tau_2 + \tau_3), g^{(3)}(\tau_2, \tau_3)\}, \\ \mathbb{G}^{(2)} &= \{g^{(2)}(\tau_1), g^{(2)}(\tau_2), g^{(2)}(\tau_3), g^{(2)}(\tau_1 + \tau_2), g^{(2)}(\tau_2 + \tau_3), g^{(2)}(\tau_1 + \tau_2 + \tau_3)\}. \end{aligned}$$

The statistical uncertainty of this process mainly comes from the uncertainty of the background count rate estimation. In practice, we use the estimated background count rate  $\hat{n}_{\text{bkg}}$  to replace the true background count rate  $n_{\text{bkg}}$ . This process will propagate the error of this estimation into the final estimation of the coherence function.

The background photon count rate is low enough that the background photon count follows the Bernoulli distribution. The probability  $p$  of this Bernoulli distribution can also be estimated by the MLE, which gives

$$\hat{p} = \hat{n}_{\text{bkg}} = \frac{C_{\text{bkg}}}{N_{\text{bkg}}}; \quad \delta\hat{p} \approx \sqrt{\frac{\hat{p}(1 - \hat{p})}{N_{\text{bkg}}}}, \quad (7.31)$$

where  $\hat{p}$  is the estimated probability of the background count, and  $N_{\text{bkg}}$  is the number of tries for the background count measurement. This uncertainty propagates into the coherence function, for instance  $g^{(3)}(\tau_1, \tau_2)$ , as

$$\begin{aligned} \delta g^{(3)}(\tau_1, \tau_1 + \tau_2) &= \sqrt{\frac{(1 - \hat{p})}{\hat{p}N_{\text{bkg}}} \epsilon (g^{(2)}(\tau_1) + g^{(2)}(\tau_2) + g^{(2)}(\tau_1 + \tau_2) - 3g^{(3)}(\tau_1, \tau_2))} \\ &\approx \sqrt{\frac{1}{C_{\text{bkg}}} \epsilon (g^{(2)}(\tau_1) + g^{(2)}(\tau_2) + g^{(2)}(\tau_1 + \tau_2) - 3g^{(3)}(\tau_1, \tau_2))}. \end{aligned} \quad (7.32)$$

In the last step, we use the small probability approximation  $p \rightarrow 0$ .

In summary, we cannot distinguish the scattered photons and other unwanted photons, such as dark photons, leaked photons and stray photons, from the data. However, we can correct the measured coherence function by measuring the ratio of the mean background

and sideband count rates at the cost of increased uncertainty.

#### 7.2.4.3 Systematic Drifts

The drifts of the system, such as laser power fluctuations or filter cavity transmissivity fluctuations, can also affect the measured coherence functions.

Considering an overall dimensionless intensity  $I(t)$  of the signal, the estimated probability of the joint event in Eq. (7.7) is modified as

$$\hat{p}((E(t) \cap E(t + \tau)) \xrightarrow{\mathcal{P}} \frac{\int I(t)I(t + \tau)dt/T}{\bar{I}^2} p(E(t) \cap E(t + \tau))), \quad (7.33a)$$

$$\hat{p}(C(t)) \xrightarrow{\mathcal{P}} \frac{\int I(t)dt/T}{\bar{I}} p(E(t)) = p(E(t)), \quad (7.33b)$$

where  $\bar{I}$  is the average intensity,  $\hat{p}$  is the estimated probability from the MLE and  $p$  is the true probability. Thus, the estimated coherence is altered by a prefactor

$$\hat{g}^{(2)}(\tau) = \frac{\int I(t)I(t + \tau)dt/T}{\bar{I}^2} g^{(2)}(\tau), \quad (7.34)$$

where  $\hat{g}^{(2)}(\tau)$  is the estimated coherence, and  $g^{(2)}(\tau)$  is the true second-order coherence. Substituting  $I(t) = \bar{I} + \sigma(t)$  into the prefactor in Eq. (7.34) yields

$$\frac{\int I(t)I(t + \tau)dt/T}{\bar{I}^2} = 1 + \frac{\langle \sigma(t)\sigma(t + \tau) \rangle}{\bar{I}^2}. \quad (7.35)$$

Applying the Wiener-Khinchin Theorem, the autocorrelation of the intensity fluctuation  $\sigma(t)$  is equivalent to

$$\langle \sigma(t)\sigma(t + \tau) \rangle = \frac{1}{\pi} \int_0^\infty S_{\sigma\sigma}(\omega) e^{-i\omega\tau} d\omega \approx \frac{1}{\pi} \int_0^{\omega_0} S_{\sigma\sigma}(\omega) d\omega. \quad (7.36)$$

The last approximation involves truncating the intensity fluctuation spectrum  $S_{\sigma\sigma}$  at a value of  $\omega_0$  which is much smaller than  $1/\tau$ .

In most analyses, the maximum delay time we choose is 500  $\mu\text{s}$ , which is much greater than the decoherence time  $1/\gamma_m \approx 50 \mu\text{s}$ . The fact that there is no obvious observed intensity fluctuations below 500  $\mu\text{s}$  justifies the approximation we made in Eq. (7.36). Combining Eq. (7.34) to (7.36), we conclude that the estimated correlation  $\hat{g}^{(2)}(\tau)$  for any delay time  $\tau \ll 1/\omega_0$  is modified by a delaytime-independent prefactor from the true correlation  $g^{(2)}(\tau)$  due to the slowly varying signal intensity.

Hence, we can normalize the measured coherence function to  $g^{(n)}(\infty)$  (whose value is extracted from fits) to approach the true value of the coherence. The uncertainty introduced by this step is usually negligible for two reasons: (i) all measured prefactor is small with a

value around 1.01 or less; (ii) the variance of the extracted value of  $g^{(n)}(\infty)$  is very small.

#### 7.2.4.4 SNSPD Afterpulsing and Deadtime

Sec. 6.1.4 describes the afterpulsing effect and the dead time of SNSPD. The data acquisition protocol requires that any count recorded within 100 ns of a preceding count to be discarded. Most of the coherences are not affected as long as the delay time is longer than the first bin, *i.e.*,  $\tau > \delta t$ . The effective measurement time in the first bin is reduced by a factor of  $(\Delta t - 100 \text{ ns})/\Delta t$ . Similar to the discussion in Sec. 7.2.4.1, the measured coherence is multiplied by  $\Delta t/(\Delta t - 100 \text{ ns})$  to compensate for the data discarding. The reduction in measurement time results in increased uncertainty. Moreover, the mean delay time of the first bin becomes  $(\Delta t + 100 \text{ ns})/2$ .

### 7.3 Characterizing the Thermal State

This section presents the experimental characterization of a thermal state. The mechanical state is thermal equilibrium with a bath at a temperature of approximately  $T_{\text{MC}} \approx 20(1) \text{ mK}$ , which resulted in a mean phonon occupancy of  $n_m = 0.9(1)$ . The temperature of the system was determined by utilizing the QSA (Eq. (7.5)), which is thoroughly discussed in Sec. 7.1.2. The phonon occupancy in the coherence measurements was estimated by measuring the photon count rate and then applying Eq. (7.6a).

#### 7.3.1 Measuring the Phonon Coherence Functions

The theoretical expectation of the coherence function of a mechanical thermal state is very similar to the discussion for photons in Sec. 3.3.1. The time-dependent correlation of phonons is obtained by solving mechanical Langevin equation Eq. (2.59b) via a formal integral

$$\langle \hat{b}^\dagger(\tau) \hat{b}(0) \rangle = n_m e^{-(\gamma_m/2 + i\omega_m)\tau}, \quad (7.37a)$$

$$\langle \hat{b}(\tau) \hat{b}^\dagger(0) \rangle = (n_m + 1) e^{-(\gamma_m/2 + i\omega_m)\tau}. \quad (7.37b)$$

Using Wick's theorem, the second-coherence of phonons is exactly the same as Eq. (3.97) except a different time constant, given by

$$g_m^{(2)}(\tau) = 1 + e^{-\gamma_m \tau}. \quad (7.38)$$

Likewise, all the results presented in Sec. 3.3 can be easily incorporated into phonon coherence functions through the substitution of  $\kappa$  with  $\gamma_m$ .

Figure 6.13 shows the schematic experimental setup (details c.f. Sec. 6.1.1). Either a

red-detuned laser  $\Delta = -\omega_m$  or blue-detuned laser  $\Delta = +\omega_m$  continuously drives the cavity during the “hold” configuration. The measurement scheme is described in Sec. 6.1.2, and the photon arrival time data is analyzed according to Sec. 7.2. The measured photon coherence  $g^{(n)}(\tau)$  of the red and blue-detuned input are mapped to the normally ordered phonon coherence (denoted by  $g_m^{(n)}(\tau)$ ) and the anti-normally ordered phonon coherence (denoted by  $h_m^{(n)}(\tau)$ ), respectively. Details are discussed in Sec. 7.1.1.

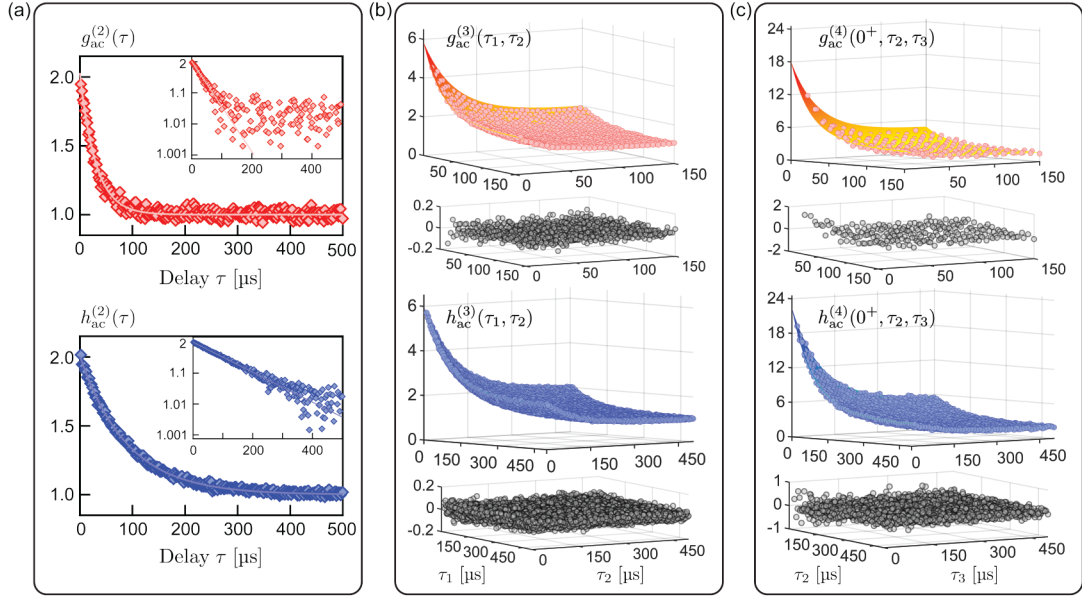


Figure 7.3: Phonon coherences: (a) The second-, (b) third-, and (c) fourth- order phonon coherences measured for  $P_{in} \approx 5 \mu\text{W}$ , with photon arrival times binned in  $2 \mu\text{s}$ ,  $5 \mu\text{s}$  and  $10 \mu\text{s}$  bins respectively. In (a), the insets show the same data on a logarithmic scale. For the three-time dependent  $g_m^{(4)}(\tau_1, \tau_2, \tau_3)$  and  $h_m^{(4)}(\tau_1, \tau_2, \tau_3)$ , we only show representative 2D slices of  $g_m^{(4)}(0^+, \tau_2, \tau_3)$  and  $h_m^{(4)}(0^+, \tau_2, \tau_3)$ , where  $\tau = 0^+$  represents the bin with  $5 \mu\text{s} < \tau < 15 \mu\text{s}$ . Solid lines/surfaces show the fits described in Sec. 3.3.1. Fits for (c) are to the entire 3D (*i.e.*,  $\tau_1$ -,  $\tau_2$ -,  $\tau_3$ - dependent) data set. Fit residuals are shown in black for (b) and (c).

### 7.3.2 Phonon Coherence Experimental Results

The second-, third-, and fourth-order phonon coherences were obtained by binning photon arrival times in  $2 \mu\text{s}$ ,  $5 \mu\text{s}$ , and  $5 \mu\text{s}$  intervals, respectively, while using an input power of approximately  $P_{in} \approx 5 \mu\text{W}$ . At this input power, the optomechanical dynamical backaction and heating effects were significant, as discussed in Sec. 6.3.2.1. These effects led to a relatively high mean phonon occupancy of  $n_m = 10.6(6)$  for the blue-detuned input and  $n_m = 4.0(2)$  for the red-detuned input.

Figure 7.3 shows the different orders of phonon coherence as a function of delay times. The measured coherences are fit to  $1 + af_n(\gamma_m \tau)$ , where  $f_n$  are chosen such that  $1 + f_n(\kappa\tau)$  are equivalent to Eq. (3.97), (3.100) and (3.101). For the fourth-order coherence  $g^{(4)}(\tau)$  and  $h^{(4)}(\tau)$ , we only show representative 2D slices of  $g_m^{(4)}(0^+, \tau_2, \tau_3)$ , where  $\tau = 0^+$  represents the bin with  $5 \mu\text{s} < \tau < 15 \mu\text{s}$ .

The zero-delay coherence values extracted from these fits yield

	exp.	thy.		exp.	thy.
$g_m^{(2)}(0)$	2.02(2)	2	$h_m^{(2)}(0)$	2.007(1)	2
$g_m^{(3)}(0)$	5.98(2)	6	$h_m^{(3)}(0)$	6.023(2)	6
$g_m^{(4)}(0)$	24.02(2)	24	$h_m^{(4)}(0)$	23.98(1)	24

where the stated uncertainty corresponds to one standard deviation of the best-fit parameter. The obtained values are in agreement with the expected outcomes for a thermal state, where  $g_m^{(n)}(0) = h_m^{(n)}(0) = n!$ . Moreover, the observed  $\tau$ -dependence of the coherences exhibits minimal residuals, indicating good agreement with the theoretical predictions. These findings collectively indicate that the mechanical mode is in thermal equilibrium with the bath. In Sec. 7.3.4, a more detailed analysis is presented to interpret the agreement in a statistical way.

### 7.3.3 Characterizing the Power Dependence of the Coherences

The mechanical linewidth can be determined by analyzing the phonon coherences. We vary the optical input power in the range of  $0.9 \mu\text{W} < P_{\text{in}} < 6 \mu\text{W}$  (which corresponds to  $1 \lesssim n_m \lesssim 10$ ) and extract the zero-delay coherence values along with the mechanical linewidth.

Figure 7.4 illustrates the power dependence of the obtained fits. Figure 7.4(a) demonstrates that the zero-delay second- and third-order coherences are consistently close to 2 and 6, respectively, across all power levels within this range. Figure 7.4(b) displays the extracted decay rates  $\gamma_m(P_{\text{in}})$ , which exhibit the expected optomechanical backaction. Fitting the results to standard optomechanics theory Eq. (6.30) (represented by solid lines) yields a value of  $g_0/2\pi = 5.2(2) \text{ kHz}$ . Fitting these results to the model including the heating effect Eq. (6.32) (represented by dashed lines), we have

$$\Delta = -\omega_m : \gamma_m/2\pi = (2.8 \pm 0.2) \text{ kHz} + (0.46 \pm 0.03) \text{ Hz}/\mu\text{W}; \quad (7.39a)$$

$$\Delta = +\omega_m : \gamma_m/2\pi = (3.19 \pm 0.06) \text{ kHz} + (0.29 \pm 0.02) \text{ Hz}/\mu\text{W}, \quad (7.39b)$$

which yields  $g_0/2\pi = 5.2(2)$ . Both extracted  $g_0$  are in agreement with the independent calibration presented in Sec. 6.3.2.2.

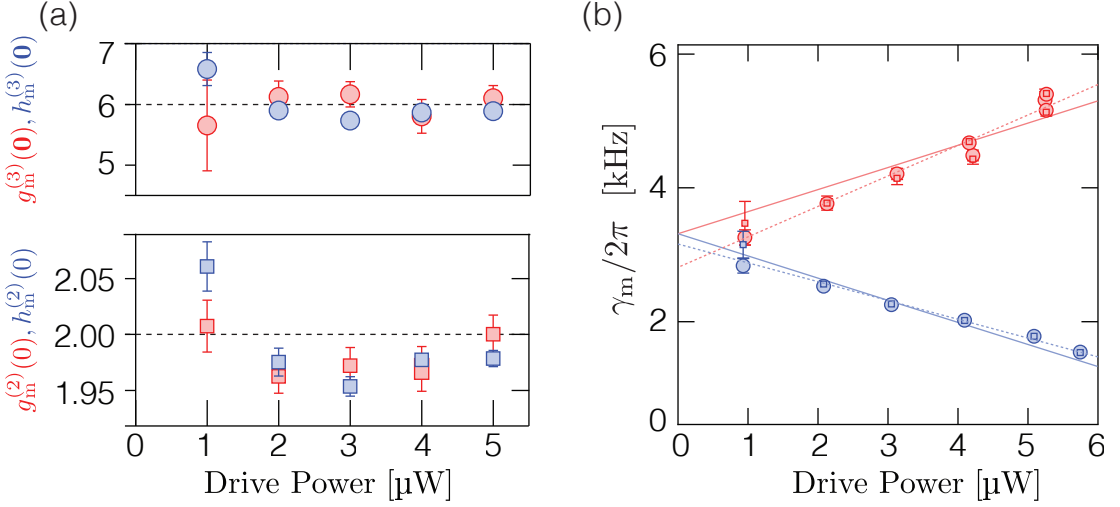


Figure 7.4: (a) The zero-delay second- and third-order coherences, and (b) the coherence decay rates ( $\gamma_m$ ), as a function of incident power  $P_{\text{in}}$ . Data is extracted from fits to the second-order (circles) and third-order (squares) coherences. Solid lines show a fit to standard optomechanics theory in Eq. (6.30). Dashed lines show a fit to Eq. (6.32)

### 7.3.4 Gaussianity Justification

Can our measured results of higher-order coherence tell us more than the state is a thermal state? The short answer is “no”. However, higher-order coherences provide more statistical information about the state and verify the state is a thermal state with stronger statistical confidence compared to only having the second-order coherence measurement.

The relation between the cumulants  $\kappa_n$  of the quasi-probability function and the zero-delay coherences is described in Sec. 3.4.4. Particularly, assuming the  $P$ -function of the state is circularly symmetric around the center, substituting the measured values of different coherence  $g_m^{(n)}(\mathbf{0})$  into Eq. (3.177) yields

$$\begin{aligned}\kappa_2 &= 2.0(1), \\ \kappa_4 &= 0.1(1), \\ \kappa_6 &= -4(4), \\ \kappa_8 &= 1(2) \times 10^2,\end{aligned}$$

where  $\kappa_n$  is the  $n$ -th cumulant of the  $P$ -function of this state. All odd-order cumulants are zero because of the circular symmetry. For an ideal Gaussian state, all cumulants of order  $n \geq 3$  are zero. Our measurements of the cumulants up to the eighth order are consistent with the predictions within one standard deviation. However, the uncertainties in the higher-order cumulant estimators are larger because they scale as  $(n_m)^n$  as shown in Eq. (3.177). To obtain more accurate results, we would need to reduce the mean phonon

number  $n_m$  to below 1 or improve the accuracy of the higher-order coherence measurements. A similar result of the  $Q$ -function can be generated by using values of  $h_m^{(n)}(0)$ .

Beyond the cumulant estimation, higher-order coherences also provide access to reconstructing the Wigner function, as discussed in Sec. 3.4.3. However, it strictly requires a small thermal occupancy  $n_m$  to make the expansion converge.

## 7.4 Characterizing Post-Selected States

In our system, the single photon cooperativity  $\mathcal{C}_0 \approx 5.7 \times 10^{-4}$  is significantly less than one, which prevents us from directly observing most of the quantum features of the mechanical resonator. Increasing  $\mathcal{C}_0$  to reach the strong single-photon cooperativity regime is challenging in practice.

To overcome this problem, we employed the concept of “measurement-backaction-induced nonlinearity” to access certain quantum states. By post-selecting the measurement outcomes, the state can be conditionally projected into some nonclassical states. This method is widely utilized in quantum optics applications, as discussed in Sec. 3.2.3. In photon counting experiments, the post-selection protocol is a powerful tool to maneuver states by conditionally selecting the state based on the measurement results of single-photon detectors [87, 88]. Recently, this method has been employed in quantum optomechanics to manipulate the mechanical state in a classical manner [72, 245, 249] and a non-classical manner [11, 75, 92, 97].

Coherences and other statistical properties of  $k$ -phonon-subtracted/-added thermal states are of interest in quantum metrology, quantum information, and quantum thermodynamics [3, 89]. The successful creation and measurement of these states in a mechanical mode, as demonstrated in this work, extends their potential applications to optomechanical platforms.

Formally, by measuring the state being  $|\beta\rangle$ , the initial state  $|\psi\rangle$  is conditionally prepared in the following state

$$|\psi\rangle \rightarrow |\beta\rangle\langle\beta|e^{-i\hat{H}t}|\psi\rangle. \quad (7.40)$$

Here, the evolution operator  $|\beta\rangle\langle\beta|e^{-i\hat{H}t}$  is non-unitary, and this conditionally prepared state is not a steady state. The coupling to the classical environment results in the decoherence of the state, which can be described by a Lindblad equation Eq. (4.15).

As shown in Eq. (7.2), by conditioning on measuring one anti-Stokes or Stokes scattered photon, one phonon is subtracted from or added to the mechanical state, which yields a *single*-phonon subtracted/added thermal state. If we condition on measuring multiple photons, we end up with a *multi*-phonon subtracted/added thermal state. The coherences of such states are summarized in Sec. 3.2.3. It is proven that the phonon-added thermal

state is always non-classical, which is associated with a negative Wigner function regardless of the initial thermal occupancy  $n_m$ . However, its nonclassicality witness is obscured by the classical thermal uncertainty, as shown in Eq. (3.165). The coherence functions of phonon-added/subtracted states are discussed in Sec. 3.2.3.

The experiment scheme is exactly the same as for the thermal state measurement, as described in Sec. 7.3. In the analysis, the conditional preparation is achieved by post-selecting  $n$  photon detection events within a time interval (delay bin size)  $\Delta t_{\text{bin}} \ll 1/\gamma_m$  (we exclude photon counts followed by another photon within 100 ns to get rid of the afterpulsing effects of SNSPDs as discussed in Sec. 6.1.4). Then such a condition is immediately followed by a count rate or a coherence analysis. In the analysis, this time interval  $\Delta t_{\text{bin}}$  is chosen to be 2, 5, 20  $\mu\text{s}$  for the second-, third-, and fourth-order phonon coherence, respectively, to obtain enough count statistics.

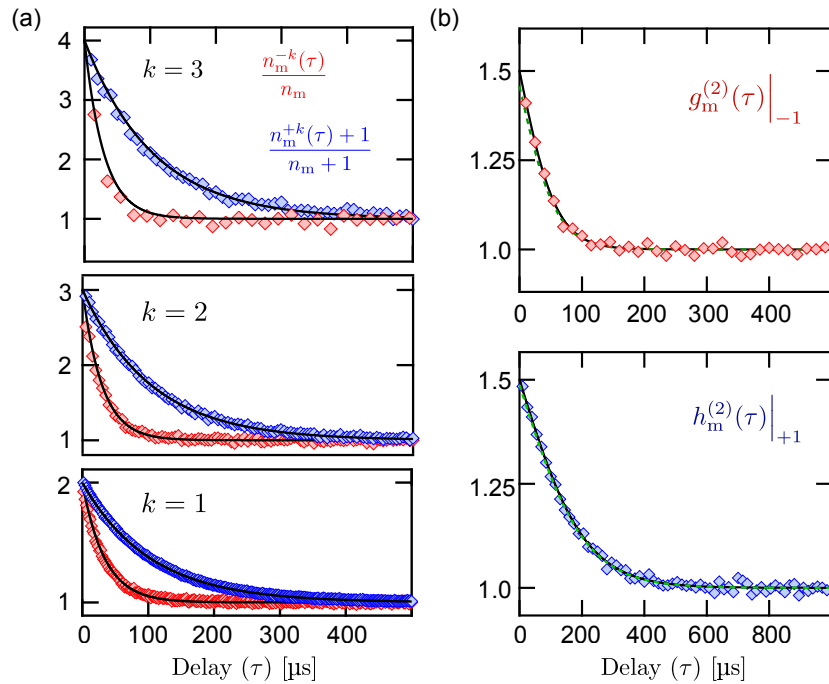


Figure 7.5: (a) Dynamics of the mean phonon occupancy upon subtraction/addition of  $k$  phonons at  $\tau = 0$ . (b) Second order coherences of a 1-phonon subtracted (red) and added (blue) thermal state. Solid lines show the theoretical predictions, as shown in Sec. 3.2.3. Data shown for  $P_{\text{in}} \approx 5 \mu\text{W}$ .

Figure 7.5(a) depicts the time-dependent evolution of normalized photon count rates for  $k$ -phonon subtracted ( $k = 1, 2, 3$ ) thermal states. Specifically, the anti-Stokes photon count rate doubles upon the detection of a single anti-Stokes photon, indicating an immediate doubling of the mean phonon number. This interpretation arises from the dependence of the anti-Stokes scattering rate  $\Gamma_{\text{AS}}$  on the mean phonon occupancy  $n_m$  of the

mechanical mode, as described in equation 6.18a. The mean phonon occupancy  $n_m^{-k}(\tau)$  of a  $k$ -phonon subtracted state can also be measured through appropriate post-selection. By a similar argument, the Stokes scattering rate doubles upon the addition of a single phonon, causing an immediate doubling of  $(n_m + 1)$ , while the addition of  $k$  phonons increases  $n_m(\tau) + 1$  by a factor of  $(k + 1)$ . These counterintuitive results regarding post-selected  $n_m$  can be understood as a Bayesian update to the thermal state (for detailed explanations, see Section 3.2.3.4). As demonstrated in Fig. 7.5(a), the phonon occupancy is observed to double/triple/quadruple immediately following 1-/2-/3- phonon subtraction and subsequently decay back to equilibrium occupancy with the predicted time dependence of an initial thermal state (indicated by the solid lines). This behavior also applies to phonon-added states and is independent of the initial phonon number. Recent experiments have reported the doubling of phonons even in a room-temperature resonator with  $n_m \gtrsim 1000$  [245, 246, 249].

Using appropriate post-selection, we construct the various coherences of the post-selected thermal states that have undergone  $k$ -phonon subtraction or addition. The  $n$ th-order coherences of  $k$ -phonon-subtracted/added states are determined by different “slices” in the  $(n+k)$ -photon detection record, which is a representation of the thermal state. However, post-selection enables the extraction of non-thermal-equilibrium post-selected state coherences, which are discussed in detail in Sec. 3.3.2.

Figure 7.5(b) displays the measured second-order coherence of a 1-phonon subtracted thermal state (normally ordered  $g_m^{(2)}(\tau)|_{-1}\rangle$ ) and a 1-phonon added thermal state (anti-normally ordered  $h_m^{(2)}(\tau)|_{+1}\rangle$ ), along with their theoretical expectations Eq. (3.103) and (3.104) (indicated by solid lines). The measured zero-delay second-order coherences agree well with the theoretical expectation of  $3/2$  and decay to unity on the mechanical timescale  $1/\gamma_m$  as we expect.

Even though the post-selected states are nontrivial, this continuous wave measurement scheme is incapable of unraveling the nonclassicality of such post-selected thermal states according to the criteria defined in Sec. 3.5.1. The thermal state is a Gaussian function in either the  $P$ -representation or the  $Q$ -representation. Thus its coherences are independent of the thermal occupancy  $n_m$ , as discussed in Sec. 3.4.4 and Sec. 3.2.2. So if the thermal state is post-selected and measured in a continuous measurement, the measured coherence of such a post-selected thermal state is also independent of  $n_m$ . In Chapter 9, we alter between the red- and blue-detuned optical inputs in a pulse scheme to verify the nonclassicality of the state.

*“We are the product of quantum fluctuations in the very early universe.”*

– Stephen Hawking

# CHAPTER 8

## Displaced Thermal States

Coherent states of linear harmonic oscillators are a significant type of quantum state in the context of the quantum-to-classical transition. Such states closely resemble the oscillatory behavior of a classical isolated harmonic oscillator (together with fluctuations at the level of the zero-point motion), and so are considered by some people as the most classical-like of quantum states [254–259]. Additionally, when weakly coupled to the environment, coherent states are the states that are least susceptible to the loss of quantum coherence, and which emerge as a stable state under decoherence [260].

Coherent states have been widely achieved experimentally in optics, atomic matter waves, and Bose–Einstein condensates [261–264]. However, generating and verifying a coherent state in a massive macroscopic object remains a challenging task.

This chapter presents the use of an optical beat note to drive the mechanical motion. A red-detuned beam continuously monitors the state of the oscillator via the anti-Stokes scattering process. We show that the thermal noise of this oscillator is comparable to its zero-point fluctuation, and so we refer to the driven state as a displaced thermal state (DTS) rather than an ideal coherent state. Displaced thermal states share many features with coherent states when the displacement amplitude is large enough. As the displacement amplitude increases, the motional state transitions from bunching ( $g_m^{(2)}(0) = 2$ ) to Poissonian statistics ( $g_m^{(2)}(0) = 1$ ). We demonstrate the control and measurement of phonon numbers ranging from sub-phonon levels to approximately  $4 \times 10^4$ , while maintaining the noise equivalent to  $\sim 3$  phonons.

In addition, we explore two potential applications of such motional states. The first application is to use the driven oscillator as a coherent phonon source in mechanical interferometric displacement measurements. We describe the standard quantum limit (SQL) for such measurements. The second application involves testing one version of modified quantum theory [1, 188] (see Sec. 4.2.2 for detailed theoretical derivations). Under this modification, the evolution of a massive mechanical oscillator is predicted to be cyclically squeezed. Such a phenomenon suggests nonlocal dynamical behavior at a very short length scale. The experimental observation of a mechanical coherent state in this work can place an upper bound of  $10^{-18}$  m on this length scale, which is comparable to the result from the Large Hadron Collider (LHC) [202].

## 8.1 Dynamics of a DTS

The dynamics of a driven state in the quantum picture can be obtained by solving the mechanical Langevin equation Eq. (2.59b) with a coherent drive  $\hat{b}_{\text{in}}[\omega] \propto \delta(\omega - \omega_d)$ , where  $\omega_d$  is the drive frequency. Starting with the ground state  $|0\rangle$ , the driven state is a coherent state  $|\alpha_0\rangle$ , whose Wigner function is

$$W_0(x, p) = \frac{1}{\pi\hbar} \exp\left[-\frac{2x_{\text{ZPF}}^2}{\hbar^2}(p + 2|\alpha_0|p_{\text{ZPF}} \sin(\omega_d t))^2 - \frac{1}{2x_{\text{ZPF}}^2}(x - 2|\alpha_0|x_{\text{ZPF}} \cos(\omega_d t))^2\right], \quad (8.1)$$

where  $x_{\text{ZPF}}^2 \equiv \hbar/2m\omega_m$  (Note this is different from the definition in Sec. 4.2.2). Or in a dimensionless coordinate  $\tilde{x} \equiv x/2x_{\text{ZPF}}$ ,  $\tilde{p} \equiv p/2p_{\text{ZPF}}$ , Eq. (8.1) can be reexpressed as

$$\begin{aligned} W_0(\tilde{x}, \tilde{p}) &= \frac{2}{\pi} \exp\left[-2(\tilde{p} + |\alpha_0| \sin(\omega_d t))^2 - 2(\tilde{x} - |\alpha_0| \cos(\omega_d t))^2\right] \\ &= \frac{2}{\pi} \exp[-2|2\alpha - |\alpha_0|e^{-i\omega_d t}|^2]. \end{aligned} \quad (8.2)$$

Intuitively, it describes a 2D Gaussian blob, whose variance is  $\sigma = 1/2$ , rotating around the origin of the phase space with a fixed amplitude  $|\alpha_0|$  at frequency  $\omega_d$ . As discussed in Sec. 3.4.1.3, this is a quantum picture of nearly-classical behavior.

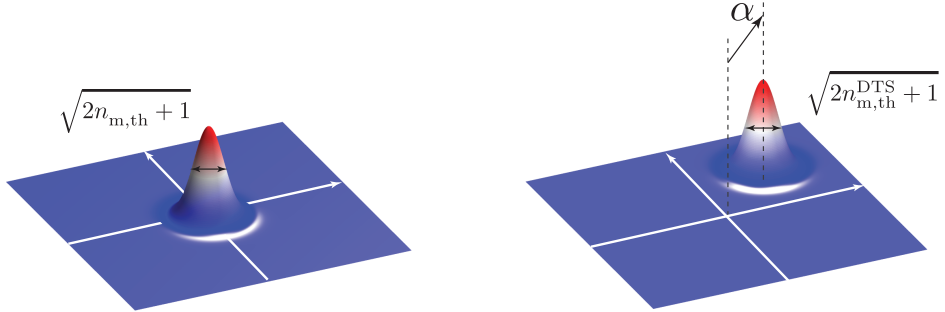


Figure 8.1: Schematic of the Wigner function of a displaced thermal state. Left: the original thermal state. Right: the displaced thermal state  $|\alpha, n_{\text{m,th}}^{\text{DTS}}\rangle$ .

In practice, we usually start with a thermal state  $\hat{\rho}_{\text{th}}$  with mean occupancy  $n_{\text{m}}$  rather than a ground state. Such a driven state is a displaced thermal state (DTS) whose Wigner function is similar to Eq. (8.2) except with a larger variance  $\sigma = (\sqrt{2n_{\text{m}} + 1})/2$ , as shown in Fig. 8.1. It is worth emphasizing the disparity between coherent states and displaced thermal states, which are both depicted by the same Wigner functions except with different variances. The origins of the two kinds of variance are different. The variance of coherent states stems from the intrinsic uncertainty of quantum mechanics. The extra variance of

displaced thermal states originates from the classical statistical uncertainty about the state, which can be eliminated in principle. Notably, only quantum uncertainty is associated with quantum dynamics. In contrast, classical uncertainty usually obscures these quantum features. Therefore, it is crucial to minimize the classical uncertainty in certain quantum-motivated applications.

## 8.2 Measurement Setup

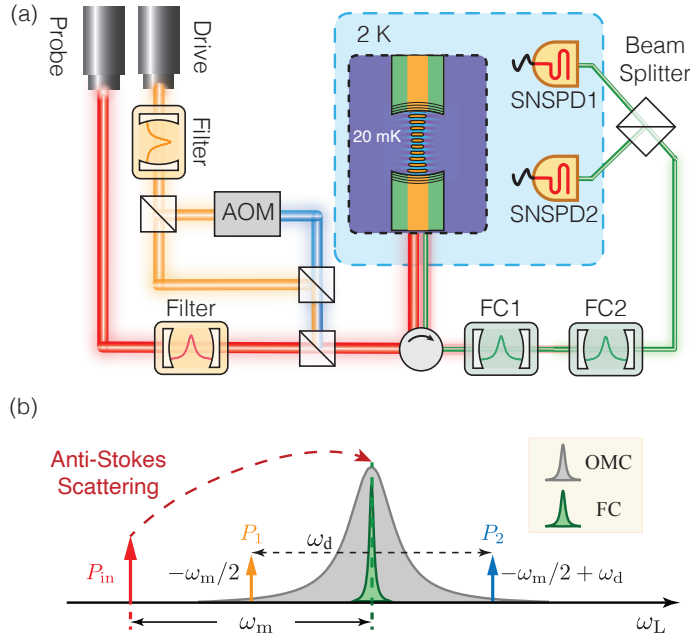


Figure 8.2: (a) A schematic of the optical setup for preparing displaced thermal states. Two filters right after two lasers are corresponding narrow-band filter cavities to stabilize the phase. (b) The frequency spectrum of the input lasers. The probe laser is detuned by  $\Delta = -\omega_m$ . The drive laser is detuned by  $\Delta = -\omega_m/2$ . Part of the drive laser is shifted by an AOM to a detuning of  $\Delta = \omega_d - \omega_m/2$ . Together with the unshifted drive laser, these two forms an optical beat note at  $\omega_d$  to drive the mechanical motion. The grey Lorentzian stands for the optomechanical cavity resonance, and the green shading area represents the filter cavity transmission spectrum.

A conceptual schematic of this experiment is shown in Fig. 8.2(a) (detailed optical setup is described in Sec. 6.1.3). The drive is set at  $\Delta = -\omega_m/2$ . After a beamsplitter, 10% of this optical input is not shifted with power  $P_1$  and the remaining 90% is shifted by the AOM to  $-\omega_2/2 + \omega_d$  with power  $P_2$  (with  $\omega_d \approx \omega_m$ , this frequency is  $\sim +\omega_m/2$ ). These two correlated lasers form an optical beat note of frequency  $\omega_d$ , which is sent to the optomechanical cavity to drive the mechanical resonator. In the experiment, we purposely

set  $P_1 \approx P_2$  unless otherwise specified. This way, we can minimize the total input laser power and cancel possible optomechanical backactions caused by these two inputs. The probe laser is set at the red-detuned mechanical sideband  $\Delta = -\omega_m$  with power  $P_{in}$  to read the state of the mechanical resonator via anti-Stokes scattered photons. The frequency spectrum of all input lasers is summarized in Fig. 8.2(b). More details can be found in Sec. 6.2.2 and Sec. 6.4.

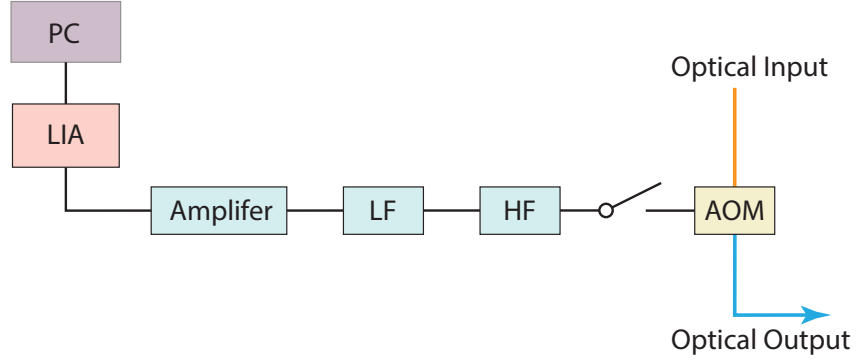


Figure 8.3: A schematic of the circuit to generate the RF drive to the AOM.

The measurement is operated in the “lock-hold” scheme described in Sec. 6.1.2. During the “hold” period, both Shutter1 and Shutter2 (shown in Fig. 6.1) are closed, and thus all three optical inputs are sent to the optomechanical cavity.  $P_1$  is controlled by a VOA (shown in Fig. 6.4). As shown in Fig. 8.3, a RF drive is generated by a LIA and then amplified. This amplified signal further passes through a low-pass filter<sup>1</sup> and a high-pass filter<sup>2</sup> before being sent to the AOM. The effective gain between the input to the AOM and the output from the LIA is measured to be 34.4 dB, which includes all insertion losses. With a fixed optical input,  $P_2$  is controlled by the power of this RF drive  $P_{RF}$  to the AOM (characterized in Sec. 6.1.3.1). The power and frequency of each optical input are fixed during one “hold” period, which can be adjusted in different “hold” periods. During the “lock” period, Shutter1 and Shutter2 are open, and FC1, FC2 are locked to the optical cavity resonance (details c.f. Sec. 6.1.2).

## 8.3 Experiment Characterization

This section describes the basic characterization of the displaced thermal state (DTS), such as the mechanical linewidth, and the quantum sideband asymmetry. We found that these characterizations agree with our expectation of the system.

<sup>1</sup>Mini Circuit BLP-450+, 450 MHz low-pass filter.

<sup>2</sup>Mini Circuit VHF-145+, 145 MHz high-pass filter.

### 8.3.1 Mechanical Susceptibility Measurement

To characterize the driven state,  $\omega_d$  is swept across the expected mechanical resonance frequency. Part of the probe laser is scattered to the optical resonance due to the anti-Stokes scattering process, which can pass through two filter cavities (FC1, FC2) and be measured by the two SNSPDs. The anti-Stokes scattered photon rate is proportional to the mean phonon occupancy  $n_m$ , in which the driven phonon number is described by Eq. (6.35) and (6.36). The photon count rate that is associated with the driven phonon number is described by Eq. (6.34). Thus, such a sweep can show the mechanical susceptibility  $|\chi_m[\omega_d]|^2$  (from which it is straightforward to extract the resonance frequency  $\omega_m$  and the mechanical linewidth  $\gamma_m$ ) from the anti-Stokes count rates. See Sec. 6.4 for details.

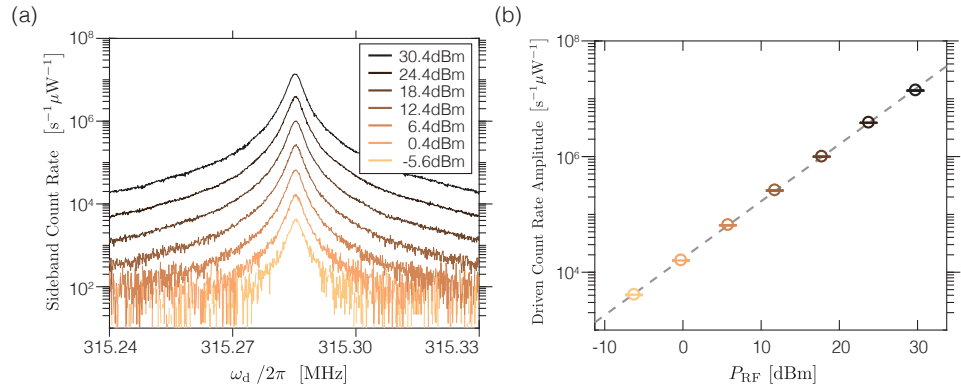


Figure 8.4: (a) Sideband photon count rates as a function of  $\omega_d$  at several  $P_{\text{RF}}$ . (b) The extracted sideband count rate amplitudes as a function of  $P_{\text{RF}}$ . This count rate is described in Eq. (6.34), which is associated with  $n_m$ . The grey dashed line is a linear fit according to Eq. (6.36).

In the experiment,  $P_{\text{in}}$  is fixed at 1  $\mu\text{W}$ ,  $P_1$  is fixed at 300 nW.  $P_2$  is proportional to  $P_{\text{RF}}$ , whose value varied from  $-5.6$  dBm to  $30.4$  dBm in 7 different sweeps. The maximal  $P_{\text{RF}} = 30.4$  dBm corresponds to  $P_2 \approx 300$  nW. In each sweep,  $\omega_d$  is changed at the beginning of each “hold” period with a frequency step size of 100 Hz and a total of 900 steps. The same sweep is repeated a few times (over a period of 10 - 20 min) to get a better signal-to-noise ratio. The sideband count rate is characterized by the average count rate during the “hold” for each frequency. Note that the data in the first 5 ms of the DAq period (during the “hold” period) is discarded to avoid the transient behavior before reaching the steady amplitude.

Figure 8.4(a) presents the anti-Stokes photon count rate spectrum obtained for different  $P_{\text{RF}}$ . Despite four orders of magnitude variation in  $n_m$ , all responses exhibit a symmetric Lorentzian shape centered around a fixed resonance frequency  $\omega_m$ . Each trace is fit to a Lorentzian with a constant background. The extracted count rate amplitudes for different  $P_{\text{RF}}$  are displayed in Fig. 8.4(b). This amplitude is associated with  $n_m$  as described in

Eq. (6.36). Notably, the linear relationship between  $P_{\text{RF}}$  and these amplitudes agree with the predicted power dependence given in Eq. (6.34), which highlights this system's control of the mean phonon number over a broad range.

### 8.3.2 Linewidth Measurement

The mechanical decay rate can be characterized by three independent measurements: (a) mechanical ringdown measurement; (b) mechanical susceptibility; (c) decoherence of  $g_m^{(2)}(\tau)$ . In this section, we explain the first two experiments. The details of the third will be discussed in the Sec. 8.4.

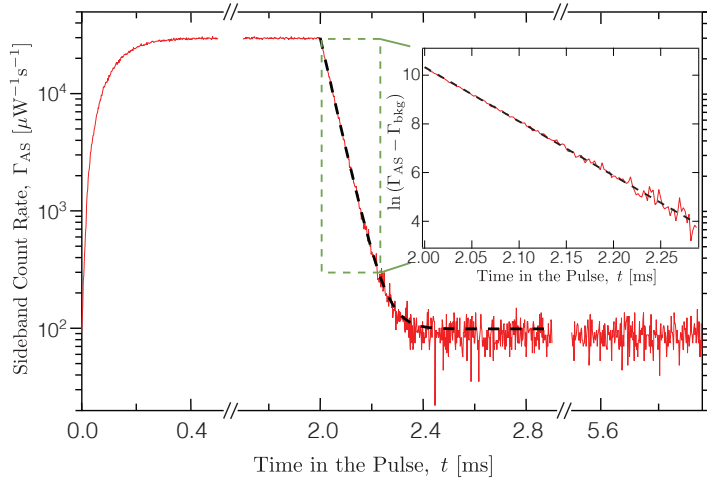


Figure 8.5: The mechanical ring-down measurement of a driven state. The sideband count rates are shown as a function of the time in the pulse. The black dashed is the fit described in the text. Inset: a zoom-in plot of data in the dashed green box in logarithm scale.

#### 8.3.2.1 Mechanical Ring-down Measurement

Similar to ring-up measurement in Sec. 6.3.2.2.1, the ring-down experiment is also performed in the pulsed scheme. The AOM drive is shuttered via an RF switch as shown in Fig. 8.3, which is used to pulse the optical beat drive “on” and “off”. During each pulse cycle, the RF switch is turned on for 2 ms to drive the mechanical resonator to reach its steady state. It is then switched off to allow the resonator to ring down freely. The same “on-off” procedure is repeated after 6 ms of off-time, which is sufficient to initialize the mechanical resonator. The mechanical state is monitored by a continuous probe laser at  $-\omega_m$  with  $P_{\text{in}} = 1 \mu\text{W}$ . The drive laser, on the other hand, is constantly on at  $-\omega_m/2$ , while the AOM-shifted tone at  $+\omega_m/2$  is pulsed “on” and “off” repetitively.

An example of the detected count rate averaged over  $1.1 \times 10^5$  cycles is shown in Fig. 8.5, in which  $\langle n_{m,d} \rangle / \langle n_{m,\text{th}} \rangle \approx 346$ . The figure is divided into three sections repre-

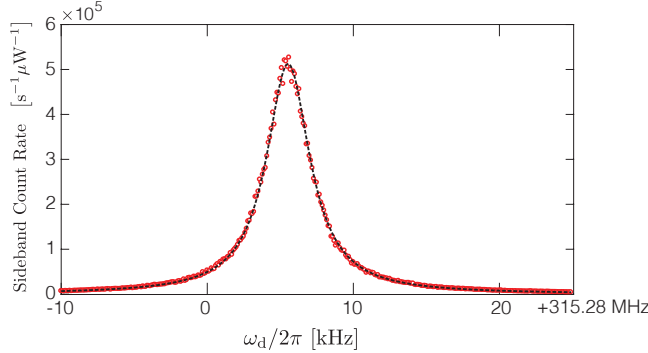


Figure 8.6: The sideband count rates as a function of  $\omega_d$ .

senting the three stages in the ring-down measurement: right-up, right-down, and initializing. During the freely ring-down stage, the photon count rate follows the exponential decay as

$$\Gamma_{\text{AS}} = \Gamma_{\text{bkg}} + \Gamma_d e^{-(t-t_0)\gamma_m}, \quad (8.3)$$

where  $t_0$  is a constant representing the time when the ringdown starts,  $\Gamma_d$  is the steady-state driven count rate.  $\Gamma_{\text{bkg}}$  is the count rate in the absence of external drive, taken to be the average count rate obtained from 3 ms to 6 ms during which the mechanical state has completely rung down. The inset of Fig. 8.5 shows a log scale plot. The black dashed line is the fit Eq. (8.3). The typical one s.d. of  $\gamma_m$  extracted from the fit is  $\sim 10$  Hz.

### 8.3.2.2 Mechanical Response

To extract  $\gamma_m$ , a frequency sweep with a step size of 100 Hz is performed using the protocol described in Sec. 8.3.1. The probe laser power ( $P_{\text{in}}$ ) is fixed at  $1 \mu\text{W}$ . The sideband count rate is proportional to  $n_m$ . Figure 8.6 shows an example of such a sweep with  $\langle n_{m,d} \rangle / \langle n_{m,\text{th}} \rangle \approx 346$ . The black dashed line is a fit to a Lorentzian on top of a constant background. The typical uncertainty (one s.d.) of the extracted linewidth is  $\sim 10$  Hz.

### 8.3.3 Quantum Sideband Asymmetry

In this section, we demonstrate the quantum sideband asymmetry for driven states, which is used to characterize the temperature of the mode.

The sideband count rates are described by Eq. (6.18a), where  $n_m = n_{m,\text{th}} + n_{m,d}$  is the total phonon number. In this experiment, we only vary the AOM optical output power  $P_2$ ,

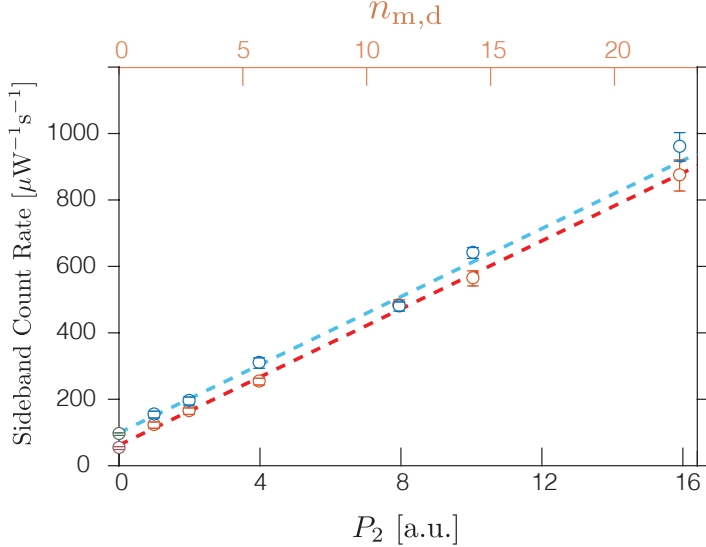


Figure 8.7: The sideband count rates of the blue- (blue circles) and red-detuned (red circles) at various  $P_2$ . Dashed lines are fit to Eq. (8.4). The calibrated  $n_{m,d}$  is shown in the top axis.

which mainly changes  $n_{m,d}$ . Therefore, we have

$$\Gamma_S = \alpha (kP_2 + n_{m,\text{th}} + 1), \quad (8.4a)$$

$$\Gamma_{AS} = \alpha (kP_2 + n_{m,\text{th}}), \quad (8.4b)$$

where  $k$  characterizes the constant of proportionality at which  $n_{m,d}$  increases with  $P_2$ . As a result, we expect that both the Stokes ( $\Gamma_S$ ) and anti-Stokes ( $\Gamma_{AS}$ ) scattered photon count rates are linear with the optical drive power  $P_2$ .

In the experiment, to measure the anti-Stokes and Stokes scattered photons, we place the probe laser either at a detuning of  $\Delta = -\omega_m$  or  $\Delta = +\omega_m$ , respectively, where  $\omega_m/2\pi = 315.2807$  MHz is characterized in spectrum described in Sec. 8.3.1. The probe laser power is set at  $P_{in} = 300$  nW, which is low enough so that the optomechanical backaction and the laser heating effect are negligible, as discussed in Sec. 6.3.2.1.  $P_1$  is set at 20 nW, while  $P_2$  is varied by changing  $P_{RF}$ .  $\omega_d$  is fixed at  $\omega_m$ . All measured count rates are subtracted by the background count rate (details c.f. Sec. 6.3.1.2) to yield the corresponding sideband count rates.

Figure 8.7 shows the measured Stokes and anti-Stokes sideband count rates at various  $P_2$ . Dashed lines represent the fit to Eq. (8.4a) and (8.4b), where the parameters  $\alpha$ ,  $k$ , and  $n_{m,\text{th}}$  are fitting parameters. The fitting outcome gives  $n_{m,\text{th}} = 1.7(5)$ . The driven phonon number  $n_{m,d}$  is calibrated based on Eq. (7.6a) and displayed on the top axis of Fig. 8.7. The constant difference between the count rates of Stokes- and anti-Stokes-scattered photons in the absence of optomechanical backactions is proof of the quantum sideband asymmetry.

Moreover,  $n_{m,\text{th}}$  can also be calibrated by the Stokes and anti-Stokes photon count rates at  $P_2 = 0$ , which are depicted as green and brown circles (data at  $P_2 = 8$ ) in Fig. 8.7. It yields  $n_{m,\text{th}} = 1.3(2)$ . This result also agrees with the result obtained from Sec. 7.1.2.

## 8.4 Statistics of Displaced Thermal States

In this section, we focus on the statistical properties of mechanical displaced thermal states, as characterized by the first- and second-order coherences of the anti-Stokes photons.

### 8.4.1 The Second-Order Coherence

A displaced thermal state  $|\alpha, n_{m,\text{th}}^{\text{DTS}}\rangle$  can be characterized by two parameters: the displacement amplitude  $\alpha$  and the fluctuation  $n_{m,\text{th}}^{\text{DTS}}$  (here, we use a different notation to distinguish it from the thermal fluctuation  $n_{m,\text{th}}$  of the initial state without being driven). The mean phonon number of such a state is

$$n_m = \langle \hat{b}^\dagger \hat{b} \rangle = n_{m,\text{d}} + n_{m,\text{th}}^{\text{DTS}}, \quad (8.5)$$

where the driven phonon number  $n_{m,\text{d}} \equiv |\alpha|^2$  is the contribution from the displacement. The zero-delay second-order coherence of a DTS is given in Eq. (3.40), whose value exclusively depends on the ratio between  $n_{m,\text{th}}^{\text{DTS}}$  and  $n_{m,\text{d}}$ . Therefore, the total phonon number  $n_m$  and  $g_m^{(2)}(0)$  can determine the displaced thermal state unambiguously.

The time dependence of the second-order coherence function of a DTS is given in Eq. (3.121), which can be reexpressed as

$$g_m^{(2)}(\tau) = 1 + \frac{2\xi e^{-\tau/2\tau_0} + \xi^2 e^{-\tau/\tau_0}}{(1 + \xi)^2}, \quad \xi \equiv \frac{n_{m,\text{th}}^{\text{DTS}}}{n_{m,\text{d}}}, \quad (8.6)$$

where  $\tau_0 = 1/\gamma_m$ .

The experiment setup is described in Sec. 8.2 and shown in a schematic in Fig. 8.2(a). Specifically, the probe laser has power 1  $\mu\text{W}$  and detuning  $\Delta = -\omega_m$ . The drive laser is detuned by  $-\omega_m/2$  and  $\omega_d = \omega_m$ . Here,  $\omega_m/2\pi = -315.2807 \text{ MHz}$  is extracted from the mechanical response described in Sec. 8.3.2.2. The optical input frequency spectrum is presented in Fig. 8.2(b). We set  $P_1 = P_2$  to maximize the optical driving force and minimize the dynamical backaction. In the experiment,  $P_1$  and  $P_2$  are also varied to achieve different displacement amplitudes  $|\alpha\rangle$  (i.e.,  $n_{m,\text{d}}$ ).

A few things are worth being addressed during the experiment:

- To minimize the effects of the systematical shifts during long data acquisition ( $\sim$ a few days), the measurement of different  $P_1, P_2$  for achieving different  $n_{m,\text{d}}$  and the

background calibration measurement are set in a loop. More specifically,  $P_1, P_2$  of one desired  $n_{m,d}$  are fixed for  $\sim 3$  min. Then they are adjusted to the powers for the next desired  $n_{m,d}$  for another  $\sim 3$  min. After we have gone through all desired  $n_{m,d}$ , it is followed by a background calibration measurement, which is described in Sec. 8.4.2.1. This loop is repeated for a few days to achieve the desired signal-to-noise ratio.

- The measured coherence is obscured by a background, whose amplitude is very sensitive to the bias current of SNSPDs. The experimental characterization of this dependence is described in Sec. 8.4.3.2. In this experiment, the bias currents of both SNSPDs are set to be  $20.0 \mu\text{A}$  to have a trade-off between the detection efficiency, the afterpulsing effect and the detection coherence.
- The count rate of a highly displaced thermal state ( $n_{m,d} > 10^4$ ) approaches the saturation count rate of SNSPDs ( $\sim 1 \text{ MHz}$ ). Therefore,  $P_{\text{in}}$  is adjusted accordingly to avoid potential compromise on the data.
- The data size of the highly displaced thermal state ( $n_{m,d} > 10^4$ ) is above 1 TB. These data are analyzed using the cluster at Yale Center for Research Computing (YCRC).
- To avoid the transient behavior right after the drive, the first 5 ms of the DAq period is discarded in the analysis.

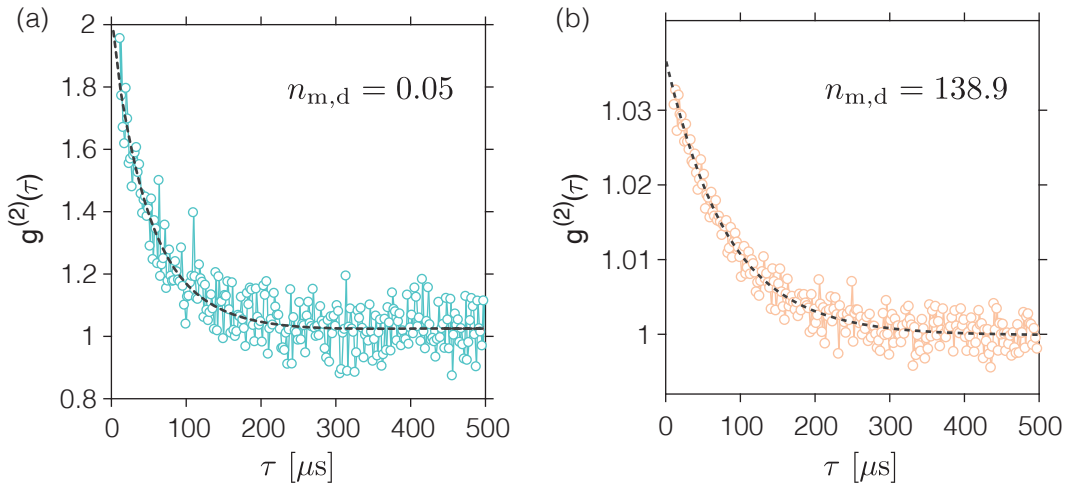


**Figure 8.8:** The second-order coherence function of two displaced thermal states with (a)  $n_{m,d} = 0.05$  and (b)  $n_{m,d} = 138.9$ , respectively. The dashed lines are the best fits to Eq. (8.6).

The phonon number is determined by the anti-Stokes scattering rate using Eq. (7.6a). The second-order coherences are constructed according to the protocol described in Sec. 7.2, which includes the correction of the coherence due to background counts (dark and stray photons) according to Sec. 7.2.4.2 To resolve  $g_m^{(2)}(\tau)$  with higher resolution ( $\sim 10^{-3}$ ), an additional coherence background subtraction process has been added in the data analysis (details c.f. Sec. 8.4.3).

Figure 8.8 shows the measured second-order coherences of anti-Stokes photons for two displacement amplitudes  $n_{m,d} = 0.05$  and  $n_{m,d} = 138.9$ . In two limits  $\xi \gg 1$  and  $\xi \ll 1$ , the corresponding  $g_m^{(2)}(\tau)$  are described by Eq. (3.91) and (3.122), respectively. Both coherences exponentially decay to 1, however, with different decay rates. In the small driven amplitude limit, where  $n_{m,d} \ll n_{m,th}^{DTS}$ , the decoherence of  $g_m^{(2)}(\tau)$  is dominated by the mechanical energy decay rate  $\gamma_m$ . In the large driven amplitude limit  $n_{m,d} \gg n_{m,th}^{DTS}$ , the decoherence is led by the mechanical amplitude decay rate  $\gamma_m/2$ .

A clear bunching effect is observed in a nearly thermal state as shown in Fig. 8.8(a). As the displacement amplitude increased, the measured  $g_m^{(2)}(0)$  approached 1 as shown in Fig. 8.8(b), which corresponds to a coherent state.

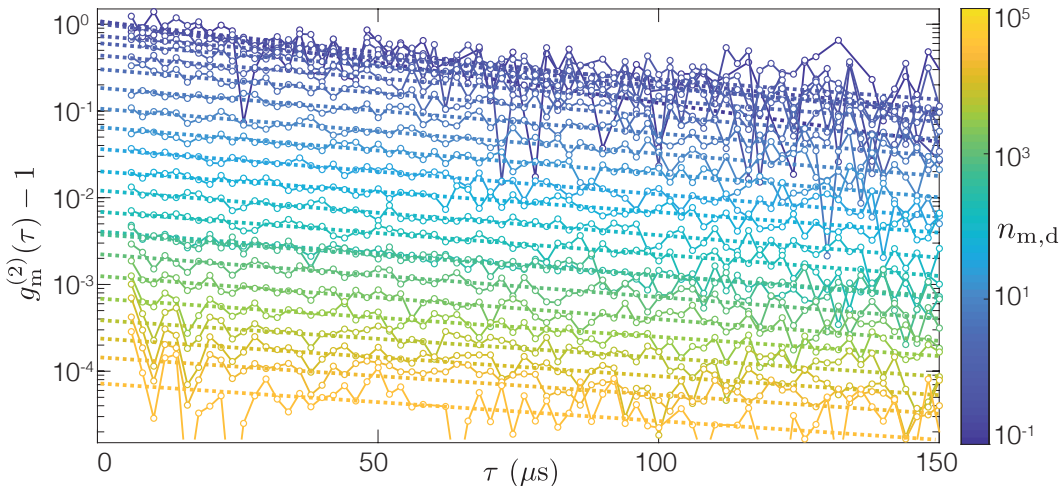


Figure 8.9: The second-order coherence of displaced thermal states as a function of the delay time  $\tau$ . Different colors represent different  $n_{m,d}$ , whose values are indicated by the color bar shown on the right. Dashed lines are fits to Eq. (8.6).

More driven amplitudes are systematically achieved by varying  $P_1$  and  $P_2$  together. Their corresponding second-order coherence functions are shown in Fig. 8.9, which have subtracted the classical background (described in Sec. 8.4.3). All coherences present clear exponential decaying features while the coherence amplitude  $g_m^{(2)}(\tau) - 1$  covers 4 orders of magnitudes. These time-dependent coherences are fitted to Eq. (8.6) to extract  $\xi$  and  $\gamma_m = 1/\tau_0$ .

As shown in Fig. 8.10(a), the mechanical linewidths  $\gamma_m$  extracted from the coherence

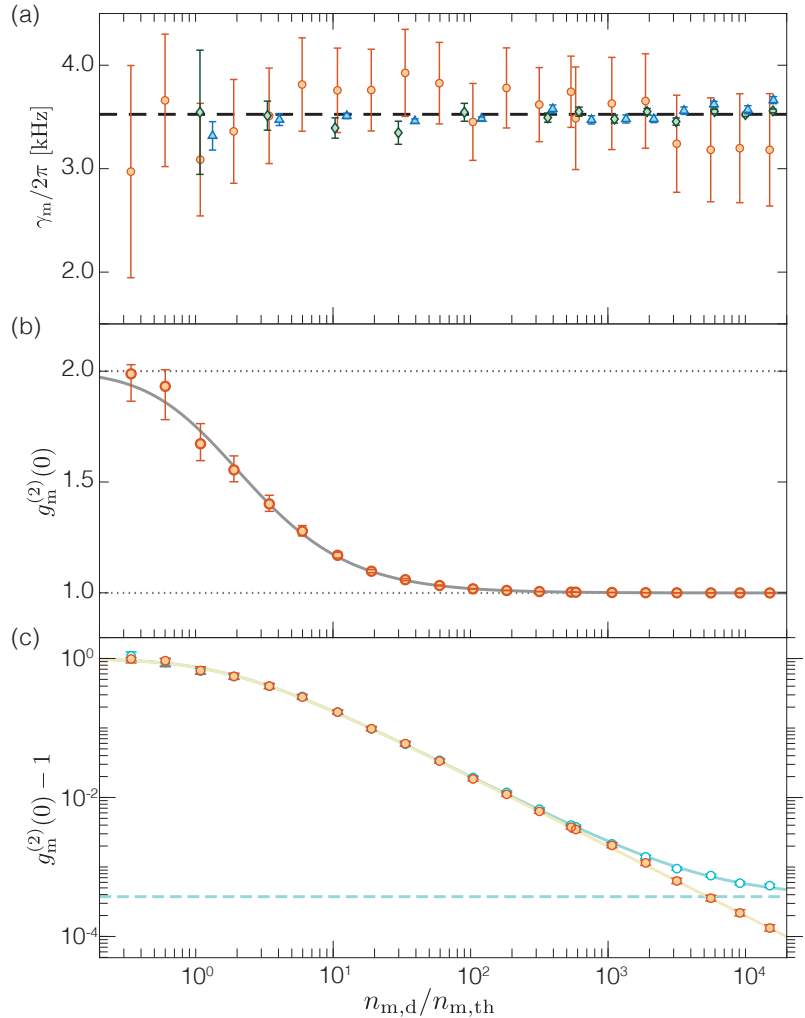


Figure 8.10: (a) Mechanical linewidth versus the  $n_{m,d}/n_{m,\text{th}}$ . These values are determined from three methods:  $g_m^{(2)}(\tau)$  (orange circles), from ring-down experiments (green diamonds), and mechanical response sweeps (blue triangles) (see Sec. 8.3.2). Error bars show two s.d. determined from the fit in each measurement. The black dashed line is the average linewidth. (b)  $g_m^{(2)}(0)$  (orange circles) as a function of the  $n_{m,d}/n_{m,\text{th}}$ . Error bars show two s.d. determined from the fits to  $g_m^{(2)}(0)$ . The grey solid line shows the theoretical prediction given in Eq. (8.6). (c)  $g_m^{(2)}(0) - 1$  in the logarithmic scale. Blue circles and orange circles represent  $g_m^{(2)}(0) - 1$  without and with background subtraction (described in Sec. 8.4.3), respectively. The blue dashed line represents the contribution from this background. Solid lines are theoretical predictions described in the main text.

remain unaffected for different amplitudes, consistent with the results of another two kinds of independent measurements discussed in Sec. 8.3.2. Because the optomechanical damping effect is evaded by using two equal power drive lasers at  $\pm\omega_m/2$  and the heating effect of the drive laser ( $P_1, P_2 \lesssim 300$  nW) is negligible.

The extracted values of the zero-delay second-order coherence  $g_m^{(2)}(0)$  from the fits in Fig. 8.9 are shown in Fig. 8.10(b).  $g_m^{(2)}(0)$  shows a smooth transition from a bunching thermal state ( $g_m^{(2)}(0) = 2$ ) to Poissonian statistics  $g_m^{(2)}(0) = 1$  as the displacement amplitude increases. The top and bottom dotted lines represent the expected  $g_m^{(2)}(0)$  for a thermal state and a coherent state, respectively. In this measurement,  $n_{m,d}$  is determined from the anti-Stokes scattering count rate according to Eq. (7.6a).  $n_{m,th}$  is the phonon occupancy including the heating effect of all input lasers without being driven, which is calibrated by the independent background measurement in the loop described in Sec. 8.4.2.1.

The grey solid line is the no-free-parameter prediction based on Eq. (8.6), which assumes that no extra noise is added to the driven state (*i.e.*,  $n_{m,th}^{DTS} = n_{m,th}$ ). To see the agreement between the data and the prediction more clearly, Fig. 8.10(c) shows  $g_m^{(2)}(0) - 1$  in a logarithmic scale. The data (orange circles) agree with the prediction (solid beige line) down to the order of  $10^{-4}$ . The blue circles represent data without background subtraction (see Sec. 8.4.3), and the blue dashed line is the extracted background. The blue solid line is the sum of Eq. (8.6) and this constant background.

The discrepancy between the data and the prediction indicates that a fraction of noise could be added to the driven states. Combining Eq. (8.5) and (8.6),  $n_{m,th}^{DTS}$  can be solved inversely as

$$n_{m,th}^{DTS} = \left( \frac{1}{\sqrt{2 - g_m^{(2)}(0)}} - 1 \right) n_{m,d}. \quad (8.7)$$

This effective thermal phonon number  $n_{m,th}^{DTS}$  is proven to be associated with the variance of the Wigner function as  $\sigma^2 = (2n_{m,th}^{DTS} + 1)/4$ , if the driven state is still Gaussian. Even discarding the Gaussianity assumption, the variance of the noise blob can be constrained as we now describe.

#### 8.4.1.1 Constraining the Variance of the $P$ -function of a displaced Thermal State

In this part, we show how the measured coherence constrains the variance of the  $P$ -function of this driven state. Similar derivations can be extended to constrain the variance of the Wigner function.

Without losing generality, we assume the state is displaced along x-axis by  $|\alpha_0|$ . That

is

$$\int d^2\alpha P(\alpha, \alpha^*)\alpha = |\alpha_0|. \quad (8.8)$$

Similar to the discussion in Sec. 3.4.4, the phonon number is given by

$$\langle \hat{b}^\dagger \hat{b} \rangle = 2\mu_2 + |\alpha_0|^2. \quad (8.9)$$

The correlation of phonons is

$$\langle \hat{b}^\dagger \hat{b}^\dagger \hat{b} \hat{b} \rangle = \frac{8}{3}\mu_4 + 8|\alpha_0|^2\mu_2 + |\alpha_0|^4. \quad (8.10)$$

Here we assume the  $P$ -function has rotational symmetry around its mean  $|\alpha_0|$  (*i.e.*, conditions given in Eq. (3.173)). Therefore, the second-order coherence can be rewritten as

$$g_m^{(2)}(0) = \frac{\frac{8}{3}\frac{\mu_4}{4\mu_2^2}\xi^2 + 4\xi + 1}{(1 + \xi)^2}. \quad (8.11)$$

If we assume the state is Gaussian, *i.e.*,  $\frac{8}{3}\frac{\mu_4}{4\mu_2^2} = 2$  (given in Eq. (3.172a)), Eq. (8.11) is equivalent to Eq. (8.7). Thus, the measured  $g_m^{(2)}$  can determine the variance as given in Eq. (8.7).

Even if the state is not Gaussian, we have

$$g_m^{(2)}(0) = \frac{\frac{8}{3}\frac{\mu_4}{4\mu_2^2}\xi^2 + 4\xi + 1}{(1 + \xi)^2} \geq \frac{\xi^2 + 4\xi + 1}{(1 + \xi)^2}, \quad (8.12)$$

where we used the inequality between  $\mu_4/\mu_2^2 \geq 3/2$  (equivalent to  $g^{(2)}(0) \geq 1$ ), which is valid for all nonnegative distributions. Notice that  $g_m^{(2)}(0, \xi)$  monotonically increases with  $\xi$  when  $\xi \ll 1$ . Thus,  $\xi$  is bounded by  $\xi \leq \xi_{g2}$  which is the solution of

$$g_m^{(2)}(0) = \frac{\xi_{g2}^2 + 4\xi_{g2} + 1}{(1 + \xi_{g2})^2}. \quad (8.13)$$

Eventually, the variance of the state is bounded by

$$2\sigma^2 = 2\mu_2 \leq \frac{n_m}{1 + \xi_{g2}^{-1}}, \quad (8.14)$$

when  $\xi_{g^2}^{-1} \ll 1$ . Notably, in the limit  $\xi \ll 1$ , both Eq. (8.11) and (8.13) reduce to

$$\lim_{\xi \rightarrow 0} g_m^{(2)}(0) = 1 + 2\xi + o(\xi^2). \quad (8.15)$$

This is similar to the result of the central limit theorem.

### 8.4.2 Fano Factor

The Fano factor is another important indicator to quantitatively evaluate the fluctuations of an oscillator. It is defined as

$$F = \frac{(\Delta n_m)^2}{n_m} = 1 + n_m(g_m^{(2)}(0) - 1). \quad (8.16)$$

For a Poisson counting process (*i.e.*, random process), the variance in the count equals the mean count, so  $F = 1$ . So the Fano factor can be viewed as a kind of noise-to-signal ratio, which is normalized to a random process. It also provides additional information to distinguish between states that may have similar values of  $g_m^{(2)}(0)$ . Particularly, for a DTS satisfying  $\xi \ll 1$ , substituting Eq. (8.6) into Eq. (8.16) yields

$$F \approx 1 + 2n_{m,\text{th}}^{\text{DTS}}, \quad (8.17)$$

which suggests the Fano factor equivalently evaluates the variance of the Wigner function of a DTS in this limit.

The Fano factors of our displaced thermal states are displayed in Fig. 8.11, where we highlight different contributions to Fano factors, such as the bath thermal fluctuation (beige), the probe laser heating (sage), the drive laser heating (turkish blue) (details c.f. Sec. 8.4.2.1). The fact that the measured Fano factors do not deviate from the expected Fano factors means the approach we use to drive the mechanical motion does not bring too much extra noise into this nearly coherent state.

We want to emphasize that the system is likely coherent even for higher amplitudes than the amplitudes achieved in Fig. 8.10. The maximum amplitude in this setup is limited by the maximal optical drive power we could send to the optomechanical cavity and the maximum count rate of the SNSPDs (which yields difficulties in measuring high amplitude  $g_m^{(2)}$ ). We expect to be able to drive three orders of magnitude more phonons without the system being affected by its intrinsic mechanical nonlinearity (discussed in Appendix A.4.2).

#### 8.4.2.1 Fano Factor Contributions

By definition, the Fano factor characterizes the phonon number fluctuation in the mechanical resonator. Any deviation from the ground state, such as the bath thermal noise, the

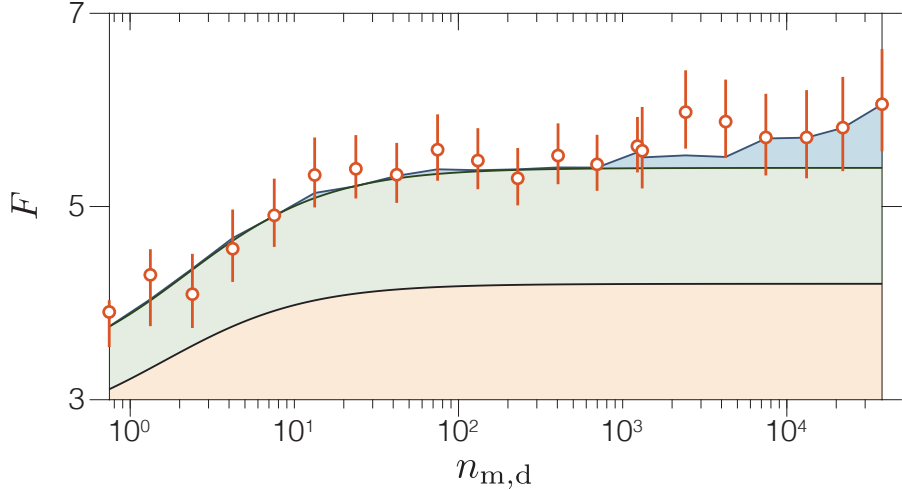


Figure 8.11: Fano factor  $F$  versus  $n_{m,d}$ . The orange circles represent the measured Fano factors  $F$ . The contributions to the Fano factors from the bath temperature, the probe laser heating, and the drive laser heating are represented by the orange, sage and turkish blue shaded areas, respectively (see Sec. 8.4.2.1). Error bars show two s.d. determined from the measured count rates, statistical errors, and the errors of  $g^{(2)}(0)$  from the fits.

heating effect of the drive laser, or the heating effect from the probe laser, increases the Fano factor  $F$ . In this section, we describe the experimental details of characterizing different contributions to the phonon number fluctuations.

Figure 8.12 summarizes the laser settings in the frequency domain for the following measurements:

**Bath Thermal Noise** The base temperature of the dilution fridge is  $\sim 20$  mK, which is comparable to  $\hbar\omega_m$ . A red-detuned probe laser at  $-\omega_m$  of  $0.1 \mu\text{W}$  (the heating effects is negligible) is sent to the cavity, and the corresponding measured sideband photon count rate is denoted as  $\Gamma_{\text{base}}$ .

Assume the mixing chamber temperature  $T_{\text{MC}}$  is fixed through the entire measurement, which yields a fixed base phonon number  $n_{m,\text{base}}$ . Therefore, the phonon reading efficiency  $\eta$ , *i.e.*, the count rate per phonon, can be calibrated by  $\eta = \Gamma_{\text{base}}/n_{m,\text{base}}$ . This phonon reading efficiency  $\eta$  will be utilized to infer the phonon number in the following steps to compensate for the slow drifts in the measurement efficiency.

**Probe Laser Heating Effect** The probe laser power  $P_{\text{in}}$  is set at  $1 \mu\text{W}$ , which is the same power in the aforementioned coherence measurements. This laser heats up the mechanical resonator and causes certain optomechanical backaction effects. The measured sideband photon count rate in this step  $\Gamma_{\text{probe}}$  can be used to infer the total phonon number in the presence of this probe laser by using the calibrated  $\eta$ , *i.e.*,

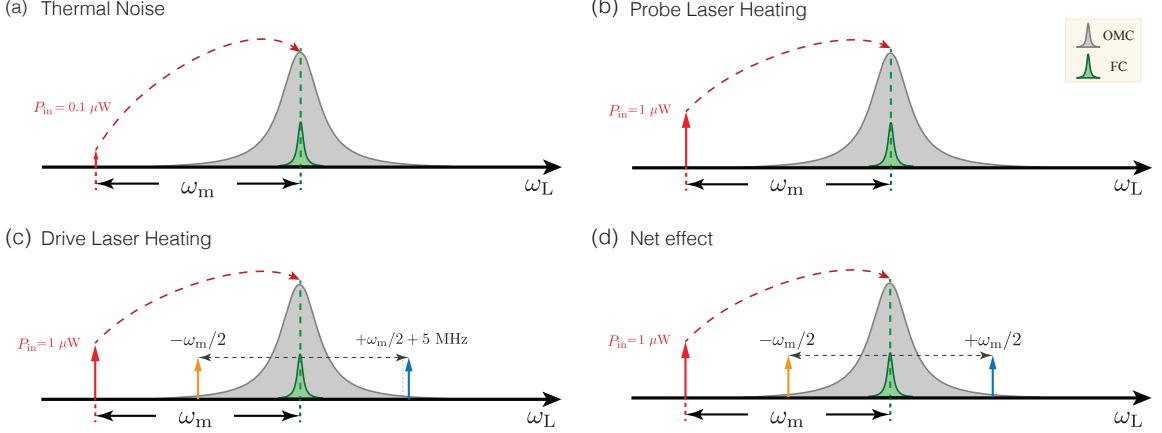


Figure 8.12: (a) One  $0.1\text{ }\mu\text{W}$  is placed on the red-detuned sideband ( $\Delta = -\omega_m$ ). The grey Lorentzian shape represents the optical cavity resonance, and the green Lorentzian is the filter cavity resonance. (b) Sent one  $1.0\text{ }\mu\text{W}$  red-detuned probe laser to the OMC to calibrate the heating effect of the probe laser in the experiment. (c) One  $1.0\text{ }\mu\text{W}$  red-detuned probe laser and two optical tones (yellow and blue) at  $-\omega_m/2$  and  $+\omega_m/2 + 5\text{ MHz}$ , respectively, to calibrate the net heating effect by all optical inputs. (d) Optical settings of displaced thermal states coherence measurements, as discussed in Sec. 8.4.1.

$n_{m,\text{probe}} = \Gamma_{\text{probe}}/\eta$ . The measured mean phonon occupancy in this step is  $\sim 2.2$ , shown as the black dashed line in Fig. 8.13.

**Drive Laser Heating Effect** We fix  $1\text{ }\mu\text{W}$  probe laser at  $-\omega_m$  and add extra off-resonance optical beat consisting of two tones of  $-\omega_m/2$  and  $+\omega_m/2 + 5\text{ MHz}$ .  $P_1$  and  $P_2$  are set to be equal to the values in each corresponding coherence measurement. Similarly, the phonon number in this step is also calibrated as  $n_{m,\text{heat}} = \Gamma_{\text{heat}}/\eta$ . Notably, the added phonon number due to the heating effect is not linear with the total heating power (see Sec. 6.3.2.1). So, we measure the heating effect of the drive lasers on top of a  $1\text{ }\mu\text{W}$  probe laser background. The measured  $n_{m,\text{th}}$  in this step as a function of  $n_{m,\text{d}}$  is shown in Fig. 8.13. As you can see, the heating effect of the drive laser becomes noticeable only after  $P_1 > 50\text{ nW}$ , i.e.,  $n_{m,\text{d}} > 10^3$ .

**Fluctuation of DTS** The displaced thermal state experiment is operated according to Sec. 8.4. We utilize the count rate of the sideband photons  $\Gamma_{\text{DTS}}$  to calibrate the total phonon number  $n_m = \Gamma_{\text{DTS}}/\eta$ . The fluctuation of the state (*i.e.*,  $n_{m,\text{th}}^{\text{DTS}}$ ) is determined by Eq. (8.7). After subtracting contributions from the bath thermal noise, probe laser heating effect and drive laser heating effect, the extra fluctuation is possibly a result of the other uncalibrated measurement imperfections or the added fluctuations in the driven states.

These steps run in a loop to diminish the drift of the overall measurement efficiency

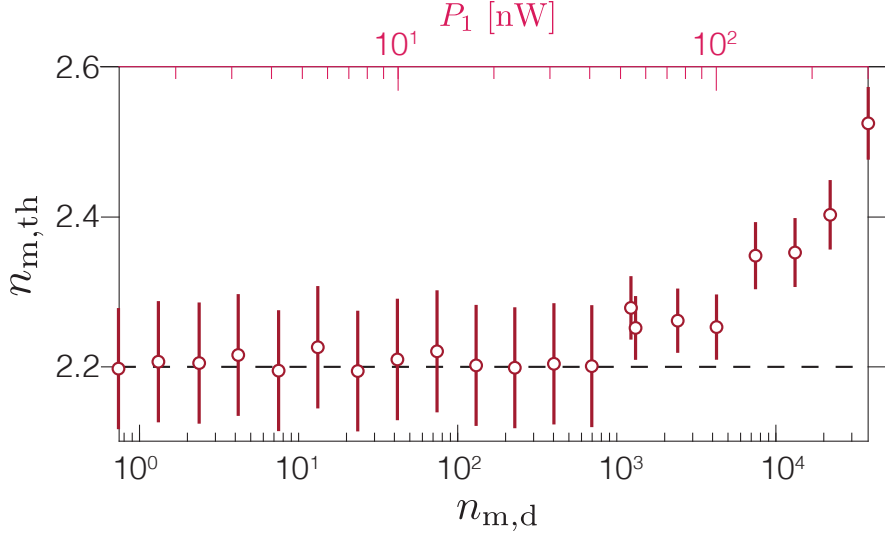


Figure 8.13: The measured  $n_{m,\text{th}}$  (red circles) versus  $n_{m,d}$ . The black dashed line is the mean  $n_{m,\text{th}}$  only with  $1\mu\text{W}$  probe laser. The top (pink) shows the power of one of the drive tones  $P_1$  ( $P_1 = P_2$ ). Error bars show two s.d. determined from the statistical errors and systematic errors.

during a long measurement ( $\sim$  days). Each such loop is followed by a dark count rate calibration (blocking the optical inputs) and a stray photon count ( $1\mu\text{W}$  laser detuned by  $-310\text{ MHz}$ ) rate calibration, which are described in Sec. 6.3.1.2.

### 8.4.3 Background Characterization and Subtraction

In this section, we describe the classical background that appears in the coherence of highly displaced thermal state, and the method implemented in the analysis to subtract such backgrounds. More specifically, we discuss the off-set in  $g_m^{(2)}(\tau)$ , a bias current dependent coherence background and the method to subtract the classical coherence background.

#### 8.4.3.1 Subtracting the Coherence Prefactor due to Slow Drifts

As discussed in Sec. 7.2.4.3, a slow varying intensity modulation (which can be caused by slow drifting polarization, filter cavity transmissivity, etc.) introduces a drifting prefactor in the measured coherence  $\hat{g}_{\text{ML}}^{(2)}(\tau)$ . In other words,  $\hat{g}_{\text{ML}}^{(2)}(\tau)$  is the product of the phonon coherence  $g_m^{(2)}(\tau)$  and a constant because of slow drifts. This effect is detailed described by Eq. (7.35). As a result, the measured coherence does not asymptote to 1 as we expect. Empirically, we can subtract the effect of slow drifts by normalizing the measured coherence to its asymptotic value (which is extracted from the fit).

In Fig. 8.14(a), we present an example of the measured  $\hat{g}_{\text{ML}}^{(2)}(\tau)$  of a displaced thermal

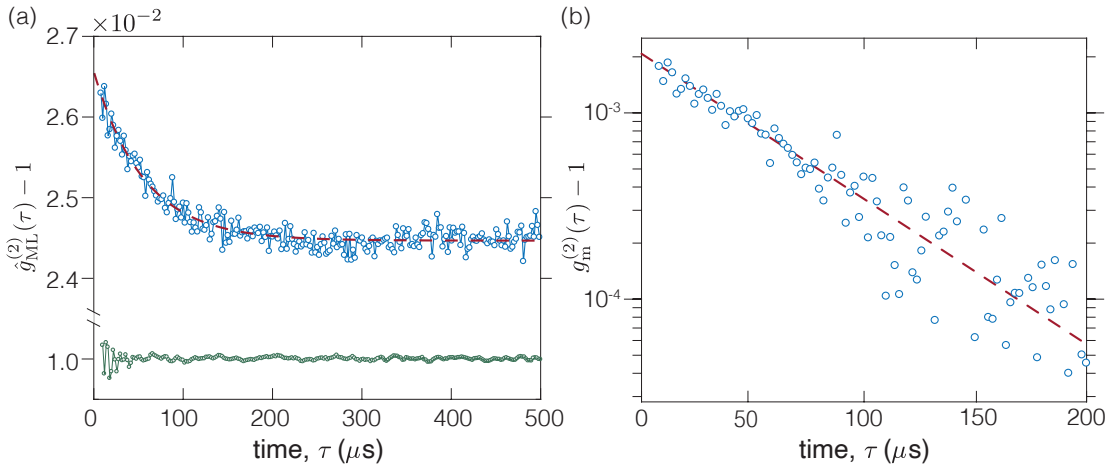


Figure 8.14: (a) Measured second-order coherence  $\hat{g}_{\text{ML}}^{(2)}(\tau)$  (blue circles) of a displaced thermal state with  $n_{\text{m,d}} \approx 2.4 \times 10^3$ . The red dashed line represents a fit to the form of  $a + be^{-\tau/2\tau_0}$  (given in Eq. (3.122)). Green circles show  $\hat{g}_{\text{ML}}^{(2)}(\tau)$  of a laser that goes through most of the optics in the system. This time-independent coherence further supports the method in Sec. 8.4.3.1. (b) The coherence of a displaced thermal state  $g_m^{(2)}(\tau)$  after the normalization (blue circles). The red dashed line shows the fit to  $1 + ae^{-\tau/2\tau_0}$ .

state without this normalization.  $\hat{g}_{\text{ML}}^{(2)}(\tau)$  of a DTS (blue circles) shows a clear exponential decay feature with a flat tail, and has an amplitude  $2 \times 10^{-3}$  and a constant offset of 0.0245 from 1 (*i.e.*, a prefactor of 1.0245) in its tail. Figure 8.14(b) shows the desired phonon coherence  $g_m^{(2)}(\tau)$  after the normalization in the logarithmic scale. The clear exponentially decaying feature after the subtraction suggests the success of this method.

Besides measuring anti-Stokes photons, we also directly sent a laser at  $\omega_{\text{cav}}$  and measured the corresponding coherence, as shown in Fig. 8.14(a).  $\hat{g}_{\text{ML}}^{(2)}(\tau)$  of this control group (green circles) is time-independent in its first 500  $\mu\text{s}$  with an offset of  $1.0(1) \times 10^{-2}$ . This result suggests the observed offset of scattered photons is likely caused by the classical systematic drifts.

#### 8.4.3.2 Bias Current Dependence of the Coherence Background

One major improvement in the resolution of  $g_m^{(2)}(\tau)$  was achieved by discovering its noteworthy dependence on the SNSPDs' bias currents. When the bias current is too low, a clear background appears in the coherence measurements.

To characterize this dependence, a laser (used as a coherent source) was split by a 50/50 beamsplitter and then directly sent to the two SNSPDs. Bypassing most of the experimental devices diminishes the possible contributions from the rest of the optical components. The bias current of SNSPD1 varies from 17.0  $\mu\text{A}$  to 20.5  $\mu\text{A}$ , while SNSPD2's bias current is fixed at 19  $\mu\text{A}$  as a reference. Figure 8.15(a) shows the measured coherences of

SNSPD1 at various bias currents (shown in the legend in (b)).  $g^{(2)}(\tau)$  of different bias currents show certain oscillation patterns, whose amplitude significantly increases with a smaller bias current.

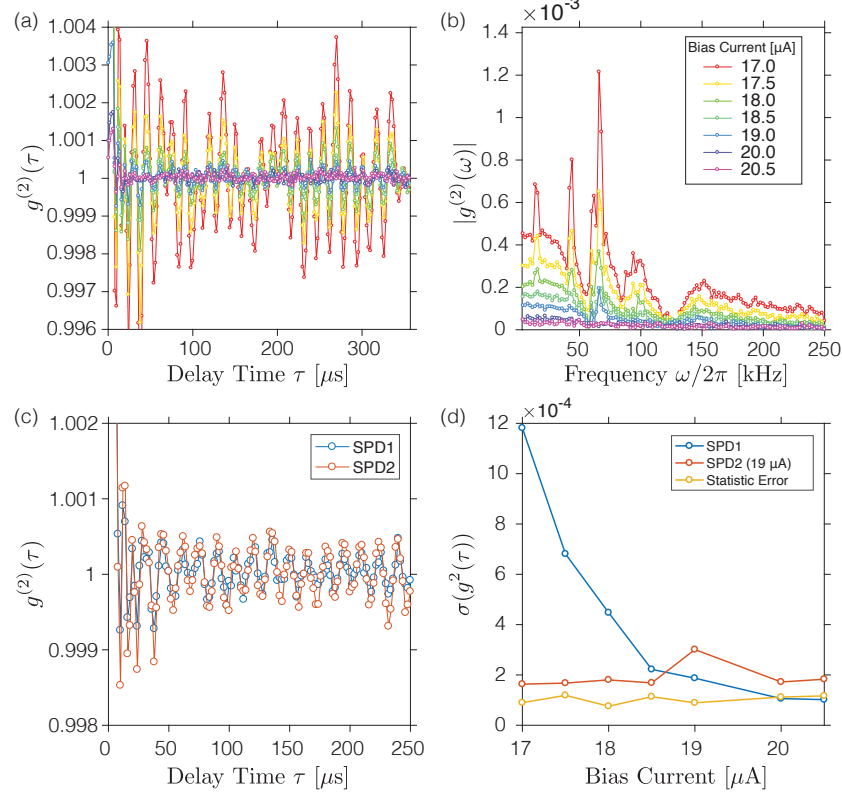


Figure 8.15: (a) Measured  $g^{(2)}(\tau)$  of a laser using SNSPD1 with different bias currents. The value of the bias current in each color is shown in (b). (b) Spectrums of the Fourier transformed of  $g^{(2)}(\tau)$  for different bias currents. (c) Comparison of  $g^{(2)}(\tau)$  measured from SNSPD1 and SNSPD2 when bias currents of both are 19 μA. (d) Standard deviations of  $g^{(2)}(\tau)$  measured from SNSPD1 (blue circles) as a function of SNSPD1 bias current. The bias current of SNSPD2 is fixed at 19 μA in each measurement as a reference (orange circles). The statistical uncertainties due to the limited number of measured coincidences are represented by yellow circles.

The Fourier transformed spectrums of these coherences are shown in Fig. 8.15(b). A clear peak appears at 66 kHz, which corresponds to the obvious oscillation pattern in the  $g^{(2)}(\tau)$ . We also show  $g^{(2)}(\tau)$  measured by SNSPD1 and SNSPD2 in Fig. 8.15(c). The bias currents of both SNSPDs are set at 19 μA in this comparison experiment. Both  $g^{(2)}(\tau)$  exhibit a similar oscillation pattern of a similar amplitude, which suggests this could be a universal problem in SNSPDs.

The standard deviation of  $g^{(2)}(\tau)$  as a function of the bias current of SNSPD1 is shown in Fig. 8.15(d). The bias current of SNSPD2 is fixed at 19 μA as a reference. The measured

standard deviation plateaus at the statistical error (estimated by the number of coincidence events in the measurement) when the bias current is greater than  $20\mu\text{A}$ . Thus, the bias currents of both SNSPDs are set at  $20\mu\text{A}$  in the displaced thermal state experiment.

#### 8.4.3.3 Subtracting Coherence Background

The intensity modulation caused by the power fluctuations, filter cavity transmissivity oscillations, optical cavity coupling rate fluctuations will contribute to the coherence of the measured coherence (details c.f. Sec. 7.2.4.3). However, we cannot simply truncate the frequency at an upper bound  $\omega_0$  to have a frequency-independent coherence background shown in Eq. (7.36) when we are interested in  $g_m^{(2)}(\tau)$  at the level of 0.001.

As shown in Eq. (3.122), the amplitude of the coherence amplitude  $g_m^{(2)}(0)-1$  of a DTS is inversely proportional to  $|\alpha|^2$ . Thus, the coherence background gradually dominates the measured coherence when  $|\alpha|^2$  increases. To extract the coherence of the DTS, we apply Eq. (7.34) in the following manner

$$g_m^{(2)}(\tau) = \hat{g}_{\text{ML}}^{(2)}(\tau)/g_{\text{bkg}}^{(2)}(\tau), \quad (8.18)$$

where  $g_m^{(2)}(\tau)$  is the coherence of the mechanical state,  $\hat{g}_{\text{ML}}^{(2)}(\tau)$  is the estimated coherence shown in Eq. (7.8) and  $g_{\text{bkg}}^{(2)}(\tau)$  is the coherence background. The coherence background is measured from the coherence of a displaced thermal state with a much higher amplitude (10 times more than the maximal  $n_{m,d}$  that we showed in this thesis) such that the coherence of the displaced thermal state part is negligible.

In Fig. 8.16(a), we show  $\hat{g}_{\text{ML}}^{(2)}(\tau)$  of various displaced thermal states ( $n_{m,d}$  of each state is shown in (b)). The grey solid line is the coherence background extracted from an ultra-high-amplitude displaced thermal state ( $n_{m,d} > 2 \times 10^5$ ). Clearly,  $\hat{g}_{\text{ML}}^{(2)}(\tau)$  approaches this coherence background with increasing amplitudes. The coherence background has an amplitude of  $1 \times 10^{-4}$  and an unidentified oscillation pattern with frequency  $\sim 20\text{ kHz}$ . This pattern is qualitatively repeatable for measurements separated by weeks. Therefore, the background characterization (measuring using a highly displaced thermal state) is inserted in the experiment loop discussed in Sec. 8.4.2.1.

The background-subtracted coherences  $g_m^{(2)}(\tau)$  are shown in Fig. 8.16(b). They present more evident exponentially decaying features. Nearly parallel decoherence lines in the log plot (shown in the inset) together with the agreement between the processed data and the prediction (shown in Fig. 8.10(c)) verifies the feasibility of this background coherence subtraction method.

In addition, the measured coherence of the sideband photons (green) is compared to the measured coherence of the laser (which is at  $\omega_{\text{cav}}$  and goes through the optomechanical cavity), as shown in Figs. 8.16(c,d). The similarity between these independent measurements suggests that the majority of the coherence background originates from the fluc-

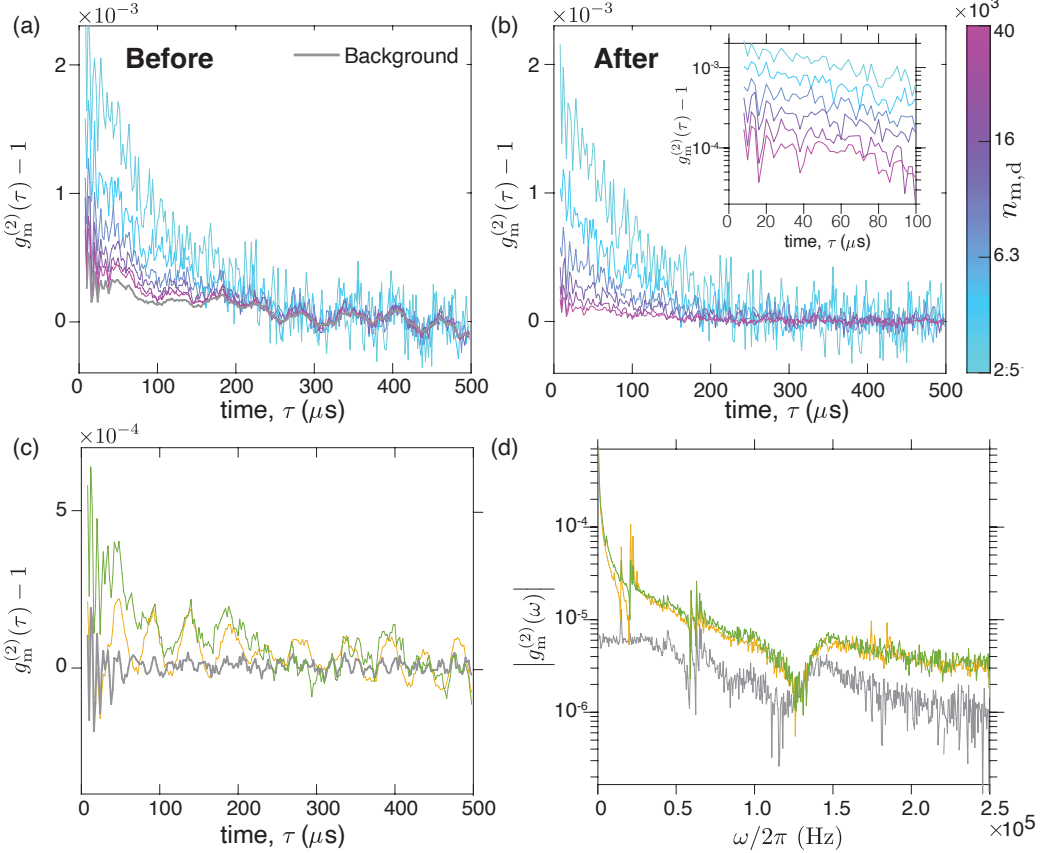


Figure 8.16: (a)  $\hat{g}_{\text{ML}}^{(2)}(\tau)$  of various displaced thermal states. The corresponding  $n_{m,d}$  are indicated in the color bar, ranging from  $2.5 \times 10^3$  to  $4 \times 10^4$ . The grey solid line represents the coherence background extracted from the extremely-high amplitude ( $n_{m,d} > 2 \times 10^5$ ) displaced thermal state. (b)  $g_m^{(2)}(\tau)$  after subtracting coherence background (grey solid line in (a)) according to Eq. (8.18). Inset: Background subtracted coherence in the log scale. Nearly parallel decoherence lines suggest the same decoherence rate. (c) Measured  $\hat{g}_{\text{ML}}^{(2)}(\tau)$  of scattered photons from a displaced thermal state (green), a laser at  $\omega_{\text{cav}}$  reflected by the optical cavity (gold) and a laser directly sent to SNSPDs (grey). The similarity between the coherences of the sideband photons and the reflected on-resonance laser in the time domain infers the dominancy of the classical measurement efficiency fluctuation in this coherence background. (d) Fast Fourier transformed coherences in (c). In the frequency domain, it also shows the similarity between the coherences of the sideband photons and the reflected on-resonance laser. Particularly, they exhibit the same peak around 20 kHz.

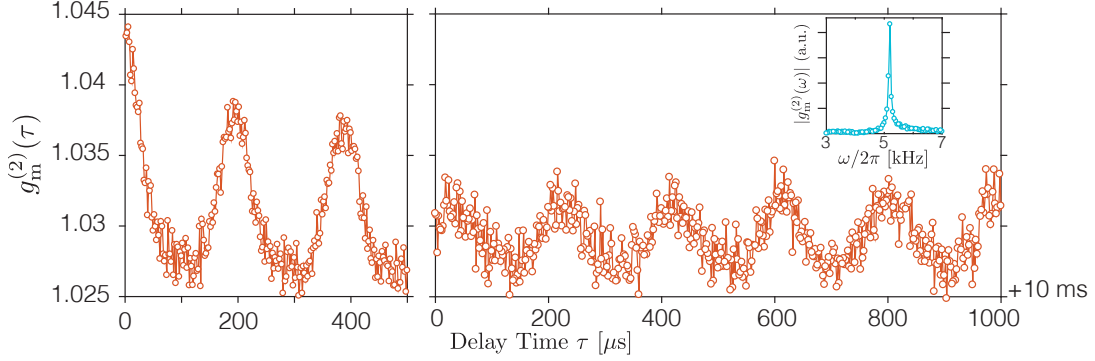


Figure 8.17: The recorded unidentified oscillation in the coherence (without subtracting background coherence) of a DTS with  $|\alpha|^2 = 2553$ . Right:  $g_m^{(2)}(\tau)$  after 10 ms. The oscillation is still clear with a smaller amplitude. Inset: The spectrum of  $g_m^{(2)}(\tau)$ . A clear peak, which corresponds to the obvious oscillation in  $g_m^{(2)}(\tau)$ , appears at 5.2 kHz.

tuations of these classical properties, including laser intensity, filter cavity transmissivity. In this characterization measurement, the same laser (at  $\omega_{\text{cav}}$ ) is directly measured by SNSPDs, the corresponding coherence (grey) is used to characterize the contribution from SNSPDs and the laser.

#### 8.4.4 Unidentified Oscillation Signal

In one of the DTS coherence measurements, we observed an unidentified oscillation in the coherence when the state is driven to  $|\alpha|^2 = 2553$ , as shown in Fig. 8.17. The frequency of this apparent oscillation is  $\sim 5.2$  kHz with an FWHM less than 100 Hz (limited by the maximal delay time we used in the coherence analysis), as shown in the inset of Fig. 8.17. This oscillation lasted for a few minutes and was observed in two consecutive data sets (each lasts 3 mins). We cannot record a real-time intensity signal because the maximum photon count in one oscillation ( $\sim 200$   $\mu$ s) is  $\sim 200$  (limited by the SNSPD maximal count rate). The contrast of the oscillation is only  $\sim 1\%$ , which cannot be resolved in a realtime measurement due to the statistical uncertainty.

The origin of this oscillation is unclear. The fact that it lasted more than 1 minute proves the quality factor of this oscillation is greater than  $3 \times 10^5$  unless it has been actively driven. Apart from possible classical systematical oscillations, such as accidentally bumping the device or fibers (which cannot explain the high-quality oscillation), it is also possible to be excited by showers of cosmological rays [265].

## 8.5 Applications of Mechanical Coherent States

Significant advances in operating optomechanical systems have improved their measurement sensitivity to the point that they are limited by the quantum zero-point fluctuations [41, 52, 53, 81, 266]. Leveraging the massiveness and macroscopicity of mechanical resonators, these devices are proposed for various sensing tasks such as detecting dark matter [182, 267–271], gravitational waves [218, 272], and testing quantum gravity effects [1, 188, 189, 273]. In this section, we describe two applications of the mechanical system in this work when it is prepared in a nearly coherent state.

In the first case, we consider using the mechanical oscillator to measure another coupled system by monitoring the phase shift of the reflected mechanical wave. As a direct analogy to the optical interferometer [44, 274], this measurement can reach the “standard quantum limit” (SQL) by tuning the intra-oscillator phonon number to balance the backaction and the imprecision noises in the measurement.

In the second case, we consider using this nearly coherent state to constrain one of the modified quantum theories [1, 188, 189]. In this test, a larger amplitude and a more massive oscillator cast a tighter bound on the nonlocal dynamical length scale  $l_k$ , which is discussed in Sec. 4.2.2.

### 8.5.1 Acoustic Interferometric Measurement

An interferometric measurement of the displacement of a macroscopic object typically consists of recording the phase shift of a reflected wave. The system shown in Fig. 8.18(a) can be regarded as such a setup, in which the displacement  $x_E$  of an external oscillator (grey pendulum) is inferred from the phase difference between the light wave that is incident on the cavity and the light wave that returns from the cavity.

The SQL limits the precision of such a measurement [44, 274], which is the result from the competition between imprecision noise and backaction noise. This noise spectrum  $S_{x_Ex_E}^{\text{add}}(\omega)$  of such a measurement satisfies [44]

$$S_{x_Ex_E}^{\text{add}}(\omega) \geq S_{x_Ex_E}^{\text{ZPF}}(\omega), \quad (8.19)$$

where  $S_{x_Ex_E}^{\text{ZPF}}(\omega)$  is the spectrum of this external oscillator that is associated with its zero-point fluctuations. If we measure at the mechanical resonance  $\omega = \omega_E$ , the equal sign is achieved at

$$n_{\text{cav}}|_{\text{SQL}} = \frac{\kappa\gamma_E}{16g_0^2}(1 + 4\frac{\omega_E^2}{\kappa^2}), \quad (8.20)$$

where  $\gamma_E$  is the linewidth of the external resonator,  $g_0$  is the single-photon coupling strength between the optical mode and the external mechanical oscillator.

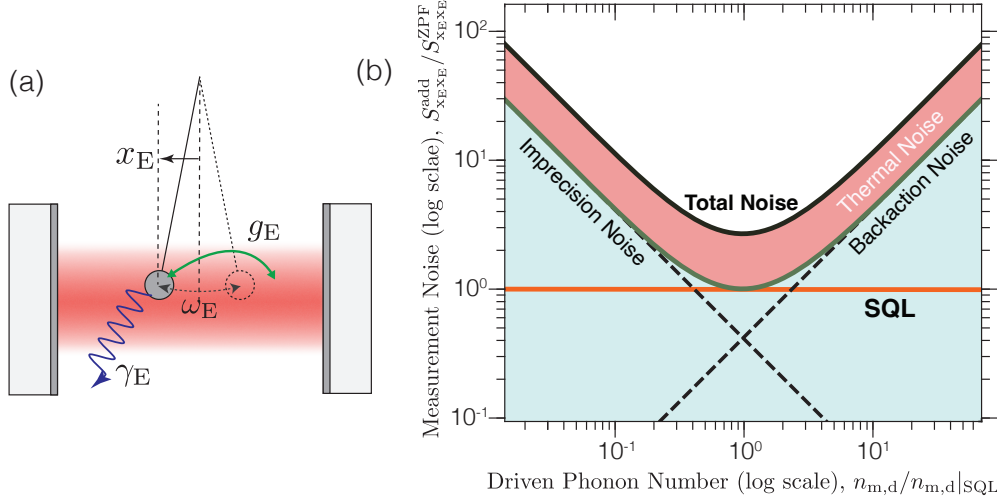


Figure 8.18: (a) Schematic of the interferometric measurement in a cavity. The grey pendulum is the external oscillator to be measured. The red field can be either optical waves or acoustic waves. (b) The measurement noise (green line) (scaled to the zero-point fluctuations of the external oscillator) as a function of intra-oscillator phonon number (scaled to  $n_{m,d}$  defined in Eq. (8.23)). The orange solid line represents the SQL. The red shaded area is the extra noise due to the thermal noise in the displaced thermal state.

The nature of such an interferometric measurement is not limited to the case of optical waves reflecting from an optical cavity. Here we consider the case that the essential geometry is the same as in Fig. 8.18(a) but that the displacement  $x_E$  of the macroscopic oscillator detunes an acoustic cavity (such as the design in this work), and this detuning is inferred from the phase shift of acoustic waves that drive the cavity.

The physics and the math for the acoustic interferometer are identical to the optical one. However, since the frequency of any practical acoustic mode is likely to be much less than the frequency of the optical modes we have considered so far, it is important to also consider how the thermal fluctuations  $n_{m,th}$  associated with the driven acoustic mode contribute to the imprecision noise and the backaction noise. We note that the same considerations apply to electromagnetic interferometers that operate with microwaves or RF cavities.

In this case, we have:

$$S_{x_ExE}^{\text{imp}}(\omega) \approx \frac{\gamma_m(2n_{m,th} + 1)}{16|\alpha|^2 G_E^2} \left(1 + 4\frac{\omega^2}{\gamma_m^2}\right), \quad (8.21)$$

$$\begin{aligned} S_{F_E F_E}(\omega) &= \left(|\alpha|^2 (2n_{m,th} + 1) + n_{m,th}^2 + n_{m,th}\right) \frac{4\hbar^2 G_E^2}{\gamma_m} \left(1 + 4\frac{\omega^2}{\gamma_m^2}\right)^{-1} \\ &\approx |\alpha|^2 (2n_{m,th} + 1) \frac{4\hbar^2 G_E^2}{\gamma_m} \left(1 + 4\frac{\omega^2}{\gamma_m^2}\right)^{-1}, \end{aligned} \quad (8.22)$$

where  $F_E$  is the force on the external oscillator, and  $G_E$  is the coupling strength between the acoustic wave and the external resonator. The minimal added displacement noise is  $(2n_{m,\text{th}} + 1)S_{x_{\text{EXE}}}^{\text{ZPF}}$ . This result can be understood by treating the broadened Gaussian noise in a displaced thermal state as a scaled zero-point fluctuation. Apparently, it is crucial to reduce the noise of the driven acoustic waves to reach SQL in such a measurement.

Similar to Eq. (8.20), the driven phonon number (*i.e.*, intra-cavity phonon number) to reach the minimal added noise is

$$n_{m,d}|_{\text{SQL}} = \frac{\gamma_m \gamma_E}{16g_E^2} \left( 1 + 4 \frac{\omega_E^2}{\gamma_m^2} \right), \quad (8.23)$$

where  $g_E$  is the single-phonon coupling strength between the acoustic mode and the external mechanical oscillator.

In Fig. 8.18(b), the added noise due to the quantum uncertainty (green) is plotted as a function of  $n_{m,d}$ . Additionally, the contribution from the thermal noise of the displaced thermal state is shown in the red-shading area.

Comparing this result to Eq. (8.20), we note that the acoustic modes' linewidth ( $\gamma_m$ ) is much less than that of the optical modes ( $\kappa$ ) may reduce the intra-cavity energy required to reach the SQL by orders of magnitude.

However, unlike the optical cavity, there is no obvious acoustic readout in the acoustic cavity. In our work, the acoustic cavity also couples with the optical cavity. How to use this optomechanical coupling to read out the phase shift of the acoustic wave and the added noise due to this optical measurement are the subject of future study.

### 8.5.2 Constraining a Modified Quantum Theory: Nonlocal Dynamics

Quantum gravity phenomenology is a broad field of research that aims to connect general features of quantum gravity with observations or experiments even without a definitive theory of quantum gravity. In Sec. 4.2.2, we discussed an example of this approach, where local Lorentz invariance (LLI) is held as a guiding principle, and spacetime is seen as emerging from more fundamental discreteness. A nonlocal dynamical modification of the standard local theory is brought up to bridge the incompatibility between LLI and the fundamental discreteness [1, 189]. In this framework, it is predicted that in the non-relativistic limit, a mechanical coherent state under a harmonic potential leads to a spontaneous time-dependent, cyclic squeezing in both the position and momentum, as shown in Eq. (4.33) and Fig. 4.2. The amplitude of this squeezing approximates as  $\sim 6\epsilon|\alpha|^2$ , where  $\epsilon = (l_k/x_{\text{ZPF}})^2$ . Details can be found in Sec. 4.2.2.

The most general single-mode Gaussian state is described as the displaced squeezed thermal state [133]. The coherence of  $|n_{m,\text{th}}, \alpha, \zeta\rangle$  is described in Eq. (3.42), where  $n_{m,\text{th}}$  is the effective mean occupancy,  $\alpha$  is the displacement, and  $\zeta$  is the squeezing parameter.

When the fluctuations of the mechanical state are close to its zero-point motion, the

squeezing due to this nonlocal dynamics (described in Eq. (4.33)) can be reparameterized as

$$\zeta = \left| \frac{1}{4} \log \left( \frac{\text{Var}(\tilde{x}(\theta))}{\text{Var}(\tilde{p}(\theta))} \right) \right|. \quad (8.24)$$

In the small squeezing ( $\zeta \ll 1$ ), large displacement ( $|\alpha|^2 \gg n_{m,\text{th}}$ ) limit, averaging Eq. (3.42) over  $\theta$  yields an average second-order coherence

$$\langle g_m^{(2)}(0) \rangle \approx 1 + \frac{2n_{m,\text{th}}}{|\alpha|^2} + \frac{32\sqrt{2}}{\pi} \left( n_{m,\text{th}} + \frac{1}{2} \right) \epsilon b_2. \quad (8.25)$$

Notably, the extra term (last term) is independent of  $|\alpha|$ . According to Eq. (8.25), the discrepancy between the measured  $g_m^{(2)}(0)$  from the theoretical prediction can cast an upper bound on the dimensionless nonlocality  $\epsilon$ .

Eq. (8.25) is only valid when  $n_{m,\text{th}} \ll 1$ . This is because Eq. (4.33) is a result of perturbation theory which is expanded near its ground state. It requires  $\epsilon \ll 1$  and  $n_{m,\text{th}} \ll 1$ . Additionally, Eq. (8.24) is able to estimate the squeezing amplitude only when its fluctuation is near its zero-point motion.

In the experiment discussed in Sec. 8.4, a massive ( $\sim 1$  ng) oscillator whose mean thermal phonon number is around 2 is prepared in highly displaced thermal states (which does not satisfy  $n_{m,\text{th}} \ll 1$ ). In the current experiment, we cannot directly measure the cyclic squeezing. Instead, we measured  $\langle g_m^{(2)}(0) \rangle$  to compare to the ideal scenario. This is a mathematically equivalent approach. However, we compromise on not observing the cyclic squeezing, which is considered the signature of this nonlocal dynamics. And other unidentified classical factors (such as the fluctuations of the RF drive power and the fluctuations of the mechanical resonance frequency) can in principle also yield a similar deviation in  $g^{(2)}(0)$ .

The discrepancy between the measured coherence and the predicted coherence is

$$\Delta g^{(2)}(0) = g_m^{(2)}(0)^{+2\sigma_u}_{-2\sigma_l} - g_{\text{pred}}^{(2)}(0), \quad (8.26)$$

where  $\Delta g^{(2)}(0)$  has an unsymmetric 95% confidence interval that originates from the unsymmetric confidence interval of measured coherences  $g_m^{(2)}(0)^{+2\sigma_u}_{-2\sigma_l}$ , where  $\sigma_u$  and  $\sigma_l$  represent the upper and lower uncertainties (one s.d.) of  $g_m^{(2)}(0)$ , respectively (the unsymmetric confidence interval is obtained by using logistic regression method discussed in Sec. 7.2.2.2).

To be more conservative in our conclusion, we used the data without the coherence background subtraction that is discussed in Sec. 8.4.3.3 (the original data are blue circles shown in Fig. 8.10(d)). Figure 8.19(a) shows  $\Delta g^{(2)}(0)$  and their corresponding 95% confidence interval as a function of  $n_{m,d}$ . The maximal absolute discrepancy in its 95%

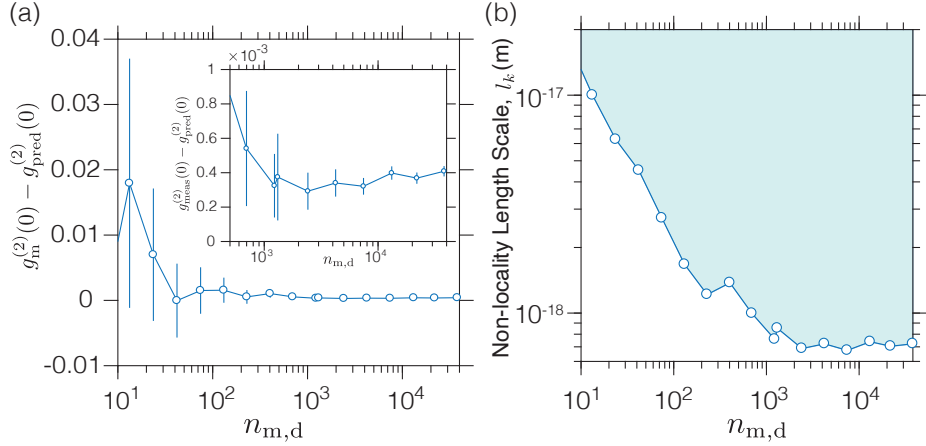


Figure 8.19: (a) Discrepancies of the measured coherence and the predicted coherence as a function of  $n_{m,d}$ , where errorbars represent 2 s.d.. Inset: a zoom-in version. (b) The non-locality length scale  $l_k$  (blue-shaded area) that is excluded by this experiment with 95% CI as a function of  $n_{m,d}$ .

confidence interval

$$\max\{|g_m^{(2)}(0) - 2\sigma_l - g_{\text{pred}}^{(2)}(0)|, |g_m^{(2)}(0) + 2\sigma_u - g_{\text{pred}}^{(2)}(0)|\} \quad (8.27)$$

can bound the extra term in Eq. (8.25) with 95% confidence levels.

As a demonstration, if we assume the measured result is from a mechanical mode in its ground state, substituting Eq. (8.27) into Eq. (8.25) yields the constraint on  $l_k$  with 95% confidence levels as shown in Fig. 8.19(b), where the unknown expansion coefficient  $b_2$  is taken to be 1 for the sake of clarity.  $l_k$  is constrained down to  $7 \times 10^{-19}$  m, which is comparable to the bound ( $\sim 10^{-19}$  m) achieved by comparing nonlocal relativistic EFTs to the 8 TeV LHC data [202]. As we discussed in Sec. 8.4.3, the majority of the discrepancy between measured and predicted values of coherences (shown in Fig. 8.19(a)) stems from trivial classical factors, such as slowly drifting experimental parameters. If we can confidently subtract the coherence backgrounds (as discussed in Sec. 8.4.3.3) and assume they are irrelevant to the squeezing induced by this nonlocal dynamics, then this data constrains  $l_k \lesssim 1 \times 10^{-19}$  m with 95% confidence levels.

*“Entanglement is the most distinctive feature of quantum mechanics and is responsible for its paradoxical nature.”*

– Asher Peres

# CHAPTER 9

## Photon-Phonon Entangled States

In chapter 7 and chapter 8, we demonstrated the measurement results for thermal states and displaced thermal states. Both of them are regarded as being members of the set of “general quantum states” in the discussion in Sec. 3.5.2, as neither exhibits distinctive quantum features. In this chapter, we move one step forward to present the preparation and measurement of photon-phonon entangled states.

Light-matter entanglement enables nonclassical correlations between the flying and stored quantum states. The pioneering work of Duan, Lukin, Cirac, and Zoller (DLCZ) [154] proposed using such entangled states as a building block for applications such as scalable quantum networks and quantum repeaters over large distances [154, 275], making such states a key component in quantum information science. To date, quantum states of matter, such as spin states of ions [276], atoms [277, 278], atomic ensembles [74, 76, 279–281], single atoms [282], nitrogen-vacancy centers [283], erbium-doped fibers [284], and solids [285], have been experimentally entangled with photons.

In recent few years, mechanical devices also stand out as possible building blocks for quantum information applications [10, 11, 28, 75]. They are highly engineerable platforms that interact unitarily with various other quantum systems. Interfacing mechanics with optical photons is highly desirable because it enables the transfer of excitation between cryogenic mechanical elements over long distances via room-temperature fiber optical connections. Thus, the mature toolbox of quantum optics can be naturally adapted in this case, such as storing photon states in matter [11, 75], entangling states of matter [97, 98], and teleporting states of matter [286, 287].

The single-photon cooperativity of the device in this thesis is three orders of magnitude shorter of the value (1) that is required in the single-photon strong cooperativity regime, and so would not enable the direct control of the quantum state of the mechanics (discussed in Sec. 2.4.1.1). In this thesis, we use the well-known DLCZ protocol [74, 154] to conditionally prepare and measured entangled photon-phonon pairs. The observed correlation violates the Cauchy-Schwarz inequality (details c.f. Sec. 3.5.1.3), which clearly proves the nonclassicality of this joint state. The result we achieve in this work also enables studies of macroscopic quantum phenomena.

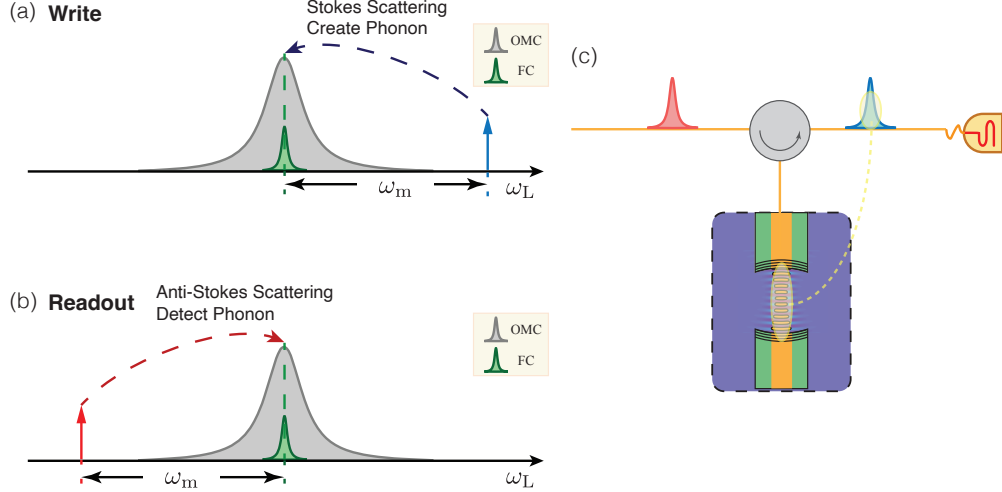


Figure 9.1: (a) A blue-detuned pulse realizes a two-mode squeezing interaction, which generates an entangled photon-phonon pair. A single photon is emitted from the cavity on resonance (green resonance), which can pass through filter cavities. (b) A red-detuned pulse is used to read out the mechanical state. The state-swap interaction swaps the mechanical excitation onto the optical cavity field, hence creating a single photon on resonance with the cavity. This single photon is emitted from the cavity and is measured by SNSPDs. (c) A schematic of the experimental procedures. The blue-detuned pulse creates an entangled photon-phonon pair. The state of the phonon is swapped out by the following red-detuned pulse. The correlation between emitted photons in each pulse is measured by SNSPDs.

## 9.1 DLCZ Scheme

The DLCZ protocol in its original form uses Raman scattering for generation and read-out of collective spin states of atomic ensembles via single photon measurements [154]. The scheme probabilistically generates entanglement through post-selecting the photon count results, and does not require strong coupling.

In the optomechanical system in this work, the interaction Hamiltonian in Eq. (2.29) allows us to select the Stokes and anti-Stokes scattering processes by having blue-detuned ( $\Delta = +\omega_m$ ) and red-detuned ( $\Delta = -\omega_m$ ) optical inputs, respectively, as discussed in Sec. 7.1.1. The experiment scheme consists of the following steps:

**Initialize** The mechanical mode is initialized to the thermal state with the mean occupancy corresponding to  $T_{MC}$ . In this setup, as discussed in Sec. 6.3.2.1, we are not able to apply sideband cooling to prepare the mechanical mode near its ground state.

**Write** A blue-detuned pulse ( $\Delta = +\omega_m$ ) is sent to the optomechanical cavity. As discussed in Sec. 7.1.1, this pulse (also known as the “write” pulse) results in two-mode squeezing with the interaction Hamiltonian  $H_{int} \propto \hbar g(\hat{a}^\dagger \hat{b}^\dagger + \hat{a} \hat{b})$ . An entangled

photon-phonon pair is generated in the optomechanical cavity by this interaction as shown in Fig. 9.1(a), where the photon is emitted from the cavity in a time scale of  $1/\kappa$ . This process is in close analogy to the photon-photon pairs generated in parametric down-conversion [288].

**Read** After a short delay time  $\tau$ , a red-detuned pulse ( $\Delta = -\omega_m$ , also known as the “read” pulse) is sent to the optomechanical cavity. This results in the state-swap interaction (also known as beam-splitter interaction) with Hamiltonian  $H_{\text{int}} \propto \hbar g(\hat{a}^\dagger \hat{b} + \hat{a} \hat{b}^\dagger)$ , which allows read-out of the mechanical state. In other words, the annihilation of one input photon corresponds to the annihilation of one cavity photon and the creation of one mechanical phonon, as shown in Fig. 9.1(b). This cavity photon is emitted from the optomechanical cavity and exhibits a non-classical correlation with the emitted photon in the write pulse.

**Measure** The emitted photons are on resonance with the optical cavity, and thus can pass through the filter cavities. The SNSPDs record the arrival time of each photon, which is used to construct cross-coherences of emitted photons between red- and blue-detuned pulses and auto-coherences in each pulse. Details are discussed in Sec. 9.3.

Figure 9.1(c) is a schematic summarizing the DLCZ protocol in the optomechanical system.

## 9.2 Cross- and Auto-Coherences of Pulses

The field operator after the filter cavities  $\hat{p}$  is described in Eq. (6.12), where the output field  $\hat{a}_{\text{out}}$  can be obtained by a formal integration of the Langevin equation Eq. (3.94) (details c.f. Sec. 2.3.1).

Since the equations of motion are linearized, only Gaussian inputs are considered, and the mechanical oscillator is prepared in a thermal state, Wick’s theorem allows us to express higher-order correlations in terms of correlations containing two operators. Thus, the cross-coherence between the output fields  $\hat{a}_{\text{out}}$  of two consecutive pulses can be written as [98, 289]

$$g_{r|b}^{(2)}(\tau) = \frac{\langle \hat{a}_{\text{out},b}^\dagger(t) \hat{a}_{\text{out},r}^\dagger(t+\tau) \hat{a}_{\text{out},r}(t+\tau) \hat{a}_{\text{out},b}(t) \rangle}{\langle \hat{a}_{\text{out},b}^\dagger(t) \hat{a}_{\text{out},b}(t) \rangle \langle \hat{a}_{\text{out},r}^\dagger(t) \hat{a}_{\text{out},r}(t) \rangle} \\ = 1 + \frac{|\langle \hat{p}_b^\dagger(t) \hat{p}_r(t+\tau) \rangle|^2 + |\langle \hat{p}_b^\dagger(t) \hat{p}_r^\dagger(t+\tau) \rangle|^2}{\langle \hat{p}_b^\dagger(t) \hat{p}_b(t) \rangle \langle \hat{p}_r^\dagger(t) \hat{p}_r(t) \rangle}, \quad (9.1)$$

where  $g_{r|b}^{(2)}(\tau)$  denotes the cross-coherence of a blue-detuned pulse and then a red-detuned pulse,  $\hat{a}_{\text{out},b}$  and  $\hat{a}_{\text{out},r}$  are output field operators of the blue- and red-detuned pulses, re-

spectively, and  $\hat{p}_b$  and  $\hat{p}_r$  are corresponding field operators after filter cavities.  $\langle \hat{p}_b^\dagger(t)\hat{p}_b(t) \rangle$  and  $\langle \hat{p}_r^\dagger(t)\hat{p}_r(t) \rangle$  are given in Eq. (6.17). Substituting the formally integrated  $\hat{p}_b$  and  $\hat{p}_r$  into the cross-correlator in the numerator of Eq. (9.1) yields

$$\langle \hat{p}_b^\dagger(t)\hat{p}_r^\dagger(t+\tau) \rangle \approx -\gamma_m \mathcal{C}(n_m + 1) \frac{\kappa_{\text{ex}}}{\kappa} e^{-(\gamma_m/2-i\omega_m)\tau} e^{-i\vartheta} |f_{\text{filter}}(\omega + \Delta = 0)|^2, \quad (9.2a)$$

$$\langle \hat{p}_b^\dagger(t)\hat{p}_r(t+\tau) \rangle \approx 0, \quad (9.2b)$$

where  $\mathcal{C}$  is the cooperativity,  $\vartheta$  is the phase factor induced by the filter cavity which won't contribute to Eq. (9.1), and  $f_{\text{filter}}$  is given in Eq. (6.11). Thus, we have

$$g_{r|b}^{(2)}(\tau) = 1 + (1 + \frac{1}{n_m}) e^{-\gamma_m \tau}. \quad (9.3)$$

The auto-coherences of the blue- and red-detuned pulses are both described by the coherence function of the thermal state

$$g_{b|b}^{(2)}(0) = g_{r|r}^{(2)}(0) = 2. \quad (9.4)$$

Therefore, we have

$$[g_{r|b}^{(2)}(0)]^2 > g_{r|r}^{(2)}(0)g_{b|b}^{(2)}(0), \quad (9.5)$$

which clearly violates the Cauchy–Schwarz inequality given in Eq. (3.191) for any  $n_m$ .

Eq. (9.1) can be rewritten as the following according to the photon-phonon correspondence discussed in Sec. 7.1.1:

$$g_{r|b}^{(2)}(0) = \frac{\langle \hat{a}_{\text{out},b}^\dagger \hat{a}_{\text{out},r}^\dagger \hat{a}_{\text{out},r} \hat{a}_{\text{out},b} \rangle}{\langle \hat{a}_{\text{out},b}^\dagger \hat{a}_{\text{out},b} \rangle \langle \hat{a}_{\text{out},r}^\dagger \hat{a}_{\text{out},r} \rangle} = \frac{\langle \hat{a}^\dagger \hat{b}^\dagger \hat{b} \hat{a} \rangle_\psi}{\langle \hat{a}^\dagger \hat{a} \rangle_\psi \langle \hat{b}^\dagger \hat{b} \rangle_\psi}, \quad (9.6)$$

where  $\hat{a}^\dagger$  and  $\hat{b}^\dagger$  are creation operators of the intra-cavity photon and phonon, respectively, and  $\langle \dots \rangle_\psi$  denotes that this expectation value is over the joint state  $|\psi\rangle$ . Similarly, we have

$$g_{r|r}^{(2)}(0) = \frac{\langle \hat{a}_{\text{out},r}^\dagger \hat{a}_{\text{out},r}^\dagger \hat{a}_{\text{out},r} \hat{a}_{\text{out},r} \rangle}{\langle \hat{a}_{\text{out},r}^\dagger \hat{a}_{\text{out},r} \rangle \langle \hat{a}_{\text{out},r}^\dagger \hat{a}_{\text{out},r} \rangle} = \frac{\langle \hat{b}^\dagger \hat{b}^\dagger \hat{b} \hat{b} \rangle_\psi}{\langle \hat{b}^\dagger \hat{b} \rangle_\psi \langle \hat{b}^\dagger \hat{b} \rangle_\psi}, \quad (9.7a)$$

$$g_{r|r}^{(2)}(0) = \frac{\langle \hat{a}_{\text{out},b}^\dagger \hat{a}_{\text{out},b}^\dagger \hat{a}_{\text{out},b} \hat{a}_{\text{out},b} \rangle}{\langle \hat{a}_{\text{out},b}^\dagger \hat{a}_{\text{out},b} \rangle \langle \hat{a}_{\text{out},b}^\dagger \hat{a}_{\text{out},b} \rangle} = \frac{\langle \hat{a}^\dagger \hat{a}^\dagger \hat{a} \hat{a} \rangle_\psi}{\langle \hat{a}^\dagger \hat{a} \rangle_\psi \langle \hat{a}^\dagger \hat{a} \rangle_\psi}. \quad (9.7b)$$

All the averages are estimated over the same state  $|\psi\rangle$ , and all operators are normally-ordered. Thus, all correlators can be expressed by integrals of the same  $P$ -function which

represents the joint state  $|\psi\rangle$ , for example,

$$\langle \hat{a}^\dagger \hat{b}^\dagger \hat{b} \hat{a} \rangle_\psi = \iint |\alpha|^2 |\beta|^2 P_\psi(\alpha, \beta) d^2\alpha d^2\beta. \quad (9.8)$$

The violation of the Cauchy–Schwarz inequality verifies that the  $P$ -function is not non-negative definite, *i.e.*, that this photon-phonon joint state is non-classical [74, 75, 98].

### 9.2.1 Effects of the Exciting Probability

The cross-coherence can be interpreted as

$$g_{r|b}^{(2)}(0) \approx \frac{n_m|_h}{n_m}, \quad (9.9)$$

where  $n_m|_h$  is the mean phonon number heralded on a detection event of the “write” pulse, and  $n_m$  is the mean phonon number of unheralded events.

Consider we start with a photon-phonon joint ground state  $|0\rangle_{\text{cav}}|0\rangle_m$ . The state after the “write” pulse is [75]

$$|\psi\rangle = |0\rangle_{\text{cav}}|0\rangle_m + \sqrt{p_b}|1\rangle_{\text{cav}}|1\rangle_m + p_b|2\rangle_{\text{cav}}|2\rangle_m + \mathcal{O}(p^{3/2}), \quad (9.10)$$

where  $p_b \ll 1$  is the exciting probability of the Stokes scattering process, and  $|n\rangle_{\text{cav}}, |n\rangle_m$  are  $n$  Fock states of the optical mode and the mechanical mode, respectively. The corresponding cross-coherence is

$$g_{r|b}^{(2)}(0) \approx 1 + \frac{1}{p_b}. \quad (9.11)$$

Clearly, the state after the “write” pulse is not the same as the initial state. However, it is treated the same in the discussion in Sec. 9.2. Therefore, Eq. (9.3) is only valid when  $p_b \approx 0$ .

A more general description of the state after the blue-detuned pulse is obtained by solving the dynamical equation [290]

$$|\psi\rangle = \frac{1}{\cosh \xi t} \sum_n (\tanh \xi t)^n |n\rangle_{\text{cav}} |n\rangle_m, \quad (9.12)$$

where  $t$  is the duration of the blue-detuned pulse,  $|n\rangle_{\text{cav}} |n\rangle_m = 1/n! \hat{a}^\dagger \hat{b}^\dagger |0\rangle_{\text{cav}} |0\rangle_m$  is the excited joint photon-phonon state, and

$$\xi t = g_0 \sqrt{\frac{4}{\kappa} \frac{P_b t}{\hbar \omega_{\text{cav}}} \frac{\kappa_{\text{ex}}}{\omega_m^2 + (\kappa/2)^2}}. \quad (9.13)$$

Comparing Eq. (9.12) and Eq. (9.10), we have

$$p_b \approx \frac{4g_0^2}{\kappa} \frac{P_b t}{\hbar \omega_{\text{cav}}} \frac{\kappa_{\text{ex}}}{\omega_m^2 + (\kappa/2)^2} \approx (E_b/5 \text{ pJ})\%, \quad (9.14)$$

where  $E_b$  is the total energy of a blue-detuned pulse, and Eq. (9.14) is only valid when  $p_b \ll 1$ .

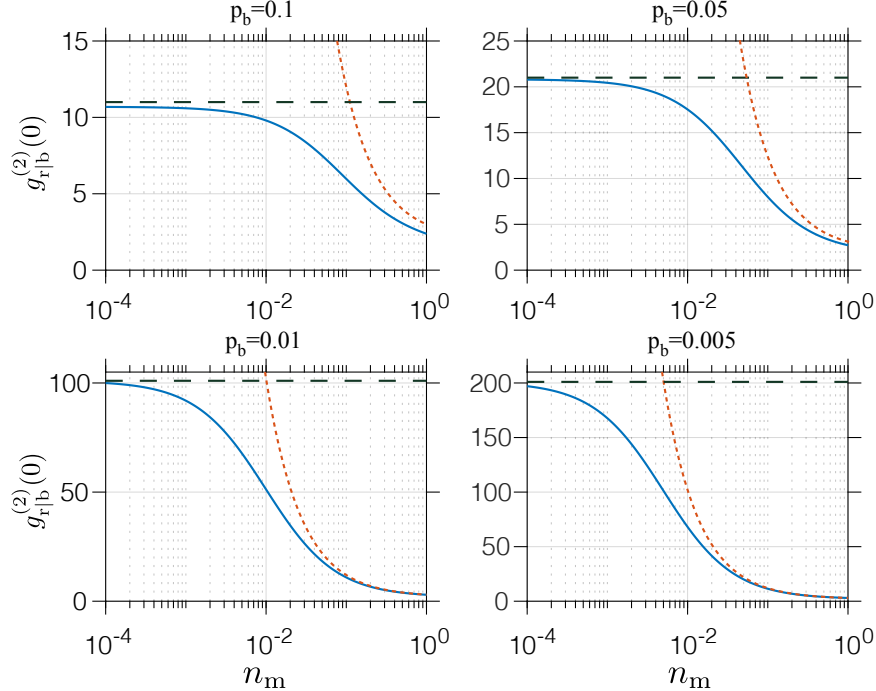


Figure 9.2:  $g_{r|b}^{(2)}(0)$  (blue solid lines) as a function of  $n_m$  at various  $p_b$ , given in Eq. (9.16). Red dashed lines represent the result in the limit  $n_m \gg \frac{p_b}{1 - p_b}$ , given in Eq. (9.3). Black dashed lines represent the result in the limit  $n_m \ll \frac{p_b}{1 - p_b}$ , given in Eq. (9.11).

The mechanical thermal state we start with has a nonnegligible occupancy  $n_m$ . The state after the blue-detuned pulse is

$$|\psi\rangle \propto \sum_{n=0}^{\infty} \sum_{m=0}^{\infty} \sqrt{\rho_n} \frac{p_b^{m/2}}{m!} \sqrt{m!} \sqrt{\frac{(n+m)!}{n!}} |m\rangle_{\text{cav}} |n+m\rangle_m, \quad (9.15)$$

where  $\rho_n$  is the probability of  $|n\rangle_m$ . The corresponding cross-coherence is

$$g_{r|b}^{(2)}(0) \approx \frac{[(2n_m + 1)(n_m + 1) + 2p_b(n_m + 1)^2(3n_m + 2)] [1 + p_b(n_m + 1)]}{[(n_m + 1) + 2(n_m + 1)^2 p_b] [n_m + p_b(2n_m + 1)(n_m + 1)]}. \quad (9.16)$$

In the limit  $n_m \ll \frac{p_b}{1 - p_b}$ , Eq. (9.16) reduces to

$$g_{r|b}^{(2)}(0) \approx \frac{(1 + 4p_b)(1 + p_b)}{(1 + 2p_b)(1 + 2p_b)} \approx 1 + \frac{1}{p_b}, \quad (9.17)$$

which is the same as Eq. (9.11).

In the limit  $n_m \gg \frac{p_b}{1 - p_b}$ , Eq. (9.16) reduces to

$$g_{r|b}^{(2)}(0) \approx \frac{(2n_m + 1)(n_m + 1)}{(n_m + 1)n_m} = 1 + \frac{n_m + 1}{n_m}, \quad (9.18)$$

which is the same as Eq. (9.3).

Figure 9.2 shows  $g_{r|b}^{(2)}(0)$  (blue solid lines) as a function of  $n_m$  at various  $p_b$ .

The blue-detuned pulse also heats up the mechanical mode, which also changes the measured cross-coherence. A theoretical model of this heating effect and the corresponding experimental characterization will be the subject of further studies.

## 9.3 Measured Non-classical Photon-Phonon Coherences

### 9.3.1 Experiment Setup

Figure 9.3(a) shows the schematic of the experiment setup. Details of the optical setup are described in Sec. 6.1.1. Two input lasers are continuously locked at  $-\omega_m$  (red) and  $+\omega_m$  (blue) with respect to the optical cavity. The experiment is running in the “Lock-Hold” scheme, which is the same measurement scheme used in the thermal state measurement (described in Sec. 6.1.2). The only difference is that the two input lasers are not continuously sent to the optomechanical cavity during the “hold” period. Shutter1 and Shutter2 (with a response time  $< 60$  ns) are controlled by a signal from the FPGA, so that the two input lasers (dashed areas) can alternatively drive the optomechanical system. Scattered photons (green circles) are on-resonance with the optical cavity, and thus can pass through the two cascaded filter cavities which are locked to the optical cavity during the “lock” period (and unshifted input lasers are rejected by these filter cavities). These passed photons are split by a 50/50 beam splitter and then measured by the two SNSPDs. The optomechanical cavity is in equilibrium with the mixing chamber at  $T_{MC} \approx 20$  mK.

Figure 9.3(b) shows the explicit pulsed scheme implemented in the experiment. A nearly square write pulse (blue) with duration  $t_b$  and power  $P_b$  is sent to the cavity. It is followed by a nearly square read pulse (red) with duration  $t_r$  and power  $P_r$ . The end of the write pulse and the beginning of the read pulse are separated by  $t_{delay}$ , which is set to be longer than  $1/\kappa_{FC}$  to distinguish which pulse the received photons come from. The delay time between the write and the read pulse is defined as the average delay time

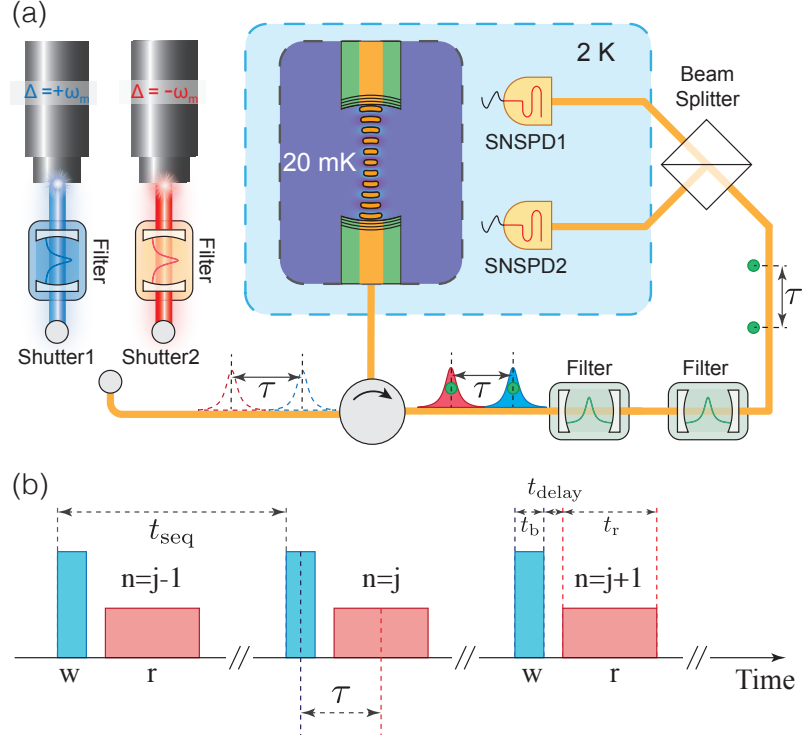


Figure 9.3: (a) Schematic of the experiment setup. Shutter1 and Shutter2 are triggered by a programmed signal so that two pulsed drives (dashed lines) with a delay  $\tau$  are sent to the optomechanical cavity. The scattered light (green circles) together with reflected light (shading area) are sent to cascade filter cavities, which only allow in-resonance photons to pass. These passed photons (green circles) are measured by two SNSPDs. (b) Schematic of the pulsed sequence. Write pulses (blue) and read pulses (red) are sent to the optomechanical cavity alternatively. The height represents the power of each pulse. Such a pulsed scheme is repeated in the entire ‘hold’ period.  $n$  is the index of the sequence.

$\tau = (t_b + t_r)/2 + t_{delay}$ . After the read pulse, all lasers are blocked off for  $\sim 500 \mu\text{s}$  to ensure the mechanical state is initialized to the same thermal state. In each measurement, such a sequence is repeated  $\sim 10^8$  times ( $\sim 1.4$  day) to get enough statistics.

### 9.3.2 Violating the Cauchy-Schwarz Inequality

In this experiment, we used a blue-detuned ‘write’ pulse that is sufficiently weak ( $t_b = 2.5 \mu\text{s}$  square pulse,  $P_b = 10 \mu\text{W}$ ) to minimize the change of the initial state and the effect of the absorption heating. This ‘write’ pulse corresponds to the Stokes scattering probability  $p_b \approx 5\%$ , as given in Eq. (9.14). After a  $t_{delay} = 1 \mu\text{s}$ , a red-detuned ‘read’ pulse ( $t_r = 4 \mu\text{s}$  square pulse,  $P_r = 10 \mu\text{W}$ ) is injected to the optomechanical cavity, resulting in a ‘read-out’ efficiency  $p_r \approx 8\%$  (the expression of  $p_r$  is identical to  $p_b$  given in Eq. (9.14) when  $p_r \ll 1$  [75]). The average delay time is  $\tau = 4.25 \mu\text{s}$ .

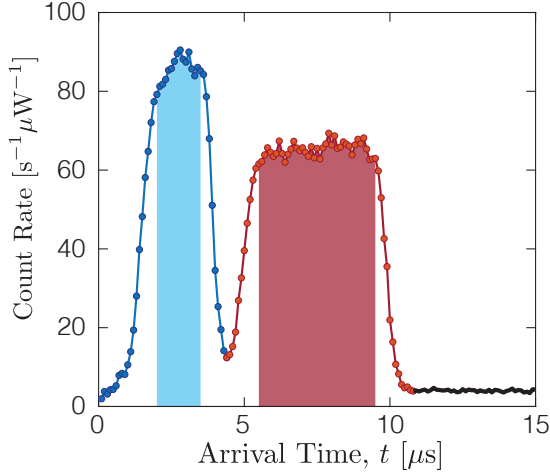


Figure 9.4: Count rates as a function of the arrival time  $t$ . Blue and red circles represent count rates from the blue- and red-detuned pulses, respectively. The highlighted colored areas represent the data we used in the analysis. This count rate asymmetry also infers  $n_{\text{th}} \approx 1.3(1)$ .

Figure 9.4 shows the count rates of the blue- and red-detuned pulses as a function of arrival time with respect to the control signal to Shutter1 in each sequence. The rising and falling edges are a result of the filter cavity transfer function. To avoid the transient behavior, we only use the portion of the data during which the count rates are relatively stable. That is  $2\text{ }\mu\text{s} - 3.5\text{ }\mu\text{s}$  for the blue-detuned pulse (blue shaded area) and  $5.5\text{ }\mu\text{s} - 9.5\text{ }\mu\text{s}$  for the red-detuned pulse (red shaded area). After subtracting dark counts and stray photon counts (see Sec. 6.3.1.2), the asymmetry of the two pulses corresponds to a thermal occupancy  $n_m = 1.3(1)$  and to a mode temperature of  $20(2)$  mK, which are consistent with independent calibrations in Sec. 7.1.2 and Sec. 8.3.3. It is worth emphasizing that the red-detuned pulse measured a state that is slightly different than the initial state, as discussed in Sec. 9.2.1. This is not accounted for in this calibration.

Counts from SNSPD1 and SNSPD2 are combined (the two SNSPDs are treated as one SNSPD) to get more coincidence events. The details of using one SNSPD to construct coherences are covered in Sec. 7.2.3.1. We only used the data with stable count rates to estimate coherences, shown as highlighted shaded areas in Fig. 9.4. The coherences are evaluated by the method described in Sec. 7.2, and we used the logistic regression method (see Sec. 7.2.2.2) to calculate the corresponding statistical uncertainties. The effects of background counts and after pulsing are corrected according to the protocols in Sec. 7.2.4.2 and Sec. 7.2.4.4, respectively. The systematic slow drifts cannot be corrected because we cannot extract  $g^{(2)}(\infty)$  from these measurements. This does not affect the violation of the Cauchy-Schwarz inequality because this common factor appears on both sides of the inequality.

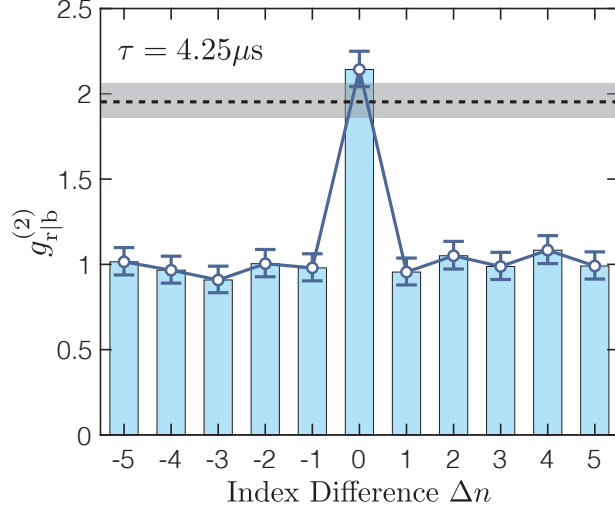


Figure 9.5: The cross-coherences (blue bars) between the “write” pulse and the “read” pulse for different sequence index differences  $\Delta n$ . The delay time is  $\tau = 4.25\mu\text{s}$ . The classical (Cauchy–Schwarz) bound obtained from the autocorrelations within the same pulse is represented by the grey-shaded area. All error bars and the width of the classical bound are 2 s.d. determined from the statistical uncertainties and the systematical uncertainties, corresponding to 95% confidence intervals. At  $\Delta n = 0$ , the Cauchy–Schwarz inequality is violated, which verifies the non-classicality of the photon-phonon state.

Figure 9.5 shows the values of the cross-coherence  $g_{r|b}^{(2)}$  between the “write” pulse and the “read” pulse for different pulse sequences (blue bars), where  $\Delta n$  is the sequence index (see Fig. 9.3(b)) difference of the “write” and the “read” pulses. For pairs emitted from the same pulse sequence (*i.e.*,  $\Delta = 0$ ), we measured

$$g_{r|b}^{(2)}(\tau = 4.25\mu\text{s}) = 2.14^{+0.10}_{-0.10}. \quad (9.19)$$

The auto-coherences of the “write” and “read” pulses are

$$g_{b|b}^{(2)}(0) = 1.89^{+0.15}_{-0.15}, \quad (9.20a)$$

$$g_{r|r}^{(2)}(0) = 2.02^{+0.14}_{-0.13}, \quad (9.20b)$$

which yields the classical bound (grey bar)

$$[g_{b|b}^{(2)}(0)g_{r|r}^{(2)}(0)]^{1/2} = 1.95^{+0.11}_{-0.10}. \quad (9.21)$$

All the uncertainties given above are 2 s.d. as determined from the statistical uncertainty and the systematical uncertainties. So each range of measured coherences corresponds to

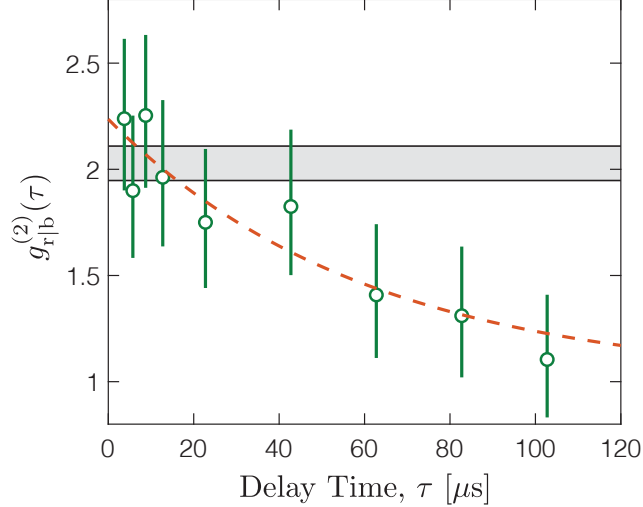


Figure 9.6: The cross-coherences (green circles) between the “write” pulse and the “read” pulse for different delay time  $\tau$ . The grey bar represents the classical (Cauchy-Schwarz) bound obtained from the average auto-coherences in each pulse (*i.e.*,  $\sqrt{\bar{g}_{r|r}^{(2)}(0)\bar{g}_{b|b}^{(2)}(0)}$ ). All error bars and the width of the classical bound are 2 s.d. determined from the statistical uncertainties and the systematical uncertainties, corresponding to 95% confidence intervals. The orange dashed line is the best fit to Eq. (9.3).

a 95% confidence interval. Clearly, we have

$$g_{r|b}^{(2)}(\tau = 4.25 \mu\text{s}) > [g_{b|b}^{(2)}(0)g_{r|r}^{(2)}(0)]^{1/2}, \quad (9.22)$$

which violates the Cauchy-Schwarz inequality by  $\sim 4$ -sigma, corresponding to a 99.95% confidence levels of this violation.

For pairs of the blue- and red-detuned pulses that emerge from different sequences (*i.e.*,  $\Delta n \neq 0$ ), their average cross-coherences is  $\bar{g}_{r|b}^{(2)} = 1.01^{+0.10}_{-0.10}$ . This result fulfills the Cauchy-Schwarz inequality and is consistent with the expected statistical independence.

### 9.3.3 The Time-Dependence of the Cross-Coherence

We also measured the time-dependence of  $g_{r|b}^{(2)}(\tau)$  by varying the delay time  $\tau$ . The measurements at different  $\tau$  were carried out by running in a loop in which each delay was running for  $\sim 3$  minutes before changing to another. The sequence of each delay was repeated  $\sim 10^7$  times. The “write” pulse lasts  $t_b = 2.5 \mu\text{s}$  with power  $P_b = 10 \mu\text{W}$  and the “read” pulse lasts  $t_r = 20 \mu\text{s}$  with power  $P_r = 4 \mu\text{W}$ , which are the same in all different  $\tau$  measurements. For the blue-detuned pulse, the window of stable count rates ( $2 \mu\text{s} - 3.5 \mu\text{s}$  in each sequence) were used in estimating the coherence. For the red-detuned pulse, only the first  $4 \mu\text{s}$  data of stable count rates ( $t_{\text{delay}} + 4.5 \mu\text{s}$  to  $t_{\text{delay}} + 8.5 \mu\text{s}$  in each sequence)

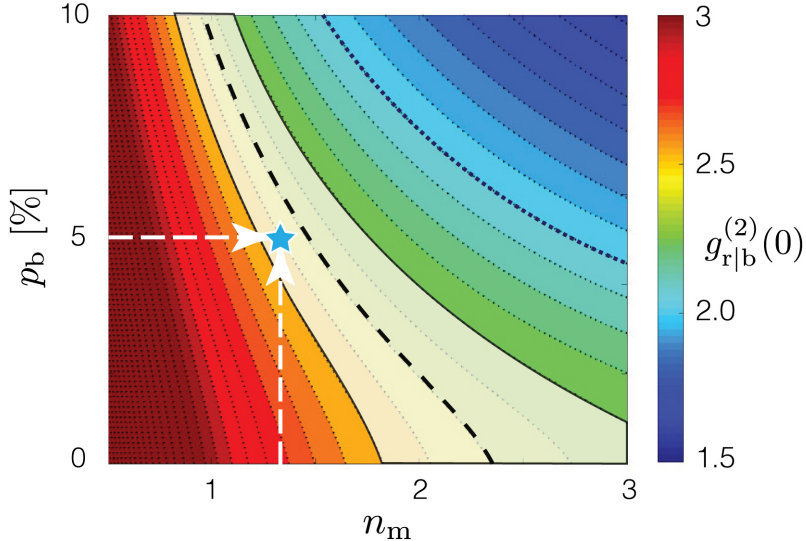


Figure 9.7: Predicted values of  $g_{r|b}^{(2)}(0)$  as a function of  $n_m$  and  $p_b$ , as given in Eq. (9.16). The white shaded area represents the extrapolated value of  $g_{r|b}^{(2)}(0) = 2.33^{+0.12}_{-0.11}$  from the experiment described in Sec. 9.3.2. The blue star is the expected value of  $g_{r|b}^{(2)}(0)$  when  $p_b = 5\%$  and  $n_m = 1.3$ , which falls in 95% confidence interval of the measured value.

are used.

Figure 9.6 shows measured  $g_{r|b}^{(2)}(\tau)$  (green circles) as a function of the delay time  $\tau$ , where error bars are 2 s.d. determined from the statistical uncertainty and the systematical uncertainties. The fit to the form  $a \times \exp(-\tau/\tau_0) + 1$  yields  $g_{r|b}^{(2)}(0) = 2.24 \pm 0.12$  and  $\tau_0 = 60 \pm 15 \mu\text{s}$ . The classical bound is represented by the grey bar in Fig. 9.6, whose value ( $2.02^{+0.09}_{-0.08}$ ) is determined from the average auto-correlations for all  $\tau$ . The violation of the Cauchy-Schwarz inequality is fulfilled for  $\tau < 7 \mu\text{s}$ . With an increasing  $\tau$ , the red- and blue-detuned pulses become less correlated.

### 9.3.4 Limits on the Non-classicality Witness

The nonclassicality (Cauchy-Schwarz) witness  $g_{r|b}^{(2)} - 2$  is pretty small in this experiment. As shown in Fig. 9.6, we cannot store and retrieve non-classical states for long. Figure 9.7 shows the expected  $g_{r|b}^{(2)}(0)$  as a function of  $n_m$  and  $p_b$ , as given in Eq. (9.16). If we extrapolate the measured cross-coherence  $g_{r|b}^{(2)}(\tau)$  to the zero-delay cross-coherence  $g_{r|b}^{(2)}(0)$  according to Eq. (9.3) (where we assume  $\gamma_m/2\pi = 3.12 \text{ kHz}$ ), we have  $g_{r|b}^{(2)}(0) = 2.33^{+0.12}_{-0.11}$ , which is shown as the white shaded area in Fig. 9.7. The theoretical prediction for  $g_{r|b}^{(2)}(0)$  is represented by a blue star, where we used  $n_m = 1.3$  and  $p_b = 5\%$ . The fact that the predicted  $g_{r|b}^{(2)}(0)$  falls into the 95% confidence interval of the extrapolated  $g_{r|b}^{(2)}(0)$  justifies the protocol we implemented in this experiment.

To increase the value of the cross-coherence in the future experiment, we need to decrease the initial phonon number  $n_m$  and the exciting probability  $p_b$ . The former can be achieved by a lower fridge temperature, a higher mechanical mode frequency, or by applying active cooling methods. The latter requires a higher detection efficiency to achieve the same statistical confidence with the same data acquisition time.

# CHAPTER 10

*“Real breakthroughs are not found because you want to develop some new technology, but because you are curious and want to find out how the world is.”*

– Anton Zeilinger

## Summary and Outlooks

The previous chapters described the device we built and the states we prepared and verified. The results shown in this thesis are a “proof-of-principle” demonstration of the basic control/measurement protocols and the basic quantum acoustic phenomena in these bulk acoustic devices. The observable quantum features in the current device are primarily limited by the minimal phonon number we can achieve.

This chapter describes two major advances which will be enabled by having a macroscopic superfluid helium-filled cavity. In the first, the new cavity design will increase the effective mass (macroscopicity) of the mechanical oscillator by roughly four orders of magnitude to reach the microgram scale, which will make it possible to test predictions of phenomenological quantum gravity and other non-standard extensions of quantum mechanics (see Chapter 4). In the second, the new design will also allow us to take full advantage of the acoustic DBR coatings (see limits of the DBR coating in the current device in Sec. 5.2). So this technical advance will increase the device’s phonon lifetime by roughly three orders of magnitude, which makes sideband cooling possible. A smaller mean phonon number will make various novel quantum phenomena (such as phonon Fock states, or entangled phonon states) accessible in the motion of macroscopic bodies, which are relevant for basic science and potential applications.

### 10.1 Optomechanics with a macroscopic cavity

#### 10.1.1 Description of the Macro cavity

Figure 10.1 shows a macroscopic Fabry-Pérot cavity that we built. The cavity spacer and mountings are made of Invar. The RoCs of the two half-inch fused-silica mirrors are both 5 cm, and their optical reflectivities are 99.998% and 99.992%, respectively. They are separated by  $L_{\text{cav}} = 12.3$  mm, so the expected beam waist is  $w_0 = 88.3 \mu\text{m}$ , and the effective mass is  $\sim 20 \mu\text{g}$  (four orders of magnitude increase compared to the current device). The optical linewidth of this empty cavity at room temperature is measured to be  $\kappa/2\pi \approx 233 \text{ kHz}$ .

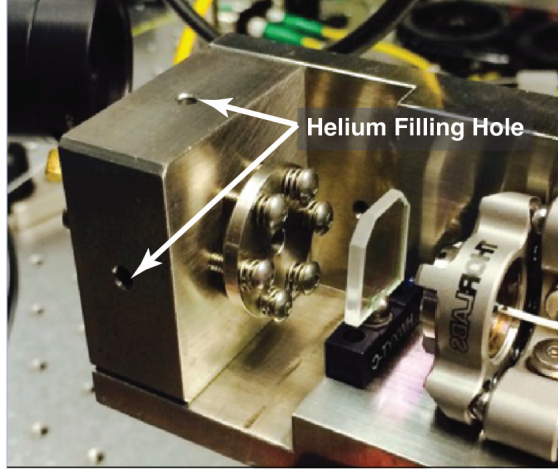


Figure 10.1: A photo of the macroscopic cavity we built. The left silver cube is the cavity, with two helium-filling holes on two sides. The right is integrated mode-matching optics.

The entire cavity and the associated aligning optics are mounted inside a brass container, which will be filled with liquid helium in the experiment. The holes on the sides allow liquid helium to flow in between the two mirrors. Such a scaled-up design still enables the single-mode optomechanical coupling (see Sec. 5.4.1) and takes advantage of using liquid helium as the host of the mechanical resonator. In the following, I discuss two technical improvements that will be enabled by this macroscopic cavity.

**Mechanical Quality Factor** One of the main drawbacks of the device used in this thesis has been its mechanical quality factor. As discussed in Sec. 5.2, most of the phonon energy dissipates by its radiation into the fiber, resulting in a modest  $Q_m \sim 10^5$ . This leads to two restrictions in achieving our scientific goals. First, the modest lifetime of phonons restricts the lifetime of the quantum features (before the quantum state decays). Second, it precludes using sideband cooling techniques to prepare the mechanical oscillator in its ground state.

The two mirrors have dual-DBR coatings that provide high reflectivity for optical and mechanical modes. The wavelength of the mechanical wave increases to  $\sim 15 \mu\text{m}$  in the DBR material. To ensure that the mechanical wavefront remains conformal with the DBR layers (which is required to achieve high reflectivity), it is necessary to satisfy  $w \gg \lambda$  so that the acoustic wave propagation is paraxial. The finite element simulation results in Refs. [70, 203] show that the mechanical finesse can reach  $\mathcal{F}_m \sim 1.5 \times 10^4$  when the beam waist  $w_0$  is  $88.3 \mu\text{m}$ , which corresponds to  $Q_m \sim 5 \times 10^8$ .

Another mechanical dissipation contribution is from the three-phonon scattering process (as discussed in Sec. 5.5.1), which gives rise to a quality factor  $Q_m \approx 118/T^4$  (Eq. (5.44)).

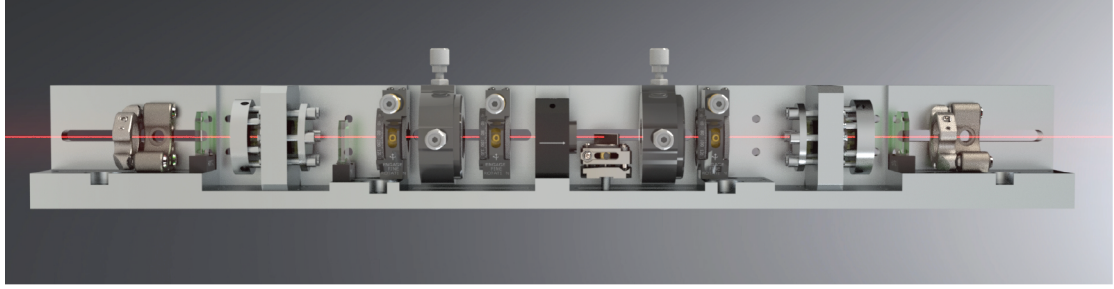


Figure 10.2: A rendered schematic picture of the new free-space filtering system.

At the base temperature  $T = 24\text{ mK}$ , these two contributions allow  $Q_m \approx 3 \times 10^8$ , corresponding to  $\gamma_m/2\pi \approx 1\text{ Hz}$ .

**Input Coupling Efficiency** In the current device, the light from the fiber's guided mode is directly delivered to the optical cavity. However, the guided mode profile is not well-matched to the cavity mode's profile (mainly due to the mismatch between the nearly flat phase front of the fiber mode and the curved phase front of the cavity mode), resulting in a modest input coupling efficiency  $\eta_\kappa = 0.29(1)$ .

The macro-cavity allows a more systematic optimization of mode-matching using integrated mode-matching optics. This approach has been demonstrated in Refs. [175, 291]. In this macro-cavity, we achieved  $\eta_\kappa \approx 65\%$ , more than a 2-fold improvement.

Besides the update of the optomechanical device, we also improved the transmission rate of the cascaded filter cavities by building a free-space filter cavity system. This free-space filtering system can provide sufficiently narrow passbands (discussed in Sec. 6.3.1.1.1) while allowing a modest total transmission rate, which has been demonstrated in several recent works [28, 57, 91]. The transmission rate of each free-space filter cavity is measured to be  $\sim 70\%$ , corresponding to a total transmission rate  $\eta_{\text{filter}} \approx 49\%$ . Figure 10.2 shows a schematic picture of the new filtering system. Compared to the filtering system deployed in this thesis (with a net transmission rate  $\approx 7\%$ ), it is expected to achieve a 7-fold improvement.

These two improvements are expected to lead to a 16-fold improvement in total detection efficiency. Note that the probability of multi-photon coincidence events depends polynomially on this efficiency. Thus such an improvement could significantly reduce the statistical uncertainty of measured coherences.

### 10.1.2 Proposed Scientific Goals

The improvements described above will enable us to achieve the following scientific goals.

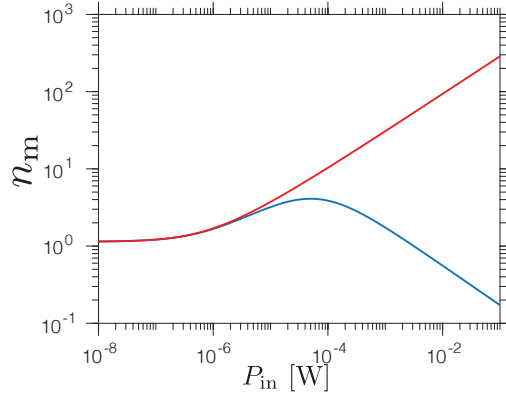


Figure 10.3: Expected sideband cooling effects in the macro-cavity. The red solid line represents the mean phonon occupancy due to the laser heating effect (the heating model is described in Sec. 6.3.2.1). The blue solid line represents the mean phonon number after including the sideband cooling.

### 10.1.2.1 Ground State Cooling

Almost all nonclassical quantum states require the mechanical mode to be prepared near its ground state to eliminate its classical uncertainty. The dilution fridge can cool the device to  $n_m \sim 1$ . With a dramatically decreased  $\gamma_m$ , this macro-cavity should allow for sideband cooling to further reduce  $n_m$ .

The model that we used to estimate the minimal achievable phonon number is described in Sec. 6.3.2.1, where we assume  $\gamma_{m0}/2\pi = 0.7$  Hz,  $\kappa/2\pi = 233$  kHz, and the coupling strength  $g_0/2\pi = 28$  Hz. To be more conservative, here, we also assume the heating effect in the macro-cavity is the same as the one characterized in Sec. 6.3.2.1 (with greater volume of liquid helium in the device, the macro-cavity is expected to be more tolerant to laser powers).

Figure 10.3 shows the effect of the sideband cooling when we optimize the drive frequency at  $-\omega_m$ . An issue with macro-cavity is that to achieve the same circulating photon number, a larger  $P_{\text{in}}$  is required. The heating effect of  $\sim 10$  mW incident power will be the subject of future study. It can possibly be circumvented by using a pulsed cooling scheme. In the rest of the discussion, we use  $n_m = 0.3$ , which can be achieved at  $P_{\text{in}} \approx 30$  mW.

### 10.1.2.2 Photon-Phonon Entangled States

In Chapter 9, we discussed the realization of the photon-phonon entangled states in the current device. One major hurdle to show significant violation is the thermal uncertainty in the initial state.

Figure 10.4 shows the expected cross-coherence function  $g_{r|b}^{(2)}(\tau)$  as a function of the delay time. In contrast to the result shown in Sec. 9.3.3, the macro-cavity will have a more obvious violation ( $g_{r|b}^{(2)}(0) = 5.3$ ), and the violation will persist for 0.2 s.

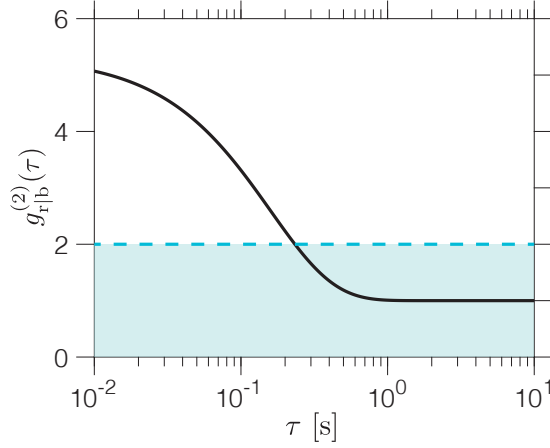


Figure 10.4: Expected violation of the Cauchy-Schwarz inequality in the macro-cavity. The black solid line is the expected value of the cross-coherence  $g_{r|b}^{(2)}(\tau)$ . The blue dashed line is the classical bound (non-negative  $P$ -function) set by the Cauchy-Schwarz inequality.

### 10.1.2.3 Fock States

The post-selection process can also conditionally prepare the mechanical mode in Fock states [92]. That is, if we start with a ground state, then by measuring one Stokes scattered photon, we add one phonon to the mechanical mode, *i.e.*, creating the  $|1\rangle$  Fock state. The auto-coherence of  $|1\rangle$  is 0, which can verify its  $P$ -function negativity (see Sec. 3.5.1.1).

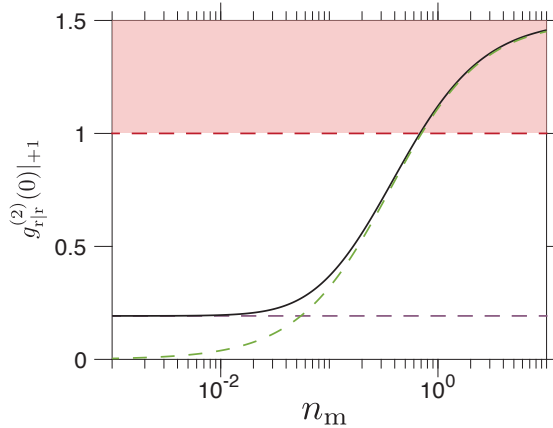


Figure 10.5: Expected Hanbury-Brown-Twiss effects in the macro-cavity. The black solid line represents the expected value of  $g_{r|r}^{(2)}(0)$  heralding measuring one Stokes photon. The red dashed line represents the classical bound for any state with a non-negative  $P$ -function. The green dashed line represents the result in low  $p_b$  limit, and the purple dashed line is the result in small  $n_m$  limit.

In practice, we usually start with a thermal state. The mechanical state after the blue-detuned pulse is described in Eq. (9.12). After heralding one Stokes photon, the auto-

coherence of the mechanical state (*i.e.*, the auto-coherence of the red-detuned pulse) is described in Eq. (3.69c).

Figure 10.5 shows the expected value of  $g_{r|r}^{(2)}(0)$  after heralding one Stokes photon. In the small  $n_m$  limit, the measured auto-coherence approach  $4p_b$  [74, 92], where  $p_b$  is the exciting probability in the blue-detuned pulse. Here, we take a modest value of  $p_b = 5\%$ . For the macro-cavity, we expect to have  $g_{r|r}^{(2)} = 0.68$ . Compared to the Hanbury-Brown-Twiss results in Ref. [92], this experiment will present a nonclassical mechanical state with  $10^7$  more mass and  $10^2$  longer decoherence time.

#### 10.1.2.4 Entanglement of Multiple Indistinguishable Devices

It is also possible to achieve entanglement across multiple devices. One promising approach is to conditionally generate such states by heralding the measurement result, which has been experimentally demonstrated in Ref. [97].

Figure 10.6 shows a schematic of the proposed experiment setup. The entanglement is generated in the following manner: A single blue-detuned photon is transformed into a superposition state (either upper path or lower path) by a beamsplitter. This optical input drives the two mechanical oscillators via the Stokes scattering process ( $H_{\text{int}} \propto (\hat{a}^\dagger \hat{b}^\dagger + \text{c.c.})$ ). The output optical fields are later combined by another beamsplitter, and only scattered photons can pass through the filter cavities and be measured by SNSPDs. If the scattered photons from the two oscillators are indistinguishable (spatial mode, polarization, timing, frequency), the detection of one Stokes scattered photon on either SNSPD heralds the addition of a single phonon across the two oscillators. This is equivalent to preparing these two oscillators in an entangled state  $(|e\rangle_1|g\rangle_2 + |g\rangle_1|e\rangle_2)/\sqrt{2}$ , where  $|g\rangle$ ,  $|e\rangle$  mean the ground state and the first excited state, and the subindex is used to distinguish the two oscillators.

The indistinguishability mentioned above is crucial to achieve entanglement. For most of the devices that have been used for this heralded entanglement distribution, the properties of the optical mode and the localized mode are not well controlled. Thus, two such devices are unlikely to be indistinguishable. The solution to this issue requires huge efforts in improving materials [292], fabrications [293], etc. Or one simply fabricates a large number of nearly identical devices and then searches for a handful that meet the indistinguishability requirement. In practice, these approaches are not efficient enough to have an array of indistinguishable devices (which would be especially useful for quantum repeaters).

Using a fluid as a host of the mechanical mode offers a natural way to tune the devices into indistinguishability. By simply tuning the length of the cavity by piezo elements (grey rectangles shown in Fig. 10.6), it should be feasible to have its mechanical and optical mode frequencies indistinguishable from other devices. More specifically, regardless of the original length of each cavity, if we can tune each cavity into resonance with the same

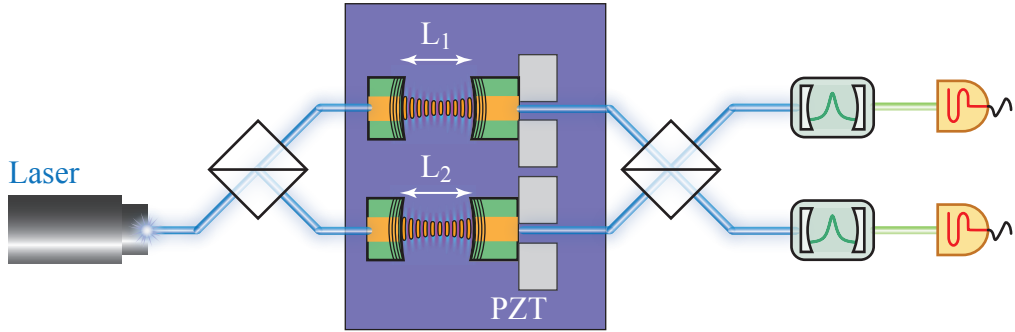


Figure 10.6: Schematic of the proposed experimental setup to entangle multiple devices. Two nearly identical macro-cavities are prepared. Piezo elements (grey rectangles) are used to tune the cavity lengths such that their optical mode frequencies are indistinguishable.

laser, the mechanical mode which couples to optical modes excited by the same laser should also have the same frequency, due to the single-mode coupling relation (discussed in Sec. 5.4.1). Therefore, all scattered photons are indistinguishable in their frequencies. Such a scheme can be easily generalized to an array of nominally identical cavities to generate entanglement across multiple devices.

## 10.2 Conclusion

The interaction of light and matter is one of the most fundamental processes occurring in nature. Recent advances in optomechanics have extended this interaction to a regime of single photon and single phonon effects. Such a realization fully harnesses the quantum nature of light to control and read out the state of the mechanical oscillator in an essentially quantum way. There are several underlying motivations for studying quantum effects in the motion of massive macroscopic objects: curiosity about quantum mechanical effects in tangible objects; potential practical applications that hinge on the quantum features of mechanical systems (such as sensing, communication, and computation); testing non-standard extensions of quantum mechanics; and utilizing the universality of the motion to bridge multiple other quantum systems.

In this thesis, we have demonstrated an optomechanical device in which the bulk mechanical mode is the spatially-varying density wave of superfluid helium. Taking material advantages of liquid helium, this optomechanical device can achieve a modest single-photon cooperativity  $\mathcal{C}_0 = 5 \times 10^{-4}$  while its effective mass reaches  $\sim 1$  ng. The simple geometrical relation between the optical and mechanical modes in this device offers a unique single-mode optomechanical coupling, *i.e.*, a given optical mode is sensitive to the motion of one and only one mechanical mode, which significantly simplifies the analysis of measurements. Leveraging photon counting techniques, we are able to interpret the

state of the mechanical mode via the statistics of scattered photons. Detection of a single scattered photon projects the mechanical mode into single-phonon-added/subtracted states. Thus it allows one to conditionally prepare the motion of this massive oscillator into non-classical states.

Specifically, we characterized the optical modes and mechanical modes and demonstrated the optomechanical dynamical backaction in this device. We measured the second-/third-/fourth-order coherence functions (both normally ordered and anti-normally ordered) of the undriven motion of the mechanical mode and justified the Gaussianity of the state with a high degree of statistical confidence. Using an optical beat note, we added  $4 \times 10^4$  phonons to the oscillator while maintaining its uncertainty near its zero-point motion. In a pulsed measurement scheme, we prepared a photon-phonon entangled state by heralding the detection of a single scattered Stokes photon. The fact that the measured coherences violated the Cauchy-Schwarz inequality verified the non-classicality of this joint state.

The work described in this thesis is a proof-of-principle demonstration of the basic quantum acoustic phenomena in superfluid-based optomechanical systems. Looking into the future, we aim to achieve two goals in a recently built macro-cavity: more ‘macroscopic’ and more ‘quantum’. With nearly  $20\text{ }\mu\text{g}$  mass, this device will be an ideal testbed for various modified quantum theories. For instance, we can improve the sensitivity in constraining  $l_k$  (described in Sec. 8.5.2) by two orders of magnitudes (which will surpass the bound set by the result from LHC). Technical advances in detection efficiency and the mechanical quality factor should provide access to prepare the mechanical oscillator in more striking quantum states, such as Fock states and entangled states.

Extending spooky quantum features into a more macroscopic world may also lead to application advances. A similar design is proposed to search for Axion dark matter particles [271] and to detect gravitational waves [218]. It has also been proposed that this system can interact with the electron bubble (*i.e.*, an atom-like defect) for prospects in quantum sensing or information processing.

In conclusion, I presented the motivation of this work, the theories behind this optomechanical system, the measurement details of the experiment, the measurement results, and future directions. I hope my work in this “soft” superfluid-based optomechanical system adds a solid brick to our understanding of quantum behavior in massive macroscopic objects and inspires more exciting discoveries in related fields.

# **Appendices**

# APPENDIX A

## Theory of Quantum Optomechanics in Superfluid Helium

### A.1 Introduction

This appendix presents the theoretical foundations of optomechanics in systems utilizing superfluid helium, which is mainly based on the framework presented in Ref. [235]. My approach begins by describing the basic semiclassical equations governing the optomechanical interactions in such systems. I then present a Hamiltonian formulation of the problem using canonical variables, allowing for the quantization of both phonon and photon fields. The theory is formulated in terms of both electromagnetic and fluid density fields, enabling the handling of situations involving numerous phonons and photons of varying frequencies. Nonlinear contributions in phononic fields are incorporated through perturbation theory, and we show the modification of phonon energy levels due to the intrinsic material nonlinearity.

### A.2 Classic Nonlinear Equations for Superfluid Helium Optomechanics

We start with the fundamental equations for the superfluid density  $\rho$  and the velocity  $\mathbf{v}$ , and we obtain modifications of these equations due to interaction with the electromagnetic fields. The basic Navier-Stokes equations for  $\rho$  and  $\mathbf{v}$  in the absence of the electromagnetic fields are

$$\frac{\partial \rho}{\partial t} + \nabla \cdot (\rho \mathbf{v}) = 0, \quad (\text{A.1a})$$

$$\frac{\partial}{\partial t}(\rho \mathbf{v}) + \nabla \cdot \overset{\leftrightarrow}{T} = 0, \quad (\text{A.1b})$$

where  $\overset{\leftrightarrow}{T}$  is the stress tensor, given by

$$T_{ij} = p\delta_{ij} + \rho v_i v_j. \quad (\text{A.2})$$

Here  $p$  is the pressure in the superfluid, and the viscosity term is zero. Generally, this set of non-linear equations can be expanded in terms of the normalized density deviation  $\tilde{\rho} = (\rho - \rho_0)/\rho_0$  from the equilibrium density  $\rho_0$  as

$$p - p_0 \approx \left( \rho \frac{\partial p}{\partial \rho} \right) \tilde{\rho} + \frac{1}{2} \left( \rho^2 \frac{\partial^2 p}{\partial \rho^2} \right) \tilde{\rho}^2 + \frac{1}{6} \left( \rho^3 \frac{\partial^3 p}{\partial \rho^3} \right) \tilde{\rho}^3 + \dots \quad (\text{A.3})$$

Considering the interaction of liquid helium and electromagnetic field, we can add the interaction term to Eq. (A.1b)

$$\frac{\partial}{\partial t}(\rho \mathbf{v}) + \nabla \cdot \overset{\leftrightarrow}{T} + \frac{1}{2} \rho \nabla \left[ \frac{\partial \epsilon}{\partial \rho} \mathbf{E}^2(\mathbf{r}) \right] = 0, \quad (\text{A.4})$$

where  $\epsilon[\rho(\mathbf{r})]$  is the relative permittivity of the superfluid as function of the local density  $\rho(\mathbf{r})$ .  $\epsilon$  is a scalar function because of the isotropy of liquid helium. The interaction term can be interpreted as adding the extra electromagnetic stress to Eq. (A.1b) in the Navier-Stokes equations. Thus, Eq. (A.1a) and (A.4) are the basic dynamical equations of superfluid helium optomechanical systems.

The electric field obeys the following equation:

$$\nabla \times \nabla \times \mathbf{E} + \frac{1}{\epsilon_0 c^2} \frac{\partial^2}{\partial t^2} (\epsilon[\rho(\mathbf{r})] \mathbf{E}) = 0. \quad (\text{A.5})$$

All equations in this section are solved and quantized in photon and phonon representations in the following sections.

### A.3 Hamiltonian Representations

In the Hamiltonian description, we introduce the conjugate variables  $\rho(\mathbf{r})$  and  $\Phi(\mathbf{r})$ , where  $\Phi$  is the velocity field potential (scalar), which satisfies

$$\mathbf{v} = -\nabla \Phi. \quad (\text{A.6})$$

The unperturbed kinetic Hamiltonian density is

$$\mathcal{H}_0 = \frac{1}{2} \rho (\nabla \Phi)^2, \quad (\text{A.7})$$

and the interaction Hamiltonian density of the density wave, which corresponds to the potential energy, is

$$\mathcal{H}_1 = \rho W(\rho) = \rho \int_{\rho_0}^{\rho} \frac{p(\rho')}{\rho'^2} d\rho'. \quad (\text{A.8})$$

The Hamiltonian density for the electromagnetic field is

$$\mathcal{H}^{(\text{em})} = \underbrace{\frac{1}{2} \left( \epsilon_0 \mathbf{E}^2 + \frac{1}{\mu_0} \mathbf{B}^2 \right)}_{\mathcal{H}_0^{(\text{em})}} + \underbrace{-\frac{\epsilon[\rho] - \epsilon_0}{2} \mathbf{E}^2}_{\mathcal{H}_1^{(\text{em})}}, \quad (\text{A.9})$$

where  $\mathcal{H}^{(\text{em})}$  is the electromagnetic field energy density, and  $\mathcal{H}_1^{(\text{em})}$  is the interaction energy with liquid helium. We could expand  $\epsilon[\rho]$  around  $\rho_0$  as,

$$\epsilon[\rho] = \epsilon[\rho_0] + \rho_0 \left( \frac{\partial \epsilon}{\partial \rho} \right) \tilde{\rho} + \frac{1}{2} \rho_0^2 \left( \frac{\partial^2 \epsilon}{\partial \rho^2} \right) \tilde{\rho}^2 + \dots. \quad (\text{A.10})$$

Thus, the interaction Hamiltonian  $\mathcal{H}_1^{(\text{em})}$  in Eq. (A.9) can be reexpressed by

$$\begin{aligned} \mathcal{H}_1^{(\text{em})} &= -\frac{\epsilon[\rho_0] - \epsilon_0}{2} \mathbf{E}^2 - \frac{1}{2} g_1 \epsilon_0 \tilde{\rho} \mathbf{E}^2 - \frac{1}{2} g_2 \epsilon_0 \tilde{\rho}^2 \mathbf{E}^2 + \dots, \\ \text{with } g_1 &= \frac{\rho_0}{\epsilon_0} \left( \frac{\partial \epsilon}{\partial \rho} \right), \quad g_2 = \frac{\rho_0^2}{2 \epsilon_0} \left( \frac{\partial^2 \epsilon}{\partial \rho^2} \right). \end{aligned} \quad (\text{A.11})$$

Here  $g_1$  and  $g_2$  are the coupling constants for the linear and quadratic optomechanical interactions, respectively. The values of the coupling strength can be retrieved from the Clausius-Mossotti relation [294]:

$$\frac{\epsilon(\rho)}{\epsilon_0} = \frac{1 + \frac{8\pi}{3} \frac{\alpha_m}{m} \rho}{1 - \frac{4\pi}{3} \frac{\alpha_m}{m} \rho}, \quad (\text{A.12})$$

where the molecular polarizability  $\alpha_m = 1.23296 \times 10^{-7} \text{ m}^3 \cdot \text{mole}^{-1}$ , the mass density  $m = 4.0026 \times 10^{-3} \text{ kg} \cdot \text{mole}^{-1}$ , and the equilibrium density  $\rho_0 = 145.1397 \text{ kg} \cdot \text{m}^{-3}$ . Thus, we have  $g_1 \cong 0.05826$ ,  $g_2 \cong 0.00111$ .

Furthermore, the intrinsic nonlinearity of the superfluid mechanical dynamics in the absence of the interaction of electromagnetic field appears in the term  $\mathcal{H}_1$ . Substituting expansion Eq. (A.3) into Eq. (A.8), we can rewrite  $\mathcal{H}_1$  up to  $\tilde{\rho}^3$  as

$$\mathcal{H}_1 = \frac{1}{2} (\rho_0 v_{\text{He}}^2) \tilde{\rho}^2 + \frac{1}{6} (A_2 - \rho_0 v_{\text{He}}^2) \tilde{\rho}^3 + \dots \quad (\text{A.13})$$

where the parameter  $A_2/(2\rho_0 v_{\text{He}}^2) = 2.84$  is the Gruneisen constant, and  $v_{\text{He}} = \sqrt{\frac{\partial p}{\partial \rho}} = 238 \text{ m s}^{-1}$  is the speed of the sound in liquid helium. The cubic term in the Hamiltonian

density raises the nonlinear conversion of phonons, *i.e.*, the three-phonon interaction [214–216].

## A.4 Quantization of the Mechanical Hamiltonian

The second quantization is realized by linearizing the Navier-Stokes equations, *i.e.*, keeping the expansion up to  $\tilde{\rho}^2$  order. Similar to the electromagnetic field, we have the linearized equations of motion for the density waves, which are given by

$$\tilde{\rho} = \sum_i \psi_i(\mathbf{r}) e^{-i\omega_i t} \sigma_i + \text{c.c.}, \quad (\text{A.14a})$$

$$\nabla^2 \psi_i + (\omega_i^2 / v_{\text{He}}^2) \psi_i = 0, \quad (\text{A.14b})$$

where  $i$  is the mode index of the normalized density wave function  $\psi_i$ , frequency  $\omega_i$ , and the amplitude  $\sigma_i$ . We can easily obtain the velocity potential  $\Phi$  as [235]

$$\Phi = \sum_i i \frac{v_{\text{He}}^2}{\omega_i} \psi_i(\mathbf{r}) e^{-i\omega_i t} \sigma_i + \text{c.c..} \quad (\text{A.15})$$

Notice  $\int d^3r (\nabla \Phi)^2 = - \int d^3r \Phi \nabla^2 \Phi$ . Hence, for a given mode, the kinetic Hamiltonian is

$$\int \mathcal{H}_0 d^3r = -\frac{1}{2} \rho_0 \int \Phi \nabla^2 \Phi d^3r = \frac{\omega_i^2}{2v_{\text{He}}^2} \rho_0 \int \Phi^2 d^3r = \rho_0 v_{\text{He}}^2 |\sigma_i|^2. \quad (\text{A.16})$$

The total Hamiltonian of the mechanical mode in the absence of the electromagnetic field is

$$H = \int \mathcal{H} d^3r = \rho_0 v_{\text{He}}^2 |\sigma_i|^2 + \int \frac{1}{2} (\rho_0 v_{\text{He}}^2) \tilde{\rho}^2 d^3r = 2\rho_0 v_{\text{He}}^2 |\sigma_i|^2 = \hbar \omega_i \hat{b}^\dagger \hat{b}. \quad (\text{A.17})$$

Thus, we can quantize the phonon field via

$$\sigma_i \rightarrow \sqrt{\frac{\hbar \omega_i}{2\rho_0 v_{\text{He}}^2}} \hat{b}_i, \quad (\text{A.18})$$

where  $\hat{b}_i$  is the Bosonic annihilation operator for the phonon field with frequency  $\omega_i$ . We could also rewrite the density deviation  $\tilde{\rho}$  and the total Hamiltonian as

$$\tilde{\rho} = \sum_i \psi_i(\mathbf{r}) \sqrt{\frac{\hbar \omega_i}{2\rho_0 v_{\text{He}}^2}} \hat{b}_i e^{-i\omega_i t} + \text{c.c.}, \quad (\text{A.19a})$$

$$H = \sum_i \hbar \omega_i \hat{b}_i^\dagger \hat{b}_i + \mathcal{O}(\tilde{\rho}^3). \quad (\text{A.19b})$$

Terms of the order higher than  $\tilde{\rho}^3$  can be obtained by using the expansion Eq. (A.3). In summary, the nonlinearity of the material and the dynamical equations together contribute to these nonlinear scattering processes.

### A.4.1 Three-Phonon Process

The three-phonon process arises from the cubic term in the total Hamiltonian.  $\nabla^2\Phi$  can be expanded as

$$\nabla^2\Phi = \dot{\tilde{\rho}} - \tilde{\rho}\dot{\tilde{\rho}} + \tilde{\rho}\dot{\tilde{\rho}} + \mathcal{O}(\tilde{\rho}^3) = \dot{\tilde{\rho}} + \mathcal{O}(\tilde{\rho}^3). \quad (\text{A.20})$$

Therefore, the total Hamiltonian can be written as

$$\mathcal{H} = \mathcal{H}_0 + \mathcal{H}_1 = (\rho_0 v_{\text{He}}^2) \tilde{\rho}^2 + \frac{1}{6} \left( A_2 - \frac{1}{2} \rho_0 v_{\text{He}}^2 \right) \tilde{\rho}^3 + \mathcal{O}(\tilde{\rho}^4). \quad (\text{A.21})$$

The second term is the first term which corresponds to the nonlinear process and can be reexpressed by  $\hat{b}$  and  $\hat{b}^\dagger$  as

$$\frac{1}{6} \left( A_2 - \frac{1}{2} \rho_0 v_{\text{He}}^2 \right) \tilde{\rho}^3 = 0.86 \rho_0 v_{\text{He}}^2 \int d\mathbf{r}^3 \sum_i (\psi(\mathbf{r}) \sqrt{\frac{\hbar\omega_i}{2\rho_0 v_{\text{He}}^2}} \hat{b}_i e^{-i\omega_i t} + \text{c.c.})^3. \quad (\text{A.22})$$

The first-order perturbation yields a zero shift on its eigenenergy, that is

$$\Delta E_i^{(1)} = \langle n_i | \frac{1}{6} \left( A_2 - \frac{1}{2} \rho_0 v_{\text{He}}^2 \right) \tilde{\rho}^3 | n_i \rangle = 0. \quad (\text{A.23})$$

This is because this perturbation term is a product of an odd number of operators. The second-order perturbation of this term is in the order of  $\tilde{\rho}^6$ .

### A.4.2 Perturbed Energy Levels

The Hamiltonian can be expanded to the order of  $\tilde{\rho}^4$  as

$$\mathcal{H}_0 = \frac{1}{2} \rho_0 v_{\text{He}}^2 \tilde{\rho}^2 (1 + \tilde{\rho} - \tilde{\rho}^2) + \mathcal{O}(\tilde{\rho}^5), \quad (\text{A.24a})$$

$$\begin{aligned} \mathcal{H}_1 = \rho W(\rho) &= \frac{1}{2} (\rho_0 v_{\text{He}}^2) \tilde{\rho}^2 + \frac{1}{6} (A_2 - \rho_0 v_{\text{He}}^2) \tilde{\rho}^3 \\ &\quad + \frac{1}{12} (\rho_0 v_{\text{He}}^2 - A_2 + \frac{1}{2} A_3) \tilde{\rho}^4 + \mathcal{O}(\tilde{\rho}^5), \end{aligned} \quad (\text{A.24b})$$

where  $A_3 = \left. \rho_0^3 \frac{\partial^3 p}{\partial \rho^3} \right|_{\rho=\rho_0}$  is the third-order pressure expansion coefficient. Thus, the

total Hamiltonian density is

$$\mathcal{H} = \mathcal{H}_{\text{cubic}} + \frac{1}{24}(-10\rho_0 v_{\text{He}}^2 - 2A_2 + A_3)\tilde{\rho}^4 + \mathcal{O}(\tilde{\rho}^5), \quad (\text{A.25})$$

where  $\mathcal{H}_{\text{cubic}}$  is the Hamiltonian up to the cubic term of  $\tilde{\rho}$ . For the sake of brevity, let's denote the coefficient of the quartic-order perturbation term as  $C \equiv \frac{1}{24}(-10\rho_0 v_{\text{He}}^2 - 2A_2 + A_3)/\rho_0 v_{\text{He}}^2$ . We can rewrite the quartic term in terms of creation and annihilation operators as

$$\begin{aligned} \Delta H &= C\rho_0 v_{\text{He}}^2 \tilde{\rho}^4 = C\rho_0 v_{\text{He}}^2 \sum_i \left( \int d\mathbf{r}^3 (\psi(\mathbf{r}) \sqrt{\frac{\hbar\omega_i}{2\rho_0 v_{\text{He}}^2}} \hat{b}_i e^{-i\omega_i t} + \text{c.c.})^4 \right) \\ &= C\rho_0 v_{\text{He}}^2 \int d\mathbf{r}^3 \sum_{i,j,k,h} \psi_i(\mathbf{r}) \psi_j(\mathbf{r}) \psi_k^*(\mathbf{r}) \psi_h^*(\mathbf{r}) \times \\ &\quad \sqrt{\frac{\hbar^4 \omega_i \omega_j \omega_h \omega_k}{(2\rho_0 v_{\text{He}}^2)^4}} \hat{b}_i \hat{b}_j \hat{b}_k^\dagger \hat{b}_h^\dagger e^{-i(-\omega_i - \omega_j + \omega_h + \omega_k)t}, \end{aligned} \quad (\text{A.26})$$

where we only keep the term having an equal number of creation and annihilation operators ( $\hat{b}_i \hat{b}_j \hat{b}_k^\dagger \hat{b}_h^\dagger$  is an example, there is no restriction on the ordering of operators). Notice that non-zero eigenenergy shifts only arise from terms consisting of one mode. This is because the value of the integral in Eq. (A.26) is approximately zero. We could further simplify the quartic perturbation Hamiltonian as

$$\begin{aligned} \Delta H &= C\rho_0 v_{\text{He}}^2 \int d\mathbf{r}^3 \sum_i \psi_i(\mathbf{r}) \psi_i(\mathbf{r}) \psi_i^*(\mathbf{r}) \psi_i^*(\mathbf{r}) \sqrt{\frac{\hbar^4 \omega_i^4}{(2\rho_0 v_{\text{He}}^2)^4}} \text{T}[(\hat{b}^\dagger + \hat{b})^4] \\ &= \sum_i \hbar\omega_i \cdot C \frac{\hbar\omega_i}{4\rho_0 v_{\text{He}}^2} \int d^3 r |\psi_i(\mathbf{r})|^4 \cdot \text{T}[(\hat{b}^\dagger + \hat{b})^4] \\ &= \sum_i \hbar\omega_i \cdot \varsigma_i \cdot \text{T}[(\hat{b}^\dagger + \hat{b})^4], \end{aligned} \quad (\text{A.27})$$

where  $\text{T}[(\hat{b}^\dagger + \hat{b})^4]$  means the original ordering of operators is kept after the expansion. Here we also define a dimensionless relative perturbation strength

$$\varsigma_i \equiv C \frac{\hbar\omega_i}{4\rho_0 v_{\text{He}}^2} \int d^3 r |\psi_i(\mathbf{r})|^4 \approx C \frac{\hbar\omega_i}{4\rho_0 v_{\text{He}}^2} \frac{1}{V}, \quad (\text{A.28})$$

where  $V$  is the mode volume. This ordered product  $\text{T}[(\hat{b}^\dagger + \hat{b})^4]$  can be simplified by using

Wick's theorem as

$$\begin{aligned}
& \text{T}[(\hat{b}^\dagger + \hat{b})(\hat{b}^\dagger + \hat{b})(\hat{b}^\dagger + \hat{b})(\hat{b}^\dagger + \hat{b})] \\
&= \text{N}[(\hat{b}^\dagger + \hat{b})(\hat{b}^\dagger + \hat{b})(\hat{b}^\dagger + \hat{b})(\hat{b}^\dagger + \hat{b})] \\
&+ \text{N}[\underbrace{(\hat{b}^\dagger + \hat{b})(\hat{b}^\dagger + \hat{b})}_{\text{N}}(\hat{b}^\dagger + \hat{b})(\hat{b}^\dagger + \hat{b})(\hat{b}^\dagger + \hat{b})] + \dots \\
&+ \text{N}[\underbrace{(\hat{b}^\dagger + \hat{b})(\hat{b}^\dagger + \hat{b})}_{\text{N}}(\hat{b}^\dagger + \hat{b})(\hat{b}^\dagger + \hat{b})\underbrace{(\hat{b}^\dagger + \hat{b})}_{\text{N}}] + \dots \\
&= \text{N}[(\hat{b}^\dagger + \hat{b})(\hat{b}^\dagger + \hat{b})(\hat{b}^\dagger + \hat{b})(\hat{b}^\dagger + \hat{b})] + 6 \text{N}[(\hat{b}^\dagger + \hat{b})(\hat{b}^\dagger + \hat{b})] + 3,
\end{aligned} \tag{A.29}$$

where  $\text{N}[\dots]$  means normally ordered operators. According to perturbation theory, the shift of eigenenergy is

$$\begin{aligned}
\Delta E_{n_i}^{(1)} &= \langle n_i | \sum_i \hbar \omega_i \varsigma_i \text{T}[(\hat{b}^\dagger + \hat{b})^4] | n_i \rangle = \hbar \omega_i \varsigma_i \langle n_i | \text{T}[(\hat{b}^\dagger + \hat{b})^4] | n_i \rangle \\
&= \hbar \omega_i \varsigma_i (6 \langle n_i | \hat{b}_i^\dagger \hat{b}_i^\dagger \hat{b}_i \hat{b}_i | n_i \rangle + 12 \langle n_i | \hat{b}_i^\dagger \hat{b}_i | n_i \rangle + 3) \\
&= \hbar \omega_i \varsigma_i (6n_i^2 + 6n_i + 3).
\end{aligned} \tag{A.30}$$

The first term is the nonlinear correction of the phonon energy, the second term is equivalent to increasing the frequency by  $6\varsigma_i$ , and the last term is the trivial overall energy shifting.

For the device in this work, the mode volume  $V \sim 1 \times 10^{-15} \text{ m}^3$ , the mode frequency  $\omega_m / 2\pi \sim 315 \text{ MHz}$ , and  $\rho_0 v_{\text{He}}^2 \approx 8213380 \text{ J} \cdot \text{m}^{-3}$ . The relative perturbation strength  $\varsigma$  is estimated to be  $\varsigma \sim 6 \times 10^{-18}$ . Since the mechanical quality factor is  $10^5$ , to have a noticeable nonlinear effect ( $\Delta E_n > \hbar \gamma_m$ ) would require the mechanical resonator to be driven up to  $n_m \approx 7 \times 10^6$ .

## A.5 Quantization of the Optomechanical Coupling

The optomechanical interaction Hamiltonian is described in Eq. (A.11). The quantized form of the optomechanical interaction can be obtained by using quantized density wave in Eq. (A.19a) and quantized electromagnetic wave in the optomechanical interaction Hamiltonian.

### A.5.1 Linear Optomechanical Interaction

The first coupling term is  $-1/2g_1\epsilon_0\tilde{\rho}\mathbf{E}^2$ , and its quantized representation is [235]

$$v_L = -\hbar \sum_{ijl} \left\{ g'_{ijl} e^{i(\omega_i - \omega_j - f_l)t} \hat{a}_i^\dagger \hat{a}_j \hat{b}_l + g'_{ijl} e^{i(\omega_i - \omega_j + f_l)t} \hat{a}_i^\dagger \hat{a}_j \hat{b}_l^\dagger \right\}, \tag{A.31}$$

with

$$g'_{ijl} = \sqrt{\frac{\hbar f_l \omega_i \omega_j}{8\rho_0 v_{\text{He}}^2}} g_1 \int \psi_l(\mathbf{r}) [\mathbf{u}^{(i)*}(\mathbf{r}) \cdot \mathbf{u}^{(j)}(\mathbf{r})] d^3 r,$$

where  $\hat{a}_i^\dagger$  and  $\hat{b}_l^\dagger$  are creation operators of the photon field of mode index  $i$  and the phonon field of mode index  $l$ , respectively.  $\mathbf{u}^{(i)}$  and  $\psi_l$  are spatial profiles of the optical mode and mechanical mode profiles, respectively.

This is the standard form of the optomechanical interaction Hamiltonian. Especially, terms like  $\hat{a}_i^\dagger \hat{a}_i (\hat{b}_l + \hat{b}_l^\dagger)$  are the coupling Hamiltonian discussed in Eq. (2.26). In this case, the mechanical wave couples with the optical intensity, and the coupling originates from the photon-elastic interaction shown in Eq. (A.10). The interaction strength can be estimated by taking  $\psi(\mathbf{r}) = 1/\sqrt{V}$  in Eq. (A.32),

$$g'_{iil} \sim \sqrt{\frac{\hbar f_l}{8\rho_0 v_{\text{He}}^2}} \frac{\omega_i g_1}{\sqrt{V}}. \quad (\text{A.32})$$

The explicit strength relies on the explicit value of the overlap integral in Eq. (A.32), as discussed in Sec. 5.4.1.

### A.5.2 Nonlinear Optomechanical Interaction

The first nonlinear interaction  $v_{\text{NL}}$  is derived from the interaction term  $-1/2g_2\epsilon_0\tilde{\rho}^2\mathbf{E}^2$ , which can be written as

$$-\hbar \sum_{ijl_1l_2} p_{ijl_1l_2} e^{i(\omega_i - \omega_j + f_{l_1} - f_{l_2})t} \hat{a}_i^\dagger \hat{a}_j \hat{b}_{l_1}^\dagger \hat{b}_{l_2}, \quad (\text{A.33})$$

which corresponds to the mechanical intensity and optical intensity coupling. The coupling strength is

$$p_{ijl_1l_2} = \sqrt{\frac{\hbar^2 f_{l_1} f_{l_2} \omega_i \omega_j}{16(\rho_0 v_{\text{He}}^2)^2}} g_2 \times \int d^3 r \psi_{l_1}^*(\mathbf{r}) \psi_{l_2}(\mathbf{r}) \mathbf{u}^{(i)*} \cdot \mathbf{u}^{(j)}. \quad (\text{A.34})$$

Similar to the argument in Appendix A.4.2, we only consider the mechanical modes with the same mode index  $l_1$  and the optical modes with the same mode index  $i$ , and we have

$$p_{ijl_1l_2} \approx \sqrt{\frac{\hbar f_{l_1}}{8\rho_0 v_{\text{He}}^2 V}} \sqrt{\frac{\hbar f_{l_1}}{2\rho_0 v_{\text{He}}^2 V}} \omega_i g_2. \quad (\text{A.35})$$

After linearizing the optical intensity by its fluctuation (similar to Sec. 2.1.3), these terms correspond to the process of annihilating/creating two phonons and creating/annihilating

one photon. Compared to the linear optomechanical coupling, this coupling strength is smaller by a factor

$$\sqrt{\frac{\hbar f_{l_1}}{2\rho_0 v_{\text{He}}^2 V}} \left( \frac{g_2}{g_1} \right). \quad (\text{A.36})$$

For the cavity we used in this work, this value of the factor is around  $1 \times 10^{-10}$ .

# APPENDIX B

## Basics of a Fabry-Pérot Cavity

Fabry-Pérot interferometers serve as optical resonators that find application in high-resolution spectroscopy. These devices possess the capability to precisely detect and differentiate the intricate characteristics of a transmission spectrum, making them widely employed for identifying the resonant modes of laser cavities. Such resonant modes typically exhibit closely spaced spectral peaks with narrow linewidths.

### B.1 Wave Equation and Paraxial Approximation

This section follows the framework discussed in Ref. [209]. The most frequently used Gaussian modes of a Fabry-Pérot cavity is a result under paraxial approximation. The generic scalar wave equation is

$$\nabla^2 u(\mathbf{r}, t) = \frac{1}{v^2} \frac{\partial^2 u(\mathbf{r}, t)}{\partial t^2}. \quad (\text{B.1})$$

The general solution of this wave equation is of the form  $f(\mathbf{r} - vt)$ . The Fourier transform of the scalar wave equation directs us to the Helmholtz equation

$$\left( \nabla^2 + \frac{\omega^2}{v^2} \right) u(\mathbf{r}, \omega) = 0. \quad (\text{B.2})$$

With a defined boundary condition, *i.e.*, a Dirichlet boundary condition, we will have a set of eigenmode characterized by mode index  $(q, m, n)$ .

Let the z-axis be the propagation axis. With  $\mathbf{r}_\perp = x\hat{x} + y\hat{y}$ , we take an ansatz of the form with  $\hat{u}(\mathbf{r}, \omega) = \Psi(\mathbf{r}) \exp(ikz)$  and another form of the Laplace operator

$$\nabla^2 = \frac{\partial^2}{\partial x^2} + \frac{\partial^2}{\partial y^2} + \frac{\partial^2}{\partial z^2} \equiv \nabla_\perp^2 + \frac{\partial^2}{\partial z^2}. \quad (\text{B.3})$$

Thus, the Helmholtz equation (Eq. (B.2)) can be rewritten as an equation for  $\Psi(\mathbf{r}_\perp, z)$ :

$$\nabla_\perp^2 \Psi + 2ik \frac{\partial \Psi}{\partial z} + \frac{\partial^2 \Psi}{\partial z^2} = 0. \quad (\text{B.4})$$

The paraxial approximation requires:

$$k \frac{\partial \Psi}{\partial z} \gg \frac{\partial^2 \Psi}{\partial z^2}, \quad (\text{B.5})$$

which is equivalent to state the change of  $\Psi$  along the  $z$ -direction over the wavelength is negligible. In the beam-like solution, the paraxial approximation requirement becomes

$$k^2 w_0^2 \gg 1, \quad (\text{B.6})$$

where  $w_0$  is the beam waist. With this, we can drop the last term in Eq. (B.4) and arrive at the paraxial wave equation:

$$-\frac{1}{2k} \nabla_\perp^2 \Psi = i \frac{\partial \Psi}{\partial z}. \quad (\text{B.7})$$

The general solution of this equation has the form of

$$\Psi(\mathbf{r}_\perp, z) = \int d^2 q_\perp \hat{\Psi}(\mathbf{q}_\perp) e^{i(\mathbf{q}_\perp \cdot \mathbf{r}_\perp - q_\perp^2 z / 2k)}. \quad (\text{B.8})$$

Notice that the reduced differential operator  $[\frac{1}{2k} \nabla_\perp^2 + i \frac{\partial}{\partial z}]$  is still a self-adjoint operator. Thus its eigenvalues are real, and eigenstates are mutually orthogonal.

## B.2 Gaussian Mode in a Fabry-Pérot Cavity

In this section, I will describe the Gaussian mode in a Fabry-Pérot cavity with given geometries. Assume a Fabry-Perot cavity consists of two mirrors with radii of curvature  $r_1$  and  $r_2$ , which are separated by a cavity length  $L_{\text{cav}}$ . The Gaussian mode in such a cavity is defined by matching the radii of curvatures of two mirrors with the radii of curvature of the Gaussian beam wavefronts. Therefore, we can constrain the Rayleigh distance  $z_R$  by

the following equations:

$$R(z_1) = z_1 \left( 1 + \left( \frac{z_R}{z_1} \right)^2 \right) = -r_1, \quad (\text{B.9a})$$

$$R(z_2) = z_2 \left( 1 + \left( \frac{z_R}{z_2} \right)^2 \right) = r_2, \quad (\text{B.9b})$$

$$L_{\text{cav}} = z_2 - z_1, \quad (\text{B.9c})$$

where  $z_1$  and  $z_2$  are the distances (with sign) from two mirrors to the center of the Gaussian beam. Solving this equation set yields

$$z_R = \sqrt{\frac{g_1 g_2 (1 - g_1 g_2)}{(g_1 + g_2 - 2g_1 g_2)^2}} L_{\text{cav}}, \quad (\text{B.10})$$

where  $g_1$  and  $g_2$  are  $g$ -parametres of two mirrors, defined as

$$g_i = 1 - \frac{L_{\text{cav}}}{r_i}. \quad (\text{B.11})$$

Thus, we have

$$z_1 = -\frac{g_2 (1 - g_1)}{g_1 + g_2 - 2g_1 g_2} L_{\text{cav}}, \quad z_2 = \frac{g_1 (1 - g_2)}{g_1 + g_2 - 2g_1 g_2} L_{\text{cav}}. \quad (\text{B.12})$$

The standing wave condition requires  $(\phi(z_2) - \phi(z_1)) = q\pi$  with an integer  $q$  as a longitudinal mode index. Substituting this condition into Eq. (5.6), we have

$$k^{(q,n,m)} = \pi q / L_{\text{cav}} + (n + m + 1) \arccos(\pm \sqrt{g_1 g_2}) / L_{\text{cav}}, \quad (\text{B.13})$$

and the corresponding Guoy phase shift is

$$\phi_G = (n + m + 1) \arccos(\pm \sqrt{g_1 g_2}) / L_{\text{cav}}, \quad (\text{B.14})$$

where “+” sign corresponds to  $r_1, r_2 > L_{\text{cav}}$  and “-” sign corresponds to  $r_1, r_2 < L_{\text{cav}}$ . The case  $r_1 > L_{\text{cav}}, r_2 < L_{\text{cav}}$  or  $r_1 < L_{\text{cav}}, r_2 > L_{\text{cav}}$  corresponds to an unstable cavity. Finally, the beam waist  $w_0$  can be obtained

$$w_0 = \sqrt{\frac{2L_{\text{cav}}}{k^{(q,n,m)}}} \left( \frac{g_1 g_2 (1 - g_1 g_2)}{(g_1 + g_2 - 2g_1 g_2)^2} \right)^{1/4}, \quad (\text{B.15})$$

and the beam radius  $w(z)$  is

$$w(z) = \sqrt{1 + \left(\frac{z}{z_R}\right)^2}. \quad (\text{B.16})$$

### B.3 Transmission Spectrum of a Fabry-Pérot cavity

The transmission spectrum  $I_t$  of a resonator as a function of the detuning from mode  $q$  (*i.e.*,  $\Delta_q = \omega - \omega_q$ ) is

$$I_t(\Delta_q) = \frac{T_1 T_2}{(1 - \sqrt{R_1 R_2})^2} \frac{I_0}{1 + \frac{4\sqrt{R_1 R_2}}{(1 - \sqrt{R_1 R_2})^2} \sin^2\left(\frac{\pi \Delta_q}{\Delta\omega_{\text{FSR}}}\right)}, \quad (\text{B.17})$$

where  $T_{1,2}$  and  $R_{1,2}$  are the transmission and reflection of the first and the second mirrors, respectively, and  $I_0$  is the incident light intensity. This is the well-known Airy formula. The on-resonance ( $\Delta_q = 0$ ) transmission is

$$T_{\text{tot}}^{\text{res}} = \frac{I_t}{I_0} = \frac{T_1 T_2}{(1 - \sqrt{R_1 R_2})^2} \approx \frac{4T_1 T_2}{(T_1 + T_2)^2}. \quad (\text{B.18})$$

In the final step, I use the high-reflectivity mirror approximation ( $T_{1,2} \ll 1$ ) and the energy conservation relation  $R_{1,2} + T_{1,2} = 1$ .

If  $T_1 = T_2$ , Eq. (B.18) can reach 1. Eq. (B.17) can also be simplified as

$$T_{\text{tot}}(\Delta_q) = T_{\text{tot}}^{\text{res}} \frac{\kappa^2}{\kappa^2 + 4\Delta_q^2}. \quad (\text{B.19})$$

In practice, besides reflection and transmission, part of the light is absorbed by mirrors. In this case, Eq. (B.17) is still valid.

# APPENDIX C

## Gauss-Hermite Quadrature

In numerical analysis, simulating or calculating 3-D wave equations with many wavelengths is costly. The performance of the numerical simulation highly depends on how you assign nodes. If we take random  $n$  nodes, the error of the simulation scales as  $\mathcal{E} \sim \mathcal{O}(n^{-1/2})$ . If we take evenly spaced  $n$  nodes, the error scales as  $\mathcal{E} \sim \mathcal{O}(n^{-1})$  [295]. To numerically evaluate the overlap integral in our experiment Fabry-Pérot cavity more precise and more efficiently, we used Gauss-Hermite quadrature to evaluate the value of the integral of the following form [295]:

$$\int_{-\infty}^{+\infty} e^{-x^2} f(x) dx. \quad (\text{C.1})$$

This integral can be better numerically evaluated by the following summation than a normal evenly-spaced nodes

$$\int_{-\infty}^{+\infty} e^{-x^2} f(x) dx \approx \sum_{i=1}^n w_i f(x_i), \quad (\text{C.2})$$

where  $n$  is the number of nodes,  $x_i$  are the roots of the Hermite polynomial  $H_n(x)$  ( $i = 1, 2, \dots, n$ ) with its corresponding weight  $w_i$

$$w_i = \frac{2^{n-1} n! \sqrt{\pi}}{n^2 [H_{n-1}(x_i)]^2}. \quad (\text{C.3})$$

The error of this summation scales as  $\mathcal{E} \sim \mathcal{O}(e^{-n})$  [295].

The general eigenmode of a Fabry-Pérot cavity is a Hermit-Gaussian function defined in Eq. (5.6). The integral over the transverse plane can implement this Gauss-Hermite quadrature summation Eq. (C.2).

# APPENDIX D

## Asymptotic Behaviors of a Maximum Likelihood Estimator

If  $X_1, X_2, \dots$  are  $\sim$  i.i.d. with a density function  $f(\theta)$ , then the log likelihood is

$$l_n(\theta) = \sum_{i=1}^n \log f_\theta(X_i) \quad (\text{D.1})$$

In most situations, the maximum likelihood estimator (MLE)  $\hat{\theta}_n$  will be a stationary point (*i.e.*, a zero of the first derivative of the log likelihood), such that

$$l'_n(\hat{\theta}) = \sum_{i=1}^n \frac{\partial}{\partial \theta} \log f_\theta(X_i) = 0. \quad (\text{D.2})$$

Let  $\theta_0$  denote the true value. We can expand Eq. (D.2) around  $\theta_0$  in a Taylor series as

$$0 = l'_n(\theta_0) + l''_n(\theta_0) (\hat{\theta}_n - \theta_0) + \frac{1}{2} l'''_n(\tilde{\theta}_n) (\hat{\theta}_n - \theta_0)^2, \quad (\text{D.3})$$

where  $\tilde{\theta}_n$  is a value between  $\theta_0$  and  $\hat{\theta}_n$ .

According to the central limit theorem (CLT) and the law of large numbers (LLN), we have

$$E_\theta \{l'_n(\theta)\} = 0 \quad (\text{D.4a})$$

$$\text{Var}_\theta \{l'_n(\theta)\} = -E \{l''_n(\theta)\} = I_n(\theta) \quad (\text{D.4b})$$

where  $I_n(\theta)$  is the expected Fisher information. Thus the CLT says

$$\frac{1}{\sqrt{n}} l'(\theta_0) \xrightarrow{\mathcal{D}} \text{Normal}(0, I_1(\theta_0)). \quad (\text{D.5})$$

Similarly, the terms in

$$-J_n(\theta) = l_n''(\theta) = \sum_{i=1}^n \frac{\partial^2}{\partial \theta^2} \log f_\theta(X_i) \quad (\text{D.6})$$

are i.i.d. with mean  $-I_1(\theta_0)$ , where  $J_n(\theta)$  is called the observed Fisher information. Hence the LLN says

$$\frac{1}{n} l_n''(\theta_0) \xrightarrow{P} -I_1(\theta_0). \quad (\text{D.7})$$

Substituting asymptotics of  $l_n'(\theta_0)$  and  $l_n''(\theta_0)$  into Eq. (D.3), we can obtain

$$\sqrt{n} (\hat{\theta}_n - \theta_0) \xrightarrow{\mathcal{D}} \text{Normal}(0, I_1(\theta_0)^{-1}) \quad (\text{D.8})$$

This relation is the key to likelihood inference. It gives the asymptotic distribution of the MLE, which we can use to estimate confidence intervals of the MLE. However, we don't know  $\theta_0$ . Instead, we use its estimator  $\hat{\theta}_n$  to replace its true value  $\theta_0$  according to

$$\hat{\theta}_n \xrightarrow{P} \theta_0. \quad (\text{D.9})$$

Thus, the corresponding confidence intervals are

$$\hat{\theta}_n \pm c J_n(\hat{\theta}_n)^{-1/2}. \quad (\text{D.10})$$

For a Bernoulli distribution whose MLE is  $\hat{p}_n = x/n$ , the observed Fisher information and the expected Fisher information are

$$J_n(\hat{p}_n) = \frac{n}{\hat{p}_n(1-\hat{p}_n)}, \quad (\text{D.11a})$$

$$I_n(\hat{p}_n) = \frac{n}{\hat{p}_n(1-\hat{p}_n)}, \quad (\text{D.11b})$$

respectively. In this case, the observed Fisher information is identical to the expected Fisher information.

# Bibliography

1. Belenchia, A. *et al.* Testing quantum gravity induced nonlocality via optomechanical quantum oscillators. *Physical Review Letters* **116**, 161303 (2016).
2. Nimmrichter, S. & Hornberger, K. Macroscopicity of mechanical quantum superposition states. *Physical Review Letters* **110**, 160403 (2013).
3. Arvidsson-Shukur, D. R. *et al.* Quantum advantage in postselected metrology. *Nature communications* **11**, 3775 (2020).
4. Mari, A. & Eisert, J. Positive Wigner functions render classical simulation of quantum computation efficient. *Physical Review Letters* **109**, 230503 (2012).
5. Ghirardi, G. C., Pearle, P. & Rimini, A. Markov processes in Hilbert space and continuous spontaneous localization of systems of identical particles. *Physical Review A* **42**, 78 (1990).
6. Bassi, A. & Ghirardi, G. Dynamical reduction models. *Physics Reports* **379**, 257–426 (2003).
7. Eibenberger, S., Gerlich, S., Arndt, M., Mayor, M. & Tüxen, J. Matter-wave interference of particles selected from a molecular library with masses exceeding 10000 amu. *Physical Chemistry Chemical Physics* **15**, 14696–14700 (2013).
8. Kovachy, T. *et al.* Quantum superposition at the half-metre scale. *Nature* **528**, 530–533 (2015).
9. Arndt, M. & Hornberger, K. Testing the limits of quantum mechanical superpositions. *Nature Physics* **10**, 271–277 (2014).
10. Zivari, A. *et al.* On-chip distribution of quantum information using traveling phonons. *Science Advances* **8**, eadd2811 (2022).
11. Wallucks, A., Marinković, I., Hensen, B., Stockill, R. & Gröblacher, S. A quantum memory at telecom wavelengths. *Nature Physics* **16**, 772–777 (2020).
12. Zivari, A., Stockill, R., Fiaschi, N. & Gröblacher, S. Non-classical mechanical states guided in a phononic waveguide. *Nature Physics* **18**, 789–793 (2022).
13. Satzinger, K. J. *et al.* Quantum control of surface acoustic-wave phonons. *Nature* **563**, 661–665 (2018).
14. Bienfait, A. *et al.* Phonon-mediated quantum state transfer and remote qubit entanglement. *Science* **364**, 368–371 (2019).
15. Zhong, Y. *et al.* Deterministic multi-qubit entanglement in a quantum network. *Nature* **590**, 571–575 (2021).

16. Dumur, É. *et al.* Quantum communication with itinerant surface acoustic wave phonons. *npj Quantum Information* **7**, 173 (2021).
17. Aasi, J. *et al.* Enhanced sensitivity of the LIGO gravitational wave detector by using squeezed states of light. *Nature Photonics* **7**, 613–619 (2013).
18. A gravitational wave observatory operating beyond the quantum shot-noise limit. *Nature Physics* **7**, 962–965 (2011).
19. Yu, H. *et al.* Quantum correlations between light and the kilogram-mass mirrors of LIGO. *Nature* **583**, 43–47 (2020).
20. Backes, K. M. *et al.* A quantum enhanced search for dark matter axions. *Nature* **590**, 238–242 (2021).
21. Wolf, F. *et al.* Motional Fock states for quantum-enhanced amplitude and phase measurements with trapped ions. *Nature communications* **10**, 2929 (2019).
22. McCormick, K. C. *et al.* Quantum-enhanced sensing of a single-ion mechanical oscillator. *Nature* **572**, 86–90 (2019).
23. Gilmore, K. A. *et al.* Quantum-enhanced sensing of displacements and electric fields with two-dimensional trapped-ion crystals. *Science* **373**, 673–678 (2021).
24. Greve, G. P., Luo, C., Wu, B. & Thompson, J. K. Entanglement-enhanced matter-wave interferometry in a high-finesse cavity. *Nature* **610**, 472–477 (2022).
25. Xia, Y. *et al.* Entanglement-enhanced optomechanical sensing. *Nature Photonics*, 1–8 (2023).
26. Forsch, M. *et al.* Microwave-to-optics conversion using a mechanical oscillator in its quantum ground state. *Nature Physics* **16**, 69–74 (2020).
27. Pistolesi, F., Cleland, A. & Bachtold, A. Proposal for a nanomechanical qubit. *Physical Review X* **11**, 031027 (2021).
28. Delaney, R. *et al.* Superconducting-qubit readout via low-backaction electro-optic transduction. *Nature* **606**, 489–493 (2022).
29. Mirhosseini, M., Sipahigil, A., Kalaei, M. & Painter, O. Superconducting qubit to optical photon transduction. *Nature* **588**, 599–603 (2020).
30. Arrangoiz-Arriola, P. *et al.* Microwave quantum acoustic processor in 2019 IEEE MTT-S International Microwave Symposium (IMS) (2019), 255–258.
31. Jiang, W. *et al.* Optically heralded microwave photons. *arXiv preprint arXiv:2210.10739* (2022).
32. Bose, S. *et al.* Spin Entanglement Witness for Quantum Gravity. *Physical Review Letters* **119**, 240401 (2017).
33. Schmöle, J., Dragosits, M., Hepach, H. & Aspelmeyer, M. A micromechanical proof-of-principle experiment for measuring the gravitational force of milligram masses. *Classical and Quantum Gravity* **33**, 125031 (2016).

34. Yang, H., Miao, H., Lee, D.-S., Helou, B. & Chen, Y. Macroscopic quantum mechanics in a classical spacetime. *Physical Review Letters* **110**, 170401 (2013).
35. Penrose, R. On gravity's role in quantum state reduction. *General Relativity and Gravitation* **28**, 581–600 (1996).
36. Kaltenbaek, R. *et al.* Macroscopic quantum resonators (MAQRO) Testing quantum and gravitational physics with massive mechanical resonators. *Experimental Astronomy* **34**, 123–164 (2012).
37. Bassi, A., Lochan, K., Satin, S., Singh, T. P. & Ulbricht, H. Models of wave-function collapse, underlying theories, and experimental tests. *Reviews of Modern Physics* **85**, 471 (2013).
38. Leggett, A. J. Testing the limits of quantum mechanics: motivation, state of play, prospects. *Journal of Physics: Condensed Matter* **14**, R415 (2002).
39. Feldmann, W. & Tumulka, R. Parameter diagrams of the GRW and CSL theories of wavefunction collapse. *Journal of Physics A: Mathematical and Theoretical* **45**, 065304 (2012).
40. Safavi-Naeini, A. H., Van Thourhout, D., Baets, R. & Van Laer, R. Controlling phonons and photons at the wavelength scale: integrated photonics meets integrated phononics. *Optica* **6**, 213–232 (2019).
41. Arrangoiz-Arriola, P. *et al.* Resolving the energy levels of a nanomechanical oscillator. *Nature* **571**, 537–540 (2019).
42. MacCabe, G. S. *et al.* Nano-acoustic resonator with ultralong phonon lifetime. *Science* **370**, 840–843 (2020).
43. Meystre, P. A short walk through quantum optomechanics. *Annalen der Physik* **525**, 215–233 (2013).
44. Aspelmeyer, M., Kippenberg, T. J. & Marquardt, F. Cavity optomechanics. *Reviews of Modern Physics* **86**, 1391 (2014).
45. Kippenberg, T. J. & Vahala, K. J. Cavity optomechanics: back-action at the mesoscale. *Science* **321**, 1172–1176 (2008).
46. Regal, C. & Lehnert, K. *From cavity electromechanics to cavity optomechanics* in *Journal of Physics: Conference Series* **264** (2011), 012025.
47. Bowen, W. P. & Milburn, G. J. *Quantum optomechanics* (CRC press, 2015).
48. Aspelmeyer, M., Meystre, P. & Schwab, K. Quantum optomechanics. *Physics Today* **65**, 29–35 (2012).
49. Aspelmeyer, M., Kippenberg, T. & Marquardt, F. *Nano-and Micromechanical Resonators Interacting with Light* (Springer-Verlag, Berlin, Heidelberg, 2014).
50. Cohadon, P.-F., Harris, J., Marquardt, F. & Cugliandolo, L. *Quantum Optomechanics and Nanomechanics: Lecture Notes of the Les Houches Summer School: Volume 105, August 2015* (Oxford University Press, 2020).

51. Chan, J. *et al.* Laser cooling of a nanomechanical oscillator into its quantum ground state. *Nature* **478**, 89–92 (2011).
52. Delić, U. *et al.* Cooling of a levitated nanoparticle to the motional quantum ground state. *Science* **367**, 892–895 (2020).
53. Magrini, L. *et al.* Real-time optimal quantum control of mechanical motion at room temperature. *Nature* **595**, 373–377 (2021).
54. Underwood, M. *et al.* Measurement of the motional sidebands of a nanogram-scale oscillator in the quantum regime. *Physical Review A* **92**, 061801 (2015).
55. Kleckner, D. *et al.* High finesse opto-mechanical cavity with a movable thirty-micron-size mirror. *Physical Review Letters* **96**, 173901 (2006).
56. Thompson, J. *et al.* Strong dispersive coupling of a high-finesse cavity to a micromechanical membrane. *Nature* **452**, 72–75 (2008).
57. Galinskiy, I., Tsaturyan, Y., Parniak, M. & Polzik, E. S. Phonon counting thermometry of an ultracoherent membrane resonator near its motional ground state. *Optica* **7**, 718–725 (2020).
58. Teufel, J. D. *et al.* Sideband cooling of micromechanical motion to the quantum ground state. *Nature* **475**, 359–363 (2011).
59. Kotler, S. *et al.* Direct observation of deterministic macroscopic entanglement. *Science* **372**, 622–625 (2021).
60. Mercier de Lépinay, L., Ockeloen-Korppi, C. F., Woolley, M. J. & Sillanpää, M. A. Quantum mechanics-free subsystem with mechanical oscillators. *Science* **372**, 625–629 (2021).
61. Chu, Y. *et al.* Quantum acoustics with superconducting qubits. *Science* **358**, 199–202 (2017).
62. Chu, Y. *et al.* Creation and control of multi-phonon Fock states in a bulk acoustic-wave resonator. *Nature* **563**, 666–670 (2018).
63. De Lorenzo, L. & Schwab, K. Ultra-High Q Acoustic Resonance in Superfluid<sup>4</sup>He. *Journal of Low Temperature Physics* **186**, 233–240 (2017).
64. Ghosh, A. & Maris, H. J. Observation of a new type of electron bubble in superfluid helium. *Physical Review Letters* **95**, 265301 (2005).
65. Guo, W., Jin, D., Seidel, G. M. & Maris, H. J. Experiments with single electrons in liquid helium. *Physical Review B* **79**, 054515 (2009).
66. Khrapak, A. & Schmidt, W. Negative ions in liquid helium. *Low Temperature Physics* **37**, 387–391 (2011).
67. Ghosh, A. & Maris, H. J. *Observation of a New Type of Negative Ion in Superfluid Helium* in *AIP Conference Proceedings* **850** (2006), 155–158.
68. Koolstra, G., Yang, G. & Schuster, D. I. Coupling a single electron on superfluid helium to a superconducting resonator. *Nature Communications* **10**, 5323 (2019).

69. Schuster, D., Fragner, A., Dykman, M., Lyon, S. & Schoelkopf, R. Proposal for manipulating and detecting spin and orbital states of trapped electrons on helium using cavity quantum electrodynamics. *Physical Review Letters* **105**, 040503 (2010).
70. Kashkanova, A. *et al.* Superfluid Brillouin optomechanics. *Nature Physics* **13**, 74–79 (2017).
71. Shkarin, A. *et al.* Quantum optomechanics in a liquid. *Physical Review Letters* **122**, 153601 (2019).
72. Patil, Y. S. *et al.* Measuring high-order phonon correlations in an optomechanical resonator. *Physical Review Letters* **128**, 183601 (2022).
73. Lachman, L. & Filip, R. Robustness of quantum nonclassicality and non-Gaussianity of single-photon states in attenuating channels. *Physical Review A* **88**, 063841 (2013).
74. Kuzmich, A. *et al.* Generation of nonclassical photon pairs for scalable quantum communication with atomic ensembles. *Nature* **423**, 731–734 (2003).
75. Riedinger, R. *et al.* Non-classical correlations between single photons and phonons from a mechanical oscillator. *Nature* **530**, 313–316 (2016).
76. De Riedmatten, H. *et al.* Direct measurement of decoherence for entanglement between a photon and stored atomic excitation. *Physical Review Letters* **97**, 113603 (2006).
77. Einstein, A. Über einen die Erzeugung und Verwandlung des Lichtes betreffenden heuristischen Gesichtspunkt [AdP 17, 132 (1905)]. *Annalen der Physik* **14**, 164–181 (2005).
78. Lebedew, P. Untersuchungen über die Druckkräfte des Lichtes. *Annalen der Physik* **311**, 433–458 (1901).
79. Nichols, E. F. & Hull, G. F. A preliminary communication on the pressure of heat and light radiation. *Physical Review (Series I)* **13**, 307 (1901).
80. Clerk, A., Marquardt, F. & Harris, J. Quantum measurement of phonon shot noise. *Physical Review Letters* **104**, 213603 (2010).
81. Purdy, T. P., Peterson, R. W. & Regal, C. Observation of radiation pressure shot noise on a macroscopic object. *Science* **339**, 801–804 (2013).
82. Acernese, F. *et al.* Quantum backaction on Kg-scale mirrors: observation of radiation pressure noise in the advanced Virgo detector. *Physical Review Letters* **125**, 131101 (2020).
83. Caves, C. M. Quantum-mechanical radiation-pressure fluctuations in an interferometer. *Physical Review Letters* **45**, 75 (1980).
84. Cohadon, P.-F., Heidmann, A. & Pinard, M. Cooling of a mirror by radiation pressure. *Physical Review Letters* **83**, 3174 (1999).
85. Zhang, H. & Miller, O. D. Quasinormal coupled mode theory. *arXiv:2010.08650* (2020).

86. Cleland, A. N. *Foundations of nanomechanics: from solid-state theory to device applications* (Springer Science & Business Media, 2013).
87. Zavatta, A., Viciani, S. & Bellini, M. Quantum-to-classical transition with single-photon-added coherent states of light. *Science* **306**, 660–662 (2004).
88. Parigi, V., Zavatta, A., Kim, M. & Bellini, M. Probing quantum commutation rules by addition and subtraction of single photons to/from a light field. *Science* **317**, 1890–1893 (2007).
89. Hloušek, J., Ježek, M. & Filip, R. Work and information from thermal states after subtraction of energy quanta. *Scientific reports* **7**, 1–9 (2017).
90. Teufel, J., Harlow, J., Regal, C. & Lehnert, K. Dynamical backaction of microwave fields on a nanomechanical oscillator. *Physical Review Letters* **101**, 197203 (2008).
91. Cohen, J. D. *et al.* Phonon counting and intensity interferometry of a nanomechanical resonator. *Nature* **520**, 522–525 (2015).
92. Hong, S. *et al.* Hanbury Brown and Twiss interferometry of single phonons from an optomechanical resonator. *Science* **358**, 203–206 (2017).
93. Elste, F., Girvin, S. & Clerk, A. Quantum noise interference and backaction cooling in cavity nanomechanics. *Physical Review Letters* **102**, 207209 (2009).
94. Vanner, M. R. *et al.* Pulsed quantum optomechanics. *Proceedings of the National Academy of Sciences* **108**, 16182–16187 (2011).
95. Weiss, T., Bruder, C. & Nunnenkamp, A. Strong-coupling effects in dissipatively coupled optomechanical systems. *New journal of physics* **15**, 045017 (2013).
96. Marquardt, F., Chen, J. P., Clerk, A. A. & Girvin, S. Quantum theory of cavity-assisted sideband cooling of mechanical motion. *Physical Review Letters* **99**, 093902 (2007).
97. Riedinger, R. *et al.* Remote quantum entanglement between two micromechanical oscillators. *Nature* **556**, 473–477 (2018).
98. Børkje, K., Nunnenkamp, A. & Girvin, S. Proposal for entangling remote micromechanical oscillators via optical measurements. *Physical Review Letters* **107**, 123601 (2011).
99. Gardiner, C. W. & Collett, M. J. Input and output in damped quantum systems: Quantum stochastic differential equations and the master equation. *Physical Review A* **31**, 3761 (1985).
100. Loudon, R. *The quantum theory of light* (OUP Oxford, 2000).
101. Safavi-Naeini, A. H. *et al.* Observation of quantum motion of a nanomechanical resonator. *Physical Review Letters* **108**, 033602 (2012).
102. Safavi-Naeini, A. H. *et al.* Laser noise in cavity-optomechanical cooling and thermometry. *New Journal of Physics* **15**, 035007 (2013).

103. Ren, H. *et al.* Two-dimensional optomechanical crystal cavity with high quantum cooperativity. *Nature communications* **11**, 3373 (2020).
104. Yuan, M., Singh, V., Blanter, Y. M. & Steele, G. A. Large cooperativity and microkelvin cooling with a three-dimensional optomechanical cavity. *Nature communications* **6**, 8491 (2015).
105. Purdy, T. P., Yu, P.-L., Peterson, R. W., Kampel, N. S. & Regal, C. A. Strong optomechanical squeezing of light. *Physical Review X* **3**, 031012 (2013).
106. Brooks, D. W. *et al.* Non-classical light generated by quantum-noise-driven cavity optomechanics. *Nature* **488**, 476–480 (2012).
107. Pirkkalainen, J.-M., Damskägg, E., Brandt, M., Massel, F. & Sillanpää, M. A. Squeezing of quantum noise of motion in a micromechanical resonator. *Physical Review Letters* **115**, 243601 (2015).
108. Safavi-Naeini, A. H. *et al.* Squeezed light from a silicon micromechanical resonator. *Nature* **500**, 185–189 (2013).
109. Schreppler, S. *et al.* Optically measuring force near the standard quantum limit. *Science* **344**, 1486–1489 (2014).
110. McNeil, K., Drummond, P. & Walls, D. Self pulsing in second harmonic generation. *Optics Communications* **27**, 292–294 (1978).
111. Børkje, K. Critical quantum fluctuations and photon antibunching in optomechanical systems with large single-photon cooperativity. *Physical Review A* **101**, 053833 (2020).
112. Han, X., Zou, C.-L. & Tang, H. X. Multimode strong coupling in superconducting cavity piezoelectromechanics. *Physical Review Letters* **117**, 123603 (2016).
113. Zoepfl, D., Juan, M., Schneider, C. & Kirchmair, G. Single-photon cooling in microwave magnetomechanics. *Physical Review Letters* **125**, 023601 (2020).
114. Gustafsson, M. V. *et al.* Propagating phonons coupled to an artificial atom. *Science* **346**, 207–211 (2014).
115. Guo, J., Norte, R. & Gröblacher, S. Feedback cooling of a room temperature mechanical oscillator close to its motional ground state. *Physical Review Letters* **123**, 223602 (2019).
116. Reinhardt, C., Müller, T., Bourassa, A. & Sankey, J. C. Ultralow-noise SiN trampoline resonators for sensing and optomechanics. *Physical Review X* **6**, 021001 (2016).
117. Huang, S. & Agarwal, G. Normal-mode splitting and antibunching in Stokes and anti-Stokes processes in cavity optomechanics: radiation-pressure-induced four-wave-mixing cavity optomechanics. *Physical Review A* **81**, 033830 (2010).
118. Ludwig, M., Kubala, B. & Marquardt, F. The optomechanical instability in the quantum regime. *New Journal of Physics* **10**, 095013 (2008).

119. Murch, K. W., Moore, K. L., Gupta, S. & Stamper-Kurn, D. M. Observation of quantum-measurement backaction with an ultracold atomic gas. *Nature Physics* **4**, 561–564 (2008).
120. Nunnenkamp, A., Børkje, K. & Girvin, S. M. Single-photon optomechanics. *Physical Review Letters* **107**, 063602 (2011).
121. Rabl, P. Photon blockade effect in optomechanical systems. *Physical Review Letters* **107**, 063601 (2011).
122. Kronwald, A., Ludwig, M. & Marquardt, F. Full photon statistics of a light beam transmitted through an optomechanical system. *Physical Review A* **87**, 013847 (2013).
123. Qian, J., Clerk, A., Hammerer, K. & Marquardt, F. Quantum signatures of the optomechanical instability. *Physical Review Letters* **109**, 253601 (2012).
124. Laplace, P.-S. *A Philosophical Essay on Probabilities* (Courier Corporation, 1814).
125. Earman, J. *A primer on determinism* (Springer Science & Business Media, 1986).
126. Malament, D. B. Norton’s slippery slope. *Philosophy of Science* **75**, 799–816 (2008).
127. Nurgalieva, N. & Renner, R. Testing quantum theory with thought experiments. *Contemporary Physics* **61**, 193–216 (2020).
128. Boyer, C., Einstein, A. & Infeld, L. *The Evolution of Physics: The Growth of Ideas From Early Concepts to Relativity and Quanta* (Cambridge: Cambridge University Press (2nd edition, 1961), 1938).
129. Scully, M. O. & Zubairy, M. S. *Quantum optics* (American Association of Physics Teachers, 1999).
130. Newell, C. *Applications of queueing theory* (Springer Science & Business Media, 2013).
131. Zou, X. & Mandel, L. Photon-antibunching and sub-Poissonian photon statistics. *Physical Review A* **41**, 475 (1990).
132. Kelley, P. & Kleiner, W. Theory of electromagnetic field measurement and photo-electron counting. *Physical Review* **136**, A316 (1964).
133. Lemonde, M.-A., Didier, N. & Clerk, A. A. Antibunching and unconventional photon blockade with Gaussian squeezed states. *Physical Review A* **90**, 063824 (2014).
134. Leonov, V. P. & Shiryaev, A. N. On a method of calculation of semi-invariants. *Theory of Probability & its applications* **4**, 319–329 (1959).
135. Zavatta, A., Viciani, S. & Bellini, M. Single-photon excitation of a coherent state: catching the elementary step of stimulated light emission. *Physical Review A* **72**, 023820 (2005).
136. Lee, C. T. Theorem on nonclassical states. *Physical Review A* **52**, 3374 (1995).
137. Kim, M., Park, E., Knight, P. & Jeong, H. Nonclassicality of a photon-subtracted Gaussian field. *Physical Review A* **71**, 043805 (2005).

138. Wenger, J., Tualle-Brouri, R. & Grangier, P. Non-Gaussian statistics from individual pulses of squeezed light. *Physical Review Letters* **92**, 153601 (2004).
139. Kiesel, T., Vogel, W., Parigi, V., Zavatta, A. & Bellini, M. Experimental determination of a nonclassical Glauber-Sudarshan P function. *Physical Review A* **78**, 021804 (2008).
140. Zavatta, A., Parigi, V., Kim, M. & Bellini, M. Subtracting photons from arbitrary light fields: experimental test of coherent state invariance by single-photon annihilation. *New Journal of Physics* **10**, 123006 (2008).
141. Brogaard, J. *Wigner function formalism in Quantum mechanics* PhD thesis (Niels Bohr Institute University of Copenhagen, 2015).
142. Ballentine, L. E. *Quantum mechanics: a modern development* (World Scientific Publishing Company, 2014).
143. Royer, A. Wigner function as the expectation value of a parity operator. *Physical Review A* **15**, 449 (1977).
144. Cahill, K. E. & Glauber, R. J. Density operators and quasiprobability distributions. *Physical Review* **177**, 1882 (1969).
145. Cahill, K. E. & Glauber, R. J. Ordered expansions in boson amplitude operators. *Physical Review* **177**, 1857 (1969).
146. Eichler, C. *et al.* Experimental state tomography of itinerant single microwave photons. *Physical Review Letters* **106**, 220503 (2011).
147. Bužek, V., Adam, G. & Drobny, G. Quantum state reconstruction and detection of quantum coherences on different observation levels. *Physical Review A* **54**, 804 (1996).
148. Haroche, S. & Raimond, J.-M. *Exploring the quantum: atoms, cavities, and photons* (Oxford university press, 2006).
149. Lachman, L., Straka, I., Hloušek, J., Ježek, M. & Filip, R. Faithful hierarchy of genuine n-photon quantum non-Gaussian light. *Physical Review Letters* **123**, 043601 (2019).
150. Filip, R. Hierarchy of quantum non-Gaussian States: Theory and Experiment, W2B–1 (2021).
151. Filip, R. & Lachman, L. Hierarchy of feasible nonclassicality criteria for sources of photons. *Physical Review A* **88**, 043827 (2013).
152. Straka, I. *et al.* Quantum non-Gaussian depth of single-photon states. *Physical Review Letters* **113**, 223603 (2014).
153. Titulaer, U. & Glauber, R. Correlation functions for coherent fields. *Physical Review* **140**, B676 (1965).
154. Duan, L.-M., Lukin, M. D., Cirac, J. I. & Zoller, P. Long-distance quantum communication with atomic ensembles and linear optics. *Nature* **414**, 413–418 (2001).

155. Clauser, J. F., Horne, M. A., Shimony, A. & Holt, R. A. Proposed experiment to test local hidden-variable theories. *Physical Review Letters* **23**, 880 (1969).
156. Leggett, A. J. & Garg, A. Quantum mechanics versus macroscopic realism: Is the flux there when nobody looks? *Physical Review Letters* **54**, 857 (1985).
157. Cirel'son, B. S. Quantum generalizations of Bell's inequality. *Letters in Mathematical Physics* **4**, 93–100 (1980).
158. Marek, P., Lachman, L., Slodička, L. & Filip, R. Deterministic nonclassicality for quantum-mechanical oscillators in thermal states. *Physical Review A* **94**, 013850 (2016).
159. Lachman, L. & Filip, R. Quantum non-Gaussian photon coincidences. *Physical Review Letters* **126**, 213604 (2021).
160. Filip, R. & Mišta Jr, L. Detecting quantum states with a positive Wigner function beyond mixtures of Gaussian states. *Physical Review Letters* **106**, 200401 (2011).
161. Zurek, W. H. Decoherence, einselection, and the quantum origins of the classical. *Reviews of Modern Physics* **75**, 715 (2003).
162. Schlosshauer, M. Decoherence, the measurement problem, and interpretations of quantum mechanics. *Reviews of Modern Physics* **76**, 1267 (2005).
163. Wheeler, J. A. Geons. *Physical Review* **97**, 511 (1955).
164. Rovelli, C. *Quantum gravity* (Cambridge university press, 2004).
165. Rovelli, C. & Smolin, L. Discreteness of area and volume in quantum gravity. *Nuclear Physics B* **442**, 593–619 (1995).
166. Loll, R. Discrete approaches to quantum gravity in four dimensions. *Living Reviews in Relativity* **1**, 1–53 (1998).
167. Snyder, H. S. Quantized space-time. *Physical Review* **71**, 38 (1947).
168. Gambini, R., Porto, R. A. & Pullin, J. Realistic clocks, universal decoherence, and the black hole information paradox. *Physical Review Letters* **93**, 240401 (2004).
169. Wang, C. H., Bingham, R. & Mendonca, J. T. Quantum gravitational decoherence of matter waves. *Classical and Quantum Gravity* **23**, L59 (2006).
170. Pikovski, I., Vanner, M. R., Aspelmeyer, M., Kim, M. & Brukner, Č. Probing Planck-scale physics with quantum optics. *Nature Physics* **8**, 393–397 (2012).
171. Bawaj, M. *et al.* Probing deformed commutators with macroscopic harmonic oscillators. *Nature Communications* **6**, 7503 (2015).
172. Marin, F. *et al.* Gravitational bar detectors set limits to Planck-scale physics on macroscopic variables. *Nature Physics* **9**, 71–73 (2013).
173. Giulini, D. & Großardt, A. The Schrödinger–Newton equation as a non-relativistic limit of self-gravitating Klein–Gordon and Dirac fields. *Classical and Quantum Gravity* **29**, 215010 (2012).

174. Schrinski, B. *et al.* Macroscopic quantum test with bulk acoustic wave resonators. *Physical Review Letters* **130**, 133604 (2023).
175. Bild, M. *et al.* Schrödinger cat states of a 16-microgram mechanical oscillator. *Science* **380**, 274–278 (2023).
176. Arndt, M. *et al.* Wave–particle duality of C<sub>60</sub> molecules. *Nature* **401**, 680–682 (1999).
177. Dimopoulos, S., Graham, P. W., Hogan, J. M. & Kasevich, M. A. Testing general relativity with atom interferometry. *Physical Review Letters* **98**, 111102 (2007).
178. Fein, Y. Y. *et al.* Quantum superposition of molecules beyond 25 kDa. *Nature Physics* **15**, 1242–1245 (2019).
179. Xu, V. *et al.* Probing gravity by holding atoms for 20 seconds. *Science* **366**, 745–749 (2019).
180. Panda, C. D. *et al.* Quantum metrology by one-minute interrogation of a coherent atomic spatial superposition. *arXiv:2210.07289* (2022).
181. Carney, D. *et al.* Snowmass 2021 White Paper: Tabletop experiments for infrared quantum gravity. *arXiv:2203.11846* (2022).
182. Carney, D., Müller, H. & Taylor, J. M. Using an atom interferometer to infer gravitational entanglement generation. *PRX Quantum* **2**, 030330 (2021).
183. Overstreet, C., Asenbaum, P., Curti, J., Kim, M. & Kasevich, M. A. Observation of a gravitational Aharonov-Bohm effect. *Science* **375**, 226–229 (2022).
184. Dickerson, S. M., Hogan, J. M., Sugarbaker, A., Johnson, D. M. & Kasevich, M. A. Multiaxis inertial sensing with long-time point source atom interferometry. *Physical Review Letters* **111**, 083001 (2013).
185. Bothwell, T. *et al.* Resolving the gravitational redshift across a millimetre-scale atomic sample. *Nature* **602**, 420–424 (2022).
186. Pikovski, I., Zych, M., Costa, F. & Brukner, Č. Universal decoherence due to gravitational time dilation. *Nature Physics* **11**, 668–672 (2015).
187. Bose, S. *et al.* Testing the quantum coherent behaviour of gravity. *Proceedings of Science* (2018).
188. Belenchia, A. *et al.* Tests of quantum-gravity-induced nonlocality via optomechanical experiments. *Physical Review D* **95**, 026012 (2017).
189. Belenchia, A. *et al.* Tests of Quantum Gravity-Induced Non-Locality: Hamiltonian formulation of a non-local harmonic oscillator. *Classical and Quantum Gravity* **36**, 155006 (2019).
190. Bose, S., Home, D. & Mal, S. Nonclassicality of the Harmonic-Oscillator Coherent State Persisting up to the Macroscopic Domain. *Physical Review Letters* **120**, 210402. ISSN: 10797114 (2018).

191. Marshall, W., Simon, C., Penrose, R. & Bouwmeester, D. Towards quantum superpositions of a mirror. *Physical Review Letters* **91**, 130401 (2003).
192. Nimmrichter, S. & Hornberger, K. Macroscopicity of mechanical quantum superposition states – Supplementary Material. <http://link.aps.org/supplemental/10.1103/PhysRevLett.110.160403>.
193. Holevo, A. S. A note on covariant dynamical semigroups. *Reports on Mathematical Physics* **32**, 211–216 (1993).
194. Vacchini, B. On the precise connection between the GRW master equation and master equations for the description of decoherence. *Journal of Physics A: Mathematical and Theoretical* **40**, 2463 (2007).
195. Bojowald, M. & Kempf, A. Generalized uncertainty principles and localization of a particle in discrete space. *Physical Review D* **86**, 085017 (2012).
196. Scardigli, F. Generalized uncertainty principle in quantum gravity from micro-black hole gedanken experiment. *Physics Letters B* **452**, 39–44 (1999).
197. Maggiore, M. A generalized uncertainty principle in quantum gravity. *Physics Letters B* **304**, 65–69 (1993).
198. Bombelli, L., Lee, J., Meyer, D. & Sorkin, R. D. Space-time as a causal set. *Physical review letters* **59**, 521 (1987).
199. Benincasa, D. M. & Dowker, F. Scalar curvature of a causal set. *Physical Review Letters* **104**, 181301 (2010).
200. Gambini, R. & Pullin, J. Emergence of stringlike physics from Lorentz invariance in loop quantum gravity. *International Journal of Modern Physics D* **23**, 1442023 (2014).
201. Woodard, R. P. The theorem of Ostrogradsky. *arXiv:1506.02210* (2015).
202. Biswas, T. & Okada, N. Towards LHC physics with nonlocal Standard Model. *Nuclear Physics B* **898**, 113–131 (2015).
203. Kashkanova, A. *Optomechanics with Superfluid Helium* PhD thesis (Yale University, 2017).
204. Shkarin, A. *Quantum Optomechanics with Superfluid Helium* PhD thesis (Yale University, 2017).
205. Yu, J. *Quantum Optomechanics with Superfluid Helium* PhD thesis (Yale University, 2023).
206. Hunger, D., Deutsch, C., Barbour, R. J., Warburton, R. J. & Reichel, J. Laser micro-fabrication of concave, low-roughness features in silica. *Aip Advances* **2**, 012119 (2012).
207. Ott, K. *et al.* Millimeter-long fiber Fabry-Perot cavities. *Optics Express* **24**, 9839–9853 (2016).

208. Hunger, D. *et al.* A fiber Fabry–Perot cavity with high finesse. *New Journal of Physics* **12**, 065038 (2010).
209. Zangwill, A. *Modern Electrodynamics* (Cambridge University Press, 2013).
210. Yu, P.-L. *et al.* A phononic bandgap shield for high-Q membrane microresonators. *Applied Physics Letters* **104**, 023510 (2014).
211. Surko, C., Dick, G., Reif, F. & Walker, W. Spectroscopic study of liquid helium in the vacuum ultraviolet. *Physical Review Letters* **23**, 842 (1969).
212. Gillan, M. & Halley, J. W. Theory of Optical Absorption in a Simple Liquid with Application to Liquid Helium. *Phys. Rev. A* **1**, 484–496 (2 1970).
213. Seidel, G., Lanou, R. & Yao, W. Rayleigh scattering in rare-gas liquids. *Nuclear Instruments and Methods in Physics Research Section A: Accelerators, Spectrometers, Detectors and Associated Equipment* **489**, 189–194 (2002).
214. Maris, H. J. & Massey, W. E. Phonon dispersion and the propagation of sound in liquid helium-4 below 0.6 K. *Physical Review Letters* **25**, 220 (1970).
215. Pethick, C. & Ter Haar, D. On the attenuation of sound in liquid helium. *Physica* **32**, 1905–1920 (1966).
216. Abraham, B., Eckstein, Y., Ketterson, J., Kuchnir, M. & Vignos, J. Sound Propagation in Liquid He 4. *Physical Review* **181**, 347 (1969).
217. Pobell, F. *Matter and methods at low temperatures* (Springer Science & Business Media, 2007).
218. Vadakkumbatt, V. *et al.* Prototype superfluid gravitational wave detector. *Physical Review D* **104**, 082001 (2021).
219. Donnelly, R. J. *Quantized vortices in helium II* (Cambridge University Press, 1991).
220. Vinen, W. & Niemela, J. Quantum turbulence. *Journal of Low Temperature Physics* **128**, 167–231 (2002).
221. Sachkou, Y. P. *et al.* Coherent vortex dynamics in a strongly interacting superfluid on a silicon chip. *Science* **366**, 1480–1485 (2019).
222. Forstner, S. *et al.* Modelling of vorticity, sound and their interaction in two-dimensional superfluids. *New Journal of Physics* **21**, 053029 (2019).
223. Atkins, K. Third and fourth sound in liquid helium II. *Physical Review* **113**, 962 (1959).
224. Sfendla, Y. L. *et al.* Extreme quantum nonlinearity in superfluid thin-film surface waves. *npj Quantum Information* **7**, 62 (2021).
225. Harris, G. *et al.* Laser cooling and control of excitations in superfluid helium. *Nature Physics* **12**, 788–793 (2016).
226. Brown, C. *et al.* Characterization of Levitated Superfluid Helium Drops in High Vacuum. *arXiv:2109.05618* (2021).

227. Spence, S., Koong, Z., Horsley, S. & Rojas, X. Superfluid optomechanics with phononic nanostructures. *Physical Review Applied* **15**, 034090 (2021).
228. He, X. *et al.* Strong optical coupling through superfluid Brillouin lasing. *Nature Physics* **16**, 417–421 (2020).
229. Childress, L. *et al.* Cavity optomechanics in a levitated helium drop. *Physical Review A* **96**, 063842 (2017).
230. Landau, L. Theory of the superfluidity of helium II. *Physical Review* **60**, 356 (1941).
231. Landau, L. & Pomeranchuk, I. *On the Movement of Foreign Particles in Helium II* in *Doklady Adademii Nauk SSSR* **59** (1948).
232. Landau, L. & Khalatnikov, I. Theory of the superfluidity of helium II. *Journal of Experimental and Theoretical Physics* **19**, 637 (1949).
233. Khalatnikov, I. & Chernikova, D. Relaxation phenomena in superfluid Helium. *Sov. Phys. JETP* **22**, 1336–1346 (1966).
234. Kurkjian, H., Castin, Y. & Sinatra, A. Three-Phonon and Four-Phonon Interaction Processes in a Pair-Condensed Fermi Gas. *Annalen der Physik* **529**, 1600352 (2017).
235. Agarwal, G. & Jha, S. S. Theory of optomechanical interactions in superfluid He. *Physical Review A* **90**, 023812 (2014).
236. Hadfield, R. H. Single-photon detectors for optical quantum information applications. *Nature Photonics* **3**, 696–705 (2009).
237. Meng, Y. *et al.* Fractal superconducting nanowires detect infrared single photons with 84% system detection efficiency, 1.02 polarization sensitivity, and 20.8 ps timing resolution. *ACS Photonics* **9**, 1547–1553 (2022).
238. Dauler, E. A. *et al.* Review of superconducting nanowire single-photon detector system design options and demonstrated performance. *Optical Engineering* **53**, 081907–081907 (2014).
239. Zheng, F. *et al.* Design of a polarization-insensitive superconducting nanowire single photon detector with high detection efficiency. *Scientific Reports* **6**, 22710 (2016).
240. Cheng, R. *et al.* A 100-pixel photon-number-resolving detector unveiling photon statistics. *Nature Photonics* **17**, 112–119 (2023).
241. Divochiy, A. *et al.* Superconducting nanowire photon-number-resolving detector at telecommunication wavelengths. *Nature Photonics* **2**, 302–306 (2008).
242. Burenkov, V., Xu, H., Qi, B., Hadfield, R. H. & Lo, H.-K. Investigations of afterpulsing and detection efficiency recovery in superconducting nanowire single-photon detectors. *Journal of Applied Physics* **113**, 213102 (2013).
243. Fujiwara, M. *et al.* Afterpulse-like phenomenon of superconducting single photon detector in high speed quantum key distribution system. *Optics Express* **19**, 19562–19571 (2011).

244. Natarajan, C. M., Tanner, M. G. & Hadfield, R. H. Superconducting nanowire single-photon detectors: physics and applications. *Superconductor Science and Technology* **25**, 063001 (2012).
245. Enzian, G. *et al.* Non-Gaussian mechanical motion via single and multiphonon subtraction from a thermal state. *Physical Review Letters* **127**, 243601 (2021).
246. Enzian, G. *et al.* Single-phonon addition and subtraction to a mechanical thermal state. *Physical Review Letters* **126**, 033601 (2021).
247. Lee, K. C. *et al.* Entangling macroscopic diamonds at room temperature. *Science* **334**, 1253–1256 (2011).
248. Velez, S. T. *et al.* Preparation and decay of a single quantum of vibration at ambient conditions. *Physical Review X* **9**, 041007 (2019).
249. Patel, R. N. *et al.* Room-temperature mechanical resonator with a single added or subtracted phonon. *Physical Review Letters* **127**, 133602 (2021).
250. Shelby, R., Levenson, M. & Bayer, P. Guided acoustic-wave Brillouin scattering. *Physical Review B* **31**, 5244 (1985).
251. Takefushi, N., Yoshida, M., Kasai, K., Hirooka, T. & Nakazawa, M. *GAWBS noise characteristics in digital coherent transmission in various optical fibers* in 2019 24th OptoElectronics and Communications Conference (OECC) and 2019 International Conference on Photonics in Switching and Computing (PSC) (2019), 1–3.
252. Li, Y., Chen, X. & Fisher, M. P. Measurement-driven entanglement transition in hybrid quantum circuits. *Physical Review B* **100**, 134306 (2019).
253. Min, Y. & Agresti, A. Modeling nonnegative data with clumping at zero: a survey (2002).
254. Schrödinger, E. Der stetige Übergang von der Mikro-zur Makromechanik. *Naturwissenschaften* **14**, 664–666 (1926).
255. Zhang, W. M., Feng, D. H. & Gilmore, R. Coherent states: Theory and some applications. *Reviews of Modern Physics* **62**, 867–927. ISSN: 00346861 (1990).
256. Glauber, R. J. Coherent and incoherent states of the radiation field. *Physical Review* **131**, 2766–2788. ISSN: 0031899X (1963).
257. Glauber, R. J. The quantum theory of optical coherence. *Physical Review* **130**, 2529–2539. ISSN: 0031899X (1963).
258. Glauber, R. J. Photon correlations. *Physical Review Letters* **10**, 84–86. ISSN: 00319007 (1963).
259. Mandel, L. & Wolf, E. *Optical coherence and quantum optics* (Cambridge university press, 1995).
260. Zurek, W. H., Habib, S. & Paz, J. P. Coherent states via decoherence. *Physical Review Letters* **70**, 1187–1190 (Mar. 1993).

261. Davidson, F. & Mandel, L. Correlation measurements of laser beam fluctuations near threshold. *Physics Letters A* **25**, 700–701. ISSN: 03759601 (1967).
262. Chopra, S. & Mandel, L. Higher-order correlation properties of a laser beam. *Physical Review Letters* **30**, 60–63. ISSN: 00319007 (1973).
263. Noel, M. W. & Stroud, C. R. Excitation of an atomic electron to a coherent superposition of macroscopically distinct states. *Physical Review Letters* **77**, 1913–1916. ISSN: 10797114 (1996).
264. Vela-Arevalo, L. V. & Fox, R. F. Coherent states of the driven Rydberg atom: Quantum-classical correspondence of periodically driven systems. *Physical Review A* **71**, 1–12. ISSN: 10502947 (2005).
265. Sato, T. Analytical model for estimating terrestrial cosmic ray fluxes nearly anytime and anywhere in the world: Extension of PARMA/EXPACS. *PloS One* **10**, e0144679 (2015).
266. Teufel, J. D., Donner, T., Castellanos-Beltran, M. A., Harlow, J. W. & Lehnert, K. W. Nanomechanical motion measured with an imprecision below that at the standard quantum limit. *Nature Nanotechnology* **4**, 820–823 (2009).
267. Afek, G., Carney, D. & Moore, D. C. Coherent Scattering of Low Mass Dark Matter from Optically Trapped Sensors. *Physical Review Letters* **128**, 101301. ISSN: 10797114 (2022).
268. Monteiro, F. *et al.* Search for Composite Dark Matter with Optically Levitated Sensors. *Physical Review Letters* **125**, 181102. ISSN: 10797114 (2020).
269. Essig, R. The Low-Mass Dark Matter Frontier. *Physics* **13**, 1–6 (2020).
270. Caputo, A., Esposito, A. & Polosa, A. D. Sub-MeV dark matter and the Goldstone modes of superfluid helium. *Physical Review D* **100**, 116007. ISSN: 24700029 (2019).
271. Murgui, C., Wang, Y. & Zurek, K. M. Axion Detection with Optomechanical Cavities. *arXiv preprint arXiv:2211.08432* (2022).
272. Singh, S., De Lorenzo, L., Pikovski, I. & Schwab, K. Detecting continuous gravitational waves with superfluid  $^4\text{He}$ . *New Journal of Physics* **19**, 073023 (2017).
273. Carney, D., Stamp, P. C. & Taylor, J. M. Tabletop experiments for quantum gravity: A user’s manual. *Classical and Quantum Gravity* **36**. ISSN: 13616382 (2019).
274. Clerk, A. A., Devoret, M. H., Girvin, S. M., Marquardt, F. & Schoelkopf, R. J. Introduction to quantum noise, measurement, and amplification. *Reviews of Modern Physics* **82**, 1155 (2010).
275. Zoller, P. *et al.* Quantum information processing and communication: Strategic report on current status, visions and goals for research in Europe. *The European Physical Journal D-Atomic, Molecular, Optical and Plasma Physics* **36**, 203–228 (2005).

276. Wang, Y. *et al.* Single-qubit quantum memory exceeding ten-minute coherence time. *Nature Photonics* **11**, 646–650 (2017).
277. Stute, A. *et al.* Quantum-state transfer from an ion to a photon. *Nature Photonics* **7**, 219–222 (2013).
278. Wilk, T., Webster, S. C., Kuhn, A. & Rempe, G. Single-atom single-photon quantum interface. *Science* **317**, 488–490 (2007).
279. Van der Wal, C. H. *et al.* Atomic memory for correlated photon states. *Science* **301**, 196–200 (2003).
280. Yang, S.-J., Wang, X.-J., Bao, X.-H. & Pan, J.-W. An efficient quantum light–matter interface with sub-second lifetime. *Nature Photonics* **10**, 381–384 (2016).
281. Wang, Y. *et al.* Efficient quantum memory for single-photon polarization qubits. *Nature Photonics* **13**, 346–351 (2019).
282. Kalb, N., Reiserer, A., Ritter, S. & Rempe, G. Heralded storage of a photonic quantum bit in a single atom. *Physical Review Letters* **114**, 220501 (2015).
283. Bradley, C. E. *et al.* A ten-qubit solid-state spin register with quantum memory up to one minute. *Physical Review X* **9**, 031045 (2019).
284. Saglamyurek, E. *et al.* Quantum storage of entangled telecom-wavelength photons in an erbium-doped optical fibre. *Nature Photonics* **9**, 83–87 (2015).
285. Yılmaz, S., Fallahi, P. & Imamoğlu, A. Quantum-dot-spin single-photon interface. *Physical Review Letters* **105**, 033601 (2010).
286. Fiaschi, N. *et al.* Optomechanical quantum teleportation. *Nature Photonics* **15**, 817–821 (2021).
287. Hu, X.-M., Guo, Y., Liu, B.-H., Li, C.-F. & Guo, G.-C. Progress in quantum teleportation. *Nature Reviews Physics*, 1–15 (2023).
288. Wu, L.-A., Kimble, H., Hall, J. & Wu, H. Generation of squeezed states by parametric down conversion. *Physical Review Letters* **57**, 2520 (1986).
289. Børkje, K., Nunnenkamp, A. & Girvin, S. Supplementary Material to “Proposal for entangling remote micromechanical oscillators via optical measurements”.
290. André, A., Duan, L.-M. & Lukin, M. Coherent atom interactions mediated by dark-state polaritons. *Physical Review Letters* **88**, 243602 (2002).
291. Gulati, G. K., Takahashi, H., Podoliak, N., Horak, P. & Keller, M. Fiber cavities with integrated mode matching optics. *Scientific Reports* **7**, 5556 (2017).
292. Raha, M. *et al.* Optical quantum nondemolition measurement of a single rare earth ion qubit. *Nature Communications* **11**, 1605 (2020).
293. Marinković, I. *et al.* Optomechanical bell test. *Physical Review Letters* **121**, 220404 (2018).

294. Donnelly, R. J. & Barenghi, C. F. The observed properties of liquid helium at the saturated vapor pressure. *Journal of Physical and Chemical Reference Data* **27**, 1217–1274 (1998).
295. Trefethen, L. N. *Approximation Theory and Approximation Practice, Extended Edition* (SIAM, 2019).